WL-TR-96-3125

DEVELOPMENT AND TESTING OF A NEW OPTIMUM DESIGN CODE FOR HYPERSONIC WIND TUNNEL NOZZLES, INCLUDING BOUNDARY LAYER, TURBULENCE, AND REAL GAS EFFECTS

RALPH C. TOLLE

OCTOBER 1996

FINAL REPORT FOR 07/01/92-11/19/95

APPROVED FOR PUBLIC RELEASE; DISTRIBUTION IS UNLIMITED.

FLIGHT DYNAMICS DIRECTORATE
WRIGHT LABORATORY
AIR FORCE MATERIEL COMMAND
WRIGHT PATTERSON AFB OH 45433-7562

NOTICE

WHEN GOVERNMENT DRAWINGS, SPECIFICATIONS, OR OTHER DATA ARE USED FOR ANY PURPOSE OTHER THAN IN CONNECTION WITH A DEFINITELY GOVERNMENT-RELATED PROCUREMENT, THE UNITED STATES GOVERNMENT INCURS NO RESPONSIBILITY OR ANY OBLIGATION WHATSOEVER. THE FACT THAT THE GOVERNMENT MAY HAVE FORMULATED OR IN ANY WAY SUPPLIED THE SAID DRAWINGS, SPECIFICATIONS, OR OTHER DATA, IS NOT TO BE REGARDED BY IMPLICATION, OR OTHERWISE IN any MANNER CONSTRUED, AS LICENSING THE HOLDER, OR ANY OTHER PERSON OR CORPORATION; OR AS CONVEYING ANY RIGHTS OR PERMISSION TO MANUFACTURE, USE, OR SELL ANY PATENTED INVENTION THAT MAY IN ANY WAY BE RELATED THERETO.

THIS REPORT IS RELEASABLE TO THE NATIONAL TECHNICAL INFORMATION SERVICE (NTIS). AT NTIS, IT WILL BE AVAILABLE TO THE GENERAL PUBLIC, INCLUDING FOREIGN NATIONS.

THE TECHNICAL REPORT HAS BEEN REVIEWED AND IS APPROVED FOR PUBLICATION.

[Monitor signature block]

[supervisor signature block]

[3-ltr chief signaure block]

IF YOUR ADDRESS HAS CHANGED, IF YOU WISH TO BE REMOVED FROM OUR MAILING LIST, OR IF THE ADDRESSEE IS NO LONGER EMPLOYED BY YOUR ORGANIZATION PLEASE NOTIFY, WL/FIM , WPAFB, OH 45433-7912 TO HELP MAINTAIN A CURRENT MAILING LIST.

Copies of this report should not be returned unless return is required by Security Consideration, contractual obligations, or notice on a specific document.

DISCLAIMER NOTICE

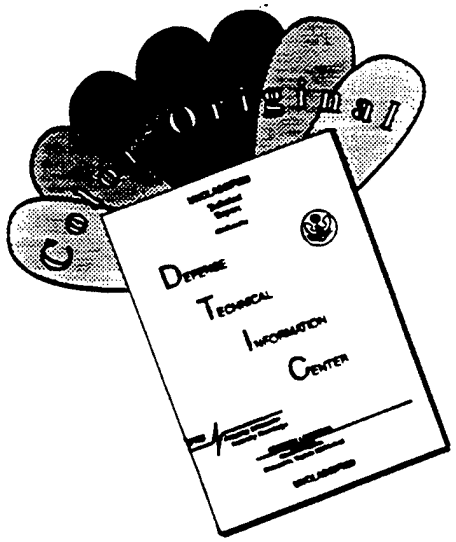

THIS DOCUMENT IS BEST QUALITY AVAILABLE. THE COPY FURNISHED TO DTIC CONTAINED A SIGNIFICANT NUMBER OF COLOR PAGES WHICH DO NOT REPRODUCE LEGIBLY ON BLACK AND WHITE MICROFICHE.

REPORT DOCUMENTATION PAGE

Form Approved
OMB No. 0704-0188

1. AGENCY USE ONLY (Leave blank)	2. REPORT DATE	3. REPORT TYPE AND DATES COVERED
	OCT 1996	FINAL 07/01/92--11/19/95

4. TITLE AND SUBTITLE DEVELOPMENT AND TESTING OF A NEW OPTIMUM DESIGN CODE FOR HYPERSONIC WIND TUNNEL NOZZLES, INCLUDING BOUNDARY LAYER, TURBULENCE, AND REAL GAS EFFECTS

5. FUNDING NUMBERS
C
PE
PR
TA
WU

6. AUTHOR(S) RALPH C. TOLLE

7. PERFORMING ORGANIZATION NAME(S) AND ADDRESS(ES)
FLIGHT DYNAMICS DIRECTORATE
WRIGHT LABORATORY
AIR FORCE MATERIEL COMMAND
WRIGHT PATTERSON AFB OH 45433-7562

8. PERFORMING ORGANIZATION REPORT NUMBER

9. SPONSORING/MONITORING AGENCY NAME(S) AND ADDRESS(ES)
FLIGHT DYNAMICS DIRECTORATE
WRIGHT LABORATORY
AIR FORCE MATERIEL COMMAND
WRIGHT PATTERSON AFB OH 45433-7562

10. SPONSORING/MONITORING AGENCY REPORT NUMBER
WL-TR-96-3125

11. SUPPLEMENTARY NOTES

12a. DISTRIBUTION/AVAILABILITY STATEMENT
APPROVED FOR PUBLIC RELEASE; DISTRIBUTION IS UNLIMITED.

12b. DISTRIBUTION CODE

13. ABSTRACT *(Maximum 200 words)*
A robust and efficient hypersonic nozzle optimization code is developed and validated. The code is used to redesign an existing axisymmetric Mach 12 wind tunnel nozzle and utilizes response surface methodology (RSM) techniques. In the nozzle optimization, only two variable design parameters are used, along with constraints of fixed nozzle length, throat radius, and exit radius. Explicit, globally second-order, flux-difference-splitting algorithms are used to solve the 2-D/axisymmetric Navier-Stokes (NS) and Parabolized Navier-Stokes (PNS) flow solvers incorporated into the optimizer code. Either the Baldwin-Lomax or the Yang-Shih k-epsilon turbulence model may be employed in the nozzle design. The optimization code is developed and validated, and is then used to optimize the Mach 12 nozzle design, and the computed results are compared with those of the original nozzle, the Wright Laboratory Mach 12 wind tunnel nozzle. The code is tested for robustness and on three separate occasions locates the global minimum synonymous with the "global best" optimized nozzle. The globally optimized nozzle is thus obtained in the two design parameter space, with modest but undesirable disturbances in the inviscid core at the nozzle exit. The RSM techniques used show good promise of greatly facilitating the hypersonic nozzle design process.

14. SUBJECT TERMS
Numerical Methods and Procedures, Computational Fluid Dynamics, Hypersonic Flow, Wind Tunnel Nozzles, Turbulence Models, Axisymmetric Nozzle Flow

15. NUMBER OF PAGES
274

16. PRICE CODE

17. SECURITY CLASSIFICATION OF REPORT	18. SECURITY CLASSIFICATION OF THIS PAGE	19. SECURITY CLASSIFICATION OF ABSTRACT	20. LIMITATION OF ABSTRACT
UNCLASSIFIED	UNCLASSIFIED	UNCLASSIFIED	SAR

GENERAL INSTRUCTIONS FOR COMPLETING SF 298

The Report Documentation Page (RDP) is used in announcing and cataloging reports. It is important that this information be consistent with the rest of the report, particularly the cover and title page. Instructions for filling in each block of the form follow. It is important to ***stay within the lines*** to meet ***optical scanning requirements***.

Block 1. Agency Use Only *(Leave blank)*.

Block 2. Report Date. Full publication date including day, month, and year, if available (e.g. 1 Jan 88). Must cite at least the year.

Block 3. Type of Report and Dates Covered. State whether report is interim, final, etc. If applicable, enter inclusive report dates (e.g. 10 Jun 87 - 30 Jun 88).

Block 4. Title and Subtitle. A title is taken from the part of the report that provides the most meaningful and complete information. When a report is prepared in more than one volume, repeat the primary title, add volume number, and include subtitle for the specific volume. On classified documents enter the title classification in parentheses.

Block 5. Funding Numbers. To include contract and grant numbers; may include program element number(s), project number(s), task number(s), and work unit number(s). Use the following labels:

C	- Contract	**PR**	- Project
G	- Grant	**TA**	- Task
PE	- Program Element	**WU**	- Work Unit Accession No.

Block 6. Author(s). Name(s) of person(s) responsible for writing the report, performing the research, or credited with the content of the report. If editor or compiler, this should follow the name(s).

Block 7. Performing Organization Name(s) and Address(es). Self-explanatory.

Block 8. Performing Organization Report Number. Enter the unique alphanumeric report number(s) assigned by the organization performing the report.

Block 9. Sponsoring/Monitoring Agency Name(s) and Address(es). Self-explanatory.

Block 10. Sponsoring/Monitoring Agency Report Number. *(If known)*

Block 11. Supplementary Notes. Enter information not included elsewhere such as: Prepared in cooperation with...; Trans. of...; To be published in.... When a report is revised, include a statement whether the new report supersedes or supplements the older report.

Block 12a. Distribution/Availability Statement. Denotes public availability or limitations. Cite any availability to the public. Enter additional limitations or special markings in all capitals (e.g. NOFORN, REL, ITAR).

- **DOD** - See DoDD 5230.24, "Distribution Statements on Technical Documents."
- **DOE** - See authorities.
- **NASA** - See Handbook NHB 2200.2.
- **NTIS** - Leave blank.

Block 12b. Distribution Code.

- **DOD** - Leave blank.
- **DOE** - Enter DOE distribution categories from the Standard Distribution for Unclassified Scientific and Technical Reports.
- **NASA** - Leave blank.
- **NTIS** - Leave blank.

Block 13. Abstract. Include a brief *(Maximum 200 words)* factual summary of the most significant information contained in the report.

Block 14. Subject Terms. Keywords or phrases identifying major subjects in the report.

Block 15. Number of Pages. Enter the total number of pages.

Block 16. Price Code. Enter appropriate price code *(NTIS only)*.

Blocks 17. - 19. Security Classifications. Self-explanatory. Enter U.S. Security Classification in accordance with U.S. Security Regulations (i.e., UNCLASSIFIED). If form contains classified information, stamp classification on the top and bottom of the page.

Block 20. Limitation of Abstract. This block must be completed to assign a limitation to the abstract. Enter either UL (unlimited) or SAR (same as report). An entry in this block is necessary if the abstract is to be limited. If blank, the abstract is assumed to be unlimited.

★U.S.GPO:1993-0-336-043

Acknowledgments

There are many people who deserve recognition for their contributions to this research. First and foremost, there is my wife who believed in me from the beginning, pushed me when she thought I needed it, and helped in more ways than I can even begin to mention here. She has been and will continue to be an inspiration to me. Additionally, my thanks to Noko and Ping for suffering much neglect throughout this research.

My thanks to the members of my committee: committee chairman Maj John Doty, Dr. Rodney Bowersox, and Capt Mike Stoecker; and to Dr. William Elrod and Col Gerald Hasen for their participation on my committee during the course of this work.

There were also a number of people whose valuable technical contributions were much appreciated and are greatly deserving of mention. Dr. Datta Gaitonde, who provided primary input in working the flow codes and who always made time for me and my incessant questions with regards to his code. Dr. John Korte of NASA Langley, who also provided much technical support; my tremendous gratitude goes to him for all that he did for me. Mr. Norm Scaggs of Wright Laboratory, who provided very valuable assistance and information concerning the test case wind tunnel nozzle. Others whose help was significant include Dr. Joe Shang, Mr. Eswar Josyula, and Dr. Don Rizzetta, all of Wright Laboratory. Last but

not least, my thanks to Dr. Vicky Tischler of Wright Laboratory for all of her help.

This work was supported in part by a grant of HPC time from the DoD HPC Shared Resource Center, CEWES, Vicksburg, MS.

Ralph C. Tolle

Table of Contents

List of Figures

List of Tables

List of Symbols

Symbol

$\mathbf{a}$	- Korte design parameters
a	- speed of sound
a_0, a_1, a_2	- Keye's Law viscosity coefficients
A	- cross-sectional area of nozzle
A^*	- cross-sectional area of nozzle throat
c	- speed of sound used in Roe scheme
c_p	- specific heat at constant pressure
c_v	- specific heat at constant volume
C_{e1}	- turbulence model constant, 1.44
C_{e2}	- turbulence model constant, 1.92
C_μ	- turbulence model constant, 0.09
D	- low-Reynolds number term for turbulence kinetic energy equation
e_i	- specific internal energy (c_vT for perfect gas air)
e_v	- vibrational energy per unit mass
$\dot{e}_v$	- vibrational energy production rate per unit mass
E	- total energy
E_e	- low-Reynolds number term for turbulence energy dissipation rate equation
Er	- nozzle exit error

Erl - nozzle centerline error

Ert - sum of nozzle exit and centerline errors

f_1 - k-ϵ model constant

f_μ, f_2 - damping functions in k-ϵ models

F, G - flux vectors (x,y)

$\tilde{F}$, $\tilde{G}$ - flux vectors (ξ,η) in computational coordinates

h_T - reservoir stagnation enthalpy

H - axisymmetric source term vector

H_T - stagnation enthalpy used in Roe scheme

i - x index; species index

I - Identity Matrix

j - y index; coordinate index

J - Jacobian of coordinate transformation

$\mathbf{J}_k$ - Jacobian matrix of $\mathbf{P}(\mathbf{a})$

k - turbulent kinetic energy

k_l - molecular thermal conductivity

k_t - turbulent thermal conductivity

L - flat plate length

M_t - turbulent Mach number, $\sqrt{\frac{k}{\gamma RT}}$

M_ξ - streamwise Mach number

p - static pressure

$p_{T_{Res}}$ - nozzle reservoir stagnation pressure

p'_T - nozzle flow stagnation pressure, compressibility accounted for

$\mathbf{P}$	- Korte objective function
P	- stagnation pressure
P_k	- turbulence production source term
Pr	- Prandtl number, 0.73 for air
Pr_t	- turbulent Prandtl number, 0.90
q	- heat transfer
R_L	- reference length
Re	- Reynolds number
Re_t	- turbulent Reynolds number, $\frac{\rho k^2}{\mu \epsilon}$
S	- k-ϵ source term vector
t	- time
t_c	- reference time unit, R_L/U_∞
$\bar{t}$	- nondimensional characteristic time unit, t/t_c
T	- temperature
T_i	- turbulence intensity
T_t	- turbulent time scale
$U, \tilde{U}$	- conserved dependent variable vector
u, v	- Cartesian velocity components in x,y directions
x, y	- Cartesian coordinates in axial and normal/radial directions
$\mathbf{X}$	- generic RSM design input tensor
X_1, X_2	- generic RSM design inputs
$\bar{X}_1, \bar{X}_2$	- generic RSM design inputs in transformed coordinates

y^+	- nondimensional wall coordinate used in turbulence modelling
$\mathbf{z}$	- RSM response vector
z	- RSM response function
α	- angle of attack
β_w, β_{cl}	- grid stretching parameters
γ	- specific heat ratio, 1.4 for perfect gas air
δ	- 2-D/axisymmetric switch (0/1)
$\delta_{i,j}$	- Kronecker delta
δ_λ	- entropy cutoff used in Roe Scheme
ϵ	- turbulence energy dissipation rate
θ_{attach}	- nozzle attachment angle
θ_{exit}	- nozzle exit angle
μ	- molecular viscosity coefficient
μ_t	- eddy viscosity coefficient
ξ, η	- computational coordinates in streamwise and normal directions
ρ	- density (kg/m^3)
σ_k, σ_ϵ	- turbulence model constants
$\tau_{xx}, \tau_{xy}, \tau_{yy}, \tau_{\theta\theta}$	- components of viscous stress tensor
ω	- weighting function used in nozzle error calculation

Subscripts

cl	- centerline
exit	- nozzle exit
I	- inviscid
inner	- inner region of the boundary layer
min	- minimum value
nc	- new nozzle throat corner
oc	- old nozzle throat corner
outer	- outer region of the boundary layer
Res	- nozzle reservoir
t	- turbulent
v	- viscous
w	- wall value
∞	- freestream value

Superscripts

c	- corrector
n	- time step or marching step index
p	- predictor

DEVELOPMENT AND TESTING OF A NEW OPTIMUM DESIGN CODE FOR HYPERSONIC WIND TUNNEL NOZZLES, INCLUDING BOUNDARY LAYER, TURBULENCE, AND REAL GAS EFFECTS

1. Introduction

This chapter presents the problem addressed by the current research, a short history of previously conducted research, the purpose and objectives for the present study, and an overview of the approach of this research to provide a foundation for the following chapters of this dissertation. It begins with a statement of the problem regarding previous and current design methods of hypersonic wind tunnel nozzles, which have inherent restrictions on accuracy or a high level of user interaction requirements. The chapter continues with a presentation of recently conducted research in the area of hypersonic nozzle design and research on the testbed nozzle for this investigation; the previously accomplished research aids in validating the developed

code. The chapter concludes with the purpose of this research and concludes with an overview of the research approach.

1.1 Problem

Both previous and current hypersonic wind tunnel nozzle design techniques have unique issues associated with them that result in some level of limitation on their application. The method of characteristics and boundary layer (MOC/BL) design technique was used by the hypersonic nozzle designers of yesteryear. The issue associated with this technique is its lack of accuracy in computing the flow in a hypersonic nozzle. Current design techniques are more accurate. However, in such methods, the optimization scheme does not account for nonequilibrium and chemical reaction effects and is somewhat restricted in its application. Such methods also require a high level of interaction and knowledge on the part of the design engineer.

In spite of the fact that hypersonic wind tunnels have been used for the last 30 to 40 years and that incredible advances have been made in CFD over the same time period, most hypersonic wind tunnels were designed based upon the MOC/BL method developed by Prandtl and Buseman in 1929 [1]. In this method, the inviscid core is determined through the MOC and is augmented by attaching a displacement thickness obtained from a BL solution. In a high Mach number wind tunnel nozzle ($M > 8$), with increasing design Mach

number this MOC/BL method suffers an increasing loss in accuracy as is shown below [2]. Such a loss in accuracy may not be acceptable for today's hypersonic aerospace vehicle designers or rocket nozzle designers; wind tunnel nozzles designed based on the MOC/BL method may be delivering test conditions different than those predicted by the original nozzle solution. Such wind tunnel nozzles are not delivering the predicted flow to the wind tunnel test section, and therefore designers of hypersonic vehicles are using less-than-desirable test section flow to obtain experimental results and to aid in validating their CFD solutions with experimental results. The hypersonics community has recognized this shortcoming associated with existing nozzles, and is currently focusing much CFD research and development on this problem.

Current hypersonic nozzle design procedures are much more accurate due to recent advances in CFD, but still fall short on several major fronts. First, the current optimization codes do not account for full vibrational nonequilibrium, chemical reaction effects which would likely be significant in a hypersonic nozzle. Second, the application of such optimization codes requires a smooth expansion corner in order to model the centerline Mach number distribution which is used to drive the optimization scheme. This requirement somewhat limits the applications to which the optimization code may be applied. And third, successful interaction at the necessary level with such codes demands that the design engineer be quite knowledgeable of the optimization

procedure; due to the complexity of the optimization scheme/code, the required understanding of the optimization procedure is at such a detailed level as to necessitate intensive training.

There is therefore a current need within the hypersonics community for an accurate, hypersonic nozzle design procedure which accounts for the possibility of chemical reaction effects, is broad in its potential applications, and requires a minimum of computer time and designer interaction.

1.2 History of Nozzle Research

This section presents two main topics: a history of research in hypersonic nozzle design, and a history of research conducted on the testbed for this investigation, that of the Wright Laboratory (WL) 20" Mach 12 wind tunnel nozzle.

1.2.1 History of Hypersonic Nozzle Design. This section is broken up into two parts which span the time in which numerical methods have been used to design hypersonic nozzles. The first part covers the classical MOC/BL method previously mentioned. The second part covers more recent hypersonic nozzle design methods.

1.2.1.1 The MOC/BL Method. The MOC/BL method is an iterative design process in which the inviscid core obtained by the MOC and the boundary layer interact in a loosely coupled fashion

through their respective boundary conditions (Fig. 1). Either a wall boundary is specified, from which the displacement thickness and inviscid core can be calculated, or the inviscid core and displacement thickness are calculated, from which the location of the wall boundary is determined. The iterations continue until some form of tolerance has been reached with regard to the location of the wall or some other parameter(s).

A detailed example of the MOC/BL process is given in detail in [2]. In this particular approach, the flow inviscid core is first generated using the MOC. The displacement thickness is then generated using the BL method and is added to the inviscid core to determine where the "hard" wall is located. Boundary layer corrections are subsequently performed and the resultant displacement thickness subtracted from the "hard" wall. At this point, the resulting streamline at the edge of the displacement thickness is compared to the inviscid streamline obtained through the MOC (Fig. 1). The nozzle exit inviscid core diameter is then resized, if necessary, to obtain a better match between the inviscid core and displacement thickness edge streamlines. Note that in this iterative method the exit diameter is constrained while the nozzle length is not.

As previously mentioned, the MOC/BL method becomes inaccurate for hypersonic nozzles with a design Mach number of 8 or more; this inaccuracy is a result of one major assumption inherent to this method [2]: the region of flow between the boundary layer edge and

the inviscid streamline is assumed to be inviscid and irrotational (Fig. 2). However, in reality, the flow in this region is both viscous and rotational, causing the "characteristic waves to curve toward the wall as the Mach number decreases" [2] (Fig. 2). Thus, the waves would likely not be reflected as they are assumed to with the inviscid, irrotational assumption. This deviation is small for low Mach numbers due to the incidence angle of the characteristic waves, which results in less distance spent in the outer viscous portion of the boundary layer (Fig. 3). However, for high Mach numbers, the incidence angle decreases, causing the characteristic wave to "remain in the viscous region for a much longer distance" [2]. Thus, "the effects of rotational flow would be more significant" [2]. Benton et al. conclude by recommending "that a (hypersonic nozzle) design method using the Parabolized Navier-Stokes Equations be developed" [2].

1.2.1.2 History of Recent Hypersonic Nozzle Design/Optimization Research.

Most of the current research in the optimization area has come about through the work of Korte, at NASA Langley. At the Naval Surface Warfare Center's Mach 14 Nozzle facility, Korte et al. have studied hypersonic flow physics through both computational and experimental efforts [9]. The research focused on providing better understanding of the flow physics for wind tunnel redesign purposes. The computational calculations

utilized the CAN-DO code developed by Korte [9]. This computer code was modified to account for vibrational equilibrium effects, and used the Baldwin-Lomax (B-L) and Cebeci-Smith (C-S) turbulence models. The vibrational equilibrium effects assumed thermally perfect, calorically imperfect gas. The gas that was studied was nitrogen (N_2). The computational results agreed well with the experimental data.

The Korte optimization method provided good results for the test case in [9] as well as those in [60]. However, as previously mentioned the method does have some inherent limitations. In boosting computational efficiency, the code was designed to account for at most vibrational equilibrium in the wind tunnel test gas. The possibility to design a hypersonic nozzle and account for vibrational nonequilibrium and chemical reaction effects is not currently available.

Additionally, the CAN-DO code requires a macroscopically smooth expansion corner in order to utilize a modification of Sivells' method for modeling the centerline Mach number distribution theoretically (Figs. 4 and 5) [9,36]. This distribution is used in the optimization scheme to drive the design nozzle's computed centerline Mach number distribution to match the theoretical one [9]. As previously mentioned, the requirement of a smooth expansion corner somewhat limits the applications to which the optimization code may be applied.

Finally, the CAN-DO code utilizes a complex optimization scheme which requires the nozzle wall to be specified with cubic splines sections. The nozzle design engineer must specify the number of cubic spline knots (junctions or nodes between adjacent cubic spline sections which define the nozzle wall) for the nozzle contour. The design engineer must also specify the axial location of the control points associated with the cubic spline knots on the nozzle contour. Determining the number of knots on the cubic spline and the location of the control points, is not a straightforward or easy process" [9]. Additional knots must be "added until a solution is obtained which satisfies the design requirements" [9]. All of these combine into a requirement for much interaction and knowledge on the part of the design engineer.

In further research associated with similar methods, Hackett has computed CFD flow field solutions for the NASA Langley Research Center's 15-Inch Mach 6 High Temperature Tunnel and 16-Inch Mach 17 Nitrogen Tunnel [26]. Full NS, PNS, and Method of Characteristics techniques were used, and the solutions were compared with tunnel calibration data. The research was performed to address the need for high-quality wind tunnel data against which to validate CFD codes. The comparisons between the CFD solutions and the experimental data for the Mach 6 tunnel were shown to be in good agreement (nozzle exit Pitot pressures up to ±3% different and excellent agreement in the exit Mach number profiles were seen between CFD solutions and the data). However, the comparisons for

the Mach 17 tunnel were not (nozzle exit Pitot pressures showed differences of up to 20% difference between CFD solutions and experimental data). This was attributed largely to inaccuracies of turbulence models for hypersonic flow (the B-L turbulence model was based upon incompressible low speed flows). Degradation of accuracies at higher Mach numbers was expounded upon, and the possibility of the necessity of compressibility effects and corrections was proposed. Also identified as a factor for the poor agreement was the fact that nitrogen is not calorically nor thermally perfect at such high temperatures and pressures.

Several research efforts have concentrated on the need to include non-ideal gas effects in the full NS solution of high Mach nozzle flow. For instance, in the work done by Johnson et al., it was shown (using the MOC/BL method) that an increase in the displacement thickness of 13% occurred when high temperature gas effects were included as compared with perfect gas results [30]. In addition, the inviscid core exit radius increased 9% when high temperature effects were included. It should be noted that the stagnation conditions for this research were somewhat extreme (stagnation pressure of 1.01325×10^8 N/m^2 and stagnation temperature of 2333°K) [30]. However, the data appears to support the need to investigate whether high temperature gas effects will have a significant impact on a particular high Mach nozzle flow.

In a high Mach nozzle study performed by Candler and Perkins, a number of interesting facts relating to non-ideal gas effects

were presented [31]. First, for the hypersonic nozzles tested, vibrational nonequilibrium provided its major effect upstream of the throat; the vibrational temperature froze near the throat and, downstream of the throat, the flow essentially acted as a perfect gas with constant γ=1.4. Second, vibrational nonequilibrium and perfect gas solutions gave very similar results, while equilibrium flow provided a substantially lower Mach number at the nozzle exit. And, third, the zero-equation algebraic turbulence model used has a significant effect upon the flow solution obtained (C-S, B-L, and Renormalization Group (RNG) models were used); a 2% to 4% difference was seen in the inviscid core exit Mach number when the different turbulence models were used.

To summarize, the history of recent hypersonic nozzle design and optimization points to a number of critical hypersonic nozzle design community needs. One, an accurate, efficient, simpler optimization code would be useful. Two, a given nozzle should be testable as a minimum with a nonequilibrium CFD code to determine if nonequilibrium effects need to be accounted for in the optimization procedure. If nonequilibrium effects prove to be significant, a nonequilibrium code should be an option such that it can at the very least be used in the final iterations of the optimization procedure. Three, the turbulence model used has a significant effect on the nozzle solution and its selection, therefore, must be addressed in a critical manner. These three

required critical technologies formed the basis of the present research.

1.2.2 The Wright Laboratory Mach 12 Nozzle - The Test Case.

Since data and personal expertise were locally available for the Wright Laboratory (WL) 20" Mach 12 wind tunnel nozzle, this facility was chosen to be the testbed for this investigation. The Air Force WL hypersonic wind tunnel is an intermittent, blowdown-to-vacuum facility with an axisymmetric 20 inch exit diameter nozzle contoured to produce uniform Mach 12 or 14 flow in an open jet test section (Fig. 6). For the Mach 12 nozzle, the tunnel reservoir pressure ranges from 4.3169×10^6 to 11.0316×10^6 N/m^2 (600 to 1600 psia), the Reynolds number ranges from 1.3123 to 3.2808 million per meter (0.4 to 1.0 million per foot), the stagnation temperatures range from 1000 to 1111 degrees Kelvin (1800 to 2000 degrees Rankine), and run times vary from 5 to 8 minutes [63].

A number of studies have been performed on the WL Mach 12 nozzle. Buck et al. performed experiments which showed the flow to be isentropic, at least in the high Mach core [3]. Trollier et al., of Science Applications International Corporation (SAIC) under contract with the Air Force Wright Aeronautical Laboratories, used CFD techniques based on the full NS and PNS equations to solve the flow fields of the wind tunnel throat and supersonic nozzle respectively. It was demonstrated computationally that the

experimental exit Pitot profile and the exit Mach profile were bracketed by the fully laminar CFD profiles on the one side and fully turbulent CFD profiles on the other (Fig. 7) [4]. It is this author's opinion that this lack of agreement with the measured exit data was likely due to uncertainty in the transition location, inaccuracies in the turbulence modelling, or simplified modeling of the physics of the flow (that is, not accounting for nonequilibrium effects).

As to the use of this facility as the testbed in the present research, it is the author's intention to use both experimental data from and CFD solutions to the WL Mach 12 nozzle to validate CFD solutions obtained herein. Additionally, experimental data from the WL Mach 12 nozzle will be used to compare with the newly designed Mach 12 nozzle obtained with the optimization procedure.

1.3 Purpose and Objectives of Present Research

The purpose of this research is to redesign an existing hypersonic wind tunnel nozzle and in the process develop a new design tool with the necessary inherent methodology. In the process of redesigning the nozzle it will be desired that the new design provide the largest uniform flow test section possible with a minimum of computer time and designer interaction. To achieve this end, state-of-the-art turbulence modelling and axisymmetric capabilities, viscous effects, and compressibility effects must be

accounted for in both NS and PNS codes. In addition, an optimization scheme/code is required to perform nozzle design. The computer program developed will be an improved tool for the redesign of existing MOC/BL-designed wind tunnels due to the complexity of the flow solvers and the simplicity of the optimization scheme. The developed optimization code can later be used for the design/redesign of more accurate hypersonic wind tunnel nozzles or other high Mach propulsive devices.

Thus, there are three objectives to this research, one primary and two minor but valuable secondary objectives:

- The primary objective is to develop and validate a computer code to be used in the optimal redesign of the testbed nozzle. The code, with state-of-the-art NS and PNS solvers incorporated, will accurately and robustly select an optimal set of design parameters based on some established design criteria, utilizing a simple optimization scheme. Specifically, the code will be used to design a hypersonic nozzle with the constraints of fixed length, throat radius, and exit radius based on the main application, the test case described in Sect. 1.2.2.
- A secondary objective is to determine if the B-L turbulence model or the Yang-Shih (Y-S) k-ϵ model would help provide a more accurate solution to the flow field of the testbed nozzle.
- The other secondary objective is to test the newly optimized nozzle for off-design conditions. Specifically, the new nozzle

design will be tested with changes in back pressure and the results analyzed.

1.4 Overview of Dissertation Approach

In order to achieve the objectives mentioned above a number of critical steps needed to be taken. The first step taken was to develop and validate a perfect gas NS axisymmetric laminar code. The second step was to develop and validate a perfect gas and a nonequilibrium, chemically reacting (NECR) NS axisymmetric turbulent code. With the preceding steps completed, a comparison could be made between nozzle flow solutions obtained with the two turbulence models incorporated in the second step; thus a turbulence model could be selected for the remainder of the research, satisfying one of the secondary objectives. The third step entailed developing and validating a perfect gas PNS axisymmetric laminar/turbulent code. The fourth step was development and validation of a simpler optimization scheme and code, with subsequent redesign of the testbed nozzle, and tests for robustness performed on the optimization code. Having completed all of the preceding steps would satisfy the primary objective of this research. The fifth and final step was to run the off-design cases of the newly designed nozzle to determine the effects of a difference in back pressure. This last step would satisfy the other secondary objective.

2. Governing Equations and Supporting Theory

The equations of fluid mechanics as pertain to the various developed codes are presented in this chapter along with important principles of optimization. First, the general form of the NS axisymmetric equations is given in Cartesian and computational coordinates, followed by the perfect gas and NECR forms. Next, the perfect gas PNS axisymmetric equations are presented. Then the turbulence model formulas are given. Finally, the pertinent methodology used in the optimization scheme is presented.

2.1 NS Axisymmetric Equations, General Form, Cartesian Coordinates

As mentioned previously, the flow field of interest is that of a hypersonic axisymmetric wind tunnel nozzle. Thus, the axisymmetric form of the NS equations is used. The equations in vector form for axisymmetric coordinates are [48]:

$$U_t + F_x + G_y = \delta \frac{(H-G)}{y} \tag{1}$$

in non-conservation form, and

$$U_t + F_x + \frac{1}{y}(yG)_y = \delta \frac{H}{y} \tag{2}$$

in strong conservation form, where

$$U = (\rho,\ \rho u,\ \rho v,\ E)^T \tag{3}$$

$$F = (\rho u,\ \rho u^2+p-\tau_{xx},\ \rho uv-\tau_{xy},\ u(E+p)-u\tau_{xx}-v\tau_{xy}+q_x)^T \tag{4}$$

$$G = (\rho v,\ \rho uv-\tau_{xy},\ \rho v^2+p-\tau_{yy},\ v(E+p)-u\tau_{xy}-v\tau_{yy}+q_y)^T \tag{5}$$

$$H = (0,\ 0,\ p-\tau_{\theta\theta},\ 0)^T \tag{6}$$

$$\tau_{xx} = \frac{2}{3}(\mu+\mu_t)\left(2u_x-v_y-\delta\frac{v}{y}\right) \tag{7}$$

$$\tau_{xy} = (\mu+\mu_t)(u_y+v_x) \tag{8}$$

$$\tau_{yy} = \frac{2}{3}(\mu+\mu_t)\left(2v_y-u_x-\delta\frac{v}{y}\right) \tag{9}$$

$$\tau_{\theta\theta} = \frac{2}{3}(\mu+\mu_t)\left(-u_x-v_y+2\frac{v}{y}\right) \tag{10}$$

$$q_x = -(k_l+k_t)T_x \tag{11}$$

$$q_y = -(k_l+k_t)T_y \tag{12}$$

(Note that Stokes' hypothesis has already been invoked; ie, $\lambda=-2/3\mu$).

2.2 NS Axisymmetric Equations, General Form, Computational Coordinates

The form of the equations given above is for that of a Cartesian coordinate system. A generalized transformation from the physical to the computational domain is made ($(x,y)<=>(\xi,\eta)$) in

order to facilitate the CFD computations, where $\xi = \xi(x,y)$ is the streamwise computational coordinate, and $\eta = \eta(x,y)$ is the crossflow computational coordinate. In the new coordinate system, Eq. 2 now becomes [48]

$$\tilde{U}_t + \tilde{F}_\xi + \tilde{G}_\eta = \delta \frac{H}{J} \tag{13}$$

where

$$\tilde{U} = yU/J \tag{14}$$

$$\tilde{F} = \frac{y}{J}(\xi_x F + \xi_y G) \tag{15}$$

$$\tilde{G} = \frac{y}{J}(\eta_x F + \eta_y G) \tag{16}$$

and J, the coordinate transformation Jacobian, is defined as

$$J = \xi_x \eta_y - \xi_y \eta_x . \tag{17}$$

2.3 Extension of NS Axisymmetric Equations to Perfect Gas Form

The extension of the governing equations from general form to the perfect gas form are now shown. First, the pressure, p, in a thermally and calorically perfect gas is given by:

$$p = (\gamma - 1)\rho e_i \tag{18}$$

while the total energy is:

$$E = \rho(e_i + \frac{1}{2}(u^2+v^2)) \tag{19}$$

where $e_i = c_v T$ (c_v a constant) for a thermally and calorically perfect gas.

The molecular viscosity is obtained with Keye's Law

$$\mu = a_0 T^{1/2} \left(1 + \left(\frac{a_1}{T}\right) 10^{-(\frac{a_2}{T})}\right)^{-1} \tag{20}$$

where

$$a_0 = 1.490x10^{-6} \quad N.sec/m^2 \tag{21}$$

$$a_1 = 122.22°K \tag{22}$$

and

$$a_2 = 5°K. \tag{23}$$

The molecular thermal conductivity can be obtained through the use of the Prandtl number, with

$$k_1 = \frac{\mu c_p}{Pr}, \tag{24}$$

and the turbulent thermal conductivity is obtained through the use

of Pr_t, through

$$k_t = \frac{\mu_t c_p}{Pr_t} \tag{25}$$

once the eddy viscosity is known from the turbulence model.

For a perfect gas, the speed of sound, a, is defined as

$$a^2 = \gamma p/\rho = \gamma RT \tag{26}$$

which is the same as the frozen speed of sound, since in both cases it is assumed that no chemical reactions are occurring. However, in the perfect gas case, γ is assumed constant; in the frozen case, γ may be a function of temperature.

2.4 NS Axisymmetric Equations, NECR Form

The governing equations presented to this point have dealt with the perfect gas case, but to determine if it were necessary to account for high temperature effects, it was necessary to use and modify the computer code of Josyula [40]. This code accounts for chemical reactions, as well as nonequilibrium vibrational effects. The form of the governing equations is modified to account for five individual species (O_2, N_2, N, O, NO) and three additional energy equations which track the vibrational energy of the three species of diatomic molecules (O_2, N_2, NO), for a total of eleven conserved variables at any given point.

To illustrate, the U vector from Eq. 2 becomes

$$U = (\rho_{N_2},\ \rho_{O_2},\ \rho_N,\ \rho_O,\ \rho_{NO},\ \rho u,\ \rho v,\ \rho_{N_2} e_{v_{N_2}},\ \rho_{O_2} e_{v_{O_2}},\ \rho_{NO} e_{v_{NO}},\ E)^T \qquad (27)$$

where ρ, the total density, is now equal to the sum of the individual species' densities ($\rho = \rho_{O_2}+\rho_{N_2}+\rho_O+\rho_N+\rho_{NO}$). The F vector from Eq. 2 is now

$$F = \begin{pmatrix} \rho_{N_2} u \\ \rho_{O_2} u \\ \rho_N u \\ \rho_O u \\ \rho_{NO} u \\ \rho u^2 + p - \tau_{xx} \\ \rho uv - \tau_{xy} \\ \rho_{N_2} e_{v_{N_2}} u + q_{v_{N_2}} \\ \rho_{O_2} e_{v_{O_2}} u + q_{v_{O_2}} \\ \rho_{NO} e_{v_{NO}} u + q_{v_{NO}} \\ (E + p - \tau_{xx})\, u - \tau_{xy} v + q_x + \sum_i q_{v_i} \end{pmatrix}, \qquad (28)$$

the G vector from Eq. 2 is

$$G = \begin{pmatrix} \rho_{N_2} v \\ \rho_{O_2} v \\ \rho_N v \\ \rho_O v \\ \rho_{NO} v \\ \rho uv - \tau_{yx} \\ \rho v^2 + p - \tau_{yy} \\ \rho_{N_2} e_{v_{N_2}} + q_{v_{N_2}} \\ \rho_{O_2} e_{v_{O_2}} v + q_{v_{O_2}} \\ \rho_{NO} e_{v_{NO}} v + q_{v_{NO}} \\ (E + p - \tau_{yy})\, v - \tau_{yx} u + q_y + \sum_i q_{v_i} \end{pmatrix}, \qquad (29)$$

and the H vector from Eq. 2 becomes

$$H = \begin{pmatrix} \dot{w}_{N_2} \\ \dot{w}_{O_2} \\ \dot{w}_{O} \\ \dot{w}_{N} \\ \dot{w}_{NO} \\ 0 \\ p - \tau_{\theta\theta} \\ \rho_{N_2}\dot{e}_{v_{N_2}} + e_{v_{N_2}}\dot{w}_{N_2} \\ \rho_{O_2}\dot{e}_{v_{O_2}} + e_{v_{O_2}}\dot{w}_{O_2} \\ \rho_{NO}\dot{e}_{v_{NO}} + e_{v_{NO}}\dot{w}_{NO} \\ 0 \end{pmatrix} \tag{30}$$

where the total energy, E, from Eq. 19 has become

$$E = \rho e_{Tr+Rot} + \frac{1}{2}\rho(u^2+v^2) + \rho_{N_2}e_{v_{N_2}} + \rho_{O_2}e_{v_{O_2}} + \rho_{NO}e_{v_{NO}} \; . \tag{31}$$

The additional terms to the above vectors account for the chemical reactions which are occurring and for energy being transferred from the translational energy mode to vibrational energy as a result of molecular collisions [50].

The chemical reaction source terms for the ith species, $\dot{w}_i$, in equation 30 derive from the law of mass action and consider the five significant reactions which may occur between the different species of the air mixture [40]. These possible reactions are represented by

$$
\begin{aligned}
N_2 + M &\rightleftharpoons 2N + M \\
O_2 + M &\rightleftharpoons 2O + M \\
NO + M &\rightleftharpoons N + O + M \\
N_2 + O &\rightleftharpoons NO + N \\
NO + O &\rightleftharpoons O_2 + N
\end{aligned}
\tag{32}
$$

in which M is merely a collision body such as an atom or molecule.

The equilibrium vibrational energy for each constituent is modelled using the simple harmonic oscillator model represented by [33]

$$
e_{v_i} = \frac{R_i \theta_{v_i}}{\exp\left(\frac{\theta_{v_i}}{T_{v_i}}\right) - 1} \tag{33}
$$

where, for the ith species, T_{v_i} is the vibrational temperature and θ_{v_i} is the characteristic temperature of vibration and is defined as [33]

$$
\theta_{v_i} = \frac{h\nu_i}{k}. \tag{34}
$$

The individual factors in the last equation are Planck's constant (h), Boltzmann's constant (k), and the frequency of oscillation of the ith species (ν_i).

In order to correctly account for creation of vibrational energy, the source terms have been added to the H vector. These source terms are modelled using the Landau-Teller model for local relaxation time and are defined as [33]

$$\dot{e}_{v_i} = \frac{e^{\star}_{v_i}(T) - e_{v_i}}{\tau_{v_i}} \tag{35}$$

where $e^{\star}_{v_i}(T)$ is the vibrational energy associated with temperature T for the ith species, and τ_{v_i} is the local relaxation time of the ith species and is a function of temperature and pressure. The local relaxation time for O_2, N_2 , and NO are obtained individually with

$$\tau_{v_i} = \frac{\sum_i X_i}{\sum_i (X_i \tau_{v_{ik}})} \tag{36}$$

where X_i is the mole fraction of the ith species and $\tau_{v_{ik}}$ is the interspecies relaxation time between species i and species k and is computed with the form developed by Millikan and White [33]. Vibration-vibration coupling is assumed negligible and not accounted for. However, vibration-dissociation for the diatomic species is computed with the two-temperature model used by Park [51]:

$$T_d = T^{0.7} T_v^{0.3} \tag{37}$$

in which T_d is the dissociation temperature and T_v is the vibration temperature.

The additions to the viscous portion of the F and G vectors are the vibrational heat fluxes, which are given by [31,32]

$$q_{v_i} = -k_{v_i} \frac{\partial e_{v_i}}{\partial x_j}. \tag{38}$$

Even though the perfect gas equation of state no longer holds, the new equation of state is still given by [35]

$$p = \rho \tilde{R} T, \tag{39}$$

where

$$\tilde{R} = \tilde{c}_p - \tilde{c}_v, \tag{40}$$

$$\tilde{c}_p = \sum_i \frac{\rho_i}{\rho} \tilde{c}_{p_i}, \tag{41}$$

$$\tilde{c}_v = \sum_i \frac{\rho_i}{\rho} \tilde{c}_{v_i}, \tag{42}$$

$$\gamma = \frac{\tilde{c}_p}{\tilde{c}_v}. \tag{43}$$

Note, however, that the specific heats correspond to the equilibrium portion of the internal energy, i.e., the translational and rotational energy.

Finally, the last equation needed is that for the speed of sound. Conveniently, the form doesn't change from that of the perfect gas. In other words, the equation remains [36]

$$a = [\frac{\gamma p}{\rho}]^{1/2} = [\gamma \tilde{R} T]^{1/2}. \qquad (44)$$

As pointed out in [36], "this result is not approximate, but (actually) corresponds to the frozen speed of sound for this ... nonequilibrium flow."

2.5 PNS Equations, Perfect Gas Form

The PNS equations are a modification of the NS equations, but they are restricted in use due to two requirements: "the inviscid outer region of the flow (must) be supersonic and the streamwise velocity component (must) be everywhere positive" [48]. However, due to the transformation from NS to PNS, the PNS space-marching technique allows for a solution to be obtained in the same time as on the order of an Euler solution [48]. As shown below, space-marching comes about as a result of dropping the time derivative and some of the stress terms in Eq. 13 and integrating in the ξ (or streamwise) direction. This efficient integration scheme is what makes the PNS equations so favorable in a well-behaved non-streamwise separated flow [48].

Similar to the NS equations, but with the time dependency removed and some modifications to the flux vectors, the primary equation in transformed coordinates , similar to Eq. 13, is [49]

$$\left(\frac{y\xi_x F^\star}{J}\right)_\xi + \left(\frac{y\eta_x F}{J} + \frac{y\eta_y G}{J}\right)_\eta - y\left[F^\star\left(\frac{\xi_x}{J}\right)_\xi + F\left(\frac{\eta_x}{J}\right)_\eta + G\left(\frac{\eta_y}{J}\right)_\eta\right] = \delta\frac{H}{J}. \qquad (45)$$

The terms in the brackets on the left hand side of Eq. 45, $F^{\star}\left(\frac{\xi_x}{J}\right)_{\xi}+F\left(\frac{\eta_x}{J}\right)_{\eta}+G\left(\frac{\eta_y}{J}\right)_{\eta}$, are the Geometric Conservation Law (GCL) terms which are necessary in this formulation due to the potential variation of the grid as the solution marches downstream [9,49]. Note that the ξ variable is only a function of x ($\xi = \xi(x)$) and not of y; this will aid in the transformation from the computed variables ($F^{\star}$) to the conserved variables (U), as will be shown below. Note also that the Ω vector,

$$\Omega = (0,\ \omega,\ 0,\ 0)^T \tag{46}$$

which Korte recommends using has been dropped due to its destabilizing effect on the PNS solver, as recommended by White et al. [37].

In the flux vectors, F and G, the streamwise (ξ) derivatives are dropped, whereas in the $F^{\star}$ vector, the stress terms are dropped completely. Also, in $F^{\star}$, the pressure term has been changed to account for upstream pressure in the boundary layer. This change comes about by multiplying the pressure by Vigneron's coefficient [49], producing

$$F^{\star} = (\rho u,\ \rho uu+\omega p,\ \rho uv,\ (E+p)u)^T. \tag{47}$$

In order to calculate Vigneron's coefficient, ω, the following equation

$$\bar{\omega} = \begin{cases} 1 & (M_\xi \geq 1) \\ \dfrac{\gamma M_\xi^2}{1+(\gamma-1)M_\xi^2} & (M_\xi < 1) \end{cases} \tag{48}$$

is first computed, where the streamwise Mach number is denoted by M_ξ. Then, Vigneron's coefficient is simply

$$\omega = \min(1, \sigma\bar{\omega}) \tag{49}$$

where σ is a safety factor used to ensure the eigenvalues of the inviscid portion of the PNS equations have real values and that the equations remain hyperbolic [49]. The value used for σ in this application was 0.75. This value seemed to provide good stability with the scheme used. Due to the inclusion of the safety factor, it was necessary to ensure that the Mach number in the inviscid core was above M_{min}, which is defined as

$$M_{min} > [1/(\sigma\gamma-\gamma+1)]^{1/2}. \tag{50}$$

With σ having the value of 0.75 and assuming a γ of 1.4, the value for M_{min} was approximately 1.24.

2.6 The Baldwin-Lomax Turbulence Model Formulation

Of the two primary zero-equation models (B-L and C-S) [28,62], the B-L model is preferred by this author for two reasons. First, one need not locate the edge of the boundary layer in the B-L

model. Second, the B-L has been validated against such flows as boundary layer over a flat plate and transonic airfoils with excellent comparative results.

Being a zero-equation model, the B-L turbulence model is based upon several concepts and assumptions. First, the necessary length and velocity scales are obtained from the mean flow; that is, closure for the eddy viscosity is obtained from the mean velocity field. Second, it is assumed that an equilibrium situation exists between the mean flow and the turbulence present. Third, for the inner region of the boundary layer it utilizes a form of Prandtl's Mixing length formulation, which defines the eddy viscosity, μ_t, as

$$\mu_t = \rho l^2 \left|\frac{\partial u}{\partial y}\right| . \tag{51}$$

Fourth, the form utilized for the outer region of the boundary layer is modelled after the Clauser formulation [28].

This model calculates the eddy viscosity (μ_t) by calculating a value for the area near the wall, giving $(\mu_t)_{inner}$, and another value for the flow beyond the inner region $(\mu_t)_{outer}$, much like the classical model of the boundary layer. In the inner region, the eddy viscosity is calculated as

$$(\mu_t)_{inner} = \rho k^2 y^2 [1-\exp(\frac{y^+}{A^+})]^2 |\omega| \tag{52}$$

where

$$\omega = \left| \frac{\partial u}{\partial y} - \frac{\partial v}{\partial x} \right| \tag{53}$$

$$y^+ = \frac{u_\tau y}{\nu} \tag{54}$$

$$u_\tau = \sqrt{\frac{\tau_w}{\rho}} \tag{55}$$

with k and A^+ constants depending on the flow (originally assigned values of 0.0168 and 26, respectively) [28].

For the outer region, the eddy viscosity is defined as [28]

$$(\mu_t)_{outer} = (0.0168\rho)(1.6F_{wake})F_{kleb} \tag{56}$$

where

$$F_{wake} = \min(y_{max}F_{max},\ 0.25y_{max}u_{diff}^2/F_{max}) \tag{57}$$

and

$$F_{max} = \max(F(y)) = \max(y|\omega|[1-\exp(-\frac{y^+}{A^+})]) \tag{58}$$

where y_{max} is that value of y (for a given x value held constant) where $F(y) = F_{max}$ and

$$u_{diff} = \max_{y=0,\infty}(\sqrt{u^2+v^2}) \tag{59}$$

$$F_{kleb} = [1 + 5.5(0.3\frac{y}{y_{max}})]^{-1} \quad (60)$$

The point where the transition from the inner region to the outer region occurs is that point (in the y-direction for a given x-coordinate) where F_{max} occurs (y_{max}).

Generally speaking, the B-L model produces excellent results in flows in which there is no adverse pressure gradient. However, it is well known that it doesn't produce a reliable solution in separation regions and recirculation regions. Hence, it is necessary to be prudent when implementing an algorithm for this turbulence model, particularly since as the back pressure is increased the flow might develop an adverse pressure gradient and separate.

2.7 The Yang-Shih k-ε Turbulence Model Formulation

Originally developed by Jones and Launder [17] to compute incompressible boundary-layer flows, the two-equation k-ε model has become a reliable, often-used turbulence model in the CFD community. A comparison of numerous 2-equation models was made by Lang and Shih [18]. The cases tested were low Reynolds number, 2-D flows; one case was the flow over a flat plate and the other was the flow through a fully developed channel. The Y-S k-ε model appeared to be one of the most accurate and robust turbulent models, and it was one of the few models which approached the

standard k-ϵ model away from the wall. For these reasons this model was chosen as the particular two-equation model to incorporate into the computer program developed in this research.

In addition to the standard Y-S k-ϵ model as proposed by Yang and Shih [52], it is necessary to add Sarkar's compressibility correction [19]. This necessity comes about since a good portion of the flow in a hypersonic nozzle will be in the high Mach number region, where compressibility effects are significant.

There are two additional equations which must be calculated throughout the flow, for, this being a two-equation model, there are two conserved variables needed to compute the eddy viscosity. One of these equations governs the conservation of the turbulent kinetic energy, k (specifically ρk is conserved), and the other governs the conservation of the turbulent energy dissipation rate, ϵ (again, specifically $\rho\epsilon$ is conserved).

The turbulent kinetic energy conservation equation is defined as

$$\frac{\partial \rho k}{\partial t} + \frac{\partial}{\partial x}\left[\rho u k - (\mu + \mu_t/\sigma_k)\frac{\partial k}{\partial x}\right] + \frac{\partial}{\partial y}\left[\rho v k - (\mu + \mu_t/\sigma_k)\frac{\partial k}{\partial y}\right] - \left[P_k - \rho\epsilon(1 + \alpha M_t^2) + D\right] = 0 \qquad (61)$$

and the turbulent energy dissipation rate conservation equation is defined as

$$\frac{\partial \rho e}{\partial t} + \frac{\partial}{\partial x}[\rho u e - (\mu + \mu_t/\sigma_e)\frac{\partial e}{\partial x}] + \frac{\partial}{\partial y}[\rho v e - (\mu + \mu_t/\sigma_e)\frac{\partial e}{\partial y}] - \tag{62}$$

$$C_{e1} f_1 \frac{\rho}{T_t} P_k - C_{e2} f_2 \frac{\rho e}{T_t} + E_e = 0$$

where

$$P_k = \tau_{t_{xx}} \frac{\partial u}{\partial x} + \tau_{t_{xy}} (\frac{\partial u}{\partial y} + \frac{\partial v}{\partial x}) + \tau_{t_{yy}} \frac{\partial v}{\partial y} \tag{63}$$

$$\tau_{t_{xx}} = \frac{2}{3}[\mu_t (2\frac{\partial u}{\partial x} - \frac{\partial v}{\partial y}) - \rho k] \tag{64}$$

$$\tau_{t_{xy}} = \mu_t (\frac{\partial u}{\partial y} + \frac{\partial v}{\partial x}) \tag{65}$$

$$\tau_{t_{yy}} = \frac{2}{3}[\mu_t (2\frac{\partial v}{\partial y} - \frac{\partial u}{\partial x}) - \rho k] \tag{66}$$

$$\mu_t = \rho C_\mu f_\mu k T_t \tag{67}$$

$$M_t^2 = \frac{k}{\gamma R T} \tag{68}$$

$$T_t = \frac{k}{e} + (\frac{\nu}{e})^{1/2} \tag{69}$$

$$E_e = (\frac{\mu \mu_t}{\rho})\left[(\frac{\partial^2 u}{\partial x^2} + \frac{\partial^2 u}{\partial y^2})^2 + (\frac{\partial^2 v}{\partial x^2} + \frac{\partial^2 v}{\partial y^2})^2\right] \tag{70}$$

$$f_1 = 1.0 \tag{71}$$

$$f_2 = 1 - 0.22\exp\left(\frac{-Re_t^2}{36}\right) \tag{72}$$

$$f_\mu = 1 - \exp(-0.004y^+ - 5e^{-5}(y^+)^2 + 2e^{-6}(y^+)^3 - 8e^{-8}(y^+)^4) \tag{73}$$

$$Re_t = \frac{k^2}{\nu\varepsilon} = \frac{\rho k^2}{\mu\varepsilon} \tag{74}$$

$$C_\mu = 0.09 \tag{75}$$

$$C_{\varepsilon 1} = 1.44 \tag{76}$$

$$C_{\varepsilon 2} = 1.92 \tag{77}$$

$$\sigma_k = 1.0 \tag{78}$$

$$\sigma_\varepsilon = 1.3 \tag{79}$$

$$Pr_t = 0.90 \tag{80}$$

The compressibility correction already appears in Eq. 61 as the term $\rho\varepsilon\alpha M_t^2$, and represents the additional dissipation of turbulent kinetic energy due to dilatation (compressibility), which only appears to be needed for hypersonic flows [20].

Note that an additional term must be added to Eqs. 7 and 9 as a result of the dependence of the eddy viscosity on the turbulent kinetic energy, k. This is due to the fact that the Reynold's shear stress, $-\langle u_i u_j \rangle$, is now defined as

$$-\langle u_i u_j \rangle = \nu_T (U_{i,j} + U_{j,i}) - \frac{2}{3} k \delta_{ij}, \tag{81}$$

whereas before, the Reynold's stress had only been modeled by the first term on the right hand side of Eq. 81. The U_i terms in Eq. 81 represent the mean velocity components of the flow, while the u_i terms represent the fluctuating velocity components. In particular, $-2/3\rho k$ must be added to each of Eqs. 7 and 9, producing

$$\tau_{xx} = \frac{2}{3}(\mu + \mu_t)\left(2u_x - v_y - \delta \frac{v}{y}\right) - \frac{2}{3}\rho k \tag{82}$$

and

$$\tau_{yy} = \frac{2}{3}(\mu + \mu_t)\left(2v_y - u_x - \delta \frac{v}{y}\right) - \frac{2}{3}\rho k. \tag{83}$$

For the perfect gas case, assuming that the NS solver were to be used, Eq. 2 would look the same as originally presented but with one additional source term on the right hand side, producing

$$U_t + F_x + \frac{1}{y}(yG)_y = \delta \frac{H}{y} + S \tag{84}$$

where S is

$$S = (0,\ 0,\ 0,\ 0,\ P_k - \rho\varepsilon(1 + \alpha M_t^2) + D,\ C_{e1} f_1 \frac{\rho}{T_t} P_k - C_{e2} f_2 \frac{\rho\varepsilon}{T_t} + E_e)^T. \tag{85}$$

The dependent variable vector, U and the flux vectors, F and G, now include the calculations for ρk and $\rho\varepsilon$. To illustrate, the following changes are made: Eq. 3 becomes

$$U = (\rho,\ \rho u,\ \rho v,\ E,\ \rho k,\ \rho e)^T, \tag{86}$$

with Eqs. 4 and 5 becoming

$$F = \begin{pmatrix} \rho u \\ \rho u^2 + p - \tau_{xx} \\ \rho uv - \tau_{xy} \\ u(E+p) - u\tau_{xx} - v\tau_{xy} + q_x \\ \rho ku - (\mu + \mu_t/\sigma_k)\dfrac{\partial k}{\partial x} \\ \rho eu - (\mu + \mu_t/\sigma_e)\dfrac{\partial e}{\partial x} \end{pmatrix}, \tag{87}$$

and

$$G = \begin{pmatrix} \rho v \\ \rho uv - \tau_{xy} \\ \rho v^2 + p - \tau_{yy} \\ v(E+p) - u\tau_{xy} - v\tau_{yy} + q_y \\ \rho kv - (\mu + \mu_t/\sigma_k)\dfrac{\partial k}{\partial y} \\ \rho ev - (\mu + \mu_t/\sigma_e)\dfrac{\partial e}{\partial y} \end{pmatrix}. \tag{88}$$

Additionally, the total energy now accounts for internal and kinetic energy, as well as turbulent kinetic energy, and is represented by

$$E = \rho\left(e_i + \frac{1}{2}(u^2+v^2) + k\right). \qquad (89)$$

Inclusion of the turbulent kinetic energy into the total energy was done per the work of Morrison [39] and has been shown to aid in convergence of the solution.

2.8 Supporting Theory for the Optimization Scheme

A new wind tunnel design is obtained efficiently by formulating an optimization problem. This must be done such that the end result is a wind tunnel nozzle which has maximized the area of the inviscid, high Mach core at the exit plane with minimal crossflow and as few as possible disturbances in that core. In other words, the solution to the optimization problem results in a smooth expansion and uniform flow at the exit plane.

Three different optimization methods are presented. First, the Korte nonlinear least-squares (LS) method is given. This is followed by two techniques of response surface methodology (RSM), those being the steepest descent method and the second-order search.

2.8.1 The Korte Non-Linear Least-Squares (LS) Method. The optimization scheme used by Korte [8,9] was based upon the research of Huddleston [29]. The Korte solver optimizes aerodynamic design through the use of a nonlinear least-squares optimization

formulation. Basically, the nonlinear optimization problem attempts to minimize an objective function through determination of design parameters.

In this method, the objective function, (**P**), is dependent on a set of design parameters, (**a**), and is constructed of a number of functions, (p_i), in the nonlinear least square form

$$\boldsymbol{P}(\mathbf{a}) = \sum_{i=1}^{m} p_i^2(\mathbf{a}). \tag{90}$$

In vector form,

$$\boldsymbol{P}(\mathbf{a}) = \boldsymbol{p}^T(\mathbf{a})\,\boldsymbol{p}(\mathbf{a}) \tag{91}$$

where

$$\boldsymbol{p} = (p_1, p_2, \ldots\ldots, p_m)^T \tag{92}$$

and

$$\mathbf{a} = (a_1, a_2, \ldots\ldots, a_n)^T. \tag{93}$$

Thus, there are n design parameters and m total functions.

The components of $\boldsymbol{p}$ are as follows: for i = 1 to m_1, the weighted residual (or p_i) is the error in axial Mach number at the nozzle exit and is defined as

$$p_k = \omega_M(M_{x_{imax,j}} - M_{design}) \qquad k = j;\ j = 1, m_1 \tag{94}$$

where $\omega_M = 4.0/M_{design}$; from m_1+1 to m_2, the weighted residual is the

error in flow angle, ϕ, at the nozzle exit and is defined as

$$p_k = \omega_\phi(\phi_{imax,j}-0) \qquad k = j+m_1;\ j = 1,m_2-m_1 \tag{95}$$

where $\omega_\phi = 2.5$; and, finally, from m_2+1 to m, the weighted residual is the error in the axial Mach number along the centerline and is defined as

$$p_k = \omega_{MA}(M_{x_{i,1}}-M_{axis}) \qquad k = i+m_2;\ i = 1,m-m_2 \tag{96}$$

where $\omega_{MA} = 1.0/M_{axis}$. (The centerline Mach number, M_{axis}, distribution is obtained using equations derived and readily available in [37].)

The design parameters, **a**, must now be defined. First, the nozzle contour is specified using the following n cubic polynomial equations:

$$r(x) = \begin{cases} a_0+a_1\bar{x}+a_2\bar{x}^2+a_3\bar{x}^3 & \bar{x} = x; \quad 0 \le x \le x_1 \\ a_4+a_5\bar{x}+a_6\bar{x}^2+a_7\bar{x}^3 & \bar{x} = x-x_1; \quad x_1 \le x \le x_2 \\ \quad . & \\ \quad . & \\ a_{4n-4}+a_{4n-3}\bar{x}+a_{4n-2}\bar{x}^2+a_{4n-1}\bar{x}^3 & \bar{x} = x-x_{n-1}; \quad x_{n-1} \le x \le x_n \end{cases} \tag{97}$$

These n cubic equations produce 4n coefficients given that the x_i are known. The x_i are the x-locations of the cubic spline knots mentioned earlier. By requiring continuity of the surface and the slope and the curvature at the endpoints of the segments, 3(n-1) of the coefficients are specified. The remaining coefficients are specified by the predetermined inlet and exit radii and slopes (4 coefficients) and by assigning wall slopes at the n-1 interior

points. The set of equations is now a linear system of equations which can be solved to determine all of the coefficient values. The design parameters are the wall slopes at each of the interior points (a_1, a_5, a_9, ... , a_{4n-3}). In other words, these are the components which make up the **a** vector.

Using the Newton method for nonlinear least squares (assuming this is a small residual problem), the equation which must be solved is

$$\boldsymbol{J}_k^T \boldsymbol{J}_k \Delta \mathbf{a}_k = -\boldsymbol{J}_k^T \mathbf{p}_k, \tag{98}$$

where k is the iteration number for the updated wall solution, and **J** is the Jacobian matrix, defined as

$$\boldsymbol{J} = \begin{bmatrix} \frac{\partial p_1}{\partial a_1} & \cdots & \frac{\partial p_1}{\partial a_{4n-3}} \\ \vdots & & \vdots \\ \frac{\partial p_m}{\partial a_1} & \cdots & \frac{\partial p_m}{\partial a_{4n-3}} \end{bmatrix}. \tag{99}$$

Once $\Delta \mathbf{a}_k$ is found, the updated wall slope coefficients are obtained using

$$\mathbf{a}_{k+1} = \mathbf{a}_k + \Delta \mathbf{a}_k. \tag{100}$$

With the updated wall coefficients, a new wall shape is obtained using Eq. 97. With the new wall shape, another CFD solution must

be obtained. This procedure is repeated until the wall shape converges; that is, the change between the kth iteration and the k+1th iteration falls within some tolerance level.

As noted by Korte et al., the computer-time expensive portion of this procedure is in obtaining the Jacobian matrix. Each interior point must have its slope changed in order to generate the columns of the J matrix. Each slope change is done independently of the other interior points' slope changes, and for each slope change made, another CFD flow field solution must be obtained in order to generate a column of the J matrix. To illustrate, if there are 100 interior points, 101 CFD solutions are needed for one iteration (100 + 1 initial solution). So it would appear to pay to minimize the design parameters in an effort to cut down on CFD solutions needed.

2.8.2 Response Surface Methodologies (RSM) Techniques. RSM techniques represent a somewhat different approach to the solving of an optimization problem. Though minimization of an objective (or response) function through variation of design parameters is still performed, the method in which the path to the minimum is taken is determined by fitting a "mathematical French curve" to a smooth response surface [45]. "By careful design and analysis of experiments, it seeks to relate a *response*, or *output* variable to

the levels of a number of *predictors*, or *input* variables, that affect it" [45].

"Response Surface Methodology (RSM) comprises a set of statistical and mathematical techniques for empirical model building and exploitation ..." [72]. It includes the development of a group of experimental runs that will produce "adequate and reliable measurements of the response(s) of interest in a region of interest"; the analysis of the experimental results to determine an empirical/mathematical model which provides a best fit to the response surface data; and the determination of the values of the design parameters which provide the desired response (possibly a maximum or a minimum) [72]. Some explanations and definitions follow.

In RSM, a response is defined as "the output of a system or process that occurs as a result of (or in response to) a set of inputs" [72]. The inputs, X_i (i = 1,k), are put through the system or process and result in the output, z (Fig. 8). In mathematical language, $z = f(X_1, X_2, \ldots, X_k) = f(\underline{X})$, and even more specifically, $z = f(\underline{X}, \underline{\theta})$, where $\underline{\theta}$ $(\theta_1, \theta_2, \ldots, \theta_p)$ represents the set of physical parameters that help to define the relationship of the response function. The latter, more specific form of z is referred to as the "mechanistic model". Unfortunately, the true response function, f, is generally not known and may be quite complex and

therefore must be approximated. Additionally, θ itself is generally unknown and must be approximated as well.

The response surface is defined as "a geometric representation of a response function" [72]. An example of a response surface is presented in Fig. 9 for a case in which the response surface parameter, yield, is plotted as a function of the two design parameters of reaction temperature and reaction time [45]. The associated contour plot is given in Fig. 10.

One tests the system with different sets of value of the design parameters to use the generated responses to aid in developing an "approximate interpolating function" to the response surface [72]. This approximating function would be given by $z \approx g(X_1, X_2, \ldots, X_k, \beta_1, \beta_2, \ldots, \beta_q) = g(\underline{X}, \underline{\beta})$ and is referred to as the "empirical model." "The operation of the system with the k design inputs adjusted to some definite set of levels (values) is referred to as an experimental run" [72].

The techniques used in RSM include designed experiments, in which sufficient and purposeful change is brought about in the design parameters to allow observation and modelling of the changes in the response(s); regression analysis, in which "statistical techniques (are) used to model the response as a linear combination" of the input/design variables, $\underline{X}$, and their interactions, $\underline{\theta}$; and steepest ascent/descent, in which a "gradient search technique" is used to determine the location of either the next point at which to begin the next search for the desired

response, or the point at which a desired response is obtained [72].

A graduating function is defined as "an empirical model that approximates the mechanistic model over a specified region of interest" [72]. A graduating function is used "to approximate the true response function" [72]. This requires a means of fitting the empirical functions to actual experimental data.

Assuming an adequate model has been postulated to represent the data, one must then obtain the best estimates of the model parameters ($\underline{\theta}$) in the attempt to fit the empirical functions to the data. In RSM, the method of least squares is used to obtain the best estimate of $\underline{\theta}$. It should be noted that z is restricted to being linear in the parameters, meaning that $z = f(\underline{X}, \underline{\theta}) = \theta_1 y_1 + \theta_2 y_2 + \cdots + \theta_p y_p$, where $y_1, y_2, , \ldots, y_p$ "denote known constants that are functions of the input variables $X_1, X_2, \ldots, X_k$ ..." [72]. Additionally, while z is restricted to being linear in the $\underline{y}$, $\underline{\theta}$, $\underline{\beta}$ parameters, it is not restricted to being linear in the $\underline{X}$ input variables.

In the designed experiments phase, one performs a "set of n experiments on the process, observing the response at each of n sets of experimental conditions denoted by $\underline{X}_1, \underline{X}_2, \ldots, \underline{X}_n$, obtaining the vector of responses $\boldsymbol{z} = (z_1, z_2, \ldots, z_n)$" [72]. In the subsequent regression analysis phase, the error between the observed response and that calculated by the mathematical model is represented by

$$e_i = z_i - f(\underline{X}_i, \underline{\theta}) \qquad i = 1,2,\ldots,n. \tag{101}$$

Assuming again that the response function is linear in the parameters mentioned above, the mathematical model can be represented by

$$\boldsymbol{z} = \boldsymbol{Y}\underline{\theta} + \boldsymbol{e} \tag{102}$$

where

$$\boldsymbol{Y} = \begin{bmatrix} y_{11} & y_{12} & \cdots & y_{1p} \\ y_{21} & y_{22} & \cdots & y_{2p} \\ \cdot & \cdot & & \cdot \\ \cdot & \cdot & & \cdot \\ \cdot & \cdot & & \cdot \\ y_{n1} & y_{n2} & \cdots & y_{np} \end{bmatrix} \tag{103}$$

Least squares is used to find that value for $\underline{\theta}$ which "minimizes the sum of squares function defined as the sum of the squared model error and given by" [72]

$$S(\underline{\theta}) = (\boldsymbol{z} - \boldsymbol{Y}\underline{\theta})^T(\boldsymbol{z} - \boldsymbol{Y}\underline{\theta}) . \tag{104}$$

The desired value for $\underline{\theta}$ is then obtained by setting $\partial S(\underline{\theta})/\partial\underline{\theta} = 0$ which produces

$$(\boldsymbol{Y}^T\boldsymbol{Y})\underline{\theta} = \boldsymbol{Y}^T\boldsymbol{z} \tag{105}$$

which represents a set of p equations which are normal and which can be solved for $\underline{\theta}$ given that $\boldsymbol{Y}^T\boldsymbol{Y}$ is non-singular. Having solved

for $\underline{\theta}$ it is now possible to use steepest ascent/descent methods (as described below) to further the search for the desired response from the system.

It is important at this juncture to take note of a point of clarification for the remainder of this paper. Both the first-order and second-order response surface methods described below are steepest descent methods. However, the first-order method will be referred to as the steepest descent method, and the second-order method will be referred to as the second-order search method.

In the steepest descent method and the second-order search method, though not absolutely necessary, a coordinate transformation may be performed in order to facilitate the search procedure. As further illustration, assume for the moment that only two generic design parameters are used and are represented by X_1 and X_2. This transformation is made to take place by first selecting a point, designated by $(X_1, X_2) = (X_{1_o}, X_{2_o})$ which is to be the center of the search. Next, a delta to X_1 and X_2, designated by dX_1 and dX_2, is chosen. Then the coordinates for the new system are obtained from

$$\bar{X}_1 = \frac{X_1 - X_{1_o}}{dX_1} \tag{106}$$

and

$$\bar{X}_2 = \frac{X_2 - X_{2_o}}{dX_2}. \qquad (107)$$

These new variables are referred to as the coded input variables. The centerpoint then becomes $(X_1, X_2) <=> (0, 0)$. For the steepest descent method, the additional points consist of the following pairs of $(\bar{X}_1, \bar{X}_2)$: (1,1), (1,-1), (-1,-1), and (-1,1) (Fig. 11). For the second-order search method, in addition to the points used in the steepest descent method, the additional points consist of $(0,\sqrt{2})$, $(0,-\sqrt{2})$, $(\sqrt{2},0)$, $(-\sqrt{2},0)$ (Fig. 12).

With the coded variables in use, Eq. 102 is now represented by

$$\boldsymbol{z} = \boldsymbol{x}\underline{\beta} + \boldsymbol{e} \qquad (108)$$

where the form of $\boldsymbol{x}$ is given in the following two sections. Once again when minimizing the sum of the squares function, the resulting equation,

$$(\boldsymbol{x}^T\boldsymbol{x})\underline{\beta} = \boldsymbol{x}^T\boldsymbol{z} \qquad (109)$$

can be solved for $\underline{\beta}$ given that $\boldsymbol{x}^T\boldsymbol{x}$ is non-singular.

Though optimization methods used by other researchers have concentrated on several design parameters, it was hoped that a reasonably accurate engineering solution to the optimized hypersonic nozzle could be obtained with the use of only two design parameters. By using only two design parameters, it would

hopefully be possible to use RSM in a straightforward manner to obtain a minimum to the objective function, and hence, find an optimized nozzle shape. The two design parameters chosen for this research consisted of the attachment angle, θ_{attach}, and the exit angle, θ_{exit} (Fig. 13). It was felt that the necessary nozzle wall shape to produce uniform nozzle exit flow at the design conditions could be obtained with just these two parameters, given that the nozzle length and the radius of the attachment circle, r_{circ}, were prescribed by the designer (Fig. 13).

2.8.2.1 The Steepest Descent Method. The steepest descent method is a first-order method which determines the direction of largest change based on the sampling of the points mentioned above. Once the response is determined for each of those points, a first-order mathematical approximation to the local response surface is obtained, then the direction of largest gradient is determined and a search is begun in that direction to find a new minimum.

In order to characterize the local surface with a linear equation, a first-order least squares bivariate regression equation of the form

$$f(\bar{X}_1, \bar{X}_2)_{fit} = b_0 + b_1\bar{X}_1 + b_2\bar{X}_2 \qquad (110)$$

must be obtained. In order to do so, the coefficients b_0, b_1, and b_2 must be determined. Recall that $f(\bar{X}_1, \bar{X}_2)_{fit}$ is merely an artifice

used to approximate the true local surface at any point, represented by $\bar{z}$. In order to best approximate the surface and solve for b_0, b_1, and b_2, the equation

$$\boldsymbol{X}^T\boldsymbol{X}\boldsymbol{b} = \boldsymbol{X}^T\boldsymbol{z} \tag{111}$$

must be solved for $\boldsymbol{b}$, where

$$\boldsymbol{b} = (b_0, b_1, b_2)^T \tag{112}$$

$$\boldsymbol{X} = \begin{pmatrix} 1 & \bar{X}_{1_1} & \bar{X}_{2_1} \\ 1 & \bar{X}_{1_2} & \bar{X}_{2_2} \\ . & . & . \\ . & . & . \\ 1 & \bar{X}_{1_N} & \bar{X}_{2_N} \end{pmatrix} \tag{113}$$

$$\boldsymbol{z} = (z_1, z_2, \ldots, z_N)^T \tag{114}$$

and N is the total number of points being sampled and z_i is the response value associated with point (X_{1_i}, X_{2_i}) [45]. Note that $\boldsymbol{b}$ is synonymous with $\underline{\beta}$ in Eq. 109 above. Another form of Eq. 111 is given by

$$\boldsymbol{A}\boldsymbol{b} = \bar{\boldsymbol{z}}, \tag{115}$$

where

$$\boldsymbol{A} = \boldsymbol{X}^T\boldsymbol{X} \tag{116}$$

and

$$\bar{\boldsymbol{Z}} = \boldsymbol{X}^{T}\boldsymbol{z}. \tag{117}$$

The matrix $\mathbf{A}$, a 3x3 matrix represented by

$$\mathbf{A} = \begin{pmatrix} a_{11} & a_{12} & a_{13} \\ a_{21} & a_{22} & a_{23} \\ a_{31} & a_{32} & a_{33} \end{pmatrix} \tag{118}$$

has the following components:

$$\begin{array}{lll} a_{11} = N & a_{12} = \sum_{i=1}^{N} \bar{X}_{1_i} & a_{13} = \sum_{i=1}^{N} \bar{X}_{2_i} \\ a_{21} = a_{12} & a_{22} = \sum_{i=1}^{N} \left(\bar{X}_{1_i}\right)^2 & a_{23} = \sum_{i=1}^{N} \left(\bar{X}_{1_i}\bar{X}_{2_i}\right) \\ a_{31} = a_{13} & a_{32} = a_{23} & a_{33} = \sum_{i=1}^{N} \left(\bar{X}_{2_i}\right)^2 \end{array} \tag{119}$$

For the steepest descent method described above N is 5. Inputting the values for N and the prespecified values for $(\bar{X}_{1_i}, \bar{X}_{2_i})$, the matrix $\mathbf{A}$ simply becomes

$$\mathbf{A} = \begin{pmatrix} 5 & 0 & 0 \\ 0 & 4 & 0 \\ 0 & 0 & 4 \end{pmatrix}. \tag{120}$$

Once the matrix $\mathbf{A}$ is obtained, in order to solve for $\boldsymbol{b}$ it is necessary to obtain $\mathbf{A}^{-1}$ and also the vector $\bar{\boldsymbol{Z}}$ $(= [\bar{Z}_1, \bar{Z}_2, \bar{Z}_3]^T)$ which is defined by

$$\bar{Z}_1 = \sum_{i=1}^{N} z_i \qquad \bar{Z}_2 = \sum_{i=1}^{N} \bar{X}_{1_i} z_i \qquad \bar{Z}_3 = \sum_{i=1}^{N} \bar{X}_{2_i} z_i. \tag{121}$$

In this particular case, since the $\bar{X}_{1_i}$ and $\bar{X}_{2_i}$ don't change, the $\mathbf{A}^{-1}$ matrix remains constant and is represented by

$$\mathbf{A}^{-1} = \begin{bmatrix} 0.2 & 0 & 0 \\ 0 & 0.25 & 0 \\ 0 & 0 & 0.25 \end{bmatrix}. \tag{122}$$

At this point, it is possible to calculate the coefficients in Eq. 110 above, which are obtained from

$$\boldsymbol{b} = \mathbf{A}^{-1}\bar{\boldsymbol{Z}}. \tag{123}$$

Once $\boldsymbol{b}$ has been computed, the direction of steepest descent has been found because the gradient vector,

$$\boldsymbol{b}' = (b_1,\ b_2)^T \tag{124}$$

has been determined [45]. In searching for a new minimum if one wishes to move a specific distance g in the steepest descent direction, one need only specify g, from which the $\bar{X}_1$ and $\bar{X}_2$ can be calculated from the equations

$$\bar{X}_1 = \frac{g}{\sqrt{1 + \left(\frac{b_2}{b_1}\right)^2}}\ sign(b_1) \tag{125}$$

and

$$\bar{X}_2 = \frac{b_2}{b_1}\bar{X}_1 \tag{126}$$

where

$$sign(b_1) = \begin{cases} 1 & b_1 \leq 0 \\ -1 & b_1 > 0 \end{cases}. \qquad (127)$$

The determination of $\bar{X}_1$ and $\bar{X}_2$ is obtained from the fact that the magnitude of the coefficient vector at any point g along the direction of steepest descent is defined by

$$g = \sqrt{\bar{X}_1^2 + \bar{X}_2^2} \qquad (128)$$

and the ratio of $\bar{X}_2/\bar{X}_1$ is the same as the ratio of b_2/b_1 since the point lies along the direction of steepest descent [45]. Note that sign(b_1) (Eq. 125) is important since the sign of b_1 and b_2 may be lost in the ratio b_2/b_1. Also, note that if b_1 is negative, then the direction of steepest descent requires that $\bar{X}_1$ be positive in order to move in the correct direction. The same holds true for b_2 and $\bar{X}_2$.

Now that the direction of steepest descent has been found, one must sample points in that direction until an inflection point has been detected. By sampling at least 3 points in the direction of steepest descent, it should be possible to determine if there is indeed a new minimum in this direction (Fig. 14). If there is a new minimum in this direction and the sampling is fine enough, then a good second-order curve fit to the response surface in the direction of steepest descent should be obtainable in trying to find the new minimum.

For example, if three points were used (g_1, g_2, and g_3, where $g_1 < g_2 < g_3$) with corresponding response functions z_i (Fig. 14)), and, assuming a new minimum occurred at point g_2, then it should be possible to obtain a least-squares second-order fit of the z_i along the direction of steepest descent to the g_i. In other words, an equation of the form

$$f1(g)_{fit} = b1_0 + b1_1 g + b1_2 g^2 \tag{129}$$

should be obtainable, where the $\boldsymbol{b1}$ vector, $(b1_0, b1_1, b1_2)^T$, is represented by

$$\boldsymbol{b1} = \boldsymbol{A1}^{-1}\bar{\boldsymbol{Z1}}. \tag{130}$$

The development of these equations can easily be seen by replacing $\bar{X}_1$ with g and $\bar{X}_2$ with g^2 in Eq. 110. The components of the $\boldsymbol{A1}$ matrix are then

$$\begin{array}{lll} a1_{11} = N1 & a1_{12} = \sum_{i=1}^{N1} g_i & a1_{13} = \sum_{i=1}^{N1} (g_i)^2 \\ a1_{21} = a1_{12} & a1_{22} = a1_{13} & a1_{23} = \sum_{i=1}^{N1} (g_i)^3 \\ a1_{31} = a1_{13} & a1_{32} = a1_{23} & a1_{33} = \sum_{i=1}^{N1} (g_i)^4 \end{array} \tag{131}$$

and the $\bar{\boldsymbol{Z1}}$ $(= [\bar{Z1}_1, \bar{Z1}_2, \bar{Z1}_3]^T)$ vector is given by

$$\bar{Z1}_1 = \sum_{i=1}^{N1} z_i \qquad \bar{Z1}_2 = \sum_{i=1}^{N1} g_i z_i \qquad \bar{Z1}_3 = \sum_{i=1}^{N1} g_i^2 z_i, \tag{132}$$

where N1 is the number of points being used to attempt a fit; in this case, N1 = 3.

Following the determination of the $\boldsymbol{b1}$ vector, since $f1(g)_{fit}$ is

a quadratic equation, by taking the derivative of Eq. 129 with respect to g and setting that derivative equal to 0 to find the minimum, the following equation is obtained:

$$g_{new} = -b1_1/(2\ b1_2) \qquad (133)$$

which, when substituted into Eq. 129, produces the curve fit minimum of $f1(g)_{fit}$. In reality, whether or not a new minimum exists at that value of g is very much dependent on how well Eq. 129 has characterized the response surface. The only way to determine the quality of the response surface characterization is to use that value of g to obtain new values of $\bar{X}_1$ and $\bar{X}_2$, and to obtain the new response function there, this to compare with the other points along the direction of steepest descent.

Assuming a new minimum is found in the direction of steepest descent, the associated point becomes the center of the next stencil and presumably a smaller stencil in non-transformed space is used in the next iteration of the steepest descent method (Fig. 15). The rationale for the next stencil to be smaller is to provide a more localized surface to be used in providing the requisite data for solving Eq. 110, and to thus provide a more accurate representation of the local surface.

If, alternatively, no new minimum is found, then a number of choices might be made. First, a second-order search can be performed since 5 of the 9 sampling points needed have already had their response functions determined (Fig. 12). Second, a smaller

stencil can be used in non-transformed space (Fig. 16). Third, the minimum of the 5 stencil points can be used as the new center, assuming the minimum doesn't occur at the old center (Fig. 17). And fourth, some combination of those three choices can be attempted.

As long as the surface can be characterized to a good approximation by a first-order fit, the method of steepest descent works well. However, in areas where strong second-order effects are evident it is likely that the first-order empirical model of the surface will fail to find a minimum and the second-order search method will need to be utilized [45].

2.8.2.2 The Second-Order Search Method. The second-order method begins much like the steepest descent method in that a number of points including a centerpoint need be sampled in order to obtain some form of characterization of the response surface. The 9 points mentioned above are sampled and each provides a response value (Fig. 18). In order to approximate the surface with a second-order polynomial, a second-order least squares bivariate regression equation of the form

$$f2(\bar{X}_1, \bar{X}_2) = b_0 + b_1\bar{X}_1 + b_2\bar{X}_2 + b_{11}(\bar{X}_1)^2 + b_{22}(\bar{X}_2)^2 + b_{12}\bar{X}_1\bar{X}_2, \qquad (134)$$

where the $\boldsymbol{b}$ vector (= $[b_0, b_1, b_2, b_{11}, b_{22}, b_{12}]^T$) is obtained from

$$\boldsymbol{A2}\,\boldsymbol{b} = \bar{\boldsymbol{Z}}. \qquad (135)$$

$\boldsymbol{A2}$ is a (6x6) matrix, and both $\boldsymbol{b}$ and $\bar{\boldsymbol{z}}$ are (1x6) vectors. The development of $\boldsymbol{A2}$ and $\bar{\boldsymbol{z}}$ is very similar to that of $\boldsymbol{A}$ and $\bar{\boldsymbol{z}}$ in Sec. 2.8.2.1, Eqs. 116 and 117 respectively. The difference between the two methods starts in the $\boldsymbol{x}$ matrix, which is now given by

$$\boldsymbol{x} = \begin{pmatrix} 1 & \bar{X}_{1_1} & \bar{X}_{2_1} & \bar{X}_{1_1}^2 & \bar{X}_{2_1}^2 & \bar{X}_{1_1}\bar{X}_{2_1} \\ 1 & \bar{X}_{1_2} & \bar{X}_{2_2} & \bar{X}_{1_2}^2 & \bar{X}_{2_2}^2 & \bar{X}_{1_2}\bar{X}_{2_2} \\ \cdot & \cdot & \cdot & \cdot & \cdot & \cdot \\ \cdot & \cdot & \cdot & \cdot & \cdot & \cdot \\ \cdot & \cdot & \cdot & \cdot & \cdot & \cdot \\ 1 & \bar{X}_{1_N} & \bar{X}_{2_N} & \bar{X}_{1_N}^2 & \bar{X}_{2_N}^2 & \bar{X}_{1_N}\bar{X}_{2_N} \end{pmatrix} \tag{136}$$

where N is the total number of points being sampled. For the second-order search method, N is fixed at 9.

For a general distribution of points, $\boldsymbol{A2}$ is represented by

$$\begin{array}{llllll} a2_{11}=N & a2_{12}=\sum_{i=1}^{N}\bar{X}_{1_i} & a2_{13}=\sum_{i=1}^{N}\bar{X}_{2_i} & a2_{14}=\sum_{i=1}^{N}\bar{X}_{1_i}^2 & a2_{15}=\sum_{i=1}^{N}\bar{X}_{2_i}^2 & a2_{16}=\sum_{i=1}^{N}\bar{X}_{1_i}\bar{X}_{2_i} \\ a2_{21}=a2_{12} & a2_{22}=a2_{14} & a2_{23}=a2_{16} & a2_{24}=\sum_{i=1}^{N}\bar{X}_{1_i}^3 & a2_{25}=\sum_{i=1}^{N}\bar{X}_{1_i}\bar{X}_{2_i}^2 & a2_{26}=\sum_{i=1}^{N}\bar{X}_{1_i}^2\bar{X}_{2_i} \\ a2_{31}=a2_{13} & a2_{32}=a2_{23} & a2_{33}=a2_{15} & a2_{34}=a2_{26} & a2_{35}=\sum_{i=1}^{N}\bar{X}_{2_i}^3 & a2_{36}=a2_{25} \\ a2_{41}=a2_{14} & a2_{42}=a2_{24} & a2_{43}=a2_{26} & a2_{44}=\sum_{i=1}^{N}\bar{X}_{1_i}^4 & a2_{45}=\sum_{i=1}^{N}\bar{X}_{1_i}^2\bar{X}_{2_i}^2 & a2_{46}=\sum_{i=1}^{N}\bar{X}_{1_i}^3\bar{X}_{2_i} \\ a2_{51}=a2_{15} & a2_{52}=a2_{25} & a2_{53}=a2_{35} & a2_{54}=a2_{45} & a2_{55}=\sum_{i=1}^{N}\bar{X}_{2_i}^4 & a2_{56}=\sum_{i=1}^{N}\bar{X}_{1_i}\bar{X}_{2_i}^3 \\ a2_{61}=a2_{16} & a2_{62}=a2_{26} & a2_{63}=a2_{36} & a2_{64}=a2_{46} & a2_{65}=a2_{56} & a2_{66}=a2_{45} \end{array} \tag{137}$$

and the $\bar{\boldsymbol{z}}$ vector is represented by

$$\bar{\boldsymbol{z}} = \begin{pmatrix} \sum_{i=1}^{N} z_i \\ \sum_{i=1}^{N} \bar{X}_{1_i} z_i \\ \sum_{i=1}^{N} \bar{X}_{2_i} z_i \\ \sum_{i=1}^{N} \bar{X}_{1_i}^{\,2} z_i \\ \sum_{i=1}^{N} \bar{X}_{2_i}^{\,2} z_i \\ \sum_{i=1}^{N} \bar{X}_{1_i} \bar{X}_{2_i} z_i \end{pmatrix} \tag{138}$$

Due to a well-chosen distribution of the sampling points (Fig. 12), the A2 matrix simply becomes

$$\boldsymbol{A2} = \begin{bmatrix} 9 & 0 & 0 & 8 & 8 & 0 \\ 0 & 8 & 0 & 0 & 0 & 0 \\ 0 & 0 & 8 & 0 & 0 & 0 \\ 8 & 0 & 0 & 12 & 4 & 0 \\ 8 & 0 & 0 & 4 & 12 & 0 \\ 0 & 0 & 0 & 0 & 0 & 4 \end{bmatrix} \tag{139}$$

and it can readily be seen that straightforward solutions can be determined for b_1, b_2 and b_{12}. These solutions are given by

$$b_1 = \frac{\bar{Z}_2}{8}, \qquad b_2 = \frac{\bar{Z}_3}{8}, \qquad b_{12} = \frac{\bar{Z}_6}{4}. \tag{140}$$

For the remaining 3 equations, Gaussian elimination is used to provide the following results:

$$b_{22} = \frac{11}{32}\left[\bar{Z}_5 - \bar{Z}_4 + \frac{18}{11}\left(\bar{Z}_4 - \frac{8}{9}\bar{Z}_1\right)\right], \tag{141}$$

$$b_{11} = \frac{9}{44}\left(\bar{Z}_4 - \frac{8}{9}\bar{Z}_1 + \frac{28}{9}b_{22}\right), \tag{142}$$

and

$$b_0 = \frac{\bar{Z}_1 - 8b_{11} - 8b_{22}}{9}. \tag{143}$$

Once $\boldsymbol{b}$ has been computed, the surface may be characterized at the stationary point (the minimum) by examining the second-order partial derivatives of Eq. 134. The stationary point, if one exists, is the point at which $\partial(f2)/\partial\bar{X}_i = 0$ for all $\bar{X}_i$. By taking the second-partial derivatives of f2, the Hessian matrix, $\boldsymbol{He}$, represented by

$$\boldsymbol{He} = \begin{bmatrix} 2b_{11} & b_{12} \\ b_{12} & 2b_{22} \end{bmatrix} \tag{144}$$

is obtained. Then, taking its inverse, $\boldsymbol{He}^{-1}$, and multiplying by the $\boldsymbol{V}$ vector, represented by $(-b_1, -b_2)^T$, the new stationary point is obtained as follows [45]

$$\begin{pmatrix} \bar{X}_{1_s} \\ \bar{X}_{2_s} \end{pmatrix} = \boldsymbol{He}^{-1}\boldsymbol{V}. \tag{145}$$

At this point in the calculations, a new theoretical minimum point

has been established at $(\bar{X}_{1_s}, \bar{X}_{2_s})$, and the only remaining step in this iteration is to obtain the response value at that point. If the stationary point provides a new minimum, then the search is begun anew with the stationary point at the center of the sampling space and presumably a smaller stencil in non-transformed coordinates to try to zero in on the global minimum (Fig. 19).

Should the stationary point not provide a new minimum, then a number of approaches exist. First, one might try a smaller stencil in non-transformed space (Fig. 20). Second, one might choose the response function minimum of the nine sampled points in the last iteration, assuming it doesn't occur at the old center, as the new center and begin a new search (Fig. 21). Third, one might revert to a first-order search and use the steepest descent method to perform the next phase of the search. And again, one might use some combination of the three choices already presented.

3. Computational Techniques

This chapter details the methods used to convert the governing equations into discretized form for CFD solution. The discrete form of the NS equations in perfect gas form is presented, followed by a short discussion on the discrete form of the nonequilibrium chemical reaction (NECR) NS equations. Subsequently, discretization of the perfect gas PNS equations, the Baldwin-Lomax (B-L) turbulence model and the Yang-Shih (Y-S) k-ϵ model are given. The boundary conditions are presented at the end of each of the sections mentioned.

3.1 Discretization of the Perfect Gas NS Equations and Boundary Conditions

Temporarily ignoring the viscous and source terms, the governing NS equation (Eq. 2) takes on the form in transformed coordinates

$$\Delta \tilde{U}^{n}_{i,j} = -\frac{\Delta t}{\Delta \xi}\left(\tilde{F}^{n}_{I_{i+1/2,j}} - \tilde{F}^{n}_{I_{i-1/2,j}}\right) - \frac{\Delta t}{\Delta \eta}\left(\tilde{G}^{n}_{I_{i,j+1/2}} - \tilde{G}^{n}_{I_{i,j-1/2}}\right) \qquad (146)$$

where

$$\tilde{F}^{n}_{I_{i+1/2,j}} = \frac{1}{2} y_{i+1/2,j} \Big[\Big(\frac{\xi_x}{J}\Big)_{i+1/2,j} \big[F_I(U^R_{i+1/2,j}) + F_I(U^L_{i+1/2,j})\big] + \Big(\frac{\xi_y}{J}\Big)_{i+1/2,j} \big[G_I(U_{i+1/2,j})^R) + G_I(U^L_{i+1/2,j})\big] + \big(R_{A_{1+1/2,j}} |\Lambda_{A_{i+1/2,j}}| R^{-1}_{A_{i+1/2,j}}\big)\,(U^R_{i+1/2,j} - U^L_{i+1/2,j})\Big] \tag{147}$$

The last term on the right hand side of Eq. 147 is the dissipative term which obviates the necessity of additional numerical damping [43].

Once a solution is obtained to Eq. 146, it is necessary to transform $\Delta\tilde{U}^n_{i,j}$ to Cartesian coordinates before performing the time integration. The transformation takes the form

$$\Delta U^n_{i,j} = \frac{\Delta\tilde{U}^n_{i,j} J}{y} . \tag{148}$$

The two-stage Runge-Kutta [42] time integration takes the form

$$U^p_{i,j} = U^n_{i,j} + \Delta U^p_{i,j} \tag{149}$$

for the predictor phase and

$$U^{n+1}_{i,j} = \frac{(U^n_{i,j} + U^p_{i,j} + \Delta U^c_{i,j})}{2} \tag{150}$$

for the corrector phase.

The factors in the last term of Eq. 147 represent A, the linearized form of the computational flux Jacobian, and consist of the following: the matrix $\boldsymbol{R}_{\mathbf{A}}$, defined as

$$\mathbf{R}_{\mathbf{A}} = \begin{bmatrix} 1 & 1 & 1 & 0 \\ u-k_2c & u & u+k_2c & -k_3 \\ v-k_3c & v & v+k_3c & k_2 \\ H_t-k_2uc-k_3vc & \frac{(u^2+v^2)}{2} & H_t+k_2uc+k_3vc & k_2v-k_3u \end{bmatrix}, \tag{151}$$

where

$$k_2 = \frac{\xi_x}{(\xi_x^2+\xi_y^2)^{1/2}} = \frac{\xi_x}{k_\xi} \tag{152}$$

$$k_3 = \frac{\xi_y}{(\xi_x^2+\xi_y^2)^{1/2}} = \frac{\xi_y}{k_\xi} \tag{153}$$

and

$$k_\xi = (\xi_x^{\,2}+\xi_y^{\,2})^{\frac{1}{2}} . \tag{154}$$

The total enthalpy, H_T, is defined as

$$H_T = \frac{\gamma p}{(\gamma-1)\rho}+\frac{1}{2}(u^2+v^2) . \tag{155}$$

The matrix $\mathbf{R}_{\mathbf{A}}^{-1}$ is defined as

$$R_A^{-1} = \begin{bmatrix} \frac{(b_1+k_2u/c+k_3v/c)}{2} & \frac{(-b_2u-k_2/c)}{2} & \frac{(-b_2v-k_3/c)}{2} & \frac{b_2}{2} \\ 1-b_1 & b_2u & b_2v & -b_2 \\ \frac{(-b_1-k_2u/c-k_3v/c)}{2} & \frac{(-b_2u+k_2/c)}{2} & \frac{(-b_2v+k_3/c)}{2} & \frac{b_2}{2} \\ k_3u-k_2v & -k_3 & k_2 & 0 \end{bmatrix} \quad (156)$$

where

$$b_2 = \frac{(\gamma-1)}{c^2} \quad (157)$$

and

$$b_1 = \frac{b_2(u^2+v^2)}{2}. \quad (158)$$

The matrix Λ_A, whose only non-zero elements are on the main diagonal and are the eigenvalues of A is defined as

$$\Lambda_A = \begin{bmatrix} \xi_x u+\xi_y v-k_\xi c & 0 & 0 & 0 \\ 0 & \xi_x u+\xi_y v & 0 & 0 \\ 0 & 0 & \xi_x u+\xi_y v+k_\xi c & 0 \\ 0 & 0 & 0 & \xi_x u+\xi_y v \end{bmatrix} \quad (159)$$

(Note that c is the speed of sound in Eqs. 151, 156, 157, and 159).

At certain points where the flow goes sonic or enters a stagnation region, the eigenvalues may be near zero. Due to numerical roundoff, the result may be a violation of the entropy condition: the scheme may produce the nonphysical solution of an expansion shock, a decrease in entropy [7]. As a result, an entropy cutoff is used to ensure that the eigenvalues never

decrease below a certain level, defined as δ_λ. The eigenvalues are resultantly defined as

$$\lambda = \begin{cases} |\lambda| = \dfrac{|\lambda^2+\delta_\lambda^2|}{2\delta_\lambda} & |\lambda|<\delta_\lambda \\ |\lambda| = |\lambda| & |\lambda|\geq\delta_\lambda \end{cases} \tag{160}$$

where δ_λ takes one of two forms. The first form is used in the body-normal direction and is represented by

$$\delta_\lambda = \bar{\delta} J^{-1}\left[|\bar{u}\cdot\bar{\nabla}\xi| + |\bar{u}\cdot\bar{\nabla}\eta| + \frac{c}{2}\left(|\nabla\xi|+|\nabla\eta|\right)\right] \tag{161}$$

where $\bar{\delta}$ is a constant value. For this application, after discussions with Gaitonde, the value was made to be 0.01 to minimize the additional dissipation associated with this cutoff [57]. The second form, the anisotropic form of δ_λ, is used in the streamwise direction to prevent excess dissipation due to large grid cell aspect ratios and is given by [7]

$$\delta_\lambda = \bar{\delta} J^{-1}\lambda^{(\xi)}\left[1 + \left(\frac{\lambda^{(\eta)}}{\lambda^{(\xi)}}\right)^{2/3}\right], \tag{162}$$

where $\lambda^{(k)} = |\bar{u}\cdot\bar{\nabla}k| + c|\bar{\nabla}k|$. Note that only the two eigenvalues associated with the speed of sound were cut off in each direction. The eigenvalue of the contravariant velocity was not altered, per [57]. Similar formulations are used to calculate $\tilde{G}^{n}_{I_{i,j+\frac{1}{2}}}$, where η replaces ξ in the eigenvector (and its inverse) and eigenvalue matrices.

Global second-order spatial accuracy is achieved through the MUSCL (Monotonic Upstream Schemes for Conservation Laws) formulation in combination with the minmod slope limiter [7]. The minmod limiter reverts the solution to first order at extrema (such as shocks) contained within the flow, thus preventing spurious oscillations. As illustrated in Fig. 22, the unconserved variables are extrapolated from the cell center to the cell interface with the MUSCL formulation of van Leer [12] in conjunction with the minmod limiter [13], in order to obtain the conserved variables immediately to the left and right of the cell interface. These are then used to calculate the flux vectors immediately to the left and right of an interface (giving the first four terms on the right hand side of Eq. 147). Subsequently, Roe-averaging is used to compute the last term in Eq. 147. Due to limitation of space, some details have been omitted; for an excellent description of the Roe-scheme as pertains to perfect gas flows, the reader is referred to the work of Morrison [39].

As for the remainder of the terms in Eq. 13, the viscous terms are handled in a central-differencing manner and the source terms are always lagged by the values from the previous half time-step.

3.1.1 Inlet Boundary Conditions. The inlet boundary conditions were taken directly from the work of Korte et al. [9],

as it was felt this was an excellent source for nozzle subsonic inlet conditions. The first two columns of cells at the inflow (Fig. 23) must be computed using these conditions in order to maintain a second-order boundary condition. The assumptions made are that the streamwise mass flow rate is conserved and the normal mass flow rate remains constant. The other two inlet conditions are made by specifying the reservoir stagnation enthalpy and pressure (h_T and p_T) and accounting for compressibility in p_T. For the testbed nozzle, h_T and p_T were specified as 502,000 J/kg and 12,410,563 N/m^2, as recommended to the author in [63]. The mass flow rate conditions are represented by

$$(\rho u)_{i,j} = (\rho u)_{i+1,j} \frac{Area_{i+1,j}}{Area_{i,j}} \tag{163}$$

and

$$(\rho v)_{i,j} = (\rho v)_{i+1,j} \frac{y_{i+1,j}}{y_{i,j}}, \tag{164}$$

while the second two conditions are given by

$$h_T = \frac{\gamma}{\gamma-1} \frac{p_{i,j}}{\rho_{i,j}} + \frac{1}{2} \left[\frac{(\rho u)^2_{i,j} + (\rho v)^2_{i,j}}{\rho^2_{i,j}} \right] \tag{165}$$

and

$$p'_T = p_{i,j} + \frac{1}{2}\left[\frac{(\rho u)^2_{i,j} + (\rho v)^2_{i,j}}{\rho_{i,j}}\right], \tag{166}$$

where

$$p'_T = p_{T_{Res}}\left[\frac{p}{p_T}\right] + \frac{1}{2}\rho_{i,j}(u^2_{i,j} + v^2_{i,j}), \tag{167}$$

and

$$\frac{p}{p_T} = \left(1 + \frac{(\gamma-1)}{2} M^2\right)^{-\gamma/(\gamma-1)}. \tag{168}$$

The second two conditions, Eqs. 165 and 166 combine to produce

$$h_T \rho^2_{i,j} - \left(\frac{\gamma p'_T}{\gamma-1}\right)\rho_{i,j} + \frac{(\rho u)^2_{i,j} + (\rho v)^2_{i,j}}{2(\gamma-1)} = 0. \tag{169}$$

In solving the inlet boundary conditions, Eq. 169 , a quadratic, must be solved for $\rho_{i,j}$ using Eqs. 163, 164, 165, and 167. Eqs. 167 and 168 account for compressibility and are generated using the last computed values (i.e., from the previous half time-step) of ρ, u, v, and M. Once the density is calculated using the quadratic above, then the pressure can be calculated from Eq. 166. Following that, the variables, u, v, e_i, and E are easily obtained with

$$u_{i,j} = \frac{(\rho u)_{i,j}}{\rho_{i,j}}, \tag{170}$$

$$v_{i,j} = \frac{(\rho v)_{i,j}}{\rho_{i,j}}, \tag{171}$$

$$e_{i_{i,j}} = c_v T; \qquad T = \frac{p_{i,j}}{\rho_{i,j} R} \tag{172}$$

and,

$$E_{i,j} = \rho_{i,j}\left[e_{i_{i,j}} + \frac{1}{2}(u_{i,j}^2 + v_{i,j}^2)\right]. \tag{173}$$

At the end of each half time-step after the computation of the interior of the flow is complete, the inflow boundary conditions are enforced, beginning with the second column of cells (i=2) (Fig. 23). After that column is completely computed, the first column of cells (i=1) is computed.

3.1.2 Nozzle Wall Boundary Conditions. The boundary conditions for the wall (Fig. 24) are as follows: no-slip, a zero first-order pressure gradient in the body-normal direction, η, and a specified wall temperature which had the following distribution:

$$T_{wall}\ (^{\circ}K) = \begin{cases} 500 & x \le 0.2032m \\ 509.51-46.81x & x > 0.2032m \end{cases} \qquad (174)$$

This wall temperature distribution was provided to the author [63].

With those three boundary conditions and the perfect gas assumption all of the variables at the wall are easily calculated. The velocity components for the ghost cells (the grid cells in the nozzle wall, used to enforce boundary conditions, j = jl) (Fig. 24) are obtained from the no-slip condition and are given by

$$u_{i,jl} = -u_{i,jl-1}\,; \qquad v_{i,jl} = -v_{i,jl-1}\,, \qquad (175)$$

while the zero first-order pressure gradient results in

$$p_{i,jl} = p_{i,jl-1}\,. \qquad (176)$$

With the temperature at the wall specified by T_{wall}, a simple average produces the internal energy of the ghost cell as

$$e_{i_{i,jl}} = 2\,c_v T_{wall} - ei_{i,jl-1}\,. \qquad (177)$$

With those four variables computed, the density is easily calculated from

$$\rho_{i,j1} = \rho_{i,j1-1} \frac{e_{i_{i,j1-1}}}{e_{i_{i,j1}}}, \qquad (178)$$

and the total energy is obtained using Eq. 173.

The inviscid flux condition at the wall is due to pressure only. The rationale behind this can be clearly seen in Eqs. 4 and 5. In the inviscid portion of these two equations, no-slip drives the velocity components at the wall to be zero, eliminating all contributions except the pressure.

3.1.3 Centerline Boundary Conditions. Reflection is used as the boundary condition at the centerline (Fig. 25). This means that all of the flow variables for the ghost cells (those on the other side of the centerline, j=1) are exactly equal from one side of the centerline to the other except for the v velocity component. The v component takes on the negative value of that of its mirrored cell. Only one row of cells is used on the other side of the centerline. The flux condition at the centerline is assumed to be zero since the formulation is finite volume and presumably no flux can occur through the centerline.

3.1.4 Nozzle Exit Boundary Conditions. The boundary conditions at the exit (Fig. 26) are to assume a second-order zero gradient in the ξ direction for the conserved variables, as

recommended to the author by Korte in one of many discussions [53]. This assumption results in

$$U_{il,j} = 2U_{il-1,j} - U_{il-2,j}. \tag{179}$$

3.2 Discretization of the NECR NS Equations and Boundary Conditions

Similar to the perfect gas case, formulations for the nonequilibrium gas case for the Roe-averaged variables and the flux-difference splitting have been developed and are available. For excellent examples, the reader is referred to [35, 36].

3.2.1 Boundary Conditions. The boundary conditions for the inflow are handled exactly as they are for the perfect gas case in Section 3.1.1, but with the assumption that the air, though at high temperature and pressure, is at equilibrium and of a fixed composition. Thus, the vibrational temperature is assumed to be equal to the temperature of the air, and the mass fractions of N_2, O_2, N, O, and NO are assumed to be constant at 0.767, 0.233, 1.E-06, 1.E-06, and 1.E-06 respectively. All other boundary conditions are done exactly as in the perfect gas case in Sections 3.1.2-3.1.4.

3.3 The Discrete Form of the PNS Equations in Perfect Gas Form

The goal was to produce a PNS solver which would match very well with the NS solver and which would have incorporated within it the same turbulence models as the NS solver. The reason that it was important that the two solvers match well was that the NS solver was to provide the input to the PNS solver (Fig. 27). Thus, the same methodology was used to minimize the differences when transferring from NS solver to PNS solver. In other words, the two codes would have in common the same grid generation technique, the same flux-difference-split calculations in the η-direction, and the same turbulence model formulations. The PNS solver is overall second-order accurate and uses the same two-stage Runge-Kutta integration scheme as the NS solver [42].

Ignoring the viscous, source, and GCL terms, the parts of the main governing equation dealing with convection and pressure, Eq. 45, becomes

$$\Delta\left(\frac{y\xi_x F^*}{J}\right)^n_{i,j} = \frac{\Delta\xi}{\Delta\eta}\left(\tilde{G}^{\,n}_{I_{i,j+1/2}} - \tilde{G}^{\,n}_{I_{i,j-1/2}}\right) \qquad (180)$$

where $\tilde{G}^{\,n}_{I_{i,j\pm1/2}}$ retains the same definition as in the NS formulation, similar to Eq. 147. The viscous terms are again centrally-differenced. The source terms are once again lagged from the previous plane (Fig. 28). It is most important to retain the differencing of the metrics in the GCL terms in the same form in

which the flux differencing is computed, otherwise instability to the solution may arise [9].

Once the F^* flux terms have been calculated, the conserved variables must be decoded from the F^* terms [49]. With

$$F^* = [\rho u,\ \rho uu+\omega p,\ \rho uv,\ (E+p)u]^T = [F_1^*,\ F_2^*,\ F_3^*,\ F_4^*]^T \tag{181}$$

the conserved variables are calculated from

$$v = \frac{F_3^*}{F_1^*};\quad u = \frac{-b + \sqrt{b^2-4ac}}{2a};\quad \rho = \frac{F_1^*}{u};\quad p = \frac{F_2^* - uF_1^*}{\omega}, \tag{182}$$

where

$$a = \frac{1}{2};\quad b = \frac{-\gamma F_2^*}{F_1^*[2\gamma - \omega(\gamma - 1)]};\quad c = \frac{\omega(\gamma - 1)}{[2\gamma - \omega(\gamma - 1)]}\left[\frac{F_4^*}{F_1^*} - \frac{1}{2}v^2\right]. \tag{183}$$

Without the stipulation that $\xi = \xi(x)$ only, the decoding would be much more complicated.

The value for Vigneron's coefficient, ω (Eq. 49), must be known before a solution can be found. In this application, ω is lagged by defining it as a function of the previous space marching step solution. Once calculated, the value remains unchanged through both the predictor and corrector phases of the solution. Any attempt to change ω in the current space marching step lead to instability and could not be remedied. It is strongly suspected that this is due to the inability of the flux-differencing to

account for this change since the eigenvalues are calculated based on the conserved variables and not on the F^* components, per Korte [49]. In other words, since the subroutine which performed the flux-difference splitting used the computational flux Jacobian, $B = \partial\tilde{G}/\partial\tilde{U}$, and not the formulation used by Korte, $B = \partial\tilde{G}/\partial F^*$, there was no accounting for a change of ω within the numerical dissipation portion of Eq. 180.

As to the space marching step itself, given that the inviscid upwind algorithm has a Courant-Friedrichs-Lewy (CFL) [48] linear stability limit of 1 and a viscous limit of 1/2 (valid for 2-D or axisymmetric), then the allowable space step is defined by [49]

$$\Delta x \leq \frac{\Delta y_{wall}}{\frac{\Delta y_{wall}}{M_\xi\sqrt{\gamma(1-\sigma)}} + \frac{2\mu}{\rho u \Delta y_{wall}}} \qquad (184)$$

where Δy_{wall} is the change in y from the wall to the first grid point off of the wall (Fig. 29) [49]. All of the other variables in the above equation were taken at the first cell-center point away from the wall. This step is applied with a safety factor of 0.9 since the geometry in this application is a simple one [49].

With an adaptive grid subroutine provided to the author by Korte [53], the Δy_{wall} (Fig. 29) is computed dependent on whether the flow is laminar or turbulent. Within the subroutine, the value for y at the jth point is given by

$$y_j = y_{c1} + \varsigma_{c1}^4 (y_w - y_{c1}) \left(1 - \beta_{c1} \left(1 - \frac{2}{1 + \left(\frac{(\beta_{c1}+1)}{(\beta_{c1}-1)} \right)^{\varsigma_{c1}}}\right) + \beta_w \left(1 - \frac{2}{1 + \left(\frac{(\beta_w+1)}{(\beta_w-1)} \right)^{\varsigma_w}}\right)\right), \quad (185)$$

where

$$\varsigma_{c1} = \frac{(j_w - j)}{(j_w - 1)}; \quad \varsigma_w = \frac{(j-1)}{(j_w-1)}; \quad \beta_{c1} = 1.02, \quad (186)$$

The stretching parameter β_w is allowed to vary in order to meet the Δy_{wall} specification.

Should the flow be laminar, the number of points inside the boundary layer is specified by user input which in turn aids in computing the Δy_{wall}. This value is currently set to 20 points inside of the laminar boundary layer. Essentially, how this works is the subroutine in this case takes 1/20th of the Mach number at the centerline of the nozzle and drives β_w such that the first point away from the wall matches that value of Mach number (Fig. 30). Though this uses a somewhat simple linear approximation to the Mach number distribution in the boundary layer, it appears to provide excellent results in obtaining the specified number of points within the boundary layer [53].

Alternately, should the flow be turbulent, the value of y^+_{min}, the y^+ value (Eq. 54) of the first point off of the wall (Fig. 31), is a user input; the specified value of y^+_{min} in turn aids in computing Δy_{wall} for the first point off of the wall. In this case,

the subroutine drives β_w such that the first point away from the wall matches the user-specified value of y^+_{min}. The required value of y^+_{min} varies depending on how accurate a solution is deemed necessary by the user.

3.3.1 Boundary Conditions. The boundary conditions for the PNS solver were developed or taken from previously mentioned boundary conditions. The NS solver produces two adjacent columns of cells which are the initial conditions for the PNS code (Fig. 27). The most critical point here is for the NS solver to give an initial starting plane which does not violate M_{min}, as will be further discussed [9]. This is done by specifying for the NS solver the value of the safety factor, σ (Eq. 49), letting the solver backmarch from the exit through the flow field solution in search of the plane at which the violation occurs, and taking the next column downstream as the initial plane for the PNS solver. The wall and centerline conditions are handled exactly as they are in Sections 3.1.2 and 3.1.3.

No outflow conditions are required for a PNS solver in supersonic flow. The last solution plane at the nozzle exit provides the exit boundary conditions. In essence, this is a zeroth-order extrapolation or boundary condition.

3.4 Discretization of the B-L Turbulence Model and Boundary Conditions

In solving for the eddy viscosity with the B-L turbulence model, it is first necessary to find the maximum vorticity, ω_{max}. This almost always occurs at the wall, but to ensure it is located, a search marching away from the wall for a given axial location is undertaken. With ω_{max} known, the value for F(y), Eq. 58, at each point can be calculated. Once that is done, the point at which F(y) has a maximum value determines F_{max} and y_{max} for that column of cells (Fig. 32). Next, $\mu_{t_{inner}}$ and $\mu_{t_{outer}}$ are calculated marching away from the wall. Until the point at which $\mu_{t_{inner}}$ is greater than $\mu_{t_{outer}}$, the eddy viscosity is equal to $\mu_{t_{inner}}$, otherwise it is equal to $\mu_{t_{outer}}$ (Fig. 33).

In general, the number of times the B-L turbulence model is updated in the time-integration scheme has an influence on the numerical solution. However, the final converged numerical solution at steady state is independent of the number of times the B-L model is updated within the solver. The B-L turbulence model is therefore called once every 5 total time integrations (that is, once every 5 predictor-corrector cycles) in the NS codes, per recommendation by Shang [64]. This is done to aid in preventing the NS solver from reacting too quickly to immediate changes in the eddy viscosity. In the PNS code, the B-L turbulence model is called after each spatial integration step (either predictor or

corrector), since there is no temporal dependence in the PNS solution, and the geometry and physics change the values of ω_{max}, F_{max}, and y_{max} at each spatial location.

3.4.1 Boundary Conditions. There are only two boundary conditions which need to be accounted for with the B-L model. At the wall, eddy viscosity equals 0, so the equation for the eddy viscosity for the wall ghost cell is handled the same as the velocity components in Section 3.1.2. The eddy viscosity for the centerline ghost cell is equal to that of its mirrored cell, just as in Section 3.1.3, where the values of the scalar parameters remain unchanged across the centerline (Fig. 34).

3.5 Discretization and Boundary Conditions of the Yang-Shih k-ϵ Model

The discretization of a k-ϵ model using Roe's flux-difference splitting is readily available in [39]. The discretization recommended by Morrison is exactly the one used. A couple of key points must be mentioned however.

First, in order to prevent negative values of k and ϵ, minimum values must be established beyond which ρk and ρϵ are not allowed to transgress. However, care must be taken in assigning these values since the eddy viscosity is proportional to the ratio of k^2/ϵ. The values of ρk_{min} and $\rho\epsilon_{min}$ therefore should have some basis

in reality or at least a reasonable value compared to the ratio. In this formulation, the values for ρk_{min} and $\rho \epsilon_{min}$ are chosen to be 1.0E-24 times the values of ρk and $\rho \epsilon$ at the centerline in the inflow of the nozzle, per recommendations by White of NASA Langley [65].

Secondly, since k is included in the total energy equation, care must be taken to account for this inclusion in the Roe scheme formulation [39]. Of specific importance is the fact that the enthalpy and the speed of sound change as a result of this inclusion. The total enthalpy, H_T (Eq. 155), is now defined as

$$H_T = \frac{\gamma p}{(\gamma-1)\rho} + \frac{1}{2}(u^2+v^2) + k, \tag{188}$$

which using Eq. 26 makes the speed of sound, c,

$$c = \left[(\gamma-1)\left(H_T - \frac{1}{2}(u^2+v^2) - k\right)\right]^{\frac{1}{2}}. \tag{189}$$

Both of these equations are used in the formulation of the Roe scheme in Eqs. 146 and 147.

The method of solution for the governing partial differential equation with the added k-ϵ equations, Eq. 84, is to first solve for the NS equations throughout the domain of interest and to update the NS CFD solution. In other words, the new values for the (ρ, ρu, ρv, E) of Eq. 84 are computed as well as the values for (u, v, p, e_i). The boundary conditions on the mean flow are

subsequently enforced. During the preceding processes, the last computed (that is, the last half step) values of k and μ_t are used. Then using the previous half step values for the pertinent flow variables, the portion of Eq. 84 represented by Eqs. 61 and 62 are solved throughout the flow field in order to obtain the most current values of k, ϵ, and μ_t . After enforcement of the k-ϵ boundary conditions, this half step (either predictor or corrector) is concluded and the next half step starts.

3.5.1 Boundary Conditions. The inflow boundary conditions are not quite as straightforward as they have been for other portions of the code. For the inflow, the eddy viscosity was assumed to be equal to the molecular viscosity at each point of the inflow. Assuming a turbulence intensity of $T_i = 0.01$ [41,59] where the turbulence intensity is defined as

$$T_i = \frac{\sqrt{(\frac{2}{3}k_{i,j})}}{u_{i,j}} \qquad (190)$$

the value for $k_{i,j}$ can be readily computed. Then, using the value for eddy viscosity and k at each point along the inflow, ϵ can be calculated using Eq. 67 [41]. In the Y-S formulation, since ϵ can't be solved for explicitly in the eddy viscosity calculation (Eq. 67), it is necessary to perform a Newton iteration to obtain ϵ.

The boundary conditions at the wall are as follows: k is zero at the wall and ε_{wall} [52], represented by

$$\varepsilon_{wall} = 2\nu\left(\frac{\partial\sqrt{k}}{\partial y}\right)^2\Bigg|_{wall}, \tag{191}$$

with the simple average given by

$$\varepsilon_{wall} = 0.5\,(\varepsilon_{i,j1}+\varepsilon_{i,j1-1}), \tag{192}$$

results in

$$\varepsilon_{i,j1} = 4\nu\left(\frac{\partial\sqrt{k}}{\partial y}\right)^2\Bigg|_{wall} - \varepsilon_{i,j1-1}. \tag{193}$$

The reflection boundary condition was again used at the centerline as in Section 3.1.3, and a zero second-order streamwise gradient was used at the outflow to obtain ρk and $\rho\varepsilon$ there, as in Section 3.1.4.

4. *Nozzle Flow Code Development/Validation*

This chapter details all of the steps involved in taking a 2-D Roe-scheme NS code to full axisymmetric, modifying the code by adding the two turbulence models, and changing the resultant code over to PNS for use in the supersonic section of the nozzle, along with the validation steps taken along the way. Results of the validations are presented immediately following the presentation of validation case details. Justification as to why procedures were followed or not followed is provided, as are any pitfalls encountered along the way.

Salient features of all of the NS and PNS codes are as follows: finite volume, capable of being run 2-D or axisymmetric, using explicit integration, and globally second-order accurate through the use of flux-difference-splitting and the minmod limiter. In addition, the NS codes can utilize local time stepping for a steady-state problem in order to accelerate convergence to a solution. The nozzle flow codes are highly vectorized, resulting in their running much faster on a Cray or similar computer. However, the solvers can be run on any UNIX machines, including Sun Microsystems. In the harshest case (nonequilibrium chemically reacting (NECR) flow, NS solver, for almost the entire length of

a ten foot nozzle), the nozzle flow codes require less than 8 Mw of computer memory on a Cray, or 263 words per grid point.

4.1 2-D NS Perfect Gas Code Modified to 2-D/Full Axisymmetric

In order to have a 2-D/axisymmetric perfect gas code with the appropriate turbulence models and changeable source code, it was determined that the most efficient process would be to modify an existing local 2-D code which utilized the Roe-scheme. Though a 2-D/full axisymmetric NS code was available locally, this code was designed to account for vibrational nonequilibrium and chemical reaction effects; in the laminar case, for instance, this code solved for eleven conserved variables at each grid point (Eqs. 2 and 27) vs. four conserved variables at each point for a strictly perfect gas NS solver (Eqs. 2 and 3). It was therefore felt that this code would spend much wasted computer time in needless computations when solving the perfect gas NS equations. However, since the nonequilibrium chemical reaction code and the original NS perfect gas 2-D code were developed by the same person, Gaitonde [61, 66], and the foundation for the nonequilibrium code was the NS perfect gas 2-D code, it was felt that the 2-D code could be efficiently and quickly converted to being alternatively axi-symmetric.

The NS perfect gas 2-D code was a proven finite volume code which incorporated the Roe-scheme [7]. The finite volume method

ensures that the basic quantities of mass, momentum and energy are conserved at the discrete level [42]. Roe's scheme was determined to be desirable for a number of reasons [7]. First, since upwinding is used, no additional numerical dissipation is needed. Second, many other schemes are highly dissipative in viscous flows, giving large errors in heat transfer and other undesirable effects. Third, the method is extremely stable and robust, both highly desirable qualities. Fourth, the scheme does an excellent job of capturing shocks.

The form of Roe's flux-difference split method used in the computer code is MUSCL (Monotonic Upstream Schemes for Conservation Laws). Essentially, in standard flux-differencing (non-MUSCL), the flux vectors (F and G in Eq. 2) at the cell centers are extrapolated to the cell interfaces. In the MUSCL approach, the conserved, dependent vector (U in Eq. 2) or the unconserved, dependent vector (ρ, u, v, p) at the cell center is extrapolated to the cell interface in order to obtain the flux vectors at the interface [11].

The perfect gas computer code as given to the author was 2-D and hard-wired to compute the laminar flow about an airfoil. The code had to be converted to solve either axisymmetric flows or 2-D flows, as mentioned previously, and be modified to compute nozzle flow. Per the recommendation of Gaitonde [57] and following the example set forth in [66], Eq. 2 was selected as the governing equation.

Thus, the change in the 2-D code to axisymmetric entailed changing the metrics to account for variation with the normal variable, y ($y\xi_x/J$, $y\xi_y/J$, $y\eta_x/J$, $y\eta_y/J$ for the axisymmetric case vs. ξ_x/J, ξ_y/J, η_x/J, η_y/J for the 2-D case); adding axisymmetric terms to the viscous terms to account for non-Cartesian coordinates being used (the terms with a factor of δ in Eqs. 7 and 9); and adding the source terms to the right-hand side of Eq. 2. In addition, since the code lacked the anisotropic entropy cutoff in the streamwise direction (Eq. 162), this formulation was added to the code; recall this cutoff alleviates large amounts of dissipation which arise with large grid cell aspect ratios.

In addition to reformulating the code to solve for axisymmetric flows, it was necessary to develop initial conditions for the nozzle. The nozzle flow was initially assumed to be uniform sonic flow. However, with the boundary conditions previously presented in Sections 5.1.1 through 5.1.4, the flow became subsonic in both the convergent and divergent sections. As a result, a 1-D approximation to the Mach number was used to speed up convergence and to ensure that the flow remained supersonic in the divergent section of the nozzle. With the reservoir pressure and temperature specified and assuming the flow was sonic (M = 1) throughout the length of the throat (Fig. 35), then the temperature, pressure, and velocity components throughout the throat could be readily obtained from [54]

$$T = \left(1 + \frac{\gamma - 1}{2} M^2\right)^{-1} T_{res} \tag{194}$$

$$p = \left(1 + \frac{\gamma - 1}{2} M^2\right)^{-\gamma/(\gamma-1)} P_{res} \tag{195}$$

and

$$u = Mc = M\sqrt{\gamma RT}\,; \qquad v = 0\,. \tag{196}$$

It was necessary to perform a Newton iteration to match the area of the nozzle with the Mach number when dealing with the convergent/divergent sections of the nozzle (Fig. 6), using [54]

$$\frac{A}{A^\star} = \frac{1}{M}\left[\left(\frac{2}{\gamma+1}\right)\left(1 + \frac{\gamma-1}{2} M^2\right)\right]^{\frac{(\gamma+1)}{2(\gamma-1)}}. \tag{197}$$

In Eq. 197, A is the cross-sectional area at the axial location where M is to determined, and $A^\star$ is the cross-sectional area of the throat. Once M had been obtained for a given axial location, Eqs. 194, 195, and 196 were used to obtain the pertinent flow variables.

At this point, it was desired to compare the reformulated perfect gas code with the nonequilibrium code being run in perfect gas mode. However, the nonequilibrium code was hardwired to compute external flows when received [66]. The boundary conditions were therefore changed to account for nozzle flow (see Sect. 3.2.1). In addition, some other minor modifications were made to

make the code match up better in perfect gas mode. These included the addition of Keyes' Law of Viscosity (Eq. 20) for hypersonic nozzle flow [63]; the hard-wiring of the gas constants to match those used in the perfect gas code, specifically, R, C_v, and C_p; the zeroing out of the vibrational energy terms with a factor, δ_{NECR}, similar to the 2-D/axisymmetric switch δ, which was 0 in perfect gas mode and 1 in nonequilibrium mode (in Eq. 27, e_v --> $\delta_{NECR}e_v$); and the addition of perfect gas boundary conditions (see Sects. 3.1.1 - 3.1.4).

4.1.1 Validation of Perfect Gas NS Solver, Laminar Axisymmetric Case. To validate the perfect gas NS solver, the two NS codes (perfect gas and nonequilibrium/perfect gas) were run in perfect gas mode on a rather coarse 53x28 (i,j) mesh of the WL Mach 12 nozzle (Fig. 36). The flow field solutions obtained were compared with the nonequilibrium solution on the same mesh and with SAIC CFD data mentioned earlier [22]. These comparisons were also made to determine whether nonequilibrium and chemical reaction effects would need to be accounted for in the final optimization code. Direct comparisons would also help to debug the codes. The case run was laminar, since no turbulence models had been added to the codes at this time. Convergence was achieved when 1.5 characteristic time units had been achieved, or when the solution's total residual dropped 6 orders of magnitude. This was the general

criteria for convergence, unless otherwise specified below. However, in all cases the residual dropped at least 2-3 orders of magnitude in achieving a converged solution.

A characteristic time unit is represented by

$$\bar{t} = t/t_c, \tag{198}$$

where

$$t_c = R_L/U_\infty, \tag{199}$$

and t is the total time over which a solution has been integrated. The variables R_L and U_∞ vary with the case and the mesh used. For the laminar case on this grid, R_L was 3.048 m and U_∞ was the u velocity component in the nozzle throat obtained using Eqs. 194 and 196.

4.1.1.1 Results of Validation of Perfect Gas NS Solver, Laminar Axisymmetric Case. The final results from the validation done with the NS perfect gas solver and the NS nonequilibrium solver in perfect gas mode, as well as with the NS nonequilibrium solver in NECR mode were very encouraging. Plots of the centerline static pressure (Fig. 37) and temperature (Fig. 38) vs. the axial direction showed no significant difference between the solutions in perfect gas form and that in NECR form. Examining Figs. 39 and 40, plots of the same flow variables show only a mild difference in the

throat region, presumably due to nonequilibrium effects. Otherwise all three solutions converged to the same result as the flow traversed the nozzle. Thus, though nonequilibrium effects were seen in the throat region, the effect on the nozzle exit flow is indiscernible; the author thus concluded that in the laminar case nonequilibrium effects were not significant for the nozzle in question.

Plots of the Mach number (Fig. 41) and Pitot pressure (Fig. 42) at the nozzle exit similarly reveal no discernible difference between all of the solutions. In addition, when comparing with similar data computed by SAIC [22] for the laminar case, the nozzle exit results were very comparable. Again, with these results the author concluded that nonequilibrium effects were not significant enough in this case to warrant inclusion of such effects in a laminar solution of this nozzle. In addition, the author concluded that the perfect gas NS solver and the nonequilibrium/perfect gas NS solver had been validated in the laminar hypersonic nozzle case.

4.2 Turbulence Models Incorporated into Perfect Gas and NECR Codes

In order to determine whether the zero-equation Baldwin-Lomax (B-L) model or the two-equation Yang-Shih (Y-S) k-ϵ model would best model the turbulence in the nozzle flow, it was necessary to incorporate both into the perfect gas code and the nonequilibrium

code. In defining the best model, the objective was to ascertain which model would provide the turbulent nozzle flow which best compared with nozzle experimental data. It was possible that some trade-offs between accuracy and central processing unit (cpu) time might need to be made, especially in light of the determination that the solvers used in the subroutine be as efficient as possible. The B-L model would undoubtedly be faster, since fewer computations were necessary, but its accuracy had yet to be determined. The Y-S k-ϵ model might prove more accurate but its cost in computer time was as yet unknown. These were items which needed to be addressed before a choice could be made as to which turbulence model to use throughout the optimization.

The B-L model added to the codes was primarily adapted from a previously developed modification to the same 2-D perfect gas code as initially used here [67]. With a minor modification, this subroutine is the one used in the code when the B-L model is used; the minor modification consisted of removing a portion of the subroutine which dealt with recirculating flow. It was felt that this portion of the subroutine was unnecessary since flow separation and recirculation were not likely to occur in the nozzle flow being researched.

The k-ϵ subroutine used in the code was developed by the author and was based on the work and turbulence model of Yang and Shih [52]. In order to simplify debugging of the code, a Steger-Warming (S-W) scheme was initially used, and the Launder-Spaulding

(L-S) k-ϵ model, used by Rizzetta [41,59], was the k-ϵ model used. The S-W scheme was used initially because of its simplicity [55]. The L-S model was initially used because the author was provided a copy of Dr Rizzetta's Beam-Warming 2-D solver, in which the L-S turbulence model is used. Details of this code are available in [41]. Hence, for debugging the 2-D/axisymmetric perfect gas solver and for comparisons with the solution obtained from the Rizzetta code, the S-W scheme with the L-S k-ϵ model was initially used. Once the debugging of the S-W scheme with the L-S k-ϵ model was completed, a switch was made to the Roe scheme, but the use of the L-S model was maintained. Finally, once all the bugs had been worked out of that code, the Roe scheme was used with the Y-S k-ϵ turbulence model in the last revision of the NS code with turbulence.

All of the work to this point had been done on the perfect gas code. Later, however, both turbulence models were included in the nonequilibrium code so that the comparison of the perfect gas solutions with the nonequilibrium solution could be made for the nozzle, as discussed in Section 4.2.3.

The turbulence model validation occurred in three phases. The turbulence models and their associated NS codes were first validated in 2-D against another CFD solution. The turbulence models and codes were then validated in 2-D against experimental data. And finally, the turbulence models and codes were validated in axisymmetric form against WL Mach 12 nozzle data.

4.2.1 Turbulence Model Validation Against a CFD Solution.

Both turbulence models were compared to previously validated CFD results from Rizzetta [68]. The test case was a flat plate at zero angle of attack (α) which the Rizzetta code had been previously used to solve. Adiabatic wall conditions were used. The length of the flat plate and the freestream values of Mach number, temperature, Reynold's number and the turbulence intensity were (Fig. 43):

$$L = 0.9144m, \quad M_\infty = 2.0, \quad T_\infty = 310.93°K, \quad Re_L = 1.0E{+}06, \quad T_{i_\infty} = 0.005.$$

It was felt that better solution comparisons could be made if the same grid were used for all CFD solutions in this validation case, so the rectangular mesh used was 102x82 (i,j), and was provided the author by Rizzetta [68]. The grid had a constant minimum wall-spacing of 2.286E-05 m. The spacing in the x-direction was a constant 9.144E-03 m. A representative grid is shown in Fig. 44.

4.2.1.1 CFD Mach 2.0 Flat Plate Results.

Initial comparisons of $\frac{\mu_t}{\mu}$, $\frac{u}{u_\infty}$, *and* $\frac{\rho}{\rho_\infty}$, plotted against the distance in the normal direction, are shown in Figs. 45, 46 and 47. The data for these plots were taken at the trailing edge of the flat plate. Though Fig. 45 shows a significant difference in the ratio of local eddy viscosity to molecular viscosity, Figs. 46 and 47 show that

this difference does not equate to as large a difference in the outcome of the normalized u and ρ.

Concern regarding such a difference in any of the parameters at the trailing edge led to a check of C_f, the coefficient of friction. The plot of C_f against the distance along the flat plate (Fig. 48) showed a large difference in the numerical transition point (as opposed to the physical one) for the different numerical models, which could indeed lead to the differences seen above in the flow parameters at the trailing edge.

A comparison of Fig. 49 with Fig. 50 [47], both plots of C_f vs Re_x, shows that the transition for the Y-S model occurs within the specified transition range of Re_x of $2x10^5$ and $6x10^5$ of the theories of Prandtl and Blasius. Note that Fig. 50 is a plot for the incompressible flow about a flat plate at zero degrees incidence; however, since the Mach number for this case is 2.0, there should be no significant change of C_f due to compressibility, nor a significant change in the curves in Fig. 50 [47]. Once again recall that this is merely a numerical transition and not the actual physical transition normally associated with turbulence.

Finally, a plot of u^+ vs y^+ at the trailing edge of the plate (Fig. 51) shows extremely good comparison between the two k-ϵ models up to approximately a y^+ of 10. From y^+ of 10 to the edge of the boundary layer, a noticeable difference exists between the two k-ϵ models.

Although there were some good comparisons between the different turbulence models and all of the models had been validated, a question still remained as to whether the L-S or the Y-S model would more accurately predict the outer layer of a turbulent boundary layer. The logical way to determine the k-ϵ model to use in the solver was to test them both on an experimental flat plate and compare the results. This need defined the subsequent step of the validation.

4.2.2 Validation of Y-S k-ϵ Model Against Experimental Data. Once the results of the CFD Mach 2.0 flat plate in Section 4.2.1.1 were obtained, there remained a question with regard to the Y-S model as to whether or not its solution provided a better representation of the turbulent boundary layer than the L-S model. It was thus decided to compare the solution obtained with the Y-S model against a solution obtained with the L-S model, both using the Roe-scheme, and compare both against well-validated and well-documented experimental results. Again, the code in which the turbulence models were incorporated was perfect gas, full NS, using a 2-D coordinate system.

The experiment chosen for validation of the Y-S k-ϵ model was that of Kussoy and Horstman due to the fact that it was a well-validated experiment [56]. It consisted of a sharp leading-edge flat plate at -2 degrees α (Fig. 52) in an approximately Mach 8.2

flow [56]. The length of the flat plate and the freestream values of Mach number, temperature, Reynold's number and the turbulence intensity were:

$$L = 1.870m, \quad M_\infty = 8.18, \quad T_\infty = 81.0°K, \quad Re_L = 7.938E{+}06, \quad T_{i_\infty} = 0.01$$

The wall temperature was assumed fixed at 300 °K.

The mesh used was 200x90 (i,j) and the minimum wall-spacing was 5.8928E-06 m (y^+ = O[1-10]. The spacing in the x-direction began at 5.893E-03 m and increased continually to 1.420E-02 m. A representative grid is shown in Fig. 53.

4.2.2.1 Experimental Mach 8.18 Flat Plate Results.

The plot of u^+ vs y^+ (Fig. 54) did not initially show particularly good agreement with the computational data although it did exhibit the proper trends. The lack of agreement was due to the value of u_τ. This value was originally determined from the flow parameters of the computer solution, and since the numerical transition point is almost assuredly different than the experimental one, the wall stress can be markedly different between a computed solution and experimental data. Once the value of u_τ from the experiment was used [56] the agreement between the computational data and the experimental data was much improved (Fig. 55). It can be seen that the trends associated with the experimental data are captured much better by the Y-S model.

Therefore the Y-S model was the k-ϵ model chosen to be carried forward for use in further turbulence model comparisons.

4.2.3 Validation of Turbulence Models Against WL Mach 12 Nozzle. The two turbulence model subroutines (B-L and Y-S) were subsequently incorporated into the perfect gas and NECR codes for validation against an axisymmetric nozzle case to determine the impact of high temperature effects on the solution, as well as to determine which turbulence model provided the best results. The validation case was the WL Mach 12 nozzle experiment [22], with boundary conditions previously presented in Sects. 3.1.1-3.1.4. Following discussions with Korte and Scaggs [53,63], the boundary layer was specified to be fully turbulent at the inflow. Should solutions obtained using this boundary condition indicate that it was erroneous, the incorporation of some transition model would be required. The turbulence intensity (T_i) for the first two columns of cells was 0.01 for the Y-S k-ϵ model.

Both turbulence models (B-L and Y-S) were run in each solver. Both solvers were run in perfect gas mode; the NECR solver was additionally run in nonequilibrium mode.

Two separate regions were used to calculate the entire nozzle flowfield, as illustrated in Fig. 56. The reason for splitting the nozzle domain into two regions was to minimize the use of the prohibitively small time-marching step associated with the

relatively small subsonic section. The first region, labelled Item A, had a mesh 81x126 (i,j) and consisted of the subsonic convergent section, the cylindrical throat, and a small portion of the supersonic divergent section. The first point of calculation at the inflow was located at an x-location of 9.228E-03 m and the last point at the outflow was located at an x-location of 3.988E-02 m. The x-spacing on the first grid varied, but the nozzle wall coordinates for the entire nozzle are presented in Appendix A. The second region, labelled item B, began 10 columns of cells before the outflow of the first grid, ended shortly before the nozzle exit, and was computed on a mesh of 242x126. For the second grid, the first point of calculation at the inflow was located at an x-location of 3.643E-02 m and the last point at the outflow was located at an x-location of 2.950 m. The value for y^+_{min} for both grids was on the order of 1, achieving a value of 2-3 in the throat region of the first grid and decreasing after that.

In order to maintain second-order accuracy at the inflow of the second mesh, it was necessary to provide two initial columns of data from the solution of the first grid. The data for these two columns of cells was never recomputed in the solver for the second mesh; the inflow boundary conditions were thus fixed.

4.2.3.1 WL Mach 12 Nozzle Results. When the computed static pressure along the wall for the two different turbulence

models was compared with that obtained experimentally (Fig. 57), the B-L turbulence model appeared to better match the experimental data. The k-ϵ model, on the other hand, displayed increasing deviation from the experimental data as the flow traversed the nozzle.

Comparing the computed Mach number and Pitot pressure near the nozzle exit with experimental data for the perfect gas case (Figs. 58 and 59), the B-L model once again provided a much better comparison than the k-ϵ model. Though the B-L model appeared to be producing a slightly thicker boundary layer than exhibited by experiment, the k-ϵ model produced a markedly thinner boundary layer and a substantially different Mach number in the inviscid core. The Mach number obtained using the B-L model was very close to that of the experiment.

Upon further investigation of the difference in the thickness of the boundary layer for the two turbulence models, an unexpected change in the thickness trend was discovered: the k-ϵ model was producing a thicker boundary layer than the B-L model at the throat exit location (Figs. 60 and 61). The k-ϵ model thus appeared to be more diffusive in the subsonic/sonic section of the nozzle and less diffusive in the supersonic portion of the nozzle. The reason for this was unclear and remains to be investigated.

Comparison of the computed exit Mach number for the perfect gas and NECR solvers and their turbulence models showed no significant difference between the perfect gas and the NECR case

(Figs. 62 and 63). The lack of difference between the perfect gas and the nonequilibrium cases was presumed to be due to the fact that the temperature and pressure in the flow never reach levels at which nonequilibrium and chemical reaction effects become of primary importance [25].

4.2.4 Interim Conclusions Drawn. As a result of the validation efforts in this section, a number of significant conclusions were drawn. One, the turbulence models had been well validated against both computational and experimental results. Two, the B-L model would be used in continuing the current research; the secondary objective of determining the turbulence model which aided in more accurately representing the turbulence in the testbed nozzle flow had thus been accomplished. Three, there was no need to use the nonequilibrium code to further the research on the optimization scheme. However, in future research, a nonequilibrium form of the code will be developed to be used in high temperature, high pressure nozzles as the perfect gas solver is limited in such hypersonic nozzle flows.

There were three additional important conclusions that were drawn at this point. First, with the use of the B-L model the flow solution would provide more accurate nozzle data. Second, the assumption that the flow was fully turbulent from the inflow had been corroborated with the excellent comparative results between

the fully turbulent flow generated with the B-L model and the experimental data. And third, the use of the B-L turbulence model would ensure a more efficient solver, thus contributing to the primary objective of this research.

4.3 Development/Validation of Perfect Gas PNS Code with Two Turbulence Models Incorporated

As mentioned previously, the template for the PNS scheme was that proposed by Korte [49] due to the fact that this was a very thorough source of PNS formulation using the Roe scheme. The upwind flux scheme used a central flux approximation for the inviscid fluxes and the viscous fluxes were centrally-differenced. Due to the manner in which the computational flux Jacobian was computed, Vigneron's coefficient (ω, Eq. 49) was lagged and based on the last complete solution of the previous column of grid cells.

4.3.1 Validation of Perfect Gas PNS Solver, Laminar 2-D Case.

A suitable validation case for the perfect gas PNS solver was needed, and Korte's supersonic laminar flow over a flat plate was chosen [49]. With this case the PNS solver could be validated against a well-published test case and its solution.

In addition to validation, the test case was run to determine if the GCL terms were or were not needed; an important question remained as to whether a finite volume scheme required the extra

GCL terms which Korte had outlined [49]. Note that the GCL terms are only necessary if the grid is varying in the y-direction as space-marching occurs. Also note that with a nozzle the y-spacing will vary in the axial direction, and so it was most important to determine the necessity of the GCL terms.

The conditions for the flat plate validation case, including the freestream Mach number and temperature, the wall temperature, the Reynold's number and the length of the plate (Fig. 64), were the following:

$$M_\infty = 2.0, \quad T_\infty = T_{wall} = 222.0°K, \quad Re_L = 1.65E+06, \quad L = 1.0m.$$

Two grids were used in order to determine the necessity of inclusion of the GCL terms. The first was a rectangular mesh which varied in spacing in the x-direction but not in the y-direction; this grid was used because it precluded the need for the GCL terms. This grid is labelled Grid A and shown in Fig. 65. The second was a grid which varied in spacing in both the x- and y-directions, being clustered closer at the leading edge in both directions and widening in both directions as the solution marched towards the back of the plate. This grid was used to determine if the GCL terms were necessary, with such varied mesh spacing, to generate a flowfield solution which compared favorably with the first grid. This second grid is labelled Grid B, as shown in Fig. 66.

The spacing in the x-direction was initially held to a constant value of 1.0E-06 until the solution reached the point

where $x \geq 0.025m$, at which point the spacing in the x-direction was allowed to begin increasing to the CFL specified space marching step. The space-marching step was initially held constant to preclude instabilities associated with the stagnation region of the flat plate leading edge. However, once allowed to vary the spacing in this direction was not allowed to grow by more than 0.01% at each space-marching step, lest instability should again occur. The spacing in the y-direction [49] was determined from

$$y(j) = y_{wall} + (y_{max} - y_{wall})\left[1 - \beta + \frac{2\beta}{1 + \left(\frac{\beta+1}{\beta-1}\right)^{\varsigma}}\right], \qquad (199)$$

where y_{wall} is the flat plate surface, y_{max} is the far field free-stream edge, and

$$\varsigma = \frac{(j-1)}{(j_{max}-1)}. \qquad (200)$$

The value of β was held constant at 1.001 for both grids in order to capture the boundary layer and to allow for a better comparison at the flat plate trailing edge. For the fixed grid, the flat plate was located at y=0 and the freestream far edge was located at y = 0.8 m. For the varying grid, the flat plate was located at y = 0 and the freestream far edge was located at y = 0.6 m at the leading edge and y = 0.8 m at the trailing edge. The flow parameters were taken from the x = 0.93m station.

4.3.1.1 CFD Laminar Mach 2.0 Flat Plate Results. Solutions for Grid A and Grid B with and without GCL terms were obtained. Comparing the respective plots of $\frac{T}{T_\infty}$ vs y against the results of Korte for the case excluding GCL terms showed poor agreement between the flow solution obtained using Grid B and the other solutions, particularly in the peak temperature region (Fig. 67). With the GCL terms included, the plots of $\frac{T}{T_\infty}$ vs y compared very well for both grids (Fig. 68). Plots of $\frac{u}{u_\infty}$ vs y also compared very well, again with GCL terms included (Fig. 69). Thus it became apparent that the GCL terms were necessary for this finite volume formulation of PNS. It was also evident that the PNS formulation had been validated for the laminar case.

4.3.2 Validation of Perfect Gas PNS Solver, Turbulent 2-D Case. Next, the perfect gas PNS solver had to be validated using each of the two turbulence models. For this validation the Mach 2.0 flat plate case used in Section 4.2.1 for the NS turbulence model validations was chosen, since validated solutions and their data were readily available and required no additional computations. The grid was varied just as it was in the second mesh of the laminar flat plate PNS validation described in Section 4.3.1.

Recall that the test case was a flat plate at zero degrees α [68]. The length of the flat plate and the freestream values of

Mach number, temperature, Reynold's number and the turbulence intensity were (Fig. 43):

$$L = 0.9144m, \quad M_\infty = 2.0, \quad T_\infty = 310.93°K, \quad Re_L = 1.0E{+}06, \quad T_{i_\infty} = 0.005.$$

Adiabatic wall conditions were used.

The validation case consisted of running the PNS code with the individual turbulence models (B-L and Y-S) activated, followed by comparing resultant solutions against previously obtained NS results for the same turbulence model. The results would be used to verify that the PNS code was computing turbulent flow correctly.

4.3.2.1 CFD Turbulent Mach 2.0 Flat Plate Results. The first case run was that of the B-L model. A plot of normalized u velocity vs normal distance from the plate and a plot of Mach number vs normal distance from the plate indicate very similar, well-matching solutions (Figs. 70 and 71). It must be remembered that the NS solution is obtained on a rather coarse mesh in comparison with the PNS solution in the streamwise direction (Fig. 27), and that the fluid center of a grid cell is not necessarily the geometric center of the grid cell. Nonetheless, because the geometric center is most easily calculated and the other is not, the geometric center was the approximated grid point associated with the flow parameters. This approximation likely leads to the slight disparity between the two solutions.

The second case run was that of the Y-S model. Again, a plot of normalized u vs normal distance and a plot of Mach number vs normal distance indicates very similar, well-matching solutions (Figs. 72 and 73). The k-ϵ model appeared to match even better with the NS solution than did the B-L model. This is possibly due to the fact that the turbulence is emulated in the k-ϵ model using conserved variables, whereas this is not the case with the B-L model. Nonetheless, the B-L model still provided a fairly good match between the two solvers and it remained the turbulence model of choice in furtherance of the research.

4.3.3 Perfect Gas PNS Code Validation Against Mach 12 Nozzle. Validation of the perfect gas PNS solver on the WL Mach 12 nozzle was subsequently performed. Having previously validated the perfect gas NS solver on the Mach 12 nozzle using each of the turbulence models as described in Sect. 4.2.3, the results of this earlier validation would provide an excellent comparison for the perfect gas PNS solver on the same case. However, a couple of minor complications presented themselves during the course of this work.

The inflow to the PNS solution was two columns of cells from the first grid of the perfect gas NS solver, just as was provided to the second grid of the perfect gas NS solver (Fig. 56). However, too large a space-marching step was required from the

cell-center of the NS solution to the cell-center of the first PNS column of grid cells (Fig. 74); the large step size resulted in instability, which caused the solution to blow up. This was remedied by extrapolation of the conserved variables using a finite difference approximation. The extrapolation was made using

$$U_{i+1,j} = U_{i,j} + \frac{(U_{i,j}-U_{i-1,j})}{(x_{i,j}-x_{i-1,j})}(x_{i+1,j}-x_{i,j}) \; . \qquad (201)$$

The space-marching technique employed for integration of the PNS equations was initially prohibitively slow. In order to accurately capture the boundary layer in the throat region of the nozzle, it was necessary, as previously mentioned, to use a grid stretching parameter (β_w, Eq. 185) of 1.001 in developing the grid for the NS solver (Fig. 56). And in order for the NS and PNS solutions to match up well at the inflow to the latter (Fig. 74), it was necessary for the PNS solver to match the β_w used for the grid in the NS solver. This value for β_w was too small a value for most of the latter portion of the nozzle, since the boundary layer grows quite large in that region; the restriction on β_w maintained the first grid cell point a very small distance off of the wall (Fig. 75), thus restricting the space-marching step size (Eq. 184).

The grid adaptation subroutine previously mentioned in Sect. 3.3 was utilized to allow the grid to vary with the thickness of the boundary layer. This subroutine allows the user to specify the number of points in the laminar boundary layer or the y^+_{min} value for

a turbulent boundary layer, while not allowing the change from one space-marching step to the next to be too large. Utilizing this subroutine and specifying y^+_{min} to have a value of 5, the PNS solver was able to compute almost 3.0 m of nozzle in approximately 30 minutes of Cray cpu time. This was vastly preferred over the hours of Cray cpu time that would have been necessary without this subroutine. In addition, the value for β_w was bounded. It was not allowed to become smaller than the initial value of 1.001, since the most restrictive region was the throat and the region upstream [53]. Nor was it allowed to get any larger than 1.1 [57,71].

A specific approach was necessary to compute the column of grid cells for the next space-marching step. Due to the fact that the space-marching step, Δx (Eq. 184), and the wall distance, $y_w(x)$ (Fig. 75), were interrelated, coupled with the fact that Δy_{wall} depended on $y_w(x)$ (Eq. 185), Δx and Δy_{wall} could not be computed simultaneously. The Δx was computed first; the Δx was thus lagged with the previous value of Δy_{wall}. Next, the β_w was calculated as previously mentioned in Section 3.3. And finally, the y(j) values for the next step were computed, using Eq. 185.

At this stage, the perfect gas PNS solver was ready to be validated against the NS solver, using the Mach 12 nozzle as the testbed. Concurrent with the validation, a determination was to be made of how restrictive to be with regard to β in order to achieve a comparable solution to that obtained using the NS solver. Recall

that the NS solver used a mesh with a β value of 1.001 and the y^+_{min} value was on the order of 1 (Fig. 56). Two cases were run, one using a y^+_{min} value of 5 and the other using a y^+_{min} value of 10. Only the B-L model was used in these calculations.

4.3.3.1 WL Mach 12 Nozzle Results. Plots of Mach number vs radial distance and Pitot pressure vs radial distance near the nozzle exit indicate no appreciable difference between the various solutions (Figs. 76 and 77). Though the value of y^+_{min} plays a large part in the calculated value of the shear stress at the wall [57], the plots show that the difference in the output of the nozzle is negligible when y^+_{min} is varied from 1, as in the PG NS code, to 5 or 10, as in the PG PNS code.

4.3.4 Interim Conclusions Drawn. Two very important conclusions were drawn at this juncture with regard to the perfect gas PNS axisymmetric nozzle code. First, based on the data presented, it was concluded that the y^+_{min} value had little effect on the nozzle exit flow as long as this value was between 1 and 10; thus, based on the recommendations of Korte [9], it was decided that the y^+_{min} value to be used in the nozzle optimization scheme would be 7. Second, the PNS solver had been well-validated, and was ready to be incorporated into an efficient optimization scheme.

4.4 Objectives Satisfied in Chapter 4

Only the one secondary objective of the current research was satisfied in this chapter. Recall that this was the objective associated with choosing a turbulence model to further the current research. Fortunately, the less computationally-intensive B-L turbulence model proved to provide the more accurate testbed nozzle flow when compared with experimental data. The B-L model was thus chosen to be the turbulence model used in the remainder of the current research. The other two objectives remained to be satisfied.

5. Development and Validation of Optimization Scheme and Code

This chapter presents the development and validation of the optimization code in order to meet the primary objective of this research, as well as the other secondary objective.

In the development of the optimization scheme, much effort was expended in order to achieve a robust computer code. Methods which did not work well or required too much user interaction were passed over in order to achieve this goal.

The performance of a number of steps was required prior to developing an automated optimization code. First, the new nozzle geometry and design parameters needed to be selected. Second, a manual optimization search was required, to determine if an optimum solution to the hypersonic nozzle design problem could be efficiently found. The rationale behind this was to minimize the use of computer time in unproductive automatic searches. In this manual search, the response functions were to be determined, the response surface was to be mapped, and the optimization method was to be selected. Following successful completion of the manual optimization search, the optimization scheme was automated, validated, and tested for robustness against the Mach 12 nozzle.

5.1 Design Parameters and New Nozzle Wall Geometry

It was now necessary to develop the design parameters which would be used to obtain a new nozzle wall geometry. As previously mentioned, the two variable design parameters chosen to be used in the optimization scheme were the nozzle attachment angle, θ_{attach}, and the nozzle exit angle, θ_{exit} (Fig. 13). These two design parameters had been used successfully by Doty in designing 2-D high Mach propulsive nozzles with MOC/BL techniques, and it was felt that the two parameters would thus be sufficient to design an axisymmetric high Mach wind tunnel nozzle [58].

A number of nozzle parameters were specified and fixed in order to minimize the number of design parameters used in the optimization procedure (Fig. 13). The x- and y-coordinate values for the old (WL Mach 12 nozzle) expansion corner, x_{oc} and y_{oc}, as well as the original expansion angle, ϕ_{oc}, were 0.03279m, 0.00518m, and 8.842°, respectively. The x- and y-coordinates of the nozzle exit, x_{exit} and y_{exit}, were fixed at constant values of 3.048m and 0.25365m since these were the coordinates of the WL Mach 12 nozzle. The radius of the attachment corner, r_{circ}, was fixed as well at a constant value of 0.00254 meters, since this value appeared to well represent the existing nozzle radius at the expansion corner, (x_{oc}, y_{oc}).

Once θ_{attach} and θ_{exit} were prescribed, the nozzle wall geometry could be obtained using mathematical equations. First, the x- and

y-coordinates of the reference point, x_a and y_a (Fig. 13) were determined using geometry to obtain

$$x_a = x_{nc} - r_{circ}\sin(\phi_2), \tag{202}$$

and

$$y_a = y_{oc}, \tag{203}$$

where

$$x_{nc} = x_{oc} - dx, \tag{204}$$

$$y_{nc} = y_{oc} + r_{circ}(1-\cos(\phi_2)), \tag{205}$$

$$\phi_2 = \frac{\pi}{2} - \phi_1, \tag{206}$$

$$\phi_1 = \frac{(\pi - \phi_{oc})}{2}, \tag{207}$$

and

$$dx = (y_{nc} - y_{oc})\tan(\phi_2). \tag{208}$$

Next, the x- and y-coordinates of the attachment point, x_b and y_b (Fig. 13), were determined from [69]

$$x_b = x_a + r_{circ}\sin(\theta_{attach}) \tag{209}$$

and

$$y_b = y_a + r_{circ}(1-\cos(\theta_{attach})) . \tag{210}$$

For the nozzle wall (Fig. 13) from the attachment point, b, to the nozzle exit, the wall was generated using the equation of a skewed parabola. The skewed parabola equation is given by [69]

$$[y_w - x\tan\tau]^2 + C_1 x + C_2 y_w + C_3 = 0 , \tag{211}$$

where

$$C_2 = \frac{(B_1-B_2) - (x_b-x_{exit})\,B_3}{(y_b-y_{exit}) - (x_b-x_{exit})\tan(\theta_{attach})} , \tag{212}$$

$$C_1 = B_3 - C_2\tan(\theta_{attach}) , \tag{213}$$

$$C_3 = B_1 - C_1 x_b - C_2 y_b , \tag{214}$$

$$B_2 = -(y_{exit} - x_{exit}\tan(\tau))^2 \tag{215}$$

$$B_1 = -(y_b - x_b\tan(\tau))^2 , \tag{216}$$

and,

$$B_3 = 2\,[y_b - x_b\tan(\tau)]\,[\tan(\tau) - \tan(\theta_{attach})] . \tag{217}$$

This equation, Eq. 211, was solved using a Newton iteration in order to obtain C_1, C_2, C_3, and τ [44]. Then, the nozzle wall ra-

dius, y_w (Eq. 211) could be easily generated, given an axial location in the nozzle, x (Fig. 13).

Thus, for the different solvers, the wall radius, y_w, was calculated using different equations, depending on what the axial location was. If the current x-location was in the throat, located in front of point a, then the wall height was constant at 0.0051816m. If the x-location were in the circular throat region, between points a and b, then the wall height was found using the geometry of a circle and determined by [69]

$$y_w = y_a + r_{circ}[1-\cos(\theta)] \qquad (218)$$

where θ is determined from $\theta = \sin^{-1}[(x-x_a)/r_{circ}]$. Otherwise, if the x-location were in the skewed parabola section of the nozzle contour beyond point b, then Eq. 211 above would be used with the appropriate coefficients and skew angle, τ, to generate the wall height.

5.2 Manual Optimization Search

The first scheme to be tried manually provided only one NS inflow to all of the PNS solutions. The point in the nozzle where the PNS inflow was initially provided was at approximately 2/3 the length of the throat (Fig. 78). The flow here was supersonic in the inviscid core and it was felt that this inflow would provide excellent results since this was well upstream of the nozzle wall

that was to be changed (Fig. 79). However, an oversight occurred by overlooking the minimum Mach number, M_{min} (Eq. 50). Recalling that the value for this parameter is about 1.24 for the stated value of the safety factor, σ, the values for the Mach number in the inviscid core for this inflow were approximately 1.1. Upon examination of the output data it was ascertained that Vigneron's coefficient, ω (Eq. 49), was being activated in the inviscid core at the inflow causing non-conservation of streamwise pressure (Fig. 80).

It was thus determined that the PNS inflow must come from the supersonic divergent section of the nozzle; the challenge associated with this determination was that the wall would change upstream of the PNS inflow necessitating a NS solution for each change in the design parameters (Fig. 81). Since a NS solution is obtained using a significantly larger amount of time than a comparable PNS solution, potentially many more hours of cpu time might be necessary.

In order to minimize the time associated with generating a new NS solution for each wall change, a smaller NS grid, grid C (Fig. 82), and associated solution were extracted from the converged solution to the first NS grid above, Item A (Fig. 56). In addition to being a smaller grid thus requiring fewer computations per iteration, the flow throughout Grid C was overall supersonic, allowing for a larger time step per iteration than would have been possible had the subsonic/sonic portion of the nozzle been

included. Grid C was started at 31 points before the outflow of the grid in Item A. This placed the first column of cells for this subgrid at 1.998E-4 m, approximately halfway back in the throat (Fig. 81). The outflow column and all the other columns of cells in between remained the same as in Item A.

A new grid which accounted for the redesigned nozzle contour due to a change in design parameters was subsequently obtained in order to generate a new NS solution; from this new NS solution would come the inflow for the PNS solver for each nozzle contour. Grid C was used to generate Grid D (Fig. 83), which had the same grid dimensions as Grid C, 31x126 (i,j).

A converged NS solution of Grid D was then computed. The NS solution to the first two columns of cells in Grid D were not recomputed; the solution for these was obtained from the converged solution to the grid in Item A and was assumed fixed, presumably a good approximation given that the cells were far upstream of the corner that would change with the design parameters (Fig. 83).

With Grid D being used in the perfect gas NS solver and the converged solution from Item A as the startup solution to Grid D, the perfect gas NS solver did not appear to require any more than 12000 iterations for a converged solution with a new nozzle wall contour (Fig. 84). Convergence in this case meant achieving a PNS inflow which varied a negligible amount with tens of thousands more iterations and a residual which had decreased 2-3 orders of magni-

tude and was merely wavering about some mean value. Each case was run to 18000 iterations to ensure convergence.

At this point, with all of the previously performed flow solver validations, one could reliably assume that a sufficiently accurate NS solution could be obtained and provide the appropriate inflow to the PNS solver, which in turn would produce a sufficiently accurate nozzle flow solution as well.

5.2.1 Determination of Response Function. The next challenge was to determine the response function to be used in the optimization. The first such function considered was a least-squares residual, specifically the error in the Mach number in the inviscid high Mach core at the nozzle exit (Fig. 85) [57]. This was the nozzle exit error, defined by

$$Er = \sum_{j=1}^{jmax} (M_{x_{imax,j}} - M_{design})^2. \tag{219}$$

If necessary, the nozzle centerline error (Fig. 86), defined by

$$Er1 = \sum_{i=1}^{imax} (M_{x_{i,1}} - M_{design})^2 \tag{220}$$

would be added to Er to produce

$$Ert = Er + Er1, \tag{221}$$

the total error function and another potential response function.

contributions from certain portions of the flow might be preferred over other portions. For example, in the nozzle exit error, Eq. 219, the errors from the inviscid core should contribute heavily to the summation, while the errors from the boundary layer should be deemphasized due to the likelihood of this portion of the flow dominating the summation. Similarly, in the nozzle centerline error, Eq. 220, the errors from the uniform core near the nozzle exit should contribute heavily to the summation, while the errors upstream of the uniform core should be deemphasized for the same reason as the boundary layer in Eq. 219.

In order to thus accentuate the contributions of a particular portion of the flow towards a given response function, a weighting factor was required. Accordingly, the computation of Er and Er1 would be modified by some normalized weighting factor, producing

$$Er = \sum_{j=1}^{jmax} [\omega_{exit}(M_{x_{imax,j}} - M_{design})^2] \qquad (222)$$

and

$$Er1 = \sum_{ii=1}^{iimax} [\omega_{CL}(M_{x_{ii,1}} - M_{design})^2], \qquad (223)$$

to diminish the error contributions of the boundary layer to the nozzle exit error, Eq. 219, and of the upstream portions of the nozzle to the nozzle centerline error, Eq. 220. The equation for the total error function, Ert (Eq. 221), would be unchanged, but would now use the results from Eqs. 222 and 223.

To ensure that the code require a minimum of user-interaction yet emphasize the preferred portions of the flow required the assumption that the designer had no a priori knowledge of how large the inviscid high Mach core might be nor of how long the uniform region might be in the latter portion of the nozzle (Figs. 87 and 88). Hence, the nozzle exit error summation (Eq. 222) was performed over the entire nozzle exit. As will be discussed next, the nozzle centerline error (Eq. 223) was performed only over the last half of the nozzle.

Since it was felt that the uniform core (Fig. 88) would be predominant only in the last half of any well-designed nozzle, the nozzle centerline summation (Eq. 223) was not performed over the first half of the nozzle. In addition, with varying nozzle geometry the number of points which would contribute to Er1 would vary due to the number of space-marching steps, potentially biasing Er1. Specifically, the size of and hence the number of space-marching steps used in the PNS solver depends upon the spacing at the wall, as shown in Sect. 3.3, Eq. 184. With a smaller attachment angle, θ_{attach}, the number of space-marching steps increases due to a smaller Δy_{wall} (Fig. 75). Conversely, with a larger θ_{attach} the number of space-marching steps decreases due to a larger Δy_{wall}.

Hence it was decided that though the number of space-marching steps would still depend on the nozzle geometry, the number of steps contributing to the nozzle centerline error

summation (Eq. 223) would be fixed; this would remove the uncertainty associated with potentially more points contributing to the error summation and the potential of biasing the result. The last half of the nozzle is divided into 50 equal regions (Fig. 89). Each time one of those regions is entered with a space-marching step, the error associated with the current point on the centerline contributes to the nozzle centerline error. When the end of the nozzle is reached, that point contributes to Eq. 223 as well. Accordingly, iimax (Eq. 223) has a constant value of 51, which is specified in the code.

Another issue which arose dealt with the aforementioned weight factors. The criteria to be met by a weighting factor were as follows: the errors associated with the boundary layer at the nozzle exit (Eq. 222) and the non-uniform portion of the centerline (Eq. 223) be diminished; the weighting factors' sum over the domain of interest be equal to 1; the weighting factors always be positive; and the weighting factors maintain the nozzle optimization as a search for a minimum.

It was decided that the nozzle exit and nozzle centerline x-coordinate Mach profiles most resembled a step-function with a finite rise time, which is represented by

$$f(t) = f(\infty)\,(1-e^{-\frac{t}{\tau}}), \qquad (224)$$

where τ is a constant (Fig. 90) [70]. Thus, when t is near 0, f(t) is near zero. And when t goes to infinity, f(t) approaches $f(\infty)$.

An analogous case exists with

$$\omega_{exit} = \frac{\exp(-|M_{imax,j}-M_{design}|)}{\sum_{j=1}^{jmax}\exp(-|M_{imax,j}-M_{design}|)} \quad (225)$$

used in Er, Eq. 222, and

$$\omega_{CL} = \frac{\exp(-|M_{ii,1}-M_{design}|)}{\sum_{ii=1}^{iimax}\exp(-|M_{ii,1}-M_{design}|)} \quad (226)$$

used in Er1, Eq. 223. In this case, when the power of the exponential is near zero, that is the Mach number is near M_{design}, the exponential term is close to 1; this would be the case in the inviscid high Mach uniform core at the exit if the nozzle were designed correctly (Fig. 85). When the power of the exponential is not near zero, that is the Mach number is not very close to M_{design}, the exponential term is close to zero; this would be the case in the boundary layer at the nozzle exit or the non-uniform portion along the nozzle centerline (Fig. 86). Hence, the portions of the flow which are most important are emphasized and the portions which are not important are deemphasized. Note that all of the aforementioned criteria for weighting factors were met with Eqs. 225 and 226.

Once again, these weighting factors preclude the need to specify some portion of the solution to sample, which would definitely change with different nozzles. This contributes to the minimum interaction nature of the computer code.

The nozzle exit error, Eq. 219, was the sole response function initially used, but merely having uniform flow at the outflow of the nozzle is no guarantee that there is indeed a uniform inviscid core with a minimum of disturbances (Fig. 91). Thus it was decided that the total response function, Ert (Eq. 221), would provide the response values, z_i (Eq. 114), for the optimization scheme since it sought to minimize both of the error functions simultaneously. Additionally, Eqs. 222 and 223 would provide the input to Ert, thus providing a more user-friendly optimization procedure.

5.2.2 Mapping the Response Surface. In order to provide some information on the response surface's appearance, the design parameters (θ_{attach}, θ_{exit}) were varied systematically. The mapping of the response functions was generated by specifying 5 fixed values of θ_{attach}, and for each of these values, 6 fixed values of θ_{exit} (Fig. 92). The values for the design parameters used in this study are presented in Table 1. Each point in Table 1 was input to the NS/PNS solver to obtain the associated error functions; these were then used to generate maps of the individual response surfaces generated by using Er (Eq. 222), Er1 (Eq. 223), and Ert (Eq. 221). The conditions for this study were previously presented in Sects. 3.1.1-3.1.4 and Sect. 3.3.1.

Table 1. Sampling matrix for response surface mapping.

θ_{attach}	θ_{exit}					
8.74°	0.00°	0.94°	1.89°	2.83°	3.78°	4.58°
10.6°	0.00°	0.94°	1.89°	2.83°	3.78°	4.58°
12.77°	0.00°	0.94°	1.89°	2.83°	3.78°	4.58°
14.9°	0.00°	0.94°	1.89°	2.83°	3.78°	4.58°
16.8°	0.00°	0.94°	1.89°	2.83°	3.78°	4.58°

Geometrical constraints placed physical limits on the design variables, θ_{attach} and θ_{exit}. The lower limit of θ_{attach} was determined by the constraint of the cone angle, seen if a line were drawn from the corner of the throat exit to the wall at the outflow of the nozzle (Fig 93). The upper limit for θ_{attach} was determined by the constraint of the angle at which flow separation would begin to occur, since this would be unacceptable as an inflow to the PNS solver. The lower limit of θ_{exit} was determined by a parallel wall, equating to a zero degree angle for the wall at the nozzle exit (Fig. 94). And finally, the upper limit of θ_{exit} was determined by the constraint of the cone angle already mentioned. It was hoped that obtaining the response surface map would accomplish several objectives. First, it would allow one to see if the optimization scheme was marching towards a minimum or not. Second, it would provide more information regarding the response surface, including

the overall appearance. Third, it would aid in the validation of the optimization procedure.

5.2.2.1 Results of Response Surface Mapping. With the design parameter coordinates provided in Table 1 above, response surfaces were generated using Tecplot to obtain maps for Er, Er1, and Ert (Figs. 95, 96 and 97). Analysis of the response surfaces provided a number of insights. First, though they each exhibited a point of global minimum, the areas associated with the global minima for Er and Er1 were substantially larger than that associated with Ert. Second, they all exhibited local minima different from the global minima for each surface. Thus, the potential existed for the optimization scheme to find a local minimum and not the global one. Third, the maps did not exhibit simple first- or second-order behavior, particularly in the low θ_{attach} region or the high θ_{exit} region; indeed, many forms of behavior were evident on the maps, including ridges and plateaus. It should be pointed out that the potential exists for other local minima not displayed by Tecplot to exist due to the methodology used within Tecplot to generate the map surface.

Two conclusions were drawn from the above observations. First, it appeared that too large an area was associated with the global minima for Er and Er1. Since its map appeared to indicate a more precise global minimum region, this confirmed that Ert should be

used as the response function. Second, since the response surface map indicated curvature in the region of the local minimum, it was decided to use a second-order search exclusively in trying to locate the global minimum. Another factor in this decision was that fewer sampling points were expected to be required than would be in the steepest descent method. It was expected that the second-order search method would find the global minimum, despite the variety of surface behavior displayed on the map.

5.2.3 First Scheme, Second-Order Response Surface Methodology (RSM) Search. With the response functions and the response surface mapping addressed above, the second-order RSM optimization procedure was implemented. The starting point for this case was (θ_{attach}, θ_{exit}) of (12.8°, 2.30°) with $d\theta_{attach}$ of 5° and $d\theta_{exit}$ of 1.5°. Each time a new minimum was found using the procedures provided in Sect. 2.8.2.2, the new center was shifted to that point, and the values of $d\theta_{attach}$ and $d\theta_{exit}$ were cut by half (Fig. 19). The search was continued with successive iterations until either a minimum had been located or it was determined that the optimization procedure was not efficiently seeking out a minimum. The conditions for this study were previously presented in Sects. 3.1.1-3.1.4 and Sect. 3.3.1.

5.2.3.1 First Scheme Results. The inability of the second-order search method to locate the global minimum in an expedient manner is evidenced by the trail on the response surface map (Fig. 98). After five iterations, the second-order search method had still not located the global minimum and appeared to be having considerable difficulty in doing so. This confirmed that, with the response surface contours, an exclusive second-order search method was not the best choice and another method needed to be explored.

5.2.4 Second Scheme, Korte Least Squares (LS) Method. To explore potential improvement, the LS method of Korte was tried next, using the procedures outlined in Sect. 2.8.1. The method of Korte was used because that method was well proven and required only one NS solution per sampling grid; this was due to the use of extremely small $d\theta$'s in obtaining the sampling grid, as will be shown. In addition, only three sampling points were necessary per iteration, as compared with at least nine for the RSM methods.

To start, the last identified minimum of the RSM second-order search method (Fig. 98) provided the starting point (point 1) of a three point stencil (Fig. 99). The three points of the stencil always consisted of the last minimum found (point 1), and two other points (points 2 and 3), which were generated by alternately holding one of the design parameters of the starting point constant, while the other was varied by some small $d\theta$. As

recommended in [57], the original $d\theta$ was 0.001 θ. Thus, the three points of the first stencil consisted of (θ_{attach}, θ_{exit}) values of (14.45°, 1.800°) for point 1, (14.46°, 1.800°) for point 2, and (14.45°, 1.798°) for point 3. The value of $d\theta$ was subsequently decreased to 0.0001 θ and lower values in an attempt to locate a minimum in an efficient manner. The conditions for this study were previously presented in Sects. 3.1.1-3.1.4 and Sect. 3.3.1.

The components of the Jacobian matrix, Eq. 99, were determined using a first order approximation, and the error functions in Eqs. 222 and 223 were used not as a sum as in Eq. 221, but independently in this case. Thus, given that p_1 is Er, p_2 is Er1, a_1 is θ_{attach}, and a_2 is θ_{exit}, then the (i,j) component of the Jacobian matrix would be determined by

$$\frac{\partial p_i}{\partial a_j} = \frac{p_{i_m} - p_{i_1}}{a_{j_m} - a_{j_1}}, \qquad (227)$$

where m is the index representing a point of the stencil (point 2 or point 3, Fig. 99); m is 2 if j is 1, accounting for a change in θ_{attach}, or m is 3 if j is 2, accounting for a change in θ_{exit}.

The solution (θ_{attach}, θ_{exit}) for the newly computed minimum point could be obtained once the Jacobian matrix, Eq. 99, had been fully computed. First, Eq. 98 was solved for $\Delta \mathbf{a}_k$ using a simple 2x2 matrix inversion procedure. Then, $\Delta \mathbf{a}_k$ was added to $\mathbf{a}_k$, Eq. 100, to obtain the newly determined minimum point, $\mathbf{a}_{k+1}$.

5.2.4.1 Second Scheme Results. Though the Korte LS method did find the global minimum at one point, it required much interaction with the code in order to maintain $d\theta$ in a range that would not cause the optimization procedure to wander wildly about the surface in search of a minimum. The path taken by the optimization procedure is shown on the response surface map (Fig. 100).

Unfortunately, local minima consistently began appearing between two very close sampling points, where presumably no local minima should be (Fig. 101). It became clear that, with such small $d\theta$'s, any changes that occurred in the response function were below the numerical noise level, meaning that the response function output was not to be trusted to determine a gradient direction. An attempt to raise the value of the $d\theta$'s led to erratic search behavior (Fig. 102). Hence, the attempt to use the Korte LS method was abandoned.

5.2.5 Third Scheme, Steepest Descent RSM Method. The next scheme developed was the steepest descent method. The procedures used were previously given in detail in Sect. 2.8.2.1. The conditions for this study were previously presented in Sects. 3.1.1-3.1.4 and Sect. 3.3.1.

Beginning with the same center and $d\theta$'s used in the beginning of the second-order search above, the five point stencil was used

to generate the presumed direction of steepest descent (Fig. 15). Initial g values (Eq. 121) of 1, $\sqrt{2}$, $\sqrt{3}$, 2 were tried. The g values next needed to be decoded into the (θ_{attach}, θ_{exit}) coordinates using Eqs. 125 and 126. Each g value was then run through the NS/PNS solvers in order to determine the response function associated with each. If the range of the initial g values was not sufficient to locate a response surface inflection point along the g vector, larger values of g were used successively until an inflection point was located (Fig. 103). For instance, if the error functions associated with the previously used g values indicated no inflection point, some amount δg was added to the last used g value to obtain the next g value to be used in the search. This continued until an inflection point was bracketed by assigned g values (Fig. 103), and then the three closest g value error functions were used to obtain g_{new}, Eq. 133, and its (θ_{attach}, θ_{exit}) coordinates. The value of g_{new} was then run through the NS/PNS solvers to verify that a new minimum did exist at that (θ_{attach}, θ_{exit}) coordinate. With the new minimum found, that (θ_{attach}, θ_{exit}) point became the center of the five point stencil (Fig. 11) and the $d\theta$'s were decreased in the hopes of zeroing in on the minimum. This procedure was iterated until a minimum had been found which could not be improved upon.

5.2.5.1 Third Scheme Results. Surprisingly enough, the steepest descent method sought out the global minimum, as evidenced by the path followed on the Ert response surface map (Fig. 104) This minimum was located within three iterations, and two subsequent iterations failed to find another in the local vicinity. Plots of the Mach number vs radial distance at the exit and Mach number vs axial distance along the centerline indicate that the minimum does correspond to a uniform Mach 12 inviscid core at the exit, at least as is likely obtainable using only the two design parameters (Figs. 105 and 106).

5.2.6 Comparison with Original Mach 12 Nozzle Design. A comparison between the solutions for the new and old Mach 12 nozzles indicates that the new nozzle design produces a more accurate test section flow, but with perhaps more disturbances in the flow. Examination of Fig. 107 shows the exit profile is much nearer to the design mach number for the new nozzle than it is for the old nozzle design. Examination of Fig. 108 however indicates more disturbances in the flow of the new nozzle design as compared with the original. This may indicate that there are limitations to the optimization scheme with the selected design parameters. The optimization scheme does nevertheless optimize the nozzle to the best of its abilities.

5.3 Automating the Search

With the steepest descent method's successful location of the global minimum, the entire optimization scheme was coded, including the NS solver of the subgrid (Grid D, Fig. 83), the PNS solver, the steepest descent method, the second-order search method, and all of the logic previously mentioned. The conditions for this study were previously presented in Sects. 3.1.1-3.1.4 and Sect. 3.3.1. The starting point and the $d\theta$'s remained unchanged from the initial starting values for the manual steepest descent method. However, the initial values for g in the direction of steepest descent were $\frac{\sqrt{2}}{4}$, $\frac{\sqrt{2}}{2}$, $\frac{3\sqrt{2}}{4}$; the reason for the difference in the initial values of g, as compared with the manual steepest descent search, was that it was feared that with such large initial values the automated search might immediately violate the coordinate limits on the response surface (Fig. 109).

If a new minimum, as compared with the center point, had not been found among those three points, the response surface was apparently increasing in the calculated direction of steepest descent (Fig. 110). The optimization scheme then reverted to the second-order search, since 5 of the 9 sampling point response functions had already been computed (Fig. 12).

If the response surface was decreasing in the direction of steepest descent, the optimization scheme then checked to see if an inflection point had been bracketed by the g values used (Fig.

103). If an inflection point had been bracketed, the optimizer then computed the g value for the calculated minimum, g_{new} (Eq. 133), using the second-order bivariate regression equation, Eq. 129, and computed the error function for that point using the NS/PNS solvers. The error function values for the bracketing g values and g_{new} were then compared, with the (θ_{attach}, θ_{exit}) point associated with the new found minimum then becoming the center for the next sampling grid (Fig. 15).

If an inflection point had not been found, the optimizer continued to search in the direction of steepest descent until one had been located. After the g value of $\sqrt{2}$ had been passed, the delta to the next g value from the current one was obtained by multiplying the previous delta by 1.1 (Fig. 103).

Assuming that a new minimum had been found, the procedure used in the steepest descent method then decreased the $d\theta$'s, and with the new minimum as the center of the new five point stencil began searching anew for the next minimum (Fig. 15). If this were the second iteration, then $d\theta_{attach}$ would be decreased to 1/5th its original value and $d\theta_{exit}$ would be decreased by 1/2; the decrementing of the $d\theta$'s was accomplished in this manner in order to diminish the height to width ratio of the sampling stencil in non-transformed space (Fig. 111). Additionally, the large initial $d\theta_{attach}$ was due to the fact that there was initially a much larger area to sample in that direction (Fig. 109). In subsequent iterations, both $d\theta$'s were decreased to 1/2 of their last values

when a new iteration began; the $d\theta$'s were however not allowed to decrease to less than 0.1 because it was felt that any changes below that level would produce changes in the error function which would be attributed to the numerical noise rather than to the design parameters.

The iterative process continued until a minimum had been located and one of two events occurred. Either the user perceived no discernible difference in the output from the nozzle (Mach number and Pitot pressure profiles) with the detection of a new minimum or no other minima had been found in the area and the limit on the $d\theta$'s had been reached.

5.4 Efficiency of Scheme Methodology Tested

To determine if a minimum could be obtained in a more efficient manner, a viscous Mach 12 hypersonic nozzle optimization search was performed with a slightly different sampling stencil. Except as mentioned here, all of the nozzle details remain unchanged from Sect. 5.3. The same initial stencil was used as that of the search performed in Sect. 5.3. However, the second and later stencils in non-transformed space each constituted a square, rather than a rectangle, with the newly found minimum at the center (Fig. 112). Thus for the second iteration, $d\theta_{attach}$ was decreased to 1/5 of its value and $d\theta_{exit}$ to 2/3 of its value in order to square up the sampling stencil. In subsequent iterations, the $d\theta$'s were

decreased to 2/3 of their previous values, rather than 1/2, as in Sect. 5.3. With these exceptions, the search was performed as it was described in Sect. 5.3.

5.5 Optimization Code Tested for Robustness

In addition to verifying that the optimization code had been developed to a satisfactory level of efficiency, it was necessary to ensure that it was also at a satisfactory level of robustness. In other words it was important to ensure that given a number of completely different starting points and non-transformed stencils, the same global minimum could be obtained. This would validate that the finding of the global minimum had not been case-specific.

Two separate test cases composed of two different starting points were run. All of the conditions for the following tests are the same as those described in Sect. 5.3.

Note that the seemingly less efficient sampling grid reduction was used in the following two test cases. This was due to the fact that the computations for these cases were performed simultaneously as an efficiency check on sampling grid, and it was expected that the square non-transformed sampling grid and lesser decrementing of the $d\theta$'s would be more efficient. As seen above, this did not appear to be the case. Although the change in sampling grid reduction resulted in more run time, the objective of the tests were not compromised.

5.5.1 First Test. The first test objective was to determine if the global minimum could be obtained with a different starting point. The search was begun with a starting point of (θ_{attach}, θ_{exit}) of (15, 1), which was towards the maximum for θ_{attach} and the minimum for θ_{exit} (Fig. 109). The $d\theta$'s were (2.5, 1), and the same decrementing occurred as in the previous search, where $d\theta_{attach}$ was decreased to 1/5 of its value and $d\theta_{exit}$ to 2/3 of its value for the second iteration. For subsequent iterations, the decrements in the $d\theta$'s were to 2/3 of their previous values.

5.5.2 Second Test. The second test for the optimizer had the objective of determining if the global minimum could be obtained starting from a point which was close to a local minimum but not the global minimum. The starting point for this search was located at (θ_{attach}, θ_{exit}) of (10, 3.5), which was located near the minimum for θ_{attach} and the maximum for θ_{exit}. As seen in Fig. 97, this point is closer to the local minimum located at approximate values of (θ_{attach}, θ_{exit}) of (12.5, 4.0). The $d\theta$'s had values of (1.0, 1.0). The decrements in the $d\theta$'s were to 2/3 of their previous values for all iterations.

5.6 Use of NECR Solver to Justify Use of Perfect Gas Solver

It was still necessary to prove that for these operating conditions a hypersonic nozzle of this type would not require the

use of a nonequilibrium solver in order to correctly optimize the nozzle contour. Thus, once the newly optimized nozzle shape was obtained, it was necessary to obtain a solution of the new nozzle with the aid of the nonequilibrium solver. All other conditions are as previously specified with the exception of the wall contour of the testbed WL Mach 12 nozzle.

5.7 Off-Design Conditions

The computational capability of testing off-design conditions is expected to be of interest in nozzle optimization. Therefore, as a further test of the perfect gas NS code two off-design conditions were run. The first case was that of increased exit pressure. The exit pressure at every point along the nozzle exit was set at twice that of the nozzle static pressure at the centerline when no back pressure was specified, as was previously the case in the NS solution for the Mach 12 nozzle (Sect. 3.1.4). This situation might be analogous to a buildup of pressure in the vacuum reservoir of a wind tunnel or to a slight blockage of the flow due to the model. The second case was that of decreased exit pressure. The exit pressure was set to half that of the nozzle at the centerline when no back pressure was specified. This situation might simulate a startup of a wind tunnel. Note that these cases could not be run using the perfect gas PNS code, since there is no

capability of specifying a back pressure using PNS in the methodology utilized in this research.

6. Results and Conclusions from Validation of Optimization Code

This chapter presents the results of the automated validation cases and the off-design cases from Ch. 5 (Sects. 5.3-5.7) and addresses conclusions drawn and objectives met or not met. Recall that the primary objective of this research was to develop and validate a computer code which, with Navier-Stokes (NS) and Parabolized Navier-Stokes (PNS) solvers incorporated, would accurately and robustly redesign the testbed nozzle utilizing a simple optimization scheme, given the fixed length, throat radius and exit radius of the original Mach 12 nozzle.

To this point, the primary objective and the secondary objective of running the off-design cases on the newly designed nozzle had yet to be achieved. However, the NS and PNS flow codes had been well-validated. In addition, the Baldwin-Lomax (B-L) model had proven to be the turbulence model of choice, satisfying one secondary objective. Also, the flow codes had been used in the manual operation of the optimization scheme and the global minimum had been achieved (Sect. 5.2). Finally, the stage was set for the testing of the automatic operation of the optimization code with the flow solvers incorporated.

6.1 Results of Automating the Search

The optimization scheme once again found the global minimum, and in this case successful automation required four to five iterations to achieve the global minimum. By four iterations, the response function minimum had attained a value of 0.02986 as compared with 0.1305 for the first iteration. The fifth iteration delivered a value for the minimum of 0.02946. The search was then terminated as the $d\theta$'s had reached their limit of 0.1. A plot of the path taken by the optimization scheme is imposed on the response surface map in Fig. 113.

In order to observe the difference associated with each of the three response function minima discussed above, plots of Mach number vs radial distance at the nozzle exit and Mach number vs axial distance along the nozzle centerline are shown (Figs. 114 and 115). While there was a noticeable difference between the plot for the first minimum and the other two, there is no discernible difference between the plots for the last two minima found.

Recall that though the initial sampling stencil was the same as used in the manual steepest descent search, the stencil along the path of steepest descent was made different to avoid the potential of violating one of the design parameter boundaries (Fig. 109). This conservative approach appears to have added one to two iterations in the search to achieve the global minimum. Complete resultant path data is presented in Appendix B.

6.2 Results of Efficiency Test

As suspected, the sampling stencil did have a minor effect in the efficiency of the optimization scheme. The new sampling method led to an increase in the number of iterations necessary to attain the global minimum. This case required six iterations to reach the global minimum, as opposed to the four to five iterations seen earlier. The path taken by the optimization scheme is shown on the response surface map (Fig. 116). The original non-transformed rectangular stencil appears to provide quicker convergence, as did the more aggressive decrementing of the $d\theta$'s. Complete resultant path data is presented in Appendix B.

6.3 Results of First Test for Robustness

The global minimum was attained using this new starting point. Five iterations were required to attain the global minimum, and the search required the code to revert to the second-order search twice. The path taken by the optimization scheme is shown plotted on the response surface map (Fig. 117). Complete resultant path data is presented in Appendix B.

6.4 Results of Second Test for Robustness

The second new starting point did not locate the global minimum. It did locate a local minimum, but not the local minimum towards which it appeared likely to be attracted. The local

minimum found did not appear on the response surface map, presumably due to the sparseness of the mapping grid and/or the methodology used by the Tecplot software package to interpolate between points. This case required 3 iterations to attain the local minimum, reverting to second-order search twice. The path taken by the optimization scheme is shown plotted on the response surface map (Fig. 118). Complete resultant path data is presented in Appendix B.

6.5 Results of NECR Solver with New Nozzle Design

The new nozzle design produced no significant differences between the perfect gas and the NECR NS solvers. Plots taken from near the nozzle exit of Mach number vs. radial distance and of Pitot pressure vs. radial distance are presented in Figs. 119 and 120. A plot of Mach number vs. axial distance along the nozzle centerline is presented in Fig. 121. Based on these results, it is concluded that the use of the NECR solver in optimizing the testbed nozzle would have resulted in much wasted computer time.

6.6 Results of Off-Design Cases

In neither case was any appreciable difference seen in the results in the inviscid core near the nozzle exit. Plots of Mach number vs. radial distance and Pitot pressure vs radial distance for the first case are presented in Figs. 122 and 123. Plots of

Mach number vs. radial distance and Pitot pressure vs radial distance for the second case are presented in Figs. 124 and 125. The largest change occurred in the near-wall boundary layer as expected, since the remainder of the flow is supersonic/hypersonic and shouldn't be affected by a downstream pressure change except through the impression of the boundary layer. It is believed that the changes in the inviscid uniform core are in large part due to the different ways in which the back pressure is specified in the two solvers.

6.7 Conclusions

Sects. 6.1-6.3 demonstrated the fact that, given a somewhat favorable starting point for the optimization scheme, the automatic code would seek out the "global best" design of a hypersonic nozzle synonymous with the response surface global minimum of the nozzle's computed composite error. Through three successful attempts to locate the global minimum, the optimization code showed indications of robustness. An indication of the accuracy associated with the optimization code can be inferred from the comparative results of Ch. 4 for the Mach 12 nozzle (Sects. 4.2.3.1 and 4.3.3.1).

Sect. 6.4 demonstrates that given a relatively unfavorable starting point, the optimization code may seek out the best nozzle design associated with the local minimum, though this might not be the global minimum. Nonetheless, the optimization code still

locates the best nozzle design in the area in which it begins its search.

The primary objective has thus been satisfied in that an accurate and robust optimization code has been developed which, with simple response surface methods and state-of-the-art NS and PNS codes, was used to redesign the testbed hypersonic nozzle with fixed values of nozzle length, throat radius and exit radius.

There are however two caveats to the statement that the optimization code is accurate and robust. First, the designer must have a fairly good idea of where to begin the optimization search for the "global best" nozzle, lest some local best nozzle be obtained. Second, and of more importance, the nozzle flow is not as disturbance-free as a designer might ultimately prefer. It is strongly suspected after discussions with Korte that this is due to the use of only two design parameters [53]. Had there been more time allowed, research into alternate or additional design parameters such as nozzle length or exit radius would have been conducted. Such was not the case and this area remains open for further research.

Regardless of the caveats, the "global best" hypersonic nozzle obtained with the two design parameters is probably only within a few percent of the perfect "global best" nozzle, that associated with the variation of all of the design parameters necessary to achieve a perfectly designed nozzle which will provide a completely disturbance-free, uniform, inviscid core at the design Mach number

at the nozzle exit. The current optimization code's "global best" nozzle thus represents an extremely good engineering solution to the hypersonic nozzle design problem, and while not delivering the perfect nozzle flow, provides at the very least a good baseline nozzle which can be adjusted with further research to provide the perfect nozzle flow. Note however that the optimization code's best nozzle is obtained in a relatively small amount of time due to the fact that only two design parameters are used. Thus, in the current optimization code trade-offs may exist between solution accuracy and time. The addition or substitution of one or more design parameters in further research may minimize or eliminate any such trade-offs.

From Sect. 6.5, it is concluded that the use of an NECR code in the optimization of the testbed nozzle would have likely amounted to much wasted computer time. This is not to suggest that in the design of a hypersonic nozzle one may completely disregard nonequilibrium and chemical reaction effects. In point of fact, it is very likely that these effects should be accounted for in at least the last optimization iteration. Though not demonstrated here, a PNS version of the NECR code was developed and validated during the course of this research and is currently ready to be assimilated along with its NS counterpart into an NECR hypersonic nozzle optimization code. This brings up the point that the optimization code as designed could be run with almost any NS and

PNS codes if one paid careful attention to the variables passed between the parts of the optimization code and the flow codes.

From Sect. 6.6 it is concluded that, though the capability to test for off-design conditions is likely important to the design engineer, unless drastic changes are made in the back pressure of the nozzle relatively insignificant changes will occur in the nozzle flow. The optimized nozzle was nevertheless tested for the effect of changing back pressure and the results analyzed, satisfying the final objective of this research.

In summary, all of the objectives for this research were satisfied and an excellent engineering design tool has been created.

Appendix A: WL Mach 12 Nozzle Wall Data (x,y) (m)

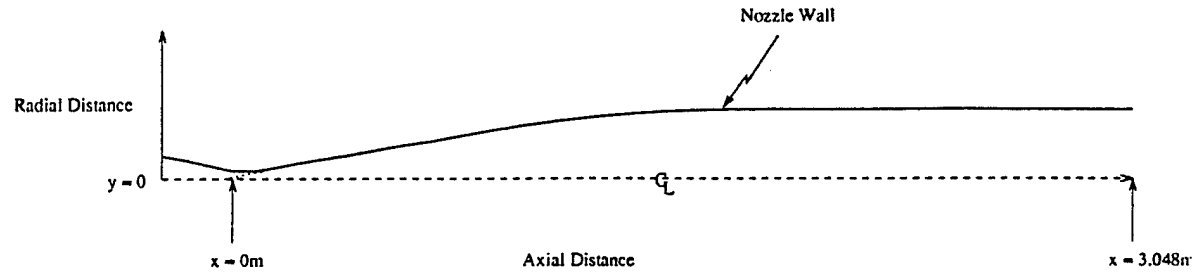

-0.74295E-01	0.32916E-01	-0.10160E-01	0.14526E-01
-0.73660E-01	0.32736E-01	-0.76200E-02	0.13797E-01
-0.71120E-01	0.32007E-01	-0.50800E-02	0.13068E-01
-0.68580E-01	0.31278E-01	-0.25400E-02	0.12342E-01
-0.66040E-01	0.30549E-01	0.00000E+00	0.11613E-01
-0.63500E-01	0.29822E-01	0.12700E-02	0.11250E-01
-0.60960E-01	0.29093E-01	0.25400E-02	0.10884E-01
-0.58420E-01	0.28364E-01	0.38100E-02	0.10521E-01
-0.55880E-01	0.27635E-01	0.50800E-02	0.10155E-01
-0.53340E-01	0.26909E-01	0.63500E-02	0.97917E-02
-0.50800E-01	0.26180E-01	0.76200E-02	0.94285E-02
-0.48260E-01	0.25451E-01	0.88900E-02	0.90627E-02
-0.45720E-01	0.24722E-01	0.10160E-01	0.86995E-02
-0.43180E-01	0.23995E-01	0.11430E-01	0.83363E-02
-0.40640E-01	0.23266E-01	0.12700E-01	0.79705E-02
-0.38100E-01	0.22537E-01	0.13970E-01	0.76073E-02
-0.35560E-01	0.21808E-01	0.15240E-01	0.72415E-02
-0.33020E-01	0.21082E-01	0.16510E-01	0.68783E-02
-0.30480E-01	0.20353E-01	0.17780E-01	0.65151E-02
-0.27940E-01	0.19624E-01	0.19050E-01	0.61493E-02
-0.25400E-01	0.18895E-01	0.20320E-01	0.57861E-02
-0.22860E-01	0.18169E-01	0.21590E-01	0.54229E-02
-0.20320E-01	0.17440E-01	0.22428E-01	0.51816E-02
-0.17780E-01	0.16711E-01	0.22860E-01	0.51816E-02
-0.15240E-01	0.15982E-01	0.23368E-01	0.51816E-02
-0.12700E-01	0.15255E-01	0.23876E-01	0.51816E-02

0.24384E-01	0.51816E-02	0.11176E+00	0.17643E-01
0.24892E-01	0.51816E-02	0.11430E+00	0.18042E-01
0.25400E-01	0.51816E-02	0.11684E+00	0.18443E-01
0.25908E-01	0.51816E-02	0.11938E+00	0.18844E-01
0.26416E-01	0.51816E-02	0.12192E+00	0.19246E-01
0.26924E-01	0.51816E-02	0.12446E+00	0.19647E-01
0.27432E-01	0.51816E-02	0.12700E+00	0.20046E-01
0.27940E-01	0.51816E-02	0.12954E+00	0.20447E-01
0.28448E-01	0.51816E-02	0.13208E+00	0.20848E-01
0.28956E-01	0.51816E-02	0.13462E+00	0.21250E-01
0.29464E-01	0.51816E-02	0.13716E+00	0.21651E-01
0.29972E-01	0.51816E-02	0.13970E+00	0.22050E-01
0.30480E-01	0.51816E-02	0.14224E+00	0.22451E-01
0.30988E-01	0.51816E-02	0.14478E+00	0.22852E-01
0.31496E-01	0.51816E-02	0.14732E+00	0.23254E-01
0.32004E-01	0.51816E-02	0.14986E+00	0.23652E-01
0.32512E-01	0.51816E-02	0.15240E+00	0.24054E-01
0.32791E-01	0.51816E-02	0.15494E+00	0.24455E-01
0.33020E-01	0.52172E-02	0.15748E+00	0.24856E-01
0.35560E-01	0.56185E-02	0.16002E+00	0.25258E-01
0.38100E-01	0.60198E-02	0.16256E+00	0.25657E-01
0.40640E-01	0.64211E-02	0.16510E+00	0.26058E-01
0.43180E-01	0.68199E-02	0.16764E+00	0.26459E-01
0.45720E-01	0.72212E-02	0.17018E+00	0.26860E-01
0.48260E-01	0.76225E-02	0.17272E+00	0.27262E-01
0.50800E-01	0.80239E-02	0.17526E+00	0.27661E-01
0.53340E-01	0.84252E-02	0.17780E+00	0.28062E-01
0.55880E-01	0.88240E-02	0.18034E+00	0.28463E-01
0.58420E-01	0.92253E-02	0.18288E+00	0.28865E-01
0.60960E-01	0.96266E-02	0.18542E+00	0.29263E-01
0.63500E-01	0.10028E-01	0.18796E+00	0.29665E-01
0.66040E-01	0.10427E-01	0.19050E+00	0.30066E-01
0.68580E-01	0.10828E-01	0.19304E+00	0.30467E-01
0.71120E-01	0.11229E-01	0.19558E+00	0.30869E-01
0.73660E-01	0.11631E-01	0.19812E+00	0.31267E-01
0.76200E-01	0.12032E-01	0.20066E+00	0.31669E-01
0.78740E-01	0.12431E-01	0.20320E+00	0.32070E-01
0.81280E-01	0.12832E-01	0.21590E+00	0.34066E-01
0.83820E-01	0.13233E-01	0.22860E+00	0.36048E-01
0.86360E-01	0.13635E-01	0.24130E+00	0.38014E-01
0.88900E-01	0.14036E-01	0.25400E+00	0.39967E-01
0.91440E-01	0.14435E-01	0.26670E+00	0.41902E-01
0.93980E-01	0.14836E-01	0.27940E+00	0.43825E-01
0.96520E-01	0.15237E-01	0.29210E+00	0.45733E-01
0.99060E-01	0.15639E-01	0.30480E+00	0.47625E-01
0.10160E+00	0.16038E-01	0.31750E+00	0.49505E-01
0.10414E+00	0.16439E-01	0.33020E+00	0.51369E-01
0.10668E+00	0.16840E-01	0.34290E+00	0.53218E-01
0.10922E+00	0.17242E-01	0.35560E+00	0.55055E-01

0.36830E+00	0.56876E-01
0.38100E+00	0.58684E-01
0.39370E+00	0.60480E-01
0.40640E+00	0.62260E-01
0.41910E+00	0.64028E-01
0.43180E+00	0.65781E-01
0.44450E+00	0.67521E-01
0.45720E+00	0.69248E-01
0.46990E+00	0.70963E-01
0.48260E+00	0.72664E-01
0.49530E+00	0.74353E-01
0.50800E+00	0.76027E-01
0.52070E+00	0.77691E-01
0.53340E+00	0.79339E-01
0.54610E+00	0.80978E-01
0.55880E+00	0.82603E-01
0.57150E+00	0.84216E-01
0.58420E+00	0.85816E-01
0.59690E+00	0.87404E-01
0.60960E+00	0.88981E-01
0.62230E+00	0.90546E-01
0.63500E+00	0.92098E-01
0.64770E+00	0.93640E-01
0.66040E+00	0.95169E-01
0.67310E+00	0.96685E-01
0.68580E+00	0.98191E-01
0.69850E+00	0.99687E-01
0.71120E+00	0.10117E+00
0.72390E+00	0.10264E+00
0.73660E+00	0.10410E+00
0.74930E+00	0.10555E+00
0.76200E+00	0.10699E+00
0.77470E+00	0.10842E+00
0.78740E+00	0.10984E+00
0.80010E+00	0.11125E+00
0.81280E+00	0.11264E+00
0.82550E+00	0.11403E+00
0.83820E+00	0.11540E+00
0.85090E+00	0.11677E+00
0.86360E+00	0.11812E+00
0.87630E+00	0.11947E+00
0.88900E+00	0.12080E+00
0.90170E+00	0.12213E+00
0.91440E+00	0.12344E+00
0.92710E+00	0.12475E+00
0.93980E+00	0.12604E+00
0.95250E+00	0.12733E+00
0.96520E+00	0.12860E+00
0.97790E+00	0.12987E+00
0.99060E+00	0.13113E+00
0.10033E+01	0.13237E+00
0.10160E+01	0.13361E+00
0.10287E+01	0.13484E+00
0.10414E+01	0.13606E+00
0.10541E+01	0.13727E+00
0.10668E+01	0.13848E+00
0.10795E+01	0.13967E+00
0.10922E+01	0.14085E+00
0.11049E+01	0.14203E+00
0.11176E+01	0.14320E+00
0.11303E+01	0.14435E+00
0.11430E+01	0.14550E+00
0.11557E+01	0.14664E+00
0.11684E+01	0.14778E+00
0.11811E+01	0.14890E+00
0.11938E+01	0.15002E+00
0.12065E+01	0.15113E+00
0.12192E+01	0.15223E+00
0.12319E+01	0.15332E+00
0.12446E+01	0.15440E+00
0.12573E+01	0.15548E+00
0.12700E+01	0.15655E+00
0.12827E+01	0.15761E+00
0.12954E+01	0.15866E+00
0.13081E+01	0.15971E+00
0.13208E+01	0.16075E+00
0.13335E+01	0.16178E+00
0.13462E+01	0.16280E+00
0.13589E+01	0.16382E+00
0.13716E+01	0.16483E+00
0.13843E+01	0.16583E+00
0.13970E+01	0.16682E+00
0.14097E+01	0.16781E+00
0.14224E+01	0.16879E+00
0.14351E+01	0.16976E+00
0.14478E+01	0.17073E+00
0.14605E+01	0.17169E+00
0.14732E+01	0.17264E+00
0.14859E+01	0.17358E+00
0.14986E+01	0.17452E+00
0.15113E+01	0.17546E+00
0.15240E+01	0.17638E+00
0.15367E+01	0.17730E+00
0.15494E+01	0.17821E+00
0.15621E+01	0.17912E+00
0.15748E+01	0.18002E+00
0.15875E+01	0.18092E+00
0.16002E+01	0.18181E+00

0.16129E+01	0.18269E+00
0.16256E+01	0.18356E+00
0.16383E+01	0.18443E+00
0.16510E+01	0.18530E+00
0.16637E+01	0.18615E+00
0.16764E+01	0.18700E+00
0.16891E+01	0.18785E+00
0.17018E+01	0.18869E+00
0.17145E+01	0.18952E+00
0.17272E+01	0.19036E+00
0.17399E+01	0.19209E+00
0.17526E+01	0.19200E+00
0.17653E+01	0.19281E+00
0.17780E+01	0.19361E+00
0.17907E+01	0.19442E+00
0.18034E+01	0.19521E+00
0.18161E+01	0.19600E+00
0.18288E+01	0.19679E+00
0.18415E+01	0.19757E+00
0.18542E+01	0.19834E+00
0.18669E+01	0.19911E+00
0.18796E+01	0.19988E+00
0.18923E+01	0.20064E+00
0.19050E+01	0.20139E+00
0.19177E+01	0.20214E+00
0.19304E+01	0.20289E+00
0.19431E+01	0.20363E+00
0.19558E+01	0.20436E+00
0.19685E+01	0.20509E+00
0.19812E+01	0.20582E+00
0.19939E+01	0.20654E+00
0.20066E+01	0.20726E+00
0.20193E+01	0.20797E+00
0.20320E+01	0.20870E+00
0.20447E+01	0.20938E+00
0.20574E+01	0.21008E+00
0.20701E+01	0.21077E+00
0.20828E+01	0.21146E+00
0.20955E+01	0.21215E+00
0.21082E+01	0.21283E+00
0.21209E+01	0.21351E+00
0.21336E+01	0.21418E+00
0.21463E+01	0.21485E+00
0.21590E+01	0.21551E+00
0.21717E+01	0.21617E+00
0.21844E+01	0.21683E+00
0.21971E+01	0.21748E+00
0.22098E+01	0.21813E+00
0.22225E+01	0.21877E+00
0.22352E+01	0.21941E+00
0.22479E+01	0.22005E+00
0.22606E+01	0.22068E+00
0.22733E+01	0.22131E+00
0.22860E+01	0.22194E+00
0.22987E+01	0.22256E+00
0.23114E+01	0.22317E+00
0.23241E+01	0.22379E+00
0.23368E+01	0.22440E+00
0.23495E+01	0.22501E+00
0.23622E+01	0.22561E+00
0.23749E+01	0.22621E+00
0.23876E+01	0.22680E+00
0.24003E+01	0.22740E+00
0.24130E+01	0.22799E+00
0.24257E+01	0.22857E+00
0.24384E+01	0.22915E+00
0.24511E+01	0.22973E+00
0.24638E+01	0.23031E+00
0.24765E+01	0.23088E+00
0.24892E+01	0.23145E+00
0.25019E+01	0.23201E+00
0.25146E+01	0.23258E+00
0.25273E+01	0.23314E+00
0.25400E+01	0.23369E+00
0.25527E+01	0.23425E+00
0.25654E+01	0.23480E+00
0.25781E+01	0.23534E+00
0.25908E+01	0.23589E+00
0.26035E+01	0.23643E+00
0.26162E+01	0.23697E+00
0.26289E+01	0.23750E+00
0.26416E+01	0.23803E+00
0.26543E+01	0.23856E+00
0.26670E+01	0.23909E+00
0.26797E+01	0.23961E+00
0.26924E+01	0.24013E+00
0.27051E+01	0.24065E+00
0.27178E+01	0.24117E+00
0.27305E+01	0.24168E+00
0.27432E+01	0.24219E+00
0.27559E+01	0.24269E+00
0.27686E+01	0.24320E+00
0.27813E+01	0.24370E+00
0.27940E+01	0.24420E+00
0.28067E+01	0.24470E+00
0.28194E+01	0.24519E+00
0.28321E+01	0.24568E+00
0.28448E+01	0.24617E+00

0.28575E+01	0.24665E+00	0.29718E+01	0.25092E+00
0.28702E+01	0.24714E+00	0.29845E+01	0.25138E+00
0.28829E+01	0.24762E+00	0.29972E+01	0.25184E+00
0.28956E+01	0.24810E+00	0.30099E+01	0.25230E+00
0.29083E+01	0.24857E+00	0.30226E+01	0.25275E+00
0.29210E+01	0.24905E+00	0.30353E+01	0.25321E+00
0.29337E+01	0.24952E+00	0.30480E+01	0.25365E+00
0.29464E+01	0.24999E+00		
0.29591E+01	0.25045E+00		

Appendix B: Search Path Tabulated Data

B.1 Tabulated Path Data for Automatic Search from Sect. 6.1

θ_{attach}	θ_{exit}	Er	Er1	Ert
(Begin first-order search)				
.1276873E+02	.2291832E+01	.7081753E-01	.9296892E-01	.1637864E+00
.1776873E+02	.3791832E+01	.1177701E+00	.1003611E+00	.2181312E+00
.1776873E+02	.7918313E+00	.2453667E-01	.1020390E+00	.1265757E+00
.7768725E+01	.7918313E+00	.1795622E+00	.1560986E+00	.3356608E+00
.7768725E+01	.3791832E+01	.5881502E-01	.1098336E+00	.1686486E+00
(Begin sampling in direction of steepest descent)				
.1436688E+02	.2518504E+01	.2513864E-01	.1702819E+00	.1954205E+00
.1596504E+02	.2745177E+01	.1965192E-01	.1108700E+00	.1305219E+00
.1756320E+02	.2971849E+01	.3326964E-01	.9911651E-01	.1323861E+00
(Inflection point detected, calculate g_{new} and run case)				
.1345775E+02	.2389559E+01	.5058493E-01	.1578817E+00	.2084667E+00
(Neighboring point, not g_{new}, is minimum; begin second iteration, first-order search)				
.1596504E+02	.2745177E+01	.1965192E-01	.1108700E+00	.1305219E+00
.1763174E+02	.3245177E+01	.2584804E-01	.1883572E+00	.2142052E+00
.1763174E+02	.2245177E+01	.1092248E+00	.1031036E+00	.2123284E+00
.1429834E+02	.2245177E+01	.1568505E-01	.9243594E-01	.1081210E+00
.1429834E+02	.3245177E+01	.1102343E+00	.1001207E+00	.2103550E+00
(Begin sampling in direction of steepest descent)				
.1554069E+02	.2622524E+01	.1907666E-01	.1085871E+00	.1276638E+00
.1511633E+02	.2499870E+01	.1804721E-01	.1062700E+00	.1243172E+00
.1469198E+02	.2377217E+01	.1649691E-01	.1105367E+00	.1270336E+00
(Inflection point detected, calculate g_{new} and run case)				
.1509428E+02	.2493496E+01	.1801868E-01	.1047688E+00	.1227875E+00
(g_{new} is new minimum, begin third iteration, first-order search)				
.1509428E+02	.2493496E+01	.1801868E-01	.1047688E+00	.1227875E+00
.1564984E+02	.2660166E+01	.1998629E-01	.1060464E+00	.1260327E+00
.1564984E+02	.2326826E+01	.1775123E-01	.9388037E-01	.1116316E+00
.1453872E+02	.2326826E+01	.1612252E-01	.1096304E+00	.1257529E+00
.1453872E+02	.2660166E+01	.3686050E-01	.1916600E+00	.2285205E+00
(Begin sampling in direction of steepest descent)				
.1523284E+02	.2451729E+01	.2239647E-01	.9700075E-01	.1193972E+00
.1537139E+02	.2409962E+01	.2656149E-01	.9102097E-01	.1175825E+00
.1550995E+02	.2368195E+01	.2174513E-01	.8891058E-01	.1106557E+00
.1564851E+02	.2326428E+01	.1775573E-01	.9413861E-01	.1118943E+00
(Inflection point detected, calculate g_{new} and run case)				
.1555821E+02	.2353647E+01	.1881112E-01	.8705963E-01	.1058707E+00

(g_{new} is new minimum, begin fourth iteration, first-order search)
.1555821E+02 .2353647E+01 .1881112E-01 .8705963E-01 .1058707E+00
.1574340E+02 .2453647E+01 .2031832E-01 .8986763E-01 .1101859E+00
.1574340E+02 .2253647E+01 .3034221E-01 .8751059E-01 .1178528E+00
.1537302E+02 .2253647E+01 .1741287E-01 .7207244E-01 .8948531E-01
.1537302E+02 .2453647E+01 .2606265E-01 .9388064E-01 .1199433E+00
(Begin sampling in direction of steepest descent)
.1551680E+02 .2326262E+01 .1816967E-01 .8889402E-01 .1070637E+00
.1547539E+02 .2298876E+01 .1777013E-01 .8367001E-01 .1014401E+00
.1543398E+02 .2271491E+01 .1752177E-01 .7724496E-01 .9476673E-01
.1539256E+02 .2244105E+01 .1709301E-01 .7169487E-01 .8878788E-01
.1534701E+02 .2213982E+01 .1654894E-01 .6469413E-01 .8124307E-01
.1529690E+02 .2180845E+01 .1662438E-01 .5798683E-01 .7461120E-01
.1524179E+02 .2144395E+01 .1541290E-01 .5056105E-01 .6597395E-01
.1518115E+02 .2104300E+01 .1595800E-01 .4277686E-01 .5873486E-01
.1511446E+02 .2060196E+01 .1565748E-01 .3553693E-01 .5119441E-01
.1504110E+02 .2011681E+01 .1593548E-01 .2789349E-01 .4382898E-01
.1496040E+02 .1958314E+01 .1597533E-01 .2160643E-01 .3758176E-01
.1487163E+02 .1899611E+01 .1635641E-01 .1584001E-01 .3219641E-01
.1477398E+02 .1835038E+01 .1622345E-01 .1383636E-01 .3005981E-01
.1466657E+02 .1764007E+01 .1789275E-01 .1607675E-01 .3396950E-01
(Inflection point detected, calculate g_{new} and run case)
.1478431E+02 .1841869E+01 .1592740E-01 .1392990E-01 .2985730E-01
(g_{new} is new minimum, begin fifth iteration, first-order search)
.1478431E+02 .1841869E+01 .1592740E-01 .1392990E-01 .2985730E-01
.1488431E+02 .1941869E+01 .1697945E-01 .1845712E-01 .3543657E-01
.1488431E+02 .1741869E+01 .1731621E-01 .1974095E-01 .3705717E-01
.1468431E+02 .1741869E+01 .1608365E-01 .1810649E-01 .3419014E-01
.1468431E+02 .1941869E+01 .2370189E-01 .1644068E-01 .4014256E-01
(Begin sampling in direction of steepest descent)
.1479813E+02 .1809325E+01 .1503192E-01 .1442836E-01 .2946028E-01
.1481194E+02 .1776781E+01 .1498256E-01 .1623601E-01 .3121857E-01
.1482576E+02 .1744236E+01 .1554608E-01 .1886545E-01 .3441153E-01
(Inflection point detected, calculate g_{new} and run case)
.1478810E+02 .1832938E+01 .1581149E-01 .1393989E-01 .2975138E-01
(New minimum at neighboring point, not g_{new}, minimum $d\theta$ reached)
.1479813E+02 .1809325E+01 .1503192E-01 .1442836E-01 .2946028E-01

B.2 Tabulated Path Data for Automatic Search/Efficiency Check from Sect. 6.2

θ_{attach}	θ_{exit}	Er	Er1	Ert
(Begin first-order search)				
.1276873E+02	.2291832E+01	.7081753E-01	.9296892E-01	.1637864E+00
.1776873E+02	.3791832E+01	.1177701E+00	.1003611E+00	.2181312E+00
.1776873E+02	.7918313E+00	.2453667E-01	.1020390E+00	.1265757E+00
.7768725E+01	.7918313E+00	.1795622E+00	.1560986E+00	.3356608E+00
.7768725E+01	.3791832E+01	.5881502E-01	.1098336E+00	.1686486E+00
(Begin sampling in direction of steepest descent)				
.1436688E+02	.2518504E+01	.2513864E-01	.1702819E+00	.1954205E+00
.1596504E+02	.2745177E+01	.1965192E-01	.1108700E+00	.1305219E+00
.1756320E+02	.2971849E+01	.3326964E-01	.9911651E-01	.1323861E+00
(Inflection point detected, calculate g_{new} and run case)				
.1345775E+02	.2389559E+01	.5058493E-01	.1578817E+00	.2084667E+00
(Neighboring point, not g_{new}, is minimum; begin second iteration, first-order search)				
.1596504E+02	.2745177E+01	.1965192E-01	.1108700E+00	.1305219E+00
.1696504E+02	.3745177E+01	.1171590E+00	.9977092E-01	.2169299E+00
.1696504E+02	.1745177E+01	.4858755E-01	.1949168E-01	.6807923E-01
.1496504E+02	.1745177E+01	.2016666E-01	.1972702E-01	.3989368E-01
.1496504E+02	.3745177E+01	.1091028E+00	.9822861E-01	.2073314E+00
(Begin sampling in direction of steepest descent)				
.1592310E+02	.2394120E+01	.2266946E-01	.9805553E-01	.1207250E+00
.1588116E+02	.2043062E+01	.5843261E-01	.5190862E-01	.1103412E+00
.1583923E+02	.1692005E+01	.3954539E-01	.1631110E-01	.5585650E-01
.1579729E+02	.1340948E+01	.2858088E-01	.9878305E-01	.1273639E+00
(Inflection point detected, calculate g_{new} and run case)				
.1584206E+02	.1715721E+01	.4048973E-01	.1600031E-01	.5649004E-01
(Neighboring point, not g_{new}, is minimum; begin third iteration, first-order search)				
.1583923E+02	.1692005E+01	.3954539E-01	.1631110E-01	.5585650E-01
.1628367E+02	.2136445E+01	.7259736E-01	.7399603E-01	.1465934E+00
.1628367E+02	.1247565E+01	.2608620E-01	.1124356E+00	.1385218E+00
.1539479E+02	.1247565E+01	.2716054E-01	.1917570E+00	.2189176E+00
.1539479E+02	.2136445E+01	.1966409E-01	.5634728E-01	.7601137E-01
(Begin sampling in direction of steepest descent)				
.1585064E+02	.1848724E+01	.4862365E-01	.2245980E-01	.7108345E-01
.1586204E+02	.2005442E+01	.5770983E-01	.4501746E-01	.1027273E+00
.1587345E+02	.2162161E+01	.5557708E-01	.7452644E-01	.1301035E+00
(Error function not decreasing in direction of steepest descent, perform second-order search)				
.1583923E+02	.2320538E+01	.2780270E-01	.1027097E+00	.1305124E+00
.1583923E+02	.1063472E+01	.2760812E-01	.1638776E+00	.1914858E+00
.1646776E+02	.1692005E+01	.4321268E-01	.1304292E-01	.5625560E-01
.1521070E+02	.1692005E+01	.3025850E-01	.2397966E-01	.5423816E-01

(With nine-point stencil done, compute new minimum location, run case)
.1530583E+02 .1954283E+01 .2867062E-01 .2958956E-01 .5826018E-01
(New minimum occurs on one of nine stencil points, not calculated minimum point; begin fourth iteration, first-order search)
.1521070E+02 .1692005E+01 .3025850E-01 .2397966E-01 .5423816E-01
.1550700E+02 .1988305E+01 .4072891E-01 .3911181E-01 .7984071E-01
.1550700E+02 .1395705E+01 .2926954E-01 .9114892E-01 .1204185E+00
.1491440E+02 .1395705E+01 .2556720E-01 .1245963E+00 .1501635E+00
.1491440E+02 .1988305E+01 .1820521E-01 .2244430E-01 .4064951E-01
(Begin sampling in direction of steepest descent)
.1520412E+02 .1796556E+01 .2915201E-01 .1974841E-01 .4890042E-01
.1519754E+02 .1901107E+01 .2635736E-01 .2358737E-01 .4994473E-01
.1519096E+02 .2005658E+01 .1989707E-01 .3163798E-01 .5153505E-01
(Inflection point detected, calculate g_{new} and run case)
.1520798E+02 .1735145E+01 .3005803E-01 .2077856E-01 .5083659E-01
(Neighboring point, not g_{new}, is minimum; begin fifth iteration, first-order search)
.1520412E+02 .1796556E+01 .2915201E-01 .1974841E-01 .4890042E-01
.1540165E+02 .1994089E+01 .3338242E-01 .3714976E-01 .7053218E-01
.1540165E+02 .1599023E+01 .3239598E-01 .3237467E-01 .6477065E-01
.1500659E+02 .1599023E+01 .2508341E-01 .4107528E-01 .6615869E-01
.1500659E+02 .1994089E+01 .1600000E-01 .2581663E-01 .4181662E-01
(Begin sampling in direction of steepest descent)
.1514637E+02 .1835824E+01 .2530014E-01 .1954487E-01 .4484501E-01
.1508861E+02 .1875092E+01 .2073894E-01 .1957144E-01 .4031038E-01
.1503086E+02 .1914359E+01 .1800037E-01 .1954044E-01 .3754081E-01
.1497311E+02 .1953627E+01 .1592261E-01 .2178841E-01 .3771103E-01
(Inflection point detected, calculate g_{new} and run case)
.1500533E+02 .1931720E+01 .1648892E-01 .2047684E-01 .3696576E-01
(g_{new} is new minimum, begin sixth iteration, first-order search)
.1500533E+02 .1931720E+01 .1648892E-01 .2047684E-01 .3696576E-01
.1513702E+02 .2063410E+01 .1564022E-01 .3569823E-01 .5133846E-01
.1513702E+02 .1800030E+01 .2606521E-01 .1901789E-01 .4508310E-01
.1487364E+02 .1800030E+01 .1539135E-01 .1578229E-01 .3117364E-01
.1487364E+02 .2063410E+01 .2304153E-01 .3118604E-01 .5422757E-01
(Begin sampling in direction of steepest descent)
.1498894E+02 .1888139E+01 .1758770E-01 .1726143E-01 .3484912E-01
.1497256E+02 .1844559E+01 .1702734E-01 .1639507E-01 .3342242E-01
.1495617E+02 .1800978E+01 .1780645E-01 .1670593E-01 .3451237E-01
(Inflection point detected, calculate g_{new} and run case)
.1497146E+02 .1841643E+01 .1727491E-01 .1612557E-01 .3340047E-01
(g_{new} is new minimum, stop search)
.1497146E+02 .1841643E+01 .1727491E-01 .1612557E-01 .3340047E-01

B.3 Tabulated Path Data for Automatic Search/First Robustness Test from Sect. 6.3

θ_{attach}	θ_{exit}	Er	Er1	Ert
(Begin first-order search)				
.1500000E+02	.1000000E+01	.1787525E+00	.4189779E+00	.5977305E+00
.1750000E+02	.2000000E+01	.2402179E+00	.5937943E-01	.2995973E+00
.1750000E+02	.0000000E+00	.2119284E+00	.1134606E+01	.1346535E+01
.1250000E+02	.0000000E+00	.5511354E+00	.1884902E+01	.2436037E+01
.1250000E+02	.2000000E+01	.2253184E+00	.1092264E+00	.3345448E+00
(Begin sampling in direction of steepest descent)				
.1529728E+02	.1332956E+01	.1730154E+00	.1282010E+00	.3012164E+00
.1559457E+02	.1665911E+01	.1856333E+00	.1978254E-01	.2054158E+00
.1589185E+02	.1998867E+01	.2120951E+00	.3823201E-01	.2503271E+00
(Inflection point detected, calculate g_{new} and run case)				
.1564833E+02	.1726119E+01	.1894446E+00	.1614928E-01	.2055939E+00
(Neighboring point, not g_{new}, is minimum; begin second iteration, first-order search)				
.1559457E+02	.1665911E+01	.1856333E+00	.1978254E-01	.2054158E+00
.1609457E+02	.2332581E+01	.2057809E+00	.9362358E-01	.2994045E+00
.1609457E+02	.9992410E+00	.1683696E+00	.2732370E+00	.4416067E+00
.1509457E+02	.9992410E+00	.1781558E+00	.4080012E+00	.5861570E+00
.1509457E+02	.2332581E+01	.1753285E+00	.7093015E-01	.2462587E+00
(Begin sampling in direction of steepest descent)				
.1562750E+02	.1897489E+01	.1985624E+00	.2482082E-01	.2233833E+00
.1566043E+02	.2129067E+01	.1914483E+00	.5584736E-01	.2472957E+00
.1569336E+02	.2360645E+01	.1609997E+00	.7938124E-01	.2403810E+00
(Error function not decreasing in direction of steepest descent, perform second-order search)				
.1559457E+02	.2608725E+01	.1693448E+00	.1224428E+00	.2917875E+00
.1559457E+02	.7230972E+00	.1844394E+00	.6543074E+00	.8387468E+00
.1630168E+02	.1665911E+01	.1931526E+00	.1207620E-01	.2052288E+00
.1488746E+02	.1665911E+01	.1609893E+00	.2866385E-01	.1896532E+00
(With nine-point stencil done, compute new minimum location, run case)				
.1631888E+02	.1821450E+01	.2068326E+00	.2065254E-01	.2274851E+00
(New minimum occurs on one of nine stencil points, not calculated minimum point; begin third iteration, first-order search)				
.1488746E+02	.1665911E+01	.1609893E+00	.2866385E-01	.1896532E+00
.1522079E+02	.2110351E+01	.1578574E+00	.3882423E-01	.1966816E+00
.1522079E+02	.1221471E+01	.1728989E+00	.2016489E+00	.3745477E+00
.1455413E+02	.1221471E+01	.1628607E+00	.2533742E+00	.4162349E+00
.1455413E+02	.2110351E+01	.1668066E+00	.4010521E-01	.2069118E+00
(Begin sampling in direction of steepest descent)				
.1490312E+02	.1821650E+01	.1539040E+00	.1456808E-01	.1684721E+00
.1491878E+02	.1977390E+01	.1581821E+00	.1942285E-01	.1776049E+00
.1493445E+02	.2133129E+01	.1703016E+00	.3713999E-01	.2074416E+00

(Inflection point detected, calculate g_{new} and run case)
.1490404E+02 .1830820E+01 .1542143E+00 .1464542E-01 .1688597E+00
(Neighboring point, not g_{new}, is minimum; begin fourth iteration, first-order search)
.1490312E+02 .1821650E+01 .1539040E+00 .1456808E-01 .1684721E+00
.1512534E+02 .2117950E+01 .1584942E+00 .3680250E-01 .1952967E+00
.1512534E+02 .1525350E+01 .1732771E+00 .5725219E-01 .2305293E+00
.1468090E+02 .1525350E+01 .1543828E+00 .6872501E-01 .2231078E+00
.1468090E+02 .2117950E+01 .1724890E+00 .3674111E-01 .2092301E+00
(Begin sampling in direction of steepest descent)
.1491345E+02 .1925499E+01 .1543873E+00 .1639539E-01 .1707827E+00
.1492377E+02 .2029348E+01 .1629900E+00 .2397354E-01 .1869635E+00
.1493410E+02 .2133197E+01 .1702498E+00 .3705599E-01 .2073058E+00
(Error function not decreasing in direction of steepest descent, perform second-order search)
.1490312E+02 .2240681E+01 .1733245E+00 .5475095E-01 .2280754E+00
.1490312E+02 .1402619E+01 .1686627E+00 .1147298E+00 .2833926E+00
.1521739E+02 .1821650E+01 .1753974E+00 .1895371E-01 .1943511E+00
.1458885E+02 .1821650E+01 .1655162E+00 .1223477E-01 .1777510E+00
(With nine-point stencil done, compute new minimum location, run case)
.1488558E+02 .1876255E+01 .1534002E+00 .1487534E-01 .1682755E+00
(New minimum occurs at calculated minimum point; begin fifth iteration, first-order search)
.1488558E+02 .1876255E+01 .1534002E+00 .1487534E-01 .1682755E+00
.1503373E+02 .2073789E+01 .1599586E+00 .3069891E-01 .1906575E+00
.1503373E+02 .1678722E+01 .1680399E+00 .2583452E-01 .1938744E+00
.1473744E+02 .1678722E+01 .1510056E+00 .2658516E-01 .1775907E+00
.1473744E+02 .2073789E+01 .1714617E+00 .2889088E-01 .2003526E+00
(Begin sampling in direction of steepest descent)
.1486885E+02 .1810076E+01 .1532397E+00 .1491032E-01 .1681500E+00
.1485212E+02 .1743896E+01 .1551282E+00 .1854150E-01 .1736697E+00
.1483539E+02 .1677717E+01 .1571629E+00 .2695767E-01 .1841206E+00
(Inflection point detected, calculate g_{new} and run case)
.1487921E+02 .1851063E+01 .1543475E+00 .1448042E-01 .1688279E+00
(Neighboring point, not g_{new}, is minimum; stop search)
.1486885E+02 .1810076E+01 .1532397E+00 .1491032E-01 .1681500E+00

B.4 Tabulated Path Data for Automatic Search/Second Robustness Test from Sect. 6.4

θ_{attach}	θ_{exit}	Er	Er1	Ert
(Begin first-order search)				
.1000000E+02	.3500000E+01	.5476815E-01	.1326148E+00	.1873830E+00
.1100000E+02	.4500000E+01	.9851435E-01	.1111902E+00	.2097045E+00
.1100000E+02	.2500000E+01	.1234776E+00	.9904838E-01	.2225260E+00
.9000000E+01	.2500000E+01	.1190515E+00	.9903943E-01	.2180910E+00
.9000000E+01	.4500000E+01	.8838512E-01	.1120428E+00	.2004279E+00
(Begin sampling in direction of steepest descent)				
.9854970E+01	.3822438E+01	.9921345E-01	.1189642E+00	.2181777E+00
.9709941E+01	.4144876E+01	.7977663E-01	.1177466E+00	.1975233E+00
.9564911E+01	.4467315E+01	.9363912E-01	.1036490E+00	.1972881E+00
(Error function not decreasing in direction of steepest descent, perform second-order search)				
.1000000E+02	.4914214E+01	.1694553E+00	.1594638E+00	.3289191E+00
.1000000E+02	.2085786E+01	.1568045E+00	.1227366E+00	.2795411E+00
.1141421E+02	.3500000E+01	.5570490E-01	.1269973E+00	.1827022E+00
.8585786E+01	.3500000E+01	.1121790E+00	.1030882E+00	.2152671E+00
(With nine-point stencil done, compute new minimum location, run case)				
.9478762E+01	.3455976E+01	.8520553E-01	.9516259E-01	.1803681E+00
(New minimum occurs at calculated minimum point, begin second iteration, first-order search)				
.9478762E+01	.3455976E+01	.8520553E-01	.9516259E-01	.1803681E+00
.1014543E+02	.4122646E+01	.9635273E-01	.1133584E+00	.2097112E+00
.1014543E+02	.2789306E+01	.6725413E-01	.9792747E-01	.1651816E+00
.8812092E+01	.2789306E+01	.1401340E+00	.1247406E+00	.2648745E+00
.8812092E+01	.4122646E+01	.5939336E-01	.1117491E+00	.1711424E+00
(Begin sampling in direction of steepest descent)				
.9662370E+01	.3603773E+01	.8559036E-01	.9771550E-01	.1833059E+00
.9845979E+01	.3751571E+01	.9233749E-01	.1087427E+00	.2010801E+00
.1002959E+02	.3899368E+01	.1073412E+00	.1126093E+00	.2199505E+00
(Error function not decreasing in direction of steepest descent, perform second-order search)				
.9478762E+01	.4398790E+01	.4761807E-01	.1309440E+00	.1785621E+00
.9478762E+01	.2513162E+01	.5294066E-01	.6948189E-01	.1224225E+00
.1042158E+02	.3455976E+01	.2966279E-01	.1328802E+00	.1625430E+00
.8535948E+01	.3455976E+01	.1147913E+00	.9866041E-01	.2134517E+00
(With nine-point stencil done, compute new minimum location, run case)				
.9517540E+01	.3749574E+01	.1074797E+00	.1162802E+00	.2237599E+00
(New minimum occurs on one of nine stencil points, not calculated minimum point; begin third iteration, first-order search)				
.9478762E+01	.2513162E+01	.5294066E-01	.6948189E-01	.1224225E+00
.9923202E+01	.2957602E+01	.3594578E-01	.9455798E-01	.1305038E+00
.9923202E+01	.2068722E+01	.1584257E+00	.1254635E+00	.2838893E+00

.9034322E+01 .2068722E+01 .1469209E+00 .8058758E-01 .2275085E+00
.9034322E+01 .2957602E+01 .1121868E+00 .1440551E+00 .2562419E+00
(Begin sampling in direction of steepest descent)
.9555162E+01 .2650472E+01 .4454022E-01 .7150533E-01 .1160455E+00
.9631562E+01 .2787781E+01 .3931737E-01 .7935443E-01 .1186718E+00
.9707962E+01 .2925091E+01 .3540313E-01 .9149022E-01 .1268933E+00
(Inflection point detected, calculate g_{new} and run case)
.9557502E+01 .2654677E+01 .4437900E-01 .7215990E-01 .1165389E+00
(Neighboring point, not g_{new}, is minimum; begin fourth iteration, first-order search)
.9555162E+01 .2650472E+01 .4454022E-01 .7150533E-01 .1160455E+00
.9851455E+01 .2946765E+01 .3535811E-01 .9140727E-01 .1267654E+00
.9851455E+01 .2354178E+01 .1008379E+00 .9185850E-01 .1926964E+00
.9258869E+01 .2354178E+01 .7955536E-01 .6492129E-01 .1444767E+00
.9258869E+01 .2946765E+01 .7615678E-01 .1402819E+00 .2164387E+00
(Begin sampling in direction of steepest descent)
.9658826E+01 .2635390E+01 .4724712E-01 .8154919E-01 .1287963E+00
.9762490E+01 .2620308E+01 .5680870E-01 .9303363E-01 .1498423E+00
.9866154E+01 .2605226E+01 .6760379E-01 .9211896E-01 .1597227E+00
(Error function not decreasing in direction of steepest descent, perform second-order search)
.9555162E+01 .2929822E+01 .4306103E-01 .9608665E-01 .1391477E+00
.9555162E+01 .2371122E+01 .6928213E-01 .8853766E-01 .1578198E+00
.9834512E+01 .2650472E+01 .5897811E-01 .8847694E-01 .1474551E+00
.9275812E+01 .2650472E+01 .6464647E-01 .8534673E-01 .1499932E+00
(With nine-point stencil done, compute new minimum location, run case)
.9650346E+01 .2738107E+01 .4089450E-01 .7930367E-01 .1201982E+00
(No new minimum, begin fifth iteration, first-order search)
.9555162E+01 .2650472E+01 .4454022E-01 .7150533E-01 .1160455E+00
.9686849E+01 .2782159E+01 .3886444E-01 .8207822E-01 .1209427E+00
.9686849E+01 .2518785E+01 .6137357E-01 .8764148E-01 .1490151E+00
.9423475E+01 .2518785E+01 .5302783E-01 .7527530E-01 .1283031E+00
.9423475E+01 .2782159E+01 .4859376E-01 .8898575E-01 .1375795E+00
(Begin sampling in direction of steepest descent)
.9545297E+01 .2695973E+01 .4306576E-01 .7976903E-01 .1228348E+00
.9535432E+01 .2741474E+01 .4167120E-01 .8223910E-01 .1239103E+00
.9525567E+01 .2786975E+01 .4124818E-01 .8468354E-01 .1259317E+00
(Error function not decreasing in direction of steepest descent, perform second-order search)
.9555162E+01 .2836710E+01 .4093964E-01 .8668329E-01 .1276229E+00
.9555162E+01 .2464234E+01 .5910196E-01 .7603489E-01 .1351368E+00
.9741400E+01 .2650472E+01 .5108793E-01 .8785197E-01 .1389399E+00
.9368924E+01 .2650472E+01 .5322508E-01 .8570497E-01 .1389300E+00
(With nine-point stencil done, compute new minimum location, run case)
.9569793E+01 .2692611E+01 .4375831E-01 .7931536E-01 .1230737E+00

```
(No new minimum, begin sixth iteration, first-order search)
.9555162E+01 .2650472E+01 .4454022E-01 .7150533E-01 .1160455E+00
.9655162E+01 .2750472E+01 .4079748E-01 .8150779E-01 .1223053E+00
.9655162E+01 .2550472E+01 .5526874E-01 .8527539E-01 .1405441E+00
.9455162E+01 .2550472E+01 .5046561E-01 .7197192E-01 .1224375E+00
.9455162E+01 .2750472E+01 .4578677E-01 .8939872E-01 .1351855E+00
(Begin sampling in direction of steepest descent)
.9530786E+01 .2676081E+01 .4371537E-01 .7678889E-01 .1205043E+00
.9506411E+01 .2701691E+01 .4396236E-01 .8187671E-01 .1258391E+00
.9482035E+01 .2727300E+01 .4468751E-01 .8088665E-01 .1255742E+00
(Search stopped, no new minimum found)
```

Bibliography

1. Anderson, J.D., Modern Compressible Flow, 1st Ed., McGraw-Hill, New York, 1982 pp303-305.

2. Benton, J., Perkins, J., and Edwards, A., "Limitations of the Method of Characteristics When Applied to Axisymmetric Hypersonic Wind-Tunnel Nozzle Design", AIAA Paper 90-0192, June 1990.

3. Buck, M.L., and Draper, A.C., "Non-Isentropic Effects on the WRDC 20 Inch Hypersonic Wind Tunnel Calibration", International Congress on Instrumentation in Aerospace Simulation Facilities, ICIASF 1989 Record, IEEE Publication 89CH 2762-3, 1989.

4. Trolier, J.W., Krawczyk, W.J., Stowell, G., Lee, R.A., and Sinhe, N., "Hypersonic Nozzle Flow Simulation; Task 3", Final Report prepared for WRDC/FIM, May 1989.

5. MacCormack, R.W., "Current Status of Numerical Solutions of the Navier-Stokes Equations", AIAA Paper No. 85-0032.

6. Roe, P.L., "Approximate Riemann Solvers, Parameter Vectors and Difference Schemes", Journal of Computational Physics, 43:357-372, 1981.

7. Gaitonde, D., and Shang, J.S., "The Performance of Flux-Split Algorithms in High-Speed Viscous Flow', AIAA Paper 92-0186, January 1992.

8. Korte, J.J., "A Comparison of Experimental Data With CFD For The NSWC Hypervelocity Wing Tunnel #9 Mach 14 Nozzle", AIAA -92-4010, July 1992.

9. Korte, J.J., Kumar, A., "CAN-DO, CFD-Based Aerodynamic Nozzle Design and Optimization Program for Supersonic/Hypersonic Wind Tunnels", AIAA-92-4009, July 1992.

10. Kaufman, L.G., "Real Gas Flow Tables for Non-Dissociated Air", WADC Technical Report 59-4, ARL, January 1959.

11. Anderson, W.K., Thomas, J.L., and Van Leer, B., "A Comparison of Finite Volume Flux Vector Splittings for the Euler Equations", AIAA 85-0122, 1985.

12. Van Leer, B., "Towards the Ultimate Conservation Difference Scheme V, a Second Order Sequel to Godunov's Method", Journal of Computational Physics, 32:101-136, 1979.

13. Yee, H.C., "A Class of High-Resolution Explicit and Implicit Shock-Capturing Methods", NASA Technical Memorandum 101088, February 1989.

14. Thomas, J.L., Walters, R.W., "Upwind Relaxation Algorithms for the Navier-Stokes Equations", AIAA Journal, Vol 25, No 4, April 1987.

15. Granville, P.S., "Baldwin-Lomax Factors for Turbulent Boundary Layers in Pressure Gradients", AIAA Journal., Vol 25, No 12, pp 1624-1627, 1987.

16. White, F.M., *Viscous Fluid Flow*, McGraw-Hill, New York, 1991.

17. Jones, W.P., Launder, B.E., "The Prediction of Laminarization with a Two-Equation Model of Turbulence", International Journal of Heat and Mass Transfer, Vol 15, pp301-314, 1972.

18. Lang, N.J., Shih, T.H., "A Critical Comparison of Two-Equation Turbulence Models", NASA TM 105237, September 1991.

19. Sarkar, S., Erlebacher, G., Hussaini, M.Y., and Kreiss, H.O., "The Analysis and Modeling of Dilatational Terms in Compressible Turbulence", NASA CR 181959, December 1989.

20. Dash, S.M., Sinha, N., York, B.J., Kenzakowski, D., and Lee, R., "Computer Codes for HSCT Exhaust Flowfield Simulation and Observations on Turbulence Modeling", AIAA 91-3297, AIAA 9th Applied Aerodynamics Conference, September 1991.

21. Gerolymos, G.A., "Implicit Multiple-Grid Solutions of the Compressible Navier Stokes Equations Using K-ϵ Turbulence Closure", AIAA Journal Vol 28, No 10, pp1707-1717, October 1990.

22. Scaggs, N., Neumann, R., Laganelli, A., "Hypersonic Wind Tunnel Nozzle Study", AIAA 92-4012, AIAA 17th Aerospace Ground Testing Conference, July 1992.

23. Hindman, R.G., "Generalized Coordinate Forms of Governing Fluid Equations and Associated Geometrically Induced Errors", AIAA Journal, Vol 20, No 10, October 1982.

24. Isaacson, E., Keller, H.B., *Analysis of Numerical Methods*, John Wiley and Sons, New York, 1966.

25. Anderson, J.D., *Hypersonics and High Temperature Gas Dynamics*, McGraw-Hill, New York, 1989.

26. Hackett, C.M., "Computational and Numerical Analysis of Hypersonic Nozzle Flows with Comparisons to Wind Tunnel Calibration Data", AIAA 92-4011, AIAA 17th Aerospace Ground Testing Conference, July 1992.

27. Witliff, C.E., "A Survey of Existing Hypersonic Ground Testing Facilities--North America", Calspan Corporation, Buffalo, NY.

28. Baldwin, B.S., Lomax, H., "Thin Layer Approximation and Algebraic Model for Separated Turbulent Flows", AIAA 78-257, AIAA 16TH Aerospace Sciences Meeting, January 1978.

29. Huddleston, D.H., "Aerodynamic Design Optimization Using Computational Fluid Dynamics", PhD Dissertation, University of Tennessee, Knoxville, 1989.

30. Johnson, C.B., Boney, L.R., Ellison, J.C., Erickson, W.D., "Real Gas Effects on Hypersonic Nozzle Contours with a Method of Calculation", NASA TN D-1622, NASA Langley Research Center, VA, 1963.

31. Candler, G., Perkins, J., "Effects of Vibrational Non-equilibrium on Axisymmetric Hypersonic Nozzle Design", AIAA 91-0297, AIAA 29th Aerospace Sciences Meeting, January 1991.

32. Canupp, P., Candler, G., Perkins, J., Erickson, W., "Analysis of Hypersonic Nozzles Including Vibrational Nonequilibrium and Intermolecular Force Effects", AIAA 92-0330, AIAA 30th Aerospace Sciences Meeting, January 1992.

33. Millikan, R.C., White, D.R., "Systematics of Vibrational Relaxation", The Journal of Computational Physics, Vol. 39, No. 12, 15 December 1963.

34. Walters, R.W., Cinnella, P., Slack, D.C., "Characteristic-Based Algorithms for Flows in Thermo-Chemical Nonequilibrium", AIAA 90-0393, AIAA 28th Aerospace Sciences Meeting, January 1990.

35. Grossman, B., Cinnella, P., "Flux-Split Algorithms for Flows with Nonequilibrium Chemistry and Vibrational Relaxation", Journal of Computational Physics, Vol. 88, 1990.

36. Sivells, J.C., "Aerodynamic Design of Axisymmetric Hypersonic Wind-Tunnel Nozzles", The Journal of Spacecraft, Vol. 7, No. 11, November 1970.

37. White, J.A.,Korte, J.J., Gaffney, R.L., "Flux-Difference Split Parabolized Navier-Stokes Algorithm for Nonequilibrium Chemically Reacting Flows", AIAA-93-0534, AIAA 31st Aerospace Sciences Meeting & Exhibit, January 1993.

38. Morrison, J.H., Korte, J.J., "Implementation of Vigneron's Streamwise Pressure Gradient Approximation in the PNS Equations", AIAA-92-0189, AIAA 30th Aerospace Sciences Meeting & Exhibit, January 1992.

39. Morrison, J., "Flux Difference Split Scheme for Turbulent Transport Equations", AIAA-90-5251, AIAA Second International Aerospace Planes Conference, October 1990.

40. Josyula, E., Shang, J.S., "Computation of Hypersonic Flow-fields in Thermal and Chemical Nonequilibrium", AIAA-92-2874, AIAA 27th Thermophysics Conference, July 1992.

41. Rizzetta, D.P., "Numerical Simulation of Slot Injection into a Turbulent Supersonic Stream", AIAA-92-0827, AIAA 30th Aerospace Sciences Meeting & Exhibition, January 1992.

42. Hirsch, C., *Numerical Computation of Internal and External flows, Volume 1: Fundamentals of Numerical Discretization*, John Wiley & Sons,Ltd., Chichester, 1988.

43. Hirsch, C., *Numerical Computation of Internal and External flows, Volume 2: Computational Methods for Inviscid and Viscous Flows*, John Wiley & Sons,Ltd., Chichester, 1990.

44. Young, D.M., Gregory, R.T., *A Survey of Numerical Mathematics, Volume 1*, Dover Publications, Inc., New York, 1972.

45. Box, G, Draper, N.R., *Empirical Model-Building and Response Surfaces*, John Wiley & Sons, New York, 1987.

46. Anderson, J.D., *Hypersonic and High Temperature Gas Dynamics*, McGraw-Hill Book Company, New York, 1989.

47. Schlichting, H., *Boundary-Layer Theory*, McGraw-Hill Publishing Company, New York, 1979.

48. Anderson, D.A., Tannehill, J.C., Pletcher, R.H., *Computational Fluid Mechanics and Heat Transfer*, Hemisphere Publishing Corporation, New York, 1984.

49. Korte, J.J., "An Explicit Upwind Algorithm for Solving the Parabolized Navier-Stokes Equations", NASA Technical Paper 3050, February 1991.

50. Vincenti, W.G., Kruger, C.H., *Introduction to Physical Gas Dynamics*, Robert E. Krieger Publishing Company, Malabar 1986.

51. Park, C., "Assessment of Two-Temperature Kinetic Model for Ionizing Air", AIAA Paper 87-1574, AIAA 22nd Thermophysics Conference, Honolulu, Hawaii, June 8-10, 1987.

52. Yang, Z., Shih, T.H., "A k-ϵ Modeling of Near Wall Turbulence", Proceedings of 4th International Symposium on Computational Fluid Dynamics, UC Davis, 1991.

53. Korte, J.J., Private Communications (1993-1995)

54. Zucrow, M.J., Hoffman, J.D., *Gas Dynamics Volume 1*, John Wiley & Sons, New York, 1976.

55. Steger, J.L., Warming, R.F., "Flux Vector Splitting of the Inviscid Gasdynamic Equations with Application to Finite-Difference Methods", Journal of Computational Physics, 40, 263-293, 1981.

56. Kussoy, M.I., Horstman, K.C., "Documentation of Two- and Three-Dimensional Shock-Wave/Turbulent-Boundary-Layer Interaction Flows at Mach 8.2, NASA TM 103838, May 1991.

57. Gaitonde, D., Private Communications (1993-1995)

58. Doty, J.H., *Performance Prediction and Design of Maximum Thrust Planar Supersonic Nozzles Using a Flux-Difference Splitting Technique*, PhD Dissertation, School of Mechanical Engineering, Purdue University, August, 1991.

59. Rizzetta, D.P., "Numerical Simulation of Turbulent Cylinder Juncture Flowfields", AIAA-93-3038, AIAA 24th Fluid Dynamics Conference, July 1993.

60. Korte, J.J., "Aerodynamic Design of Axisymmetric Hypersonic Wind-Tunnel Nozzles Using Least Squares/Parabolized Navier-Stokes Procedure", AIAA-92-0332, AIAA 30th Aerospace Sciences Meeting & Exhibit, January 1992,

61. Gaitonde 2-D Wright Laboratory Roe-Scheme Code.

62. Cebici, T., Smith, A.M.O., *Analysis of Turbulent Boundary Layers*, Academic Press, Inc., New York, 1974.

63. Scaggs, N.E., Private Communications (1993-1995).

64. Shang, J.S., Private Communications (1993-1995).

65. White, J.A., Private Communications (1993-1994).

66. Gaitonde, D., Josyula, E., 2-D/Full Axisymmetric Non-equilibrium, Chemically Reacting Code.

67. Fenlason, N.L., *A Navier-Stokes Solution for the NASP/ General Dynamics Generic Inlet with Slot Injection*, Masters' Thesis, School of Engineering, Air Force Institute of Technology (AU), Wright Patterson AFB, OH, pp.28-33,104-112, December, 1991.

68. Rizzetta, D.P., Wright Laboratory Beam-Warming 2-D Navier-Stokes Code and Grid.

69. Doty, J.H., Private Communications, (1992-1995).

70. Doebelin, E.O., *Measurement Systems, Application and Design*, McGraw Hill, New York, 1983.

71. Von Lavante, E., "Accuracy of Upwind Schemes Applied to the Navier-Stokes Equations," AIAA Journal, Vol. 28 No. 7, pp 1312-1314, 1990.

72. AFIT OPER683 Class Notes, no date.

FIGURES

(This page intentionally left blank)

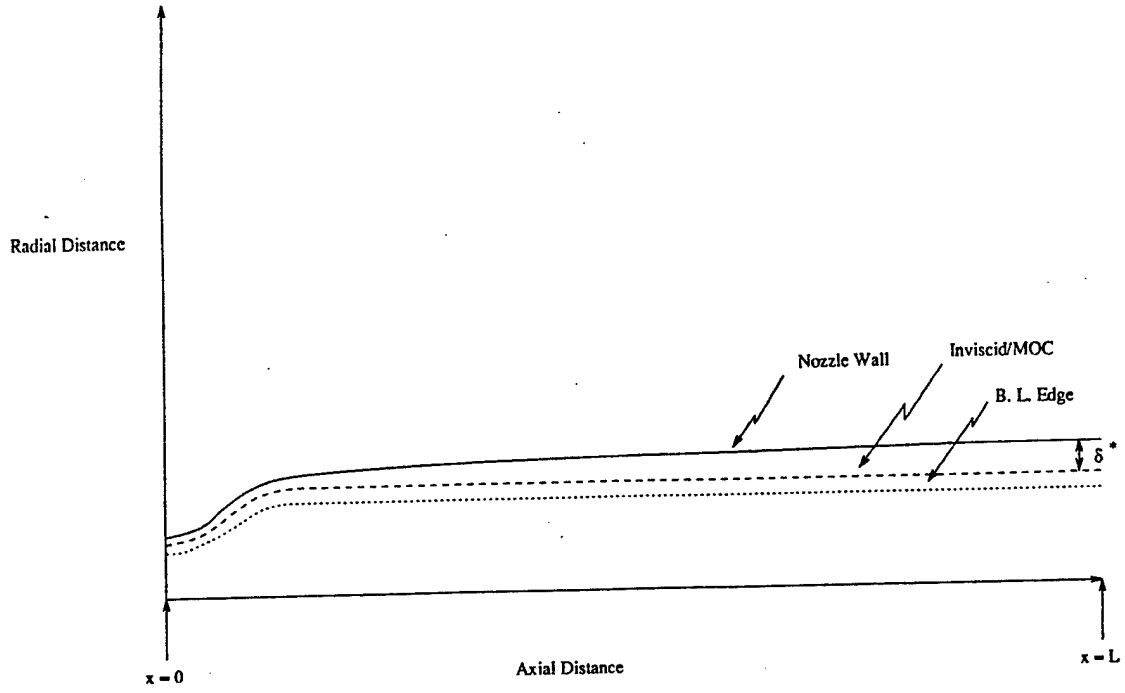

Fig. 1 MOC/BL Schematic for Nozzle Flow

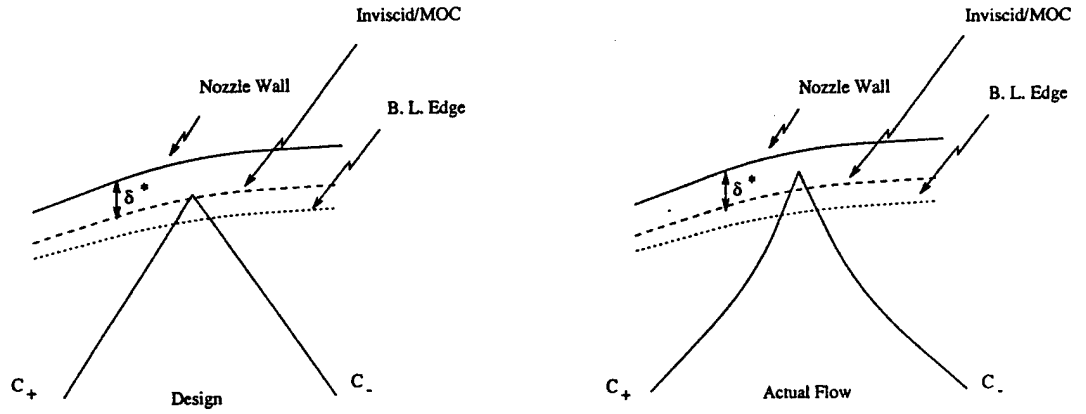

Fig. 2 Departure of Actual Flow from MOC/BL Design Due to Viscous Boundary Layer Region

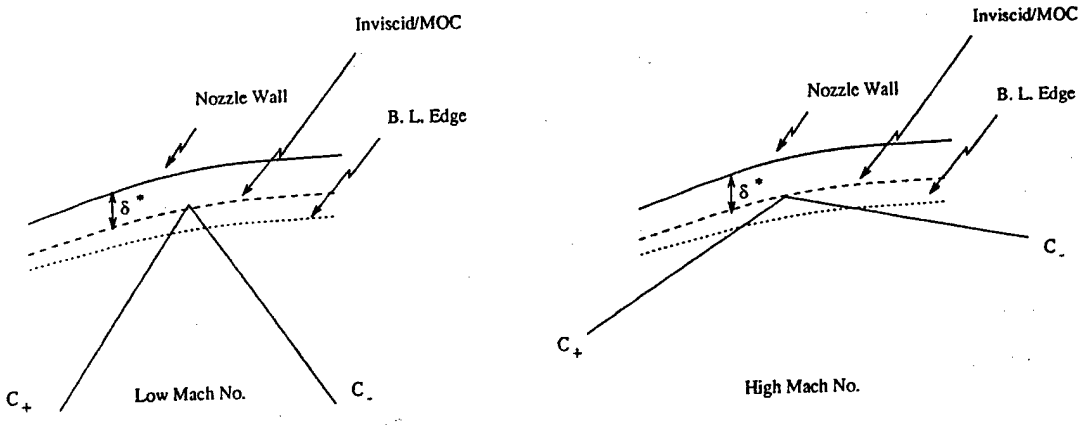

Fig. 3 Effect of Increased Edge Mach Number on Characteristic Waves in Viscous Region of Boundary Layer

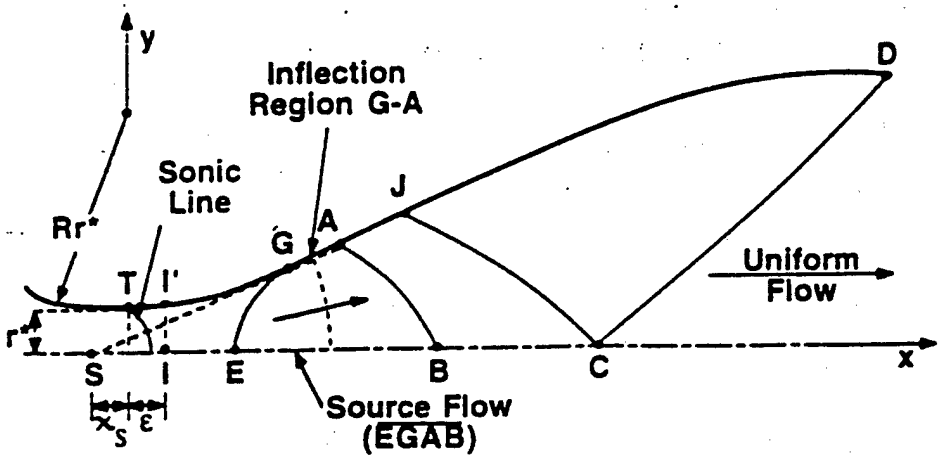

Fig. 4 Sivell's Diagram for Wind-Tunnel Nozzle Design

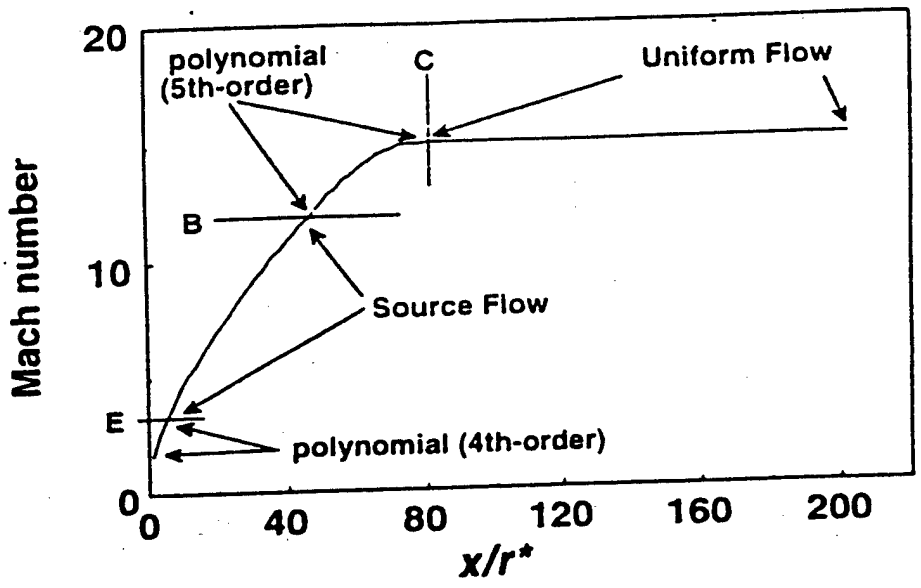

Fig. 5 Centerline Mach Number Distribution for Hypersonic Nozzle

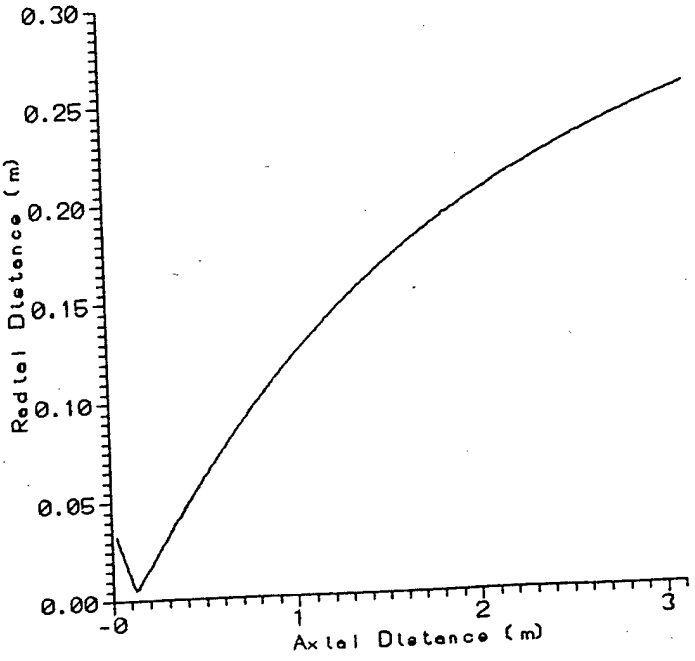

Fig. 6 AF WL Mach 12 Wind Tunnel Nozzle Profile

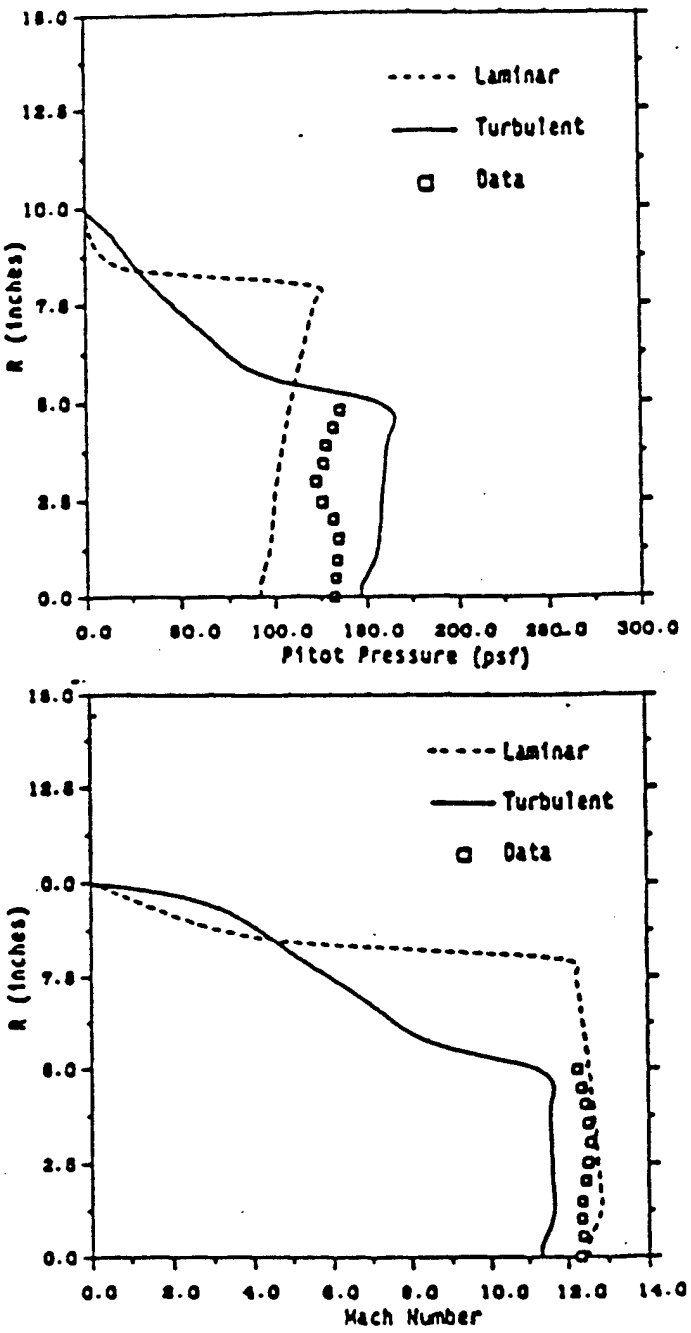

Fig. 7 SAIC CFD Mach 12 Nozzle Exit Pitot Pressure and Mach No. Profiles

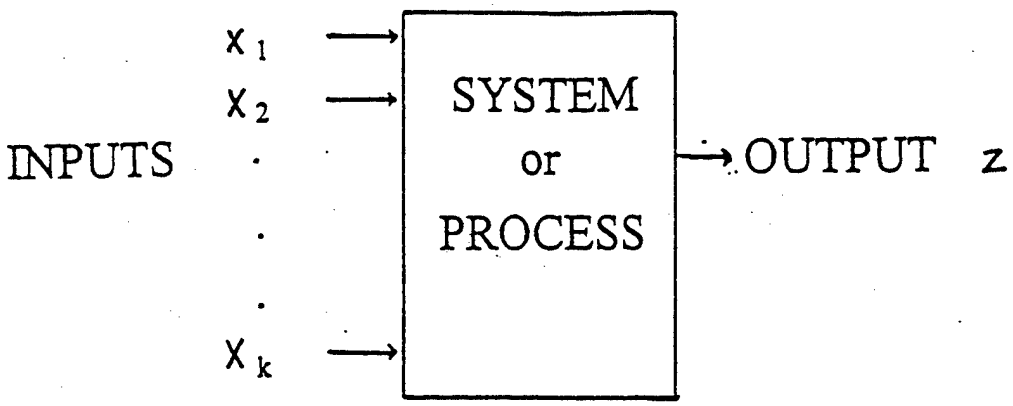

Fig. 8 Diagram of Response System/Process

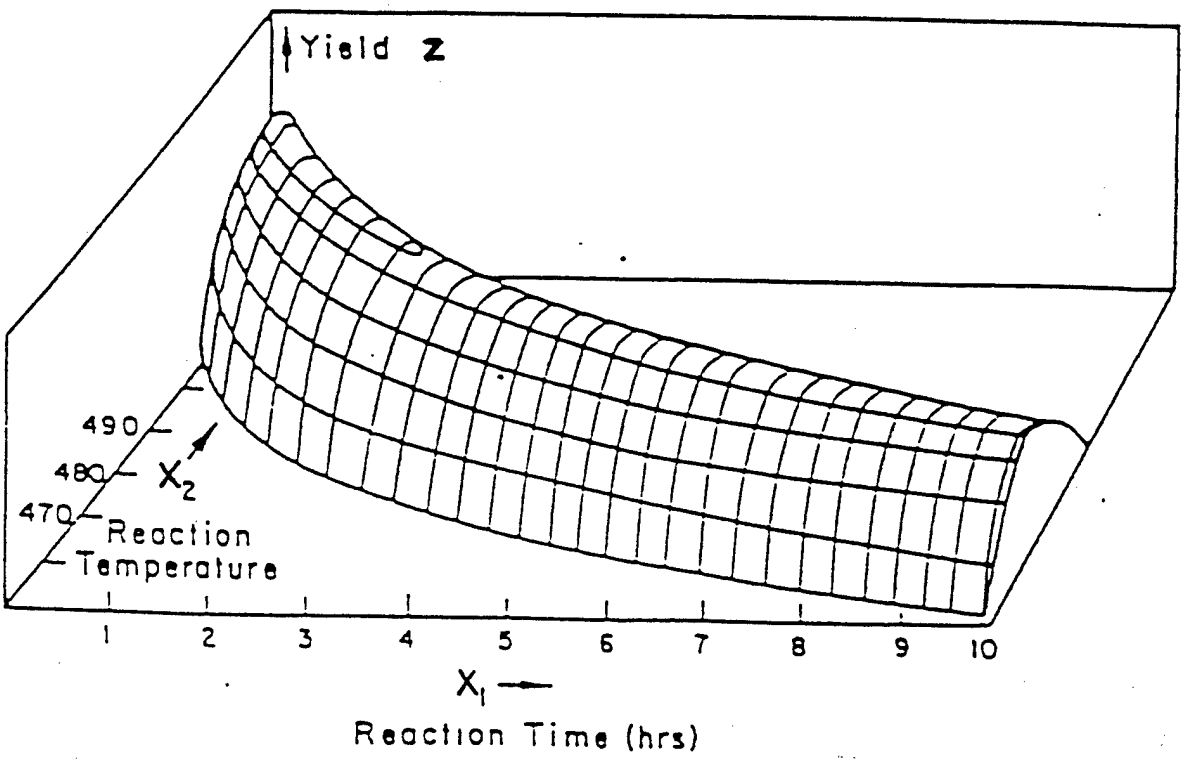

Fig. 9 Representative Response Surface

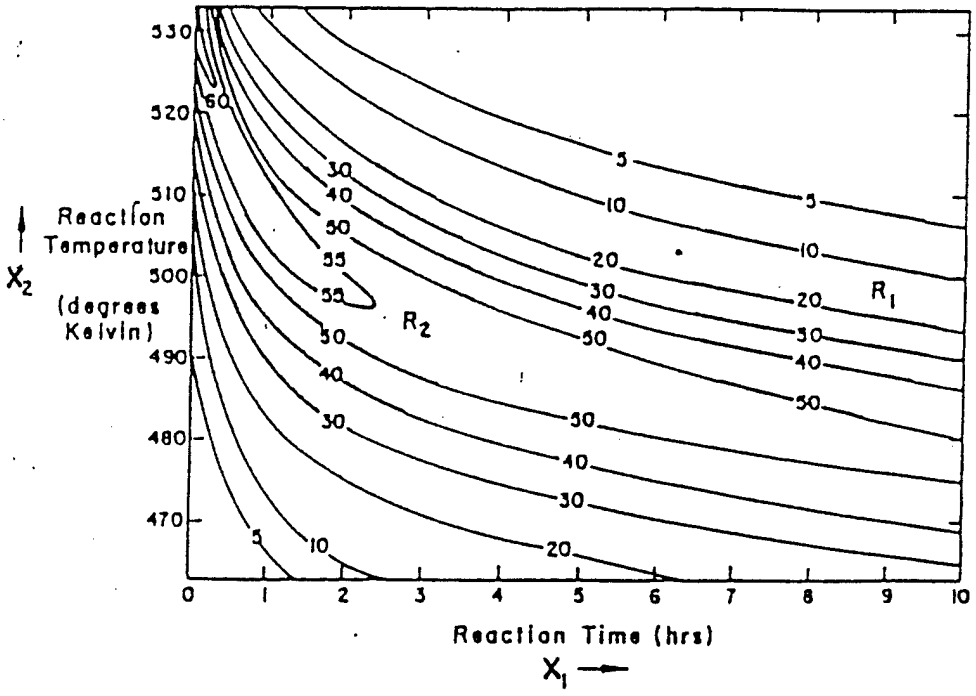

Fig. 10 Representative Response Surface Contour Plot

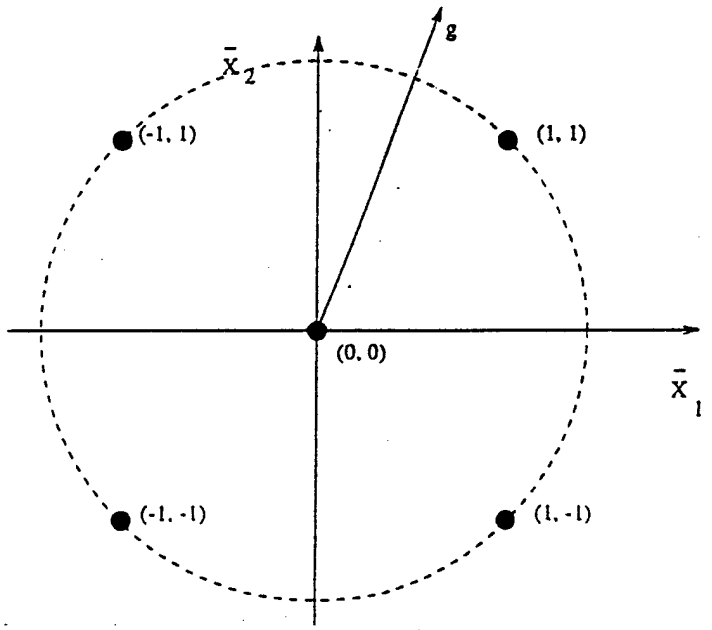

Fig. 11 Steepest Descent Method Five-Point Sampling Stencil in Transformed Space

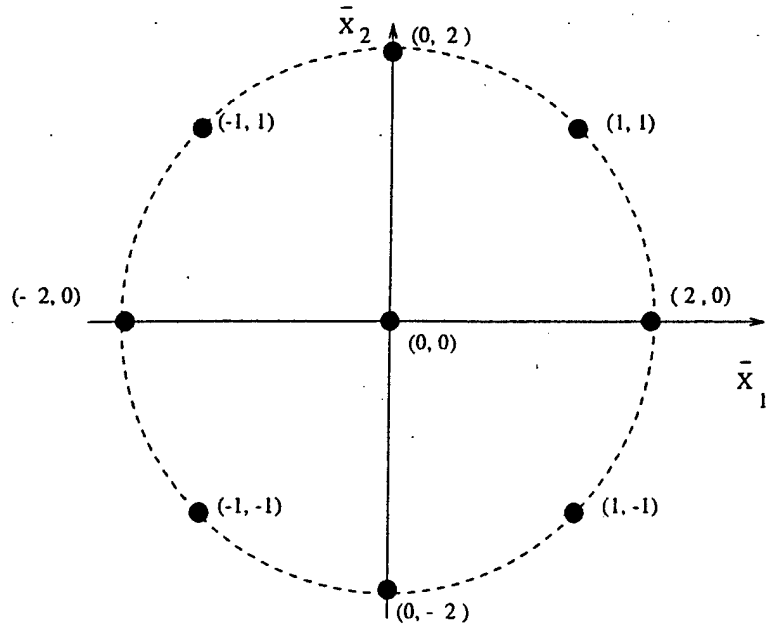

Fig. 12 Second-Order Search Method Nine-Point Sampling Stencil in Transformed Space

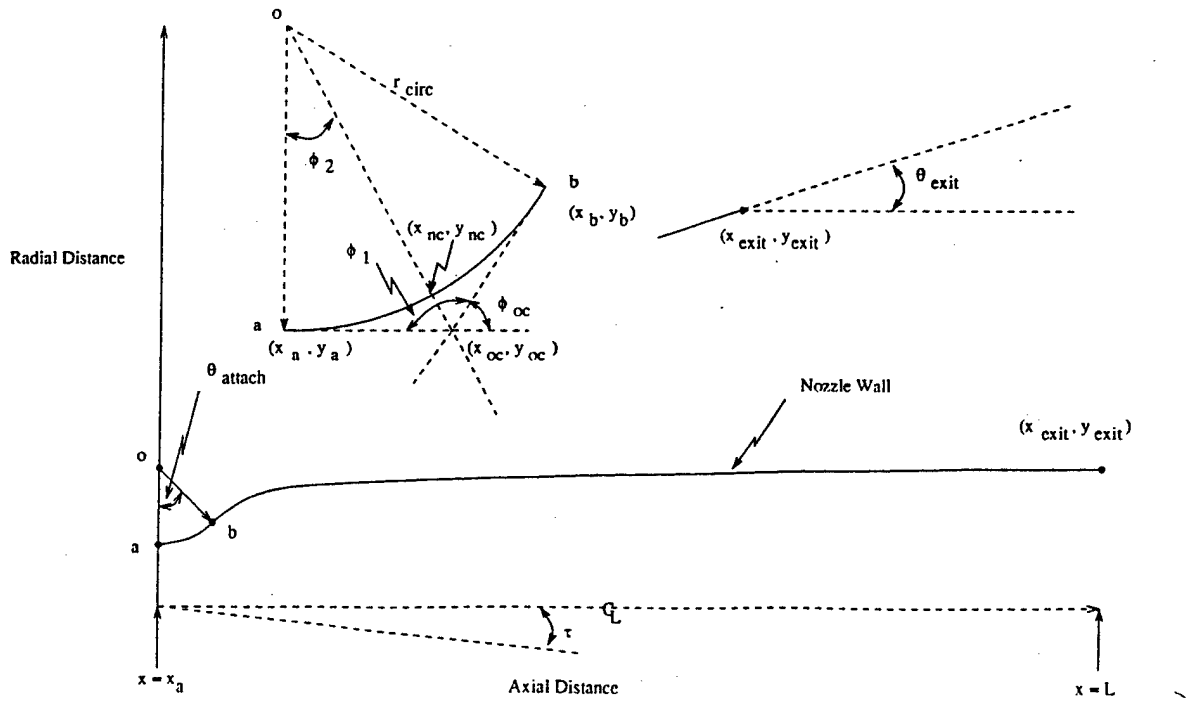

Fig. 13 Current Research Design Parameters (θ_{attach}, θ_{exit})

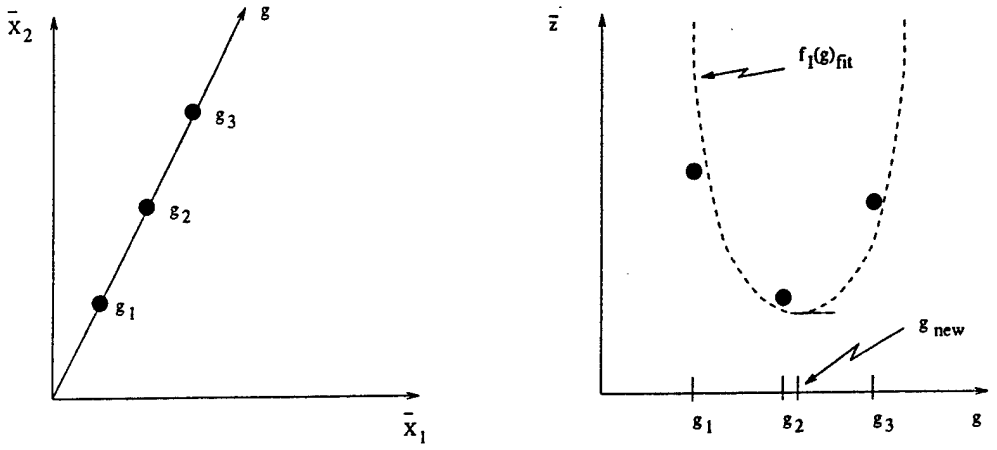

Fig. 14 Seeking a Minimum in the Direction of Steepest Descent

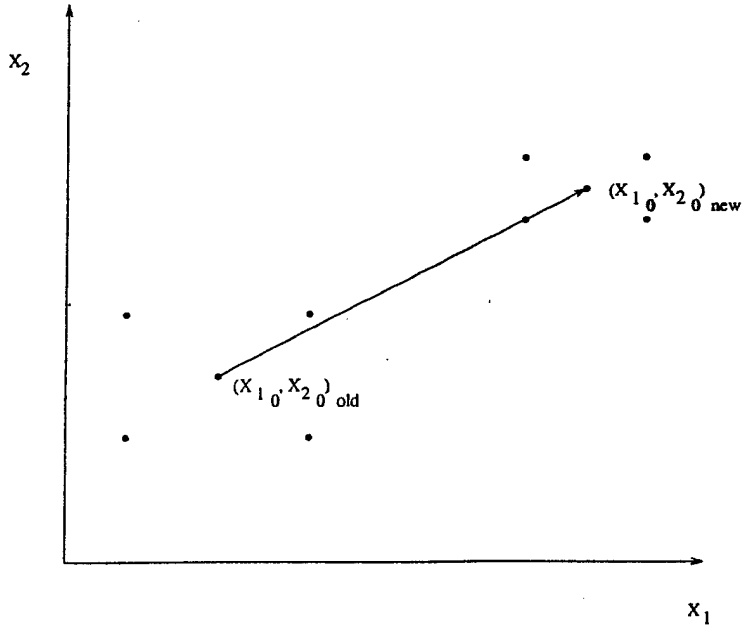

Fig. 15 Transition to Next Sampling Stencil in Non-transformed Space, Steepest Descent Method

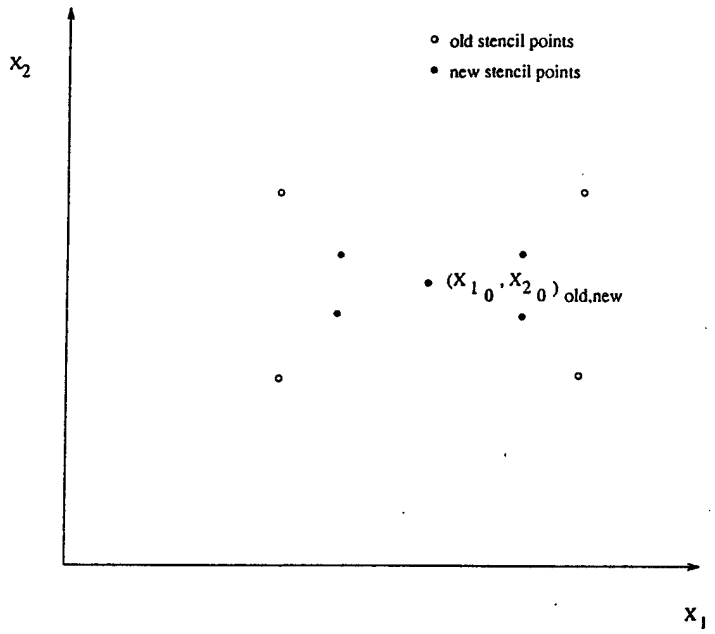

Fig. 16 Size Reduction of Sampling Stencil in Non-transformed Space, Steepest Descent Method

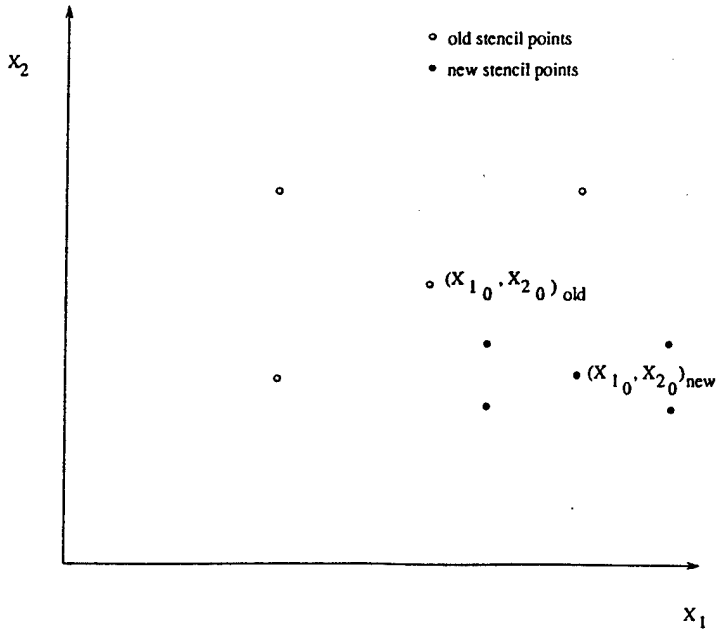

Fig. 17 Shift of Sampling Stencil in Non-transformed Space to New Sampling Stencil Point Minimum, Steepest Descent Method

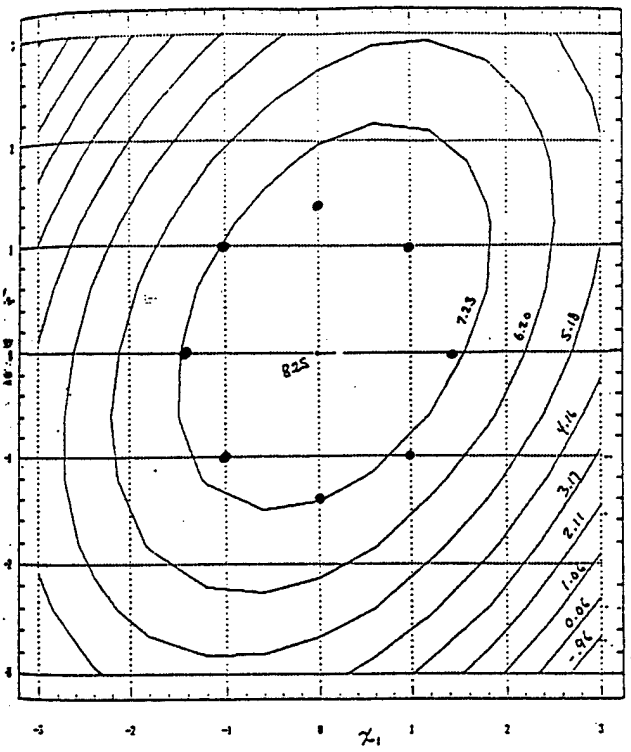

Fig. 18 Second-Order Search Sampling Stencil and Example of Associated Response Functions

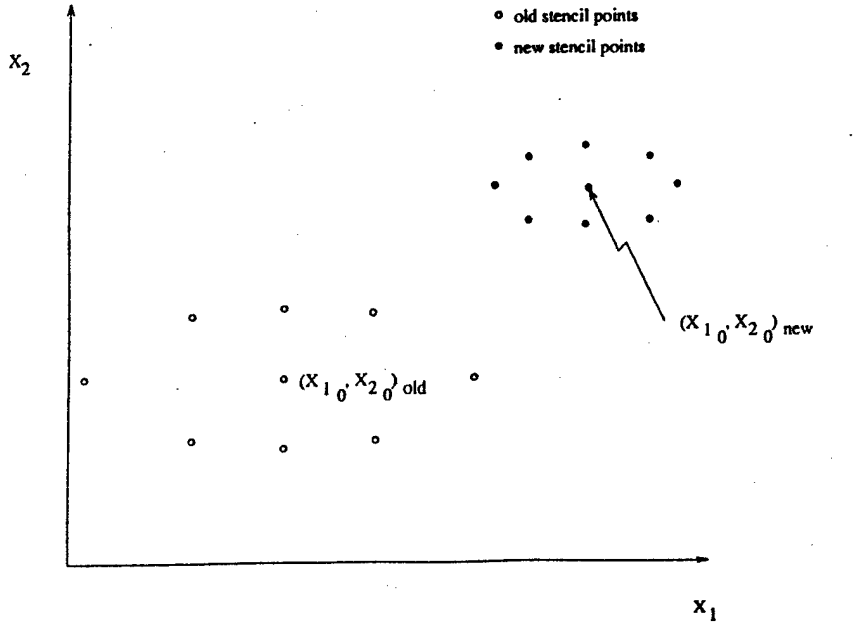

Fig. 19 Transition to Next Sampling Stencil in Non-transformed Space, Second-Order Search Method

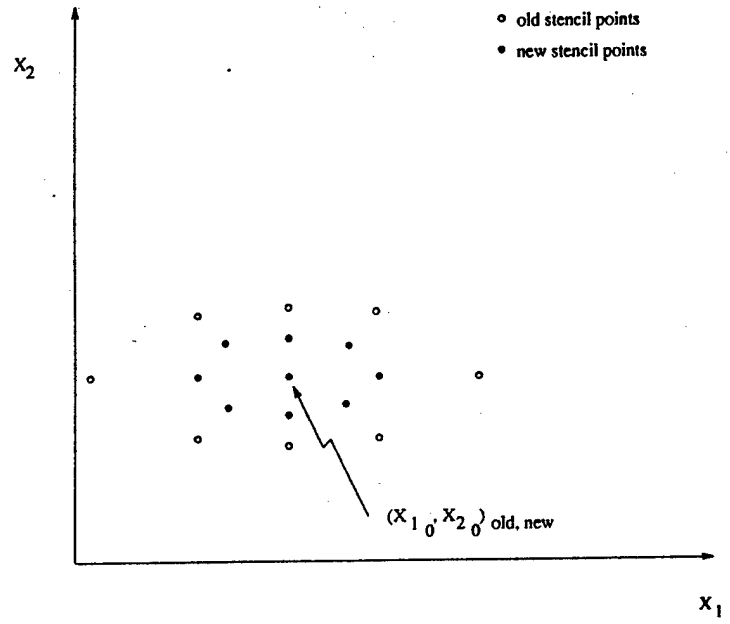

Fig. 20 Size Reduction of Sampling Stencil in Non-transformed Space, Second-Order Search Method

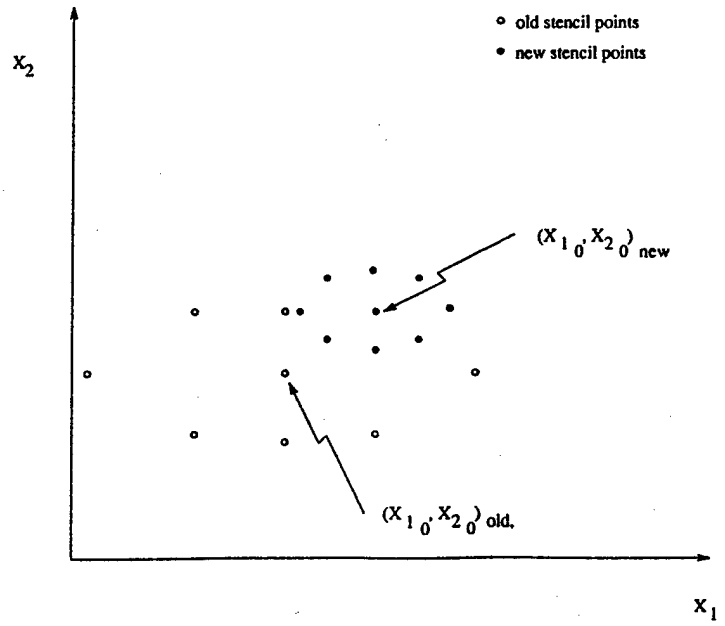

Fig. 21 Shift of Sampling Stencil in Non-transformed Space to New Sampling Stencil Point Minimum, Second-Order Search Method

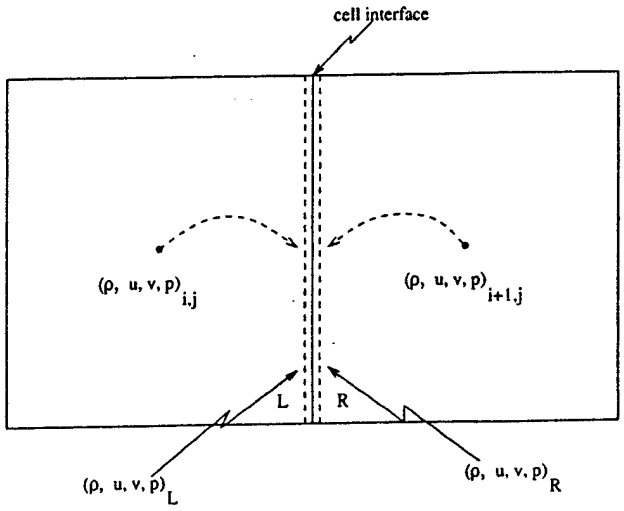

Fig. 22 Unconserved Variables Extrapolated from Cell Centers

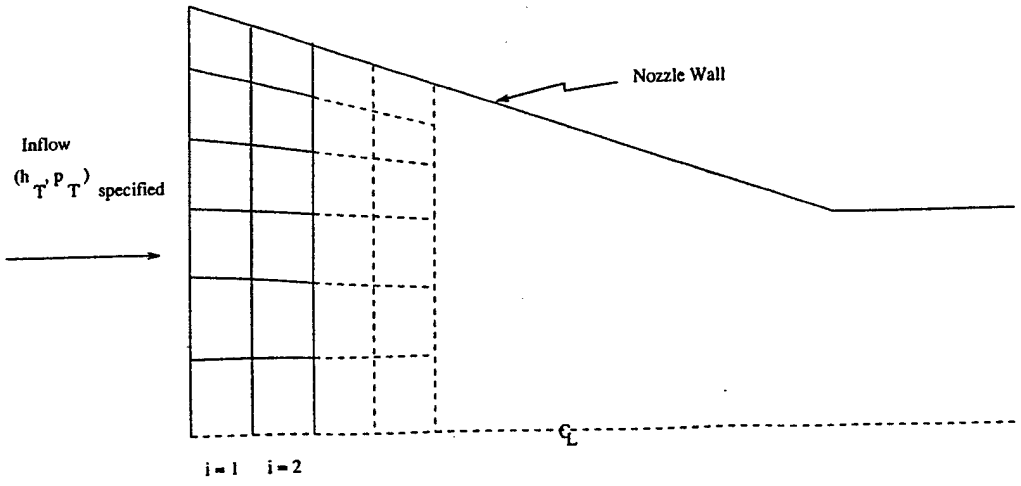

Fig. 23 Nozzle Inflow Boundary Conditions

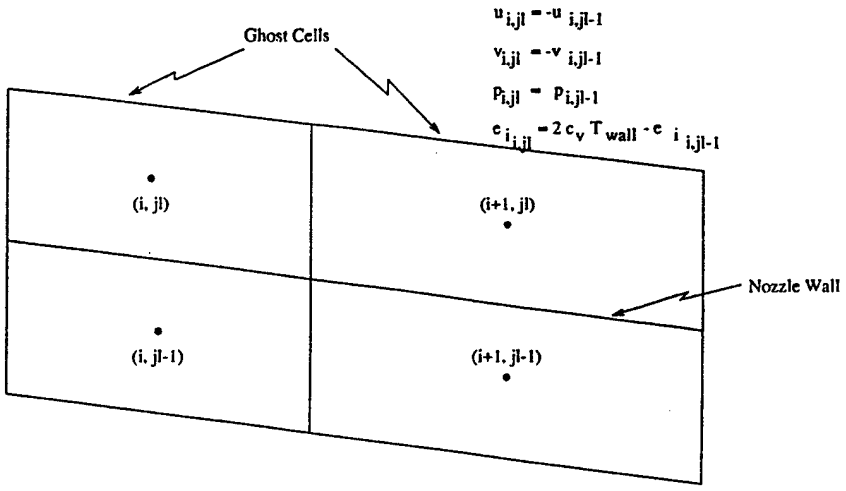

Fig. 24 Nozzle Wall Boundary Conditions

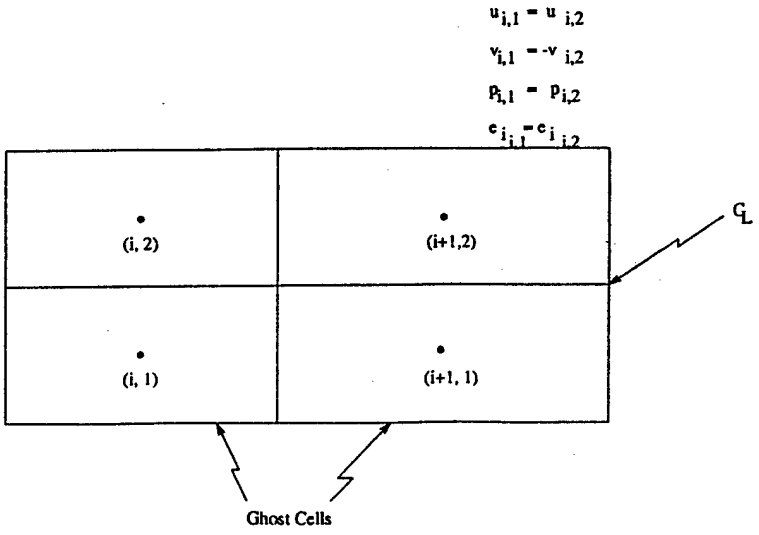

Fig. 25 Nozzle Centerline Boundary Conditions

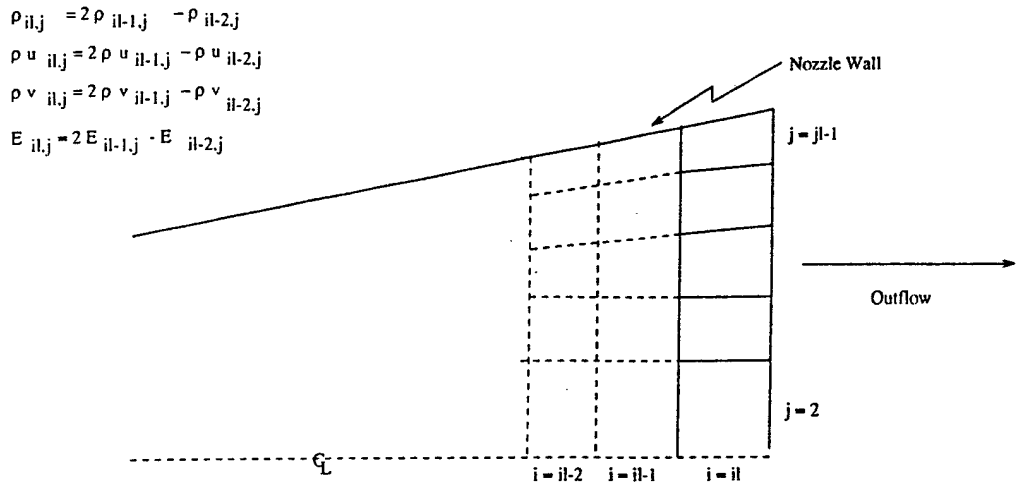

Fig. 26 Nozzle Exit Boundary Conditions

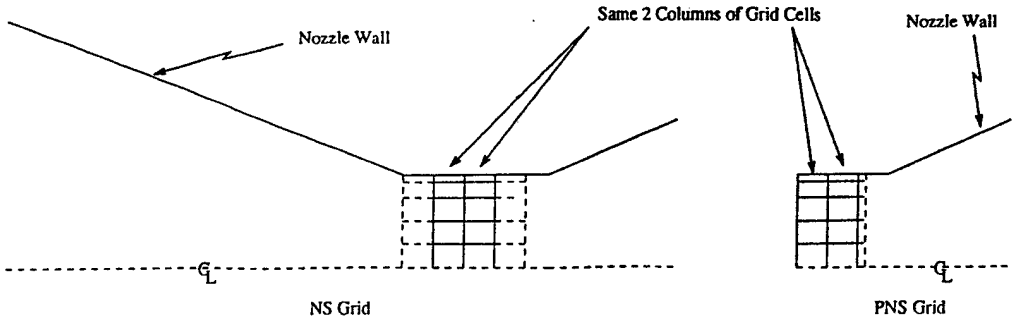

Fig. 27 NS Solver Provides Inflow for PNS Solver

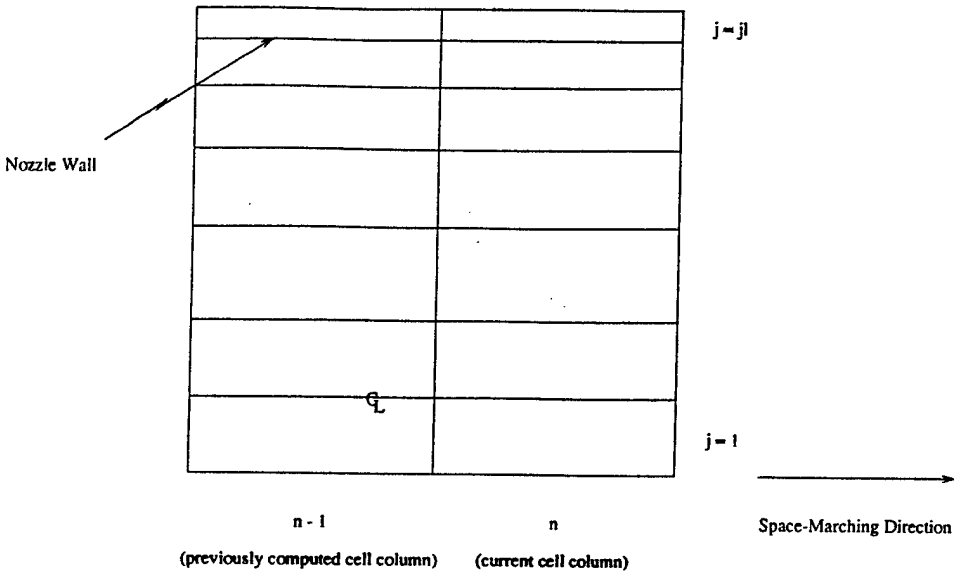

Fig. 28 PNS Computational Grid

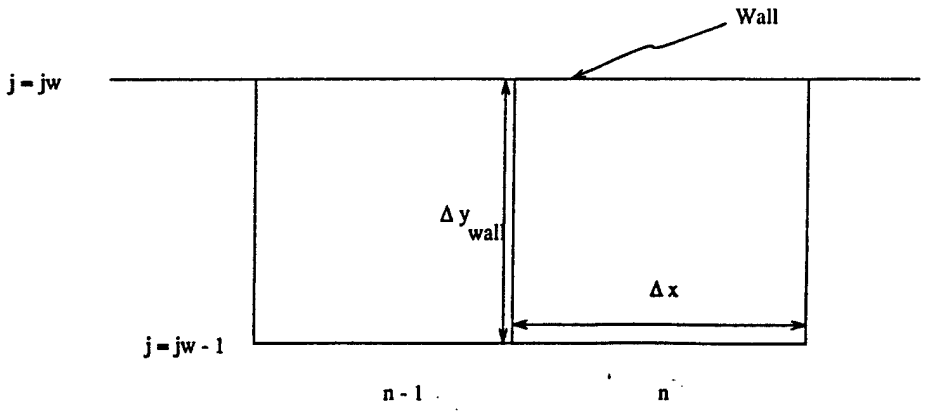

Fig. 29 Grid Spacing at the Wall

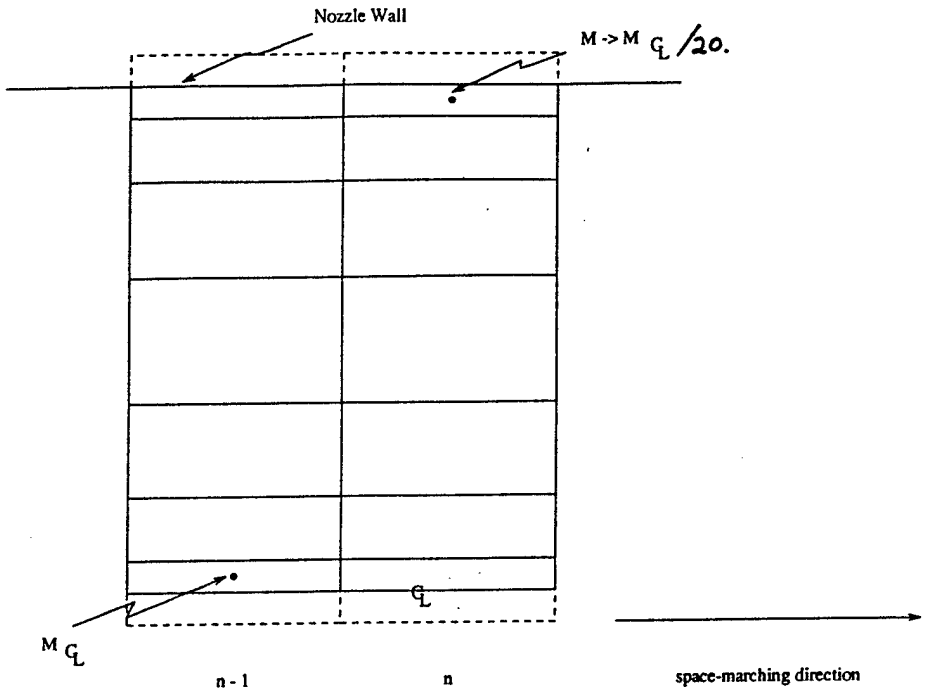

Fig. 30 Determination of Wall Spacing for Laminar Flow

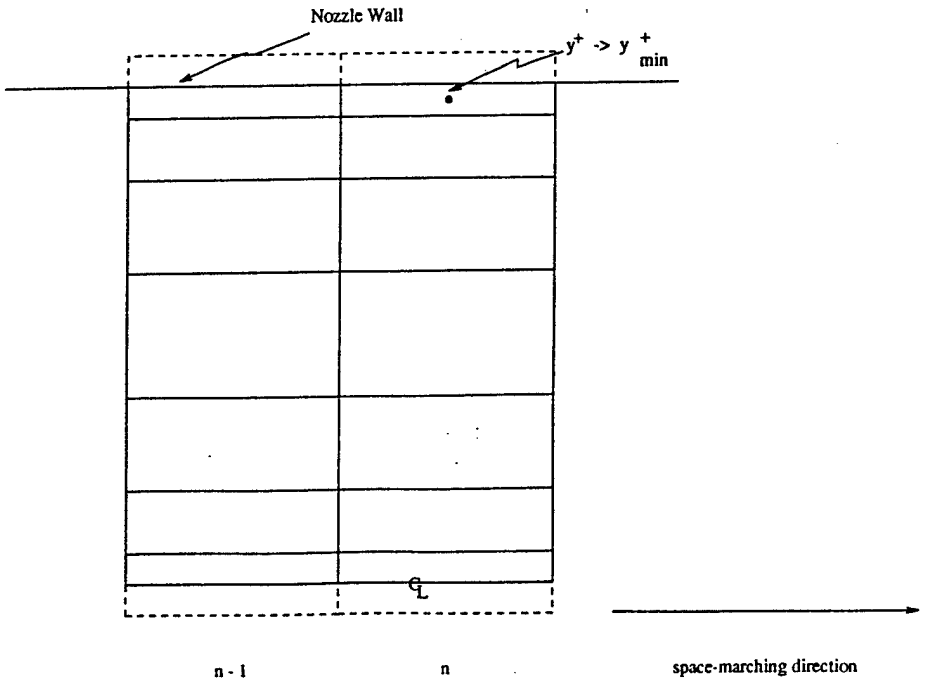

Fig. 31 Determination of Wall Spacing for Turbulent Flow

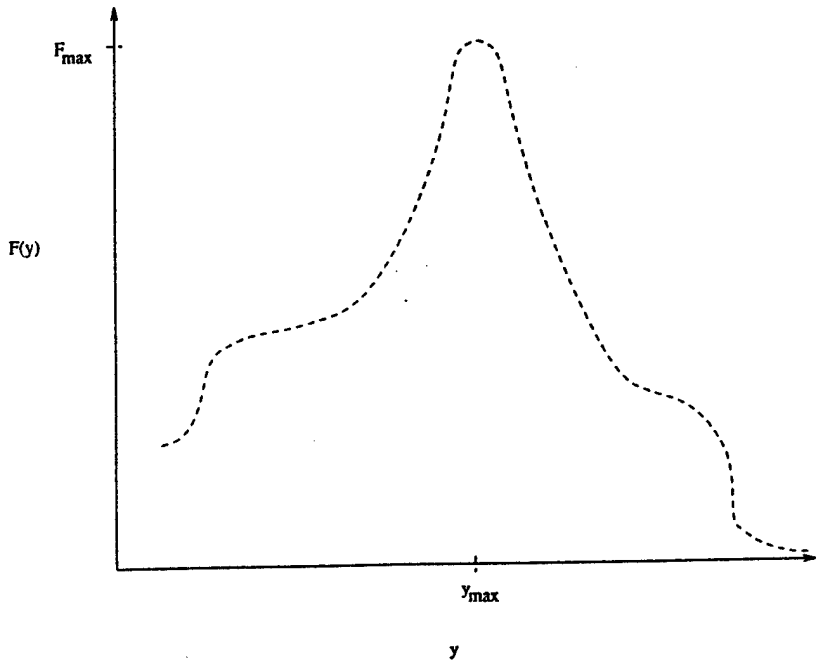

Fig. 32 Determination of Location of F_{max}, y_{max} for B-L Turbulence Model

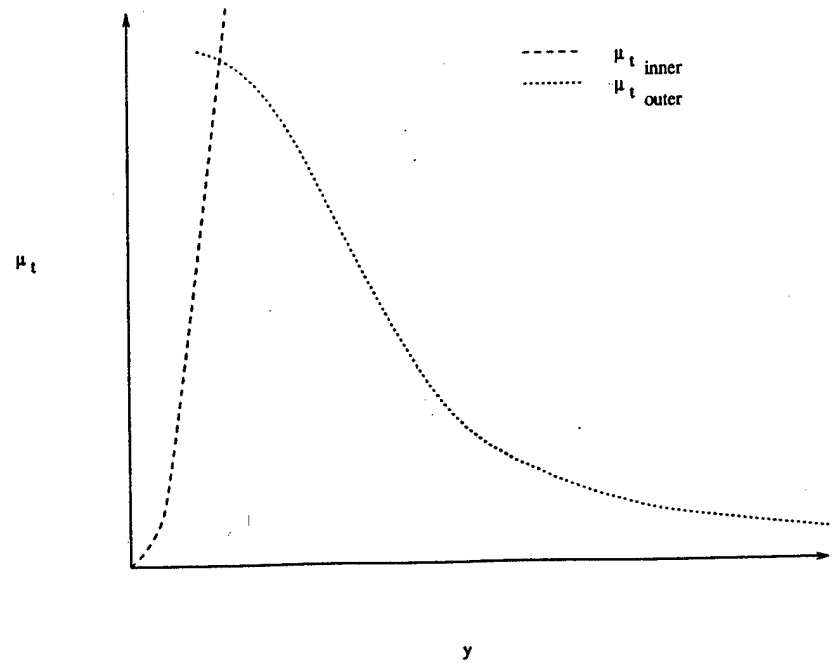

Fig. 33 B-L Eddy Viscosity Determination

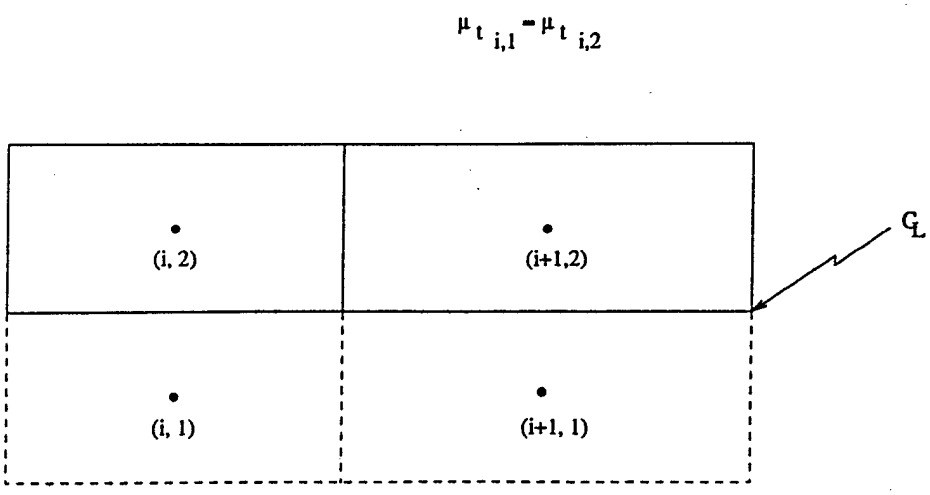

Fig. 34 B-L Nozzle Centerline Boundary Condition

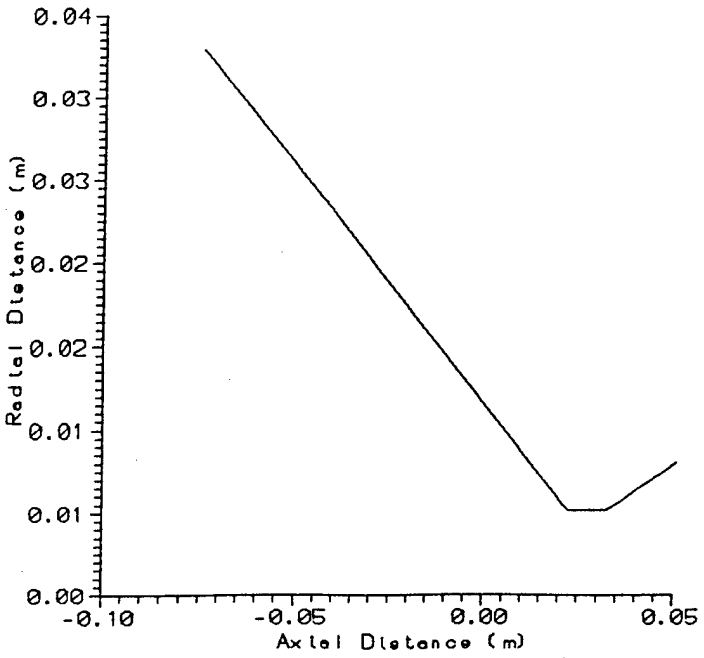

Fig. 35 WL Mach 12 Wind Tunnel Nozzle Subsonic/Throat Section

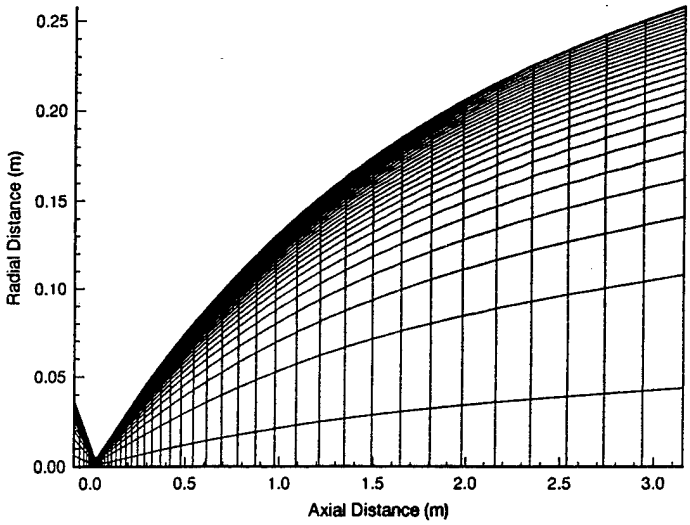

Fig. 36 Coarse 53x28 (i,j) Grid Used for Laminar Nozzle Validation

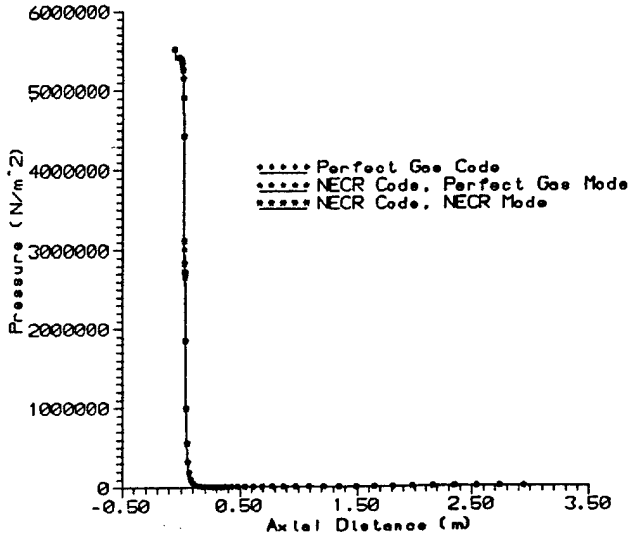

Fig. 37 Centerline Static Pressure Plot for Laminar Mach 12 Nozzle CFD Solutions (53x28)

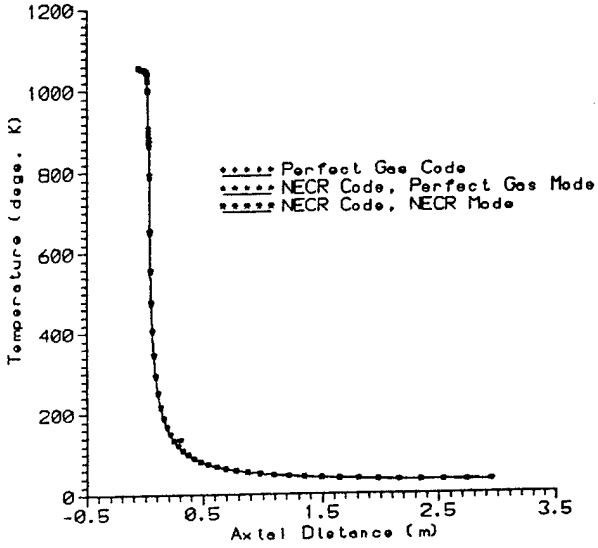

Fig. 38 Centerline Static Temperature Plot for Laminar Mach 12 Nozzle CFD Solutions (53x28)

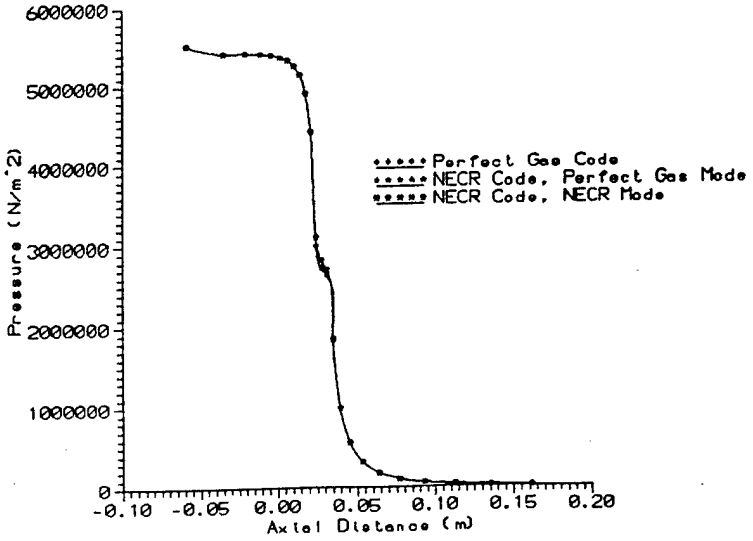

Fig. 39 Centerline Static Pressure Plot for Laminar Mach 12 Nozzle CFD Solutions, Throat Region (53x28)

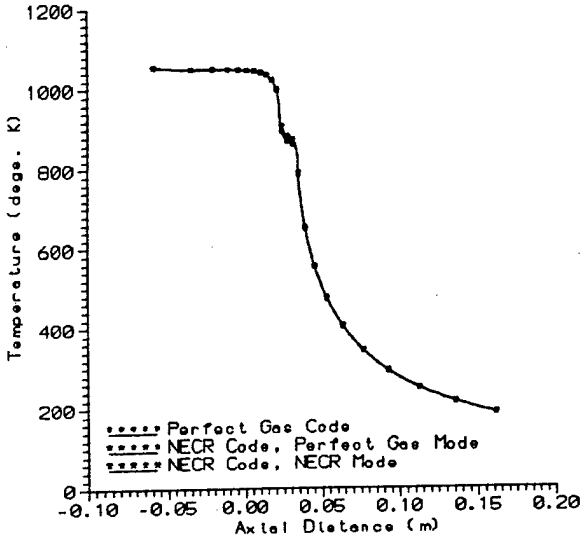

Fig. 40 Centerline Static Temperature Plot for Laminar Mach 12 Nozzle CFD Solutions, Throat Region (53x28)

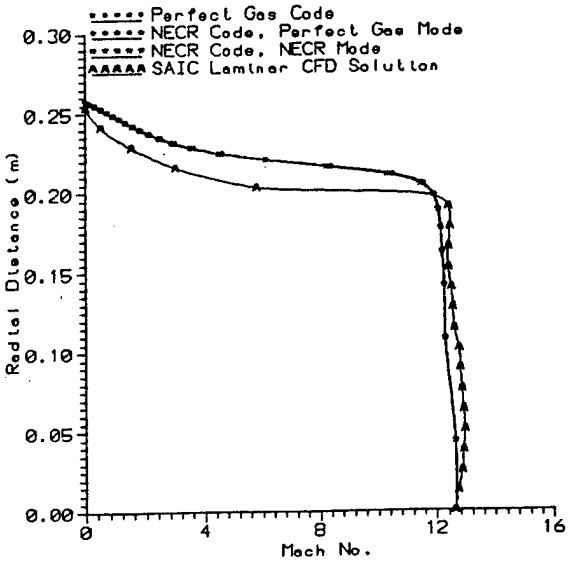

Fig. 41 Mach No. Profile of Mach 12 Nozzle Exit, Laminar Flow, (53x28)

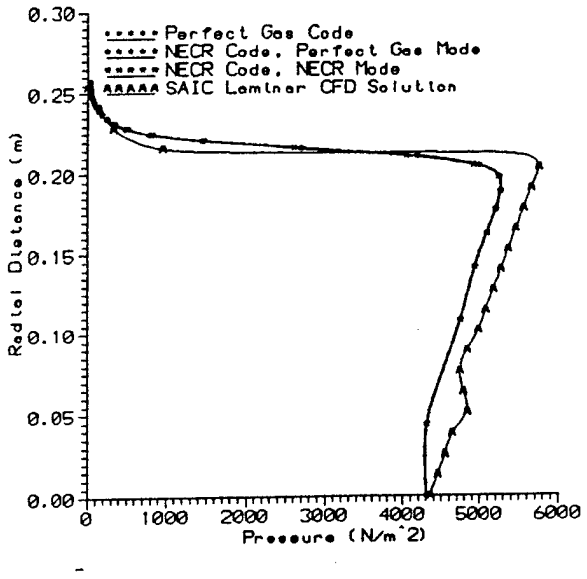

Fig. 42 Pitot Pressure of Mach 12 Nozzle Exit, Laminar Flow, (53x28)

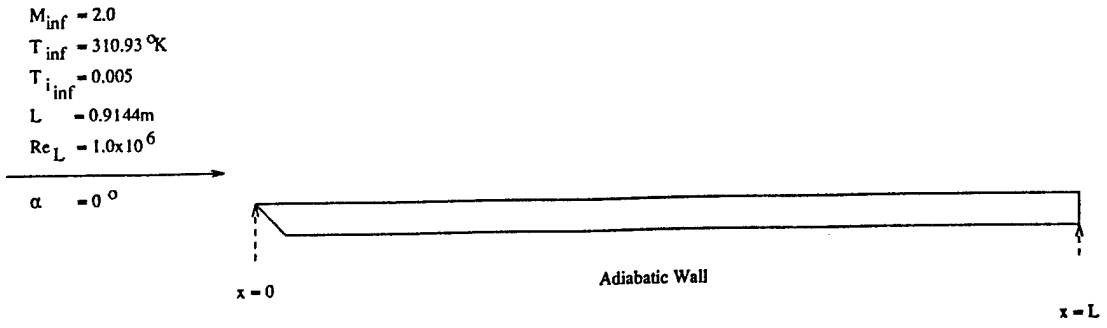

Fig. 43 Mach 2.0 Flat Plate w/Freestream Data

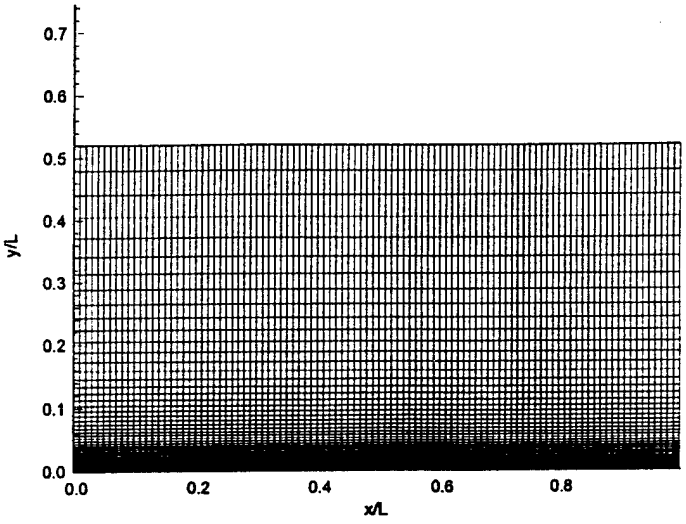

Fig. 44 Mach 2.0 Flat Plate CFD Grid

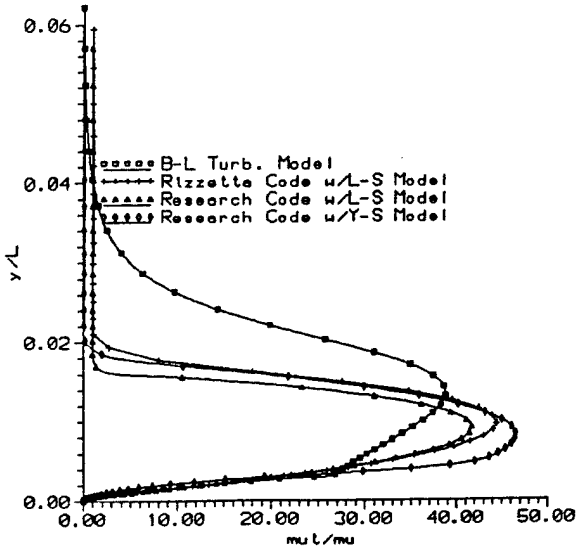

Fig. 45 CFD Comparison of Viscosity Ratio for Mach 2.0 Flat Plate

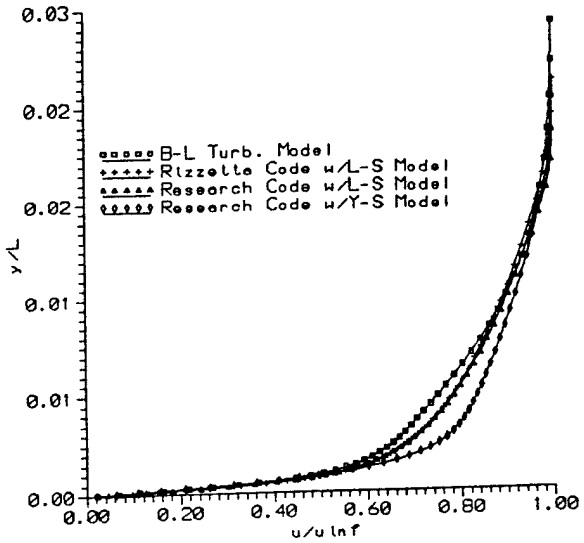

Fig. 46 CFD Comparison of Normalized U Component for Mach 2.0 Flat Plate

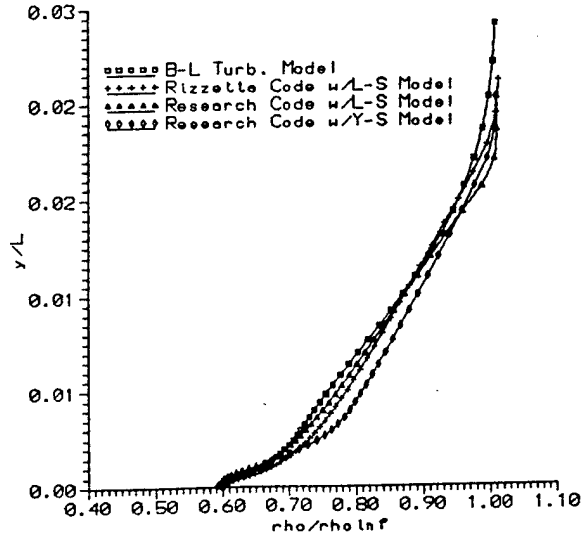

Fig. 47 CFD Comparison of Normalized Density for Mach 2.0 Flat Plate

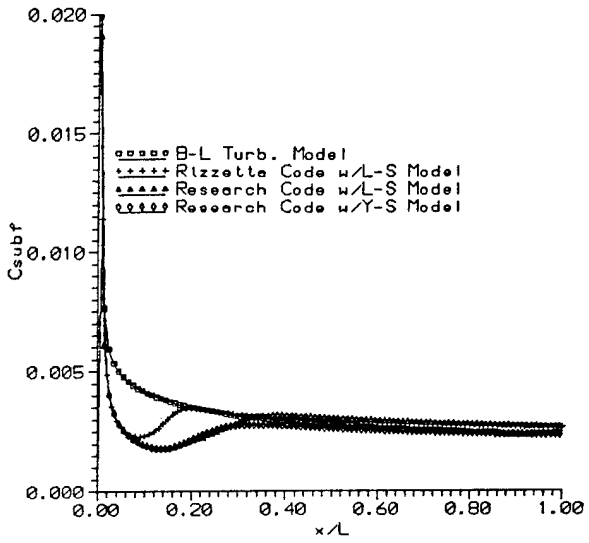

Fig. 48 CFD Comparison of x/L vs. C_f for Mach 2.0 Flat Plate

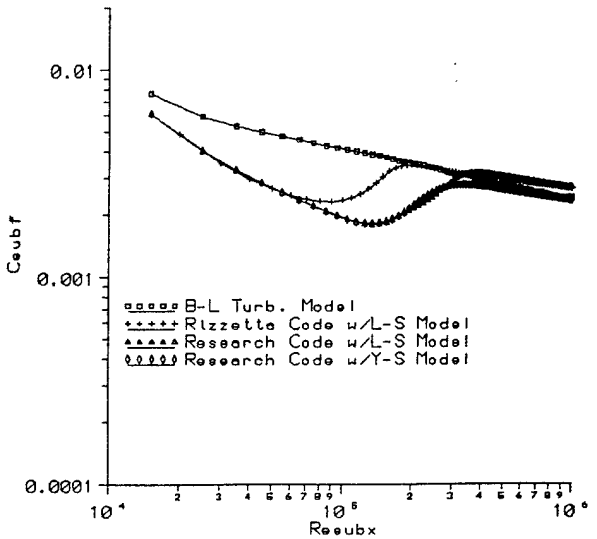

Fig. 49 CFD Comparison of Re_x vs. C_f for Mach 2.0 Flat Plate

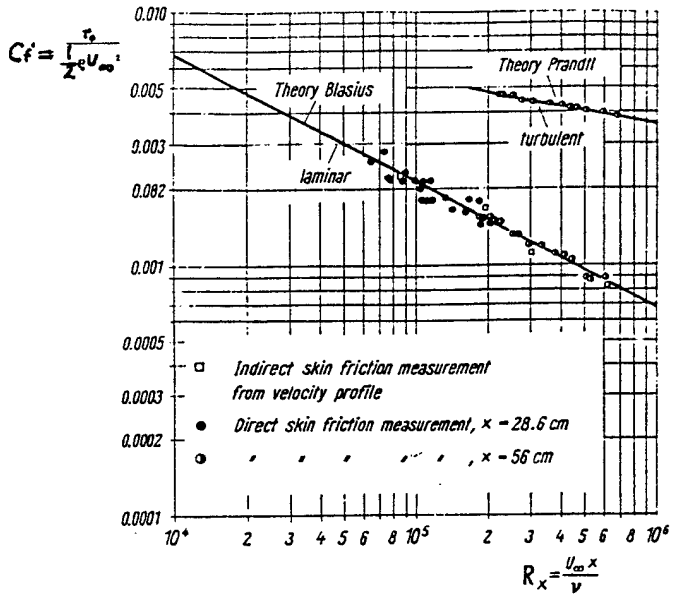

Fig. 50 Local C_f on a Flat Plate at Zero Incidence in Incompressible Flow

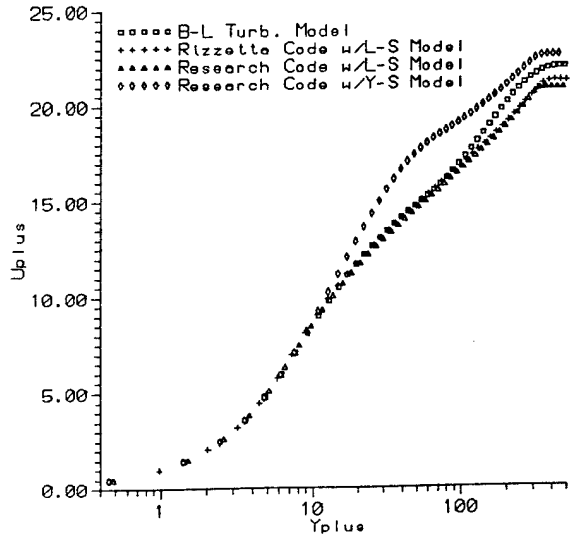

Fig. 51 CFD Comparison of U^+ vs. y^+ for Mach 2.0 Flat Plate

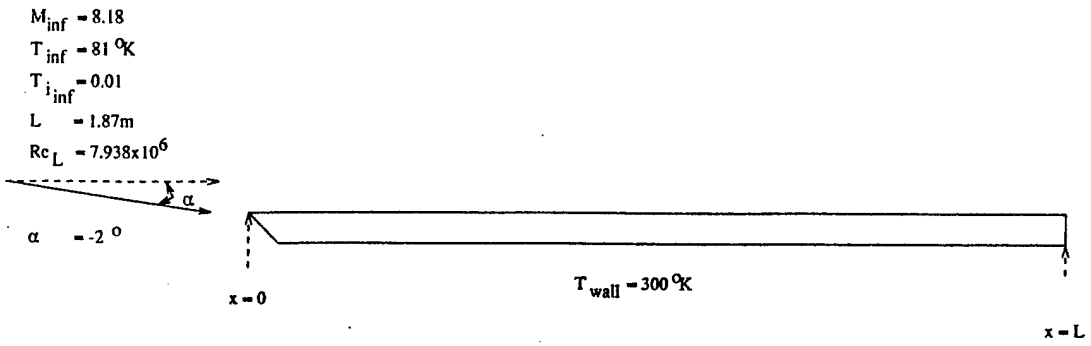

Fig. 52 Mach 8.18 Flat Plate w/Freestream Data

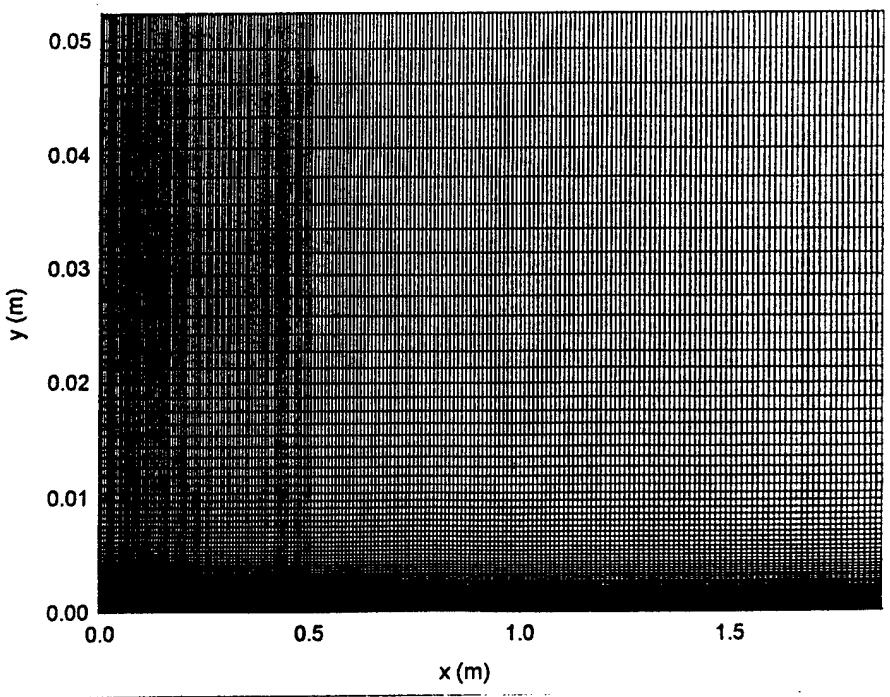

Fig. 53 Mach 8.18 Flat Plate CFD Grid Representation

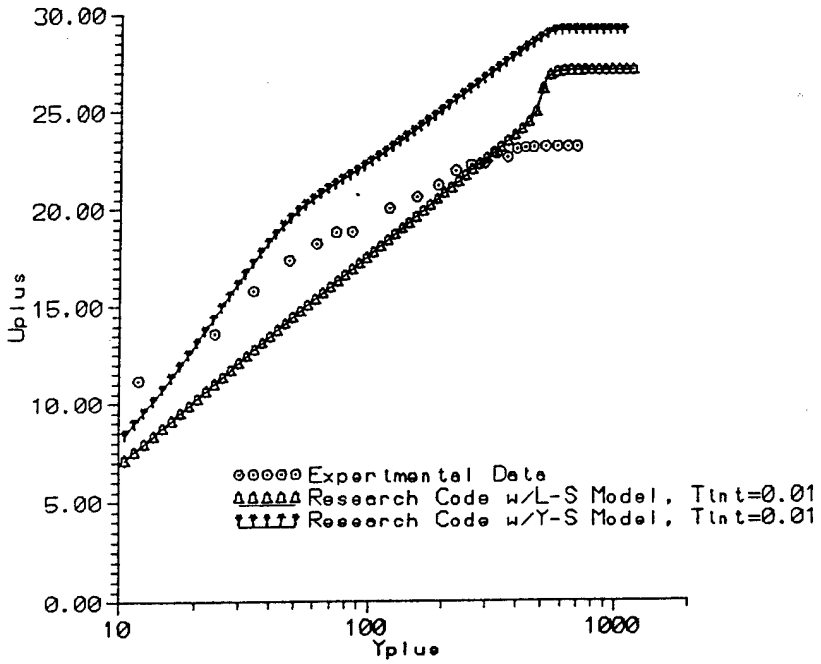

Fig. 54 Comparison of CFD Results with Experimental Data, Mach 8.18 Flat Plate, computed u_τ used in CFD

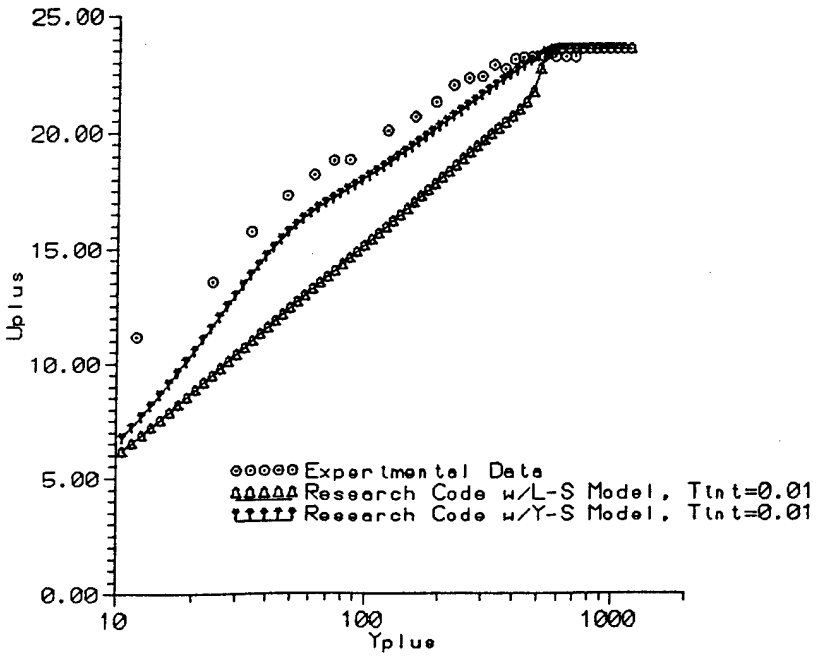

Fig. 55 Comparison of CFD Results with Experimental Data, Mach 8.18 Flat Plate, experimental u_τ used in CFD

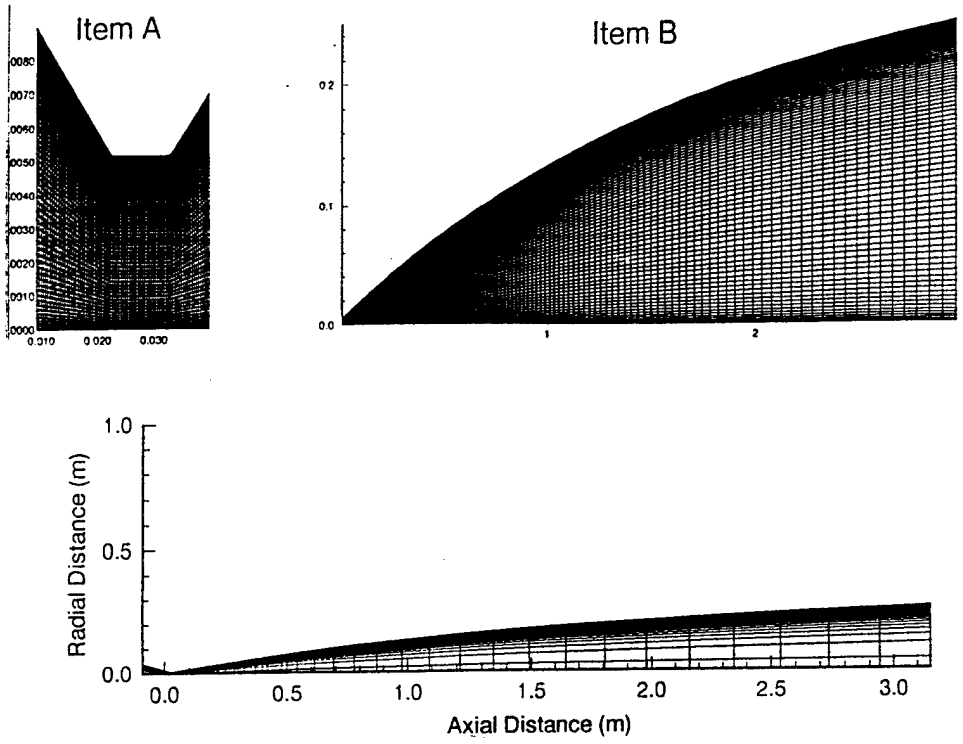

Fig. 56 Mach 12 Nozzle Split into Two Regions

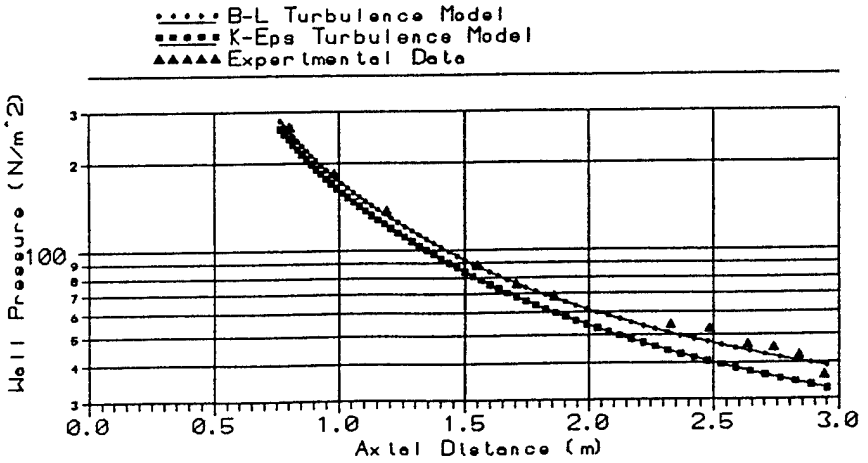

Fig. 57 Comparison of Static Wall Pressure for WL Mach 12 Nozzle

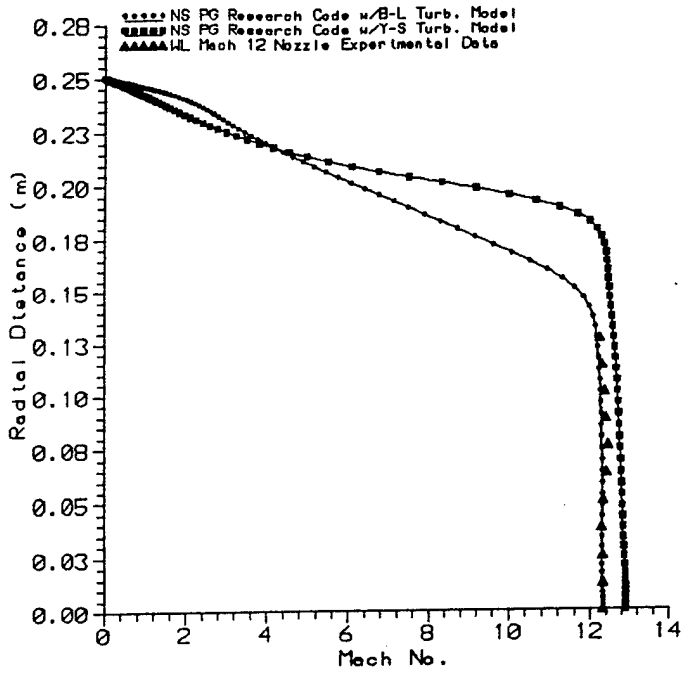

Fig. 58 Mach No. Comparison Near End of WL Mach 12 Nozzle

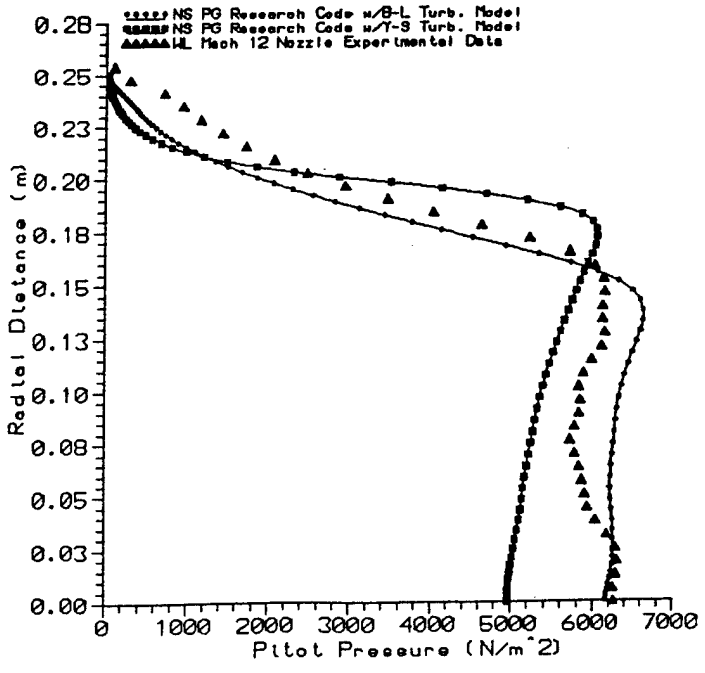

Fig. 59 Pitot Pressure Comparison Near End of WL Mach 12 Nozzle

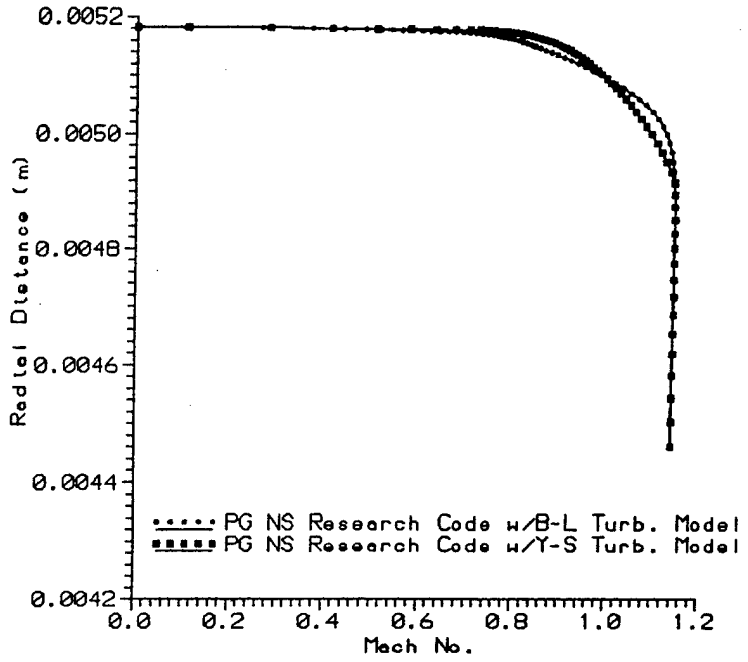

Fig. 60 Mach No. Comparison at WL Mach 12 Nozzle Throat Exit

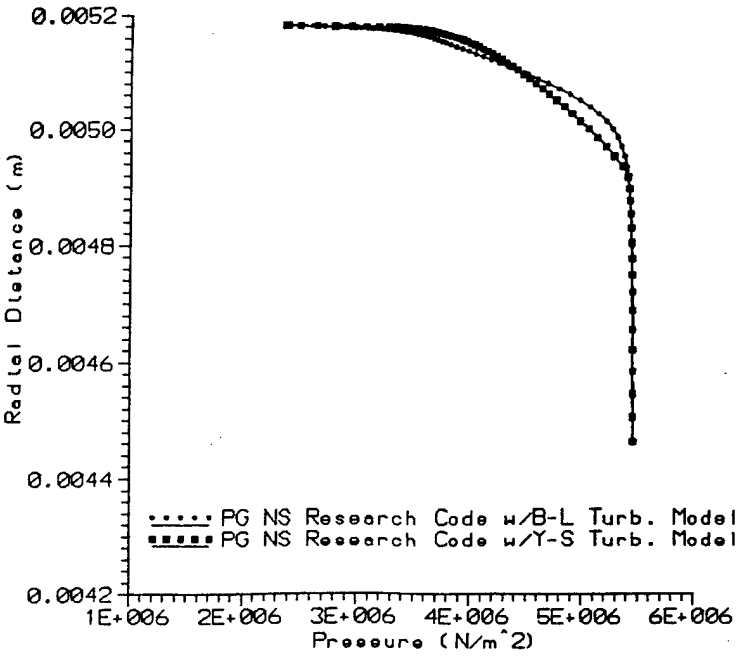

Fig. 61 Static Pressure Comparison at Mach 12 Nozzle Throat Exit

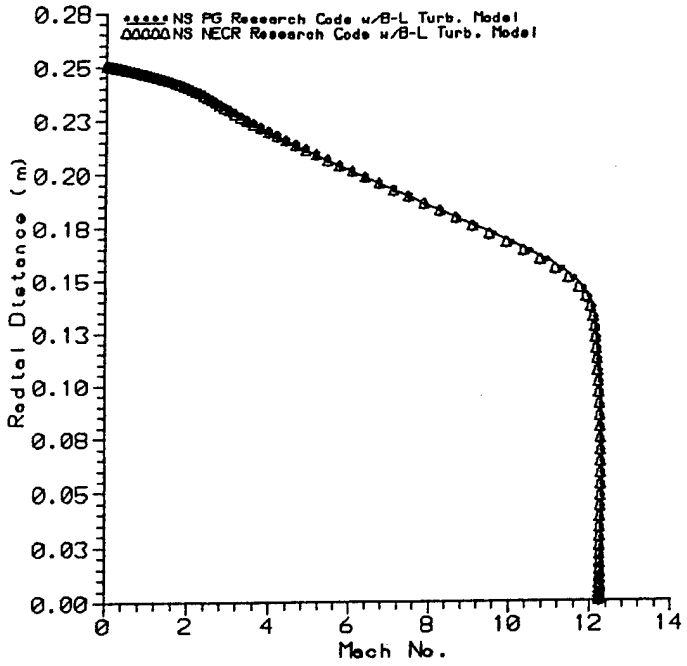

Fig. 62 CFD Mach No. Comparison Near End of Mach 12 Nozzle, B-L Model Used

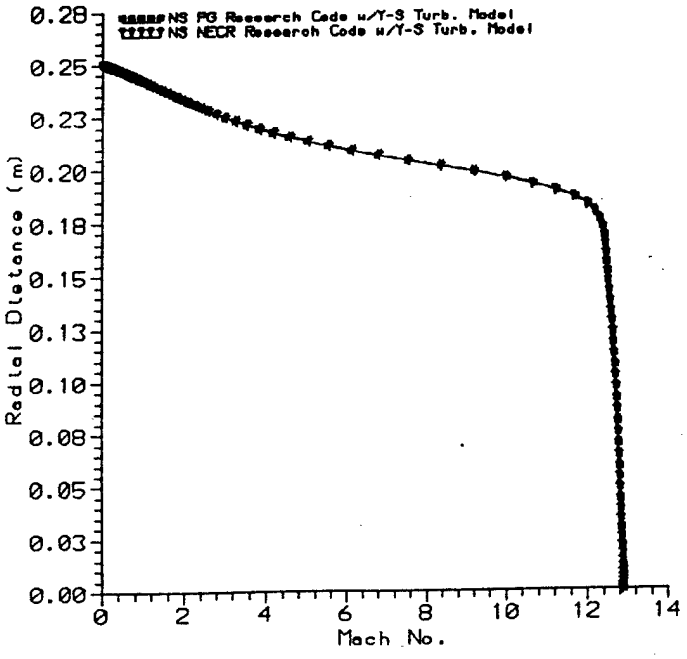

Fig. 63 CFD Mach No. Comparison Near End of Mach 12 Nozzle, Y-S Model Used

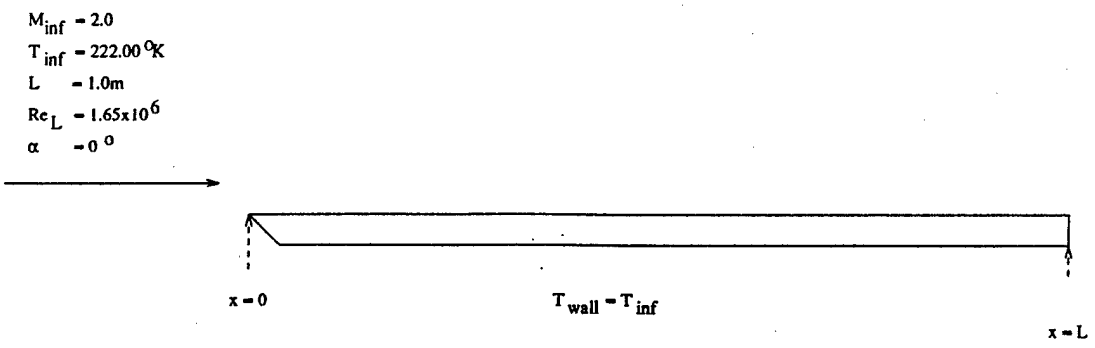

Fig. 64 Korte Mach 2.0 Flat Plate w/Freestream Data

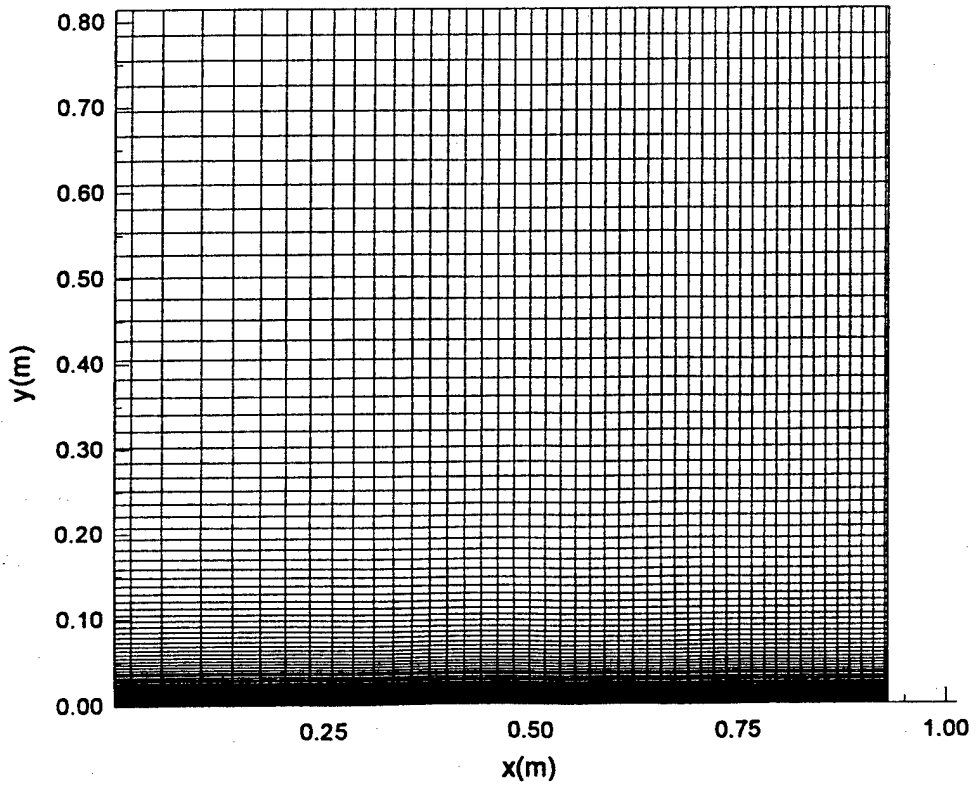

Fig. 65 Grid A, Korte Mach 2.0 Flat Plate

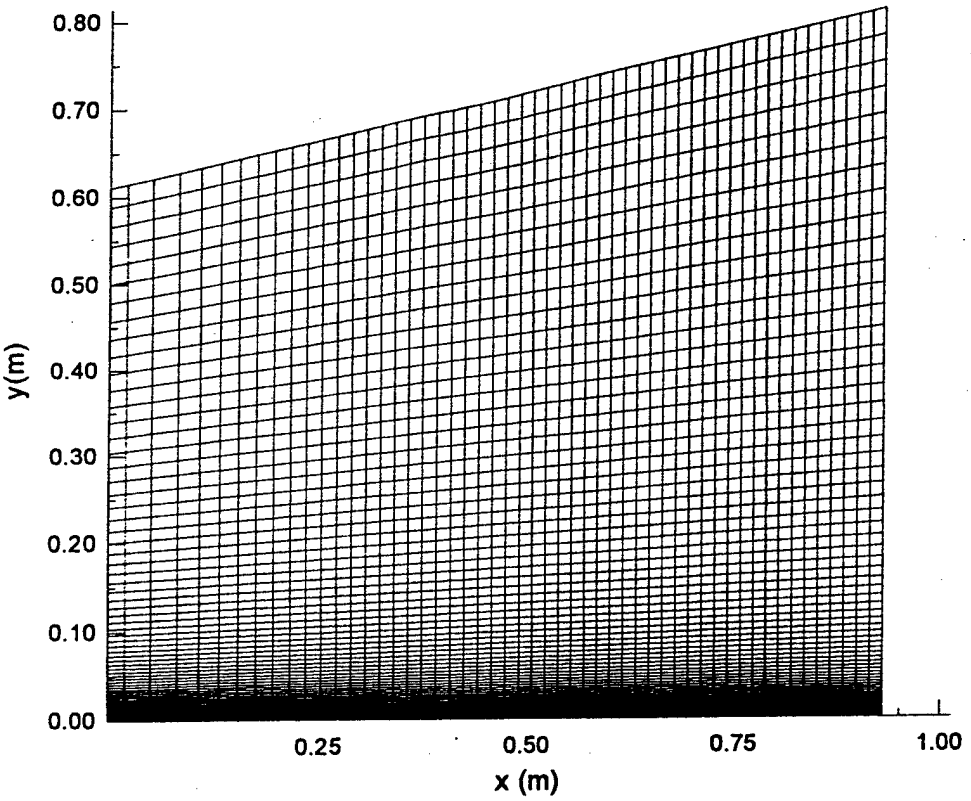

Fig. 66 Grid B, Korte Mach 2.0 Flat Plate

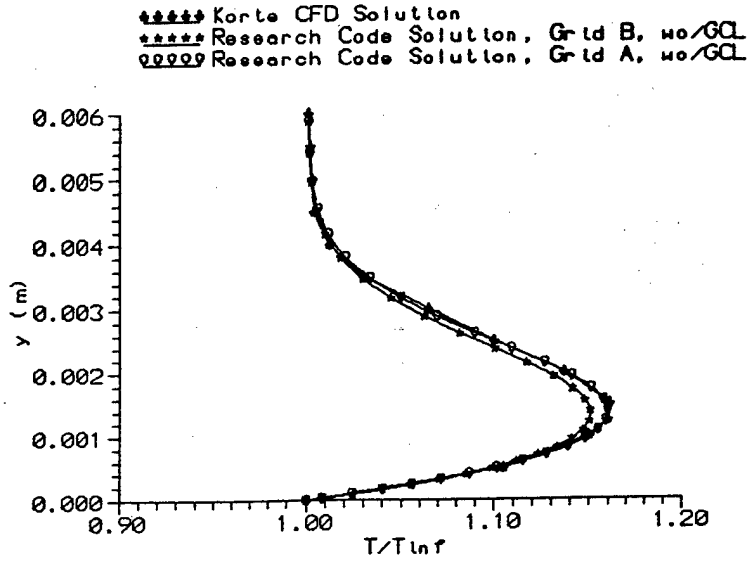

Fig. 67 Normalized Temperature vs. y, Korte Mach 2.0 Flat Plate, GCL Terms Not Included in Research Code

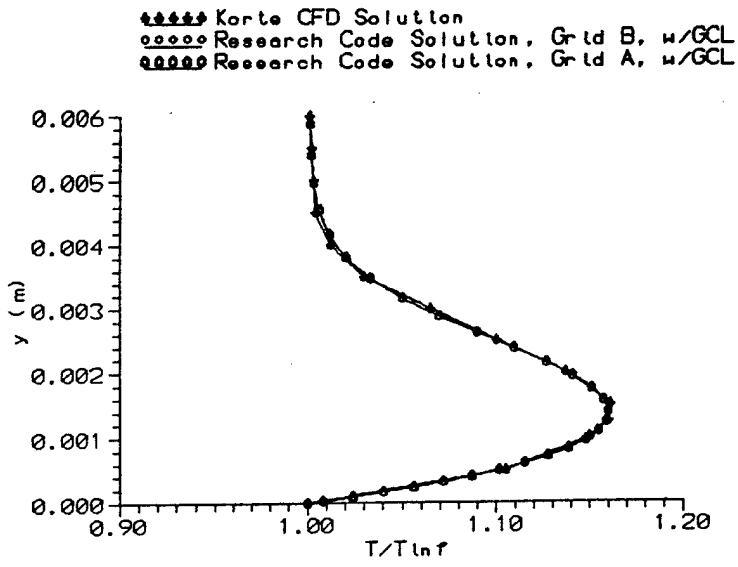

Fig. 68 Normalized Temperature vs. y, Korte Mach 2.0 Flat Plate, GCL Terms Included in Research Code

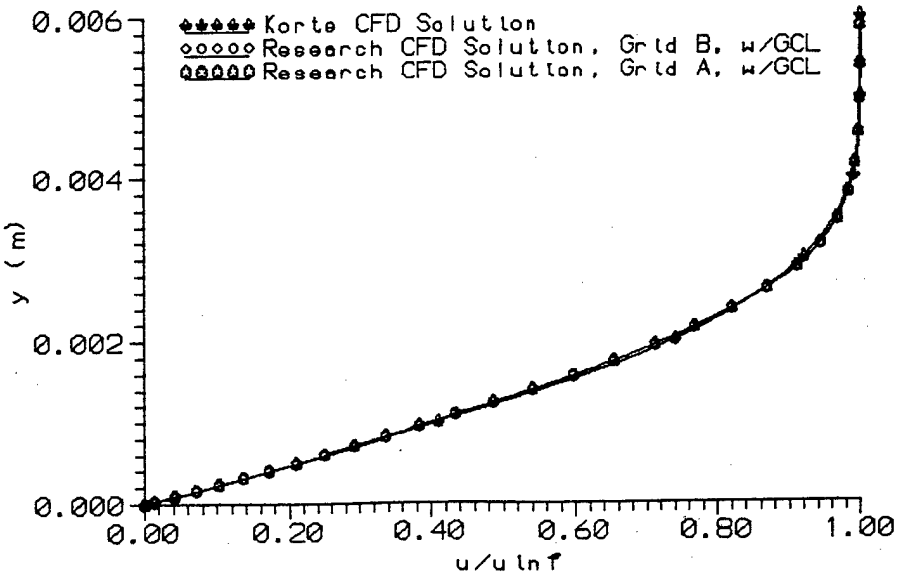

Fig. 69 Normalized U Component vs. y, Korte Mach 2.0 Flat Plate, GCL Terms Included in Research Code

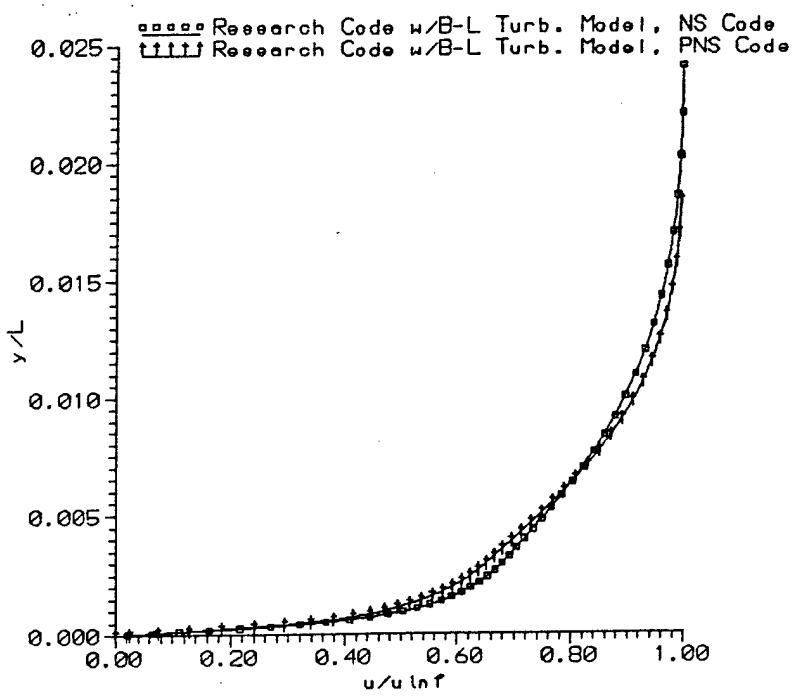

Fig. 70 CFD Comparison of Normalized U Component for Mach 2.0 Flat Plate, B-L Model Used

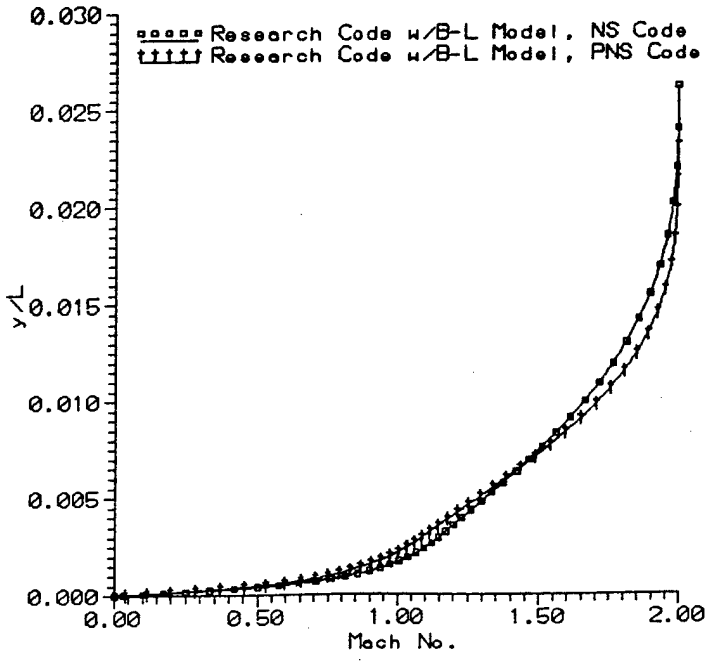

Fig. 71 CFD Comparison of Mach Number Profile for Mach 2.0 Flat Plate, B-L Model Used

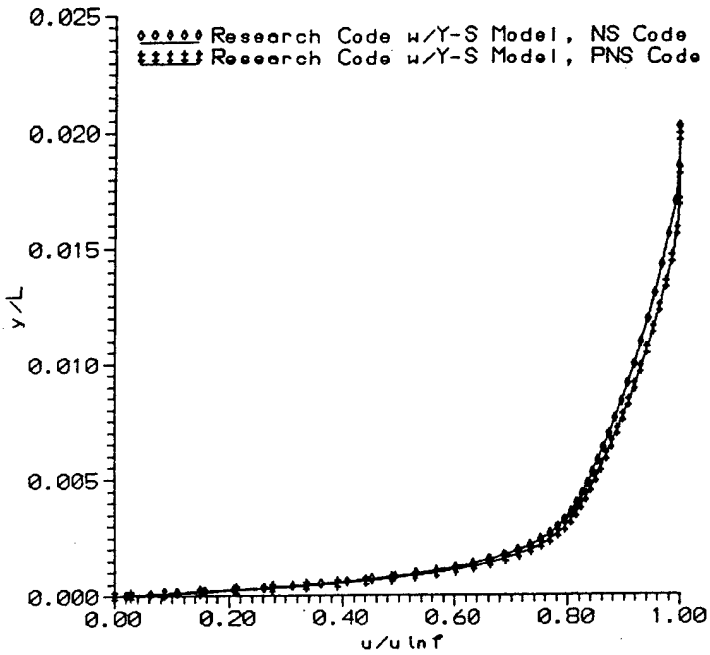

Fig. 72 CFD Comparison of Normalized U Component for Mach 2.0 Flat Plate, Y-S Model Used

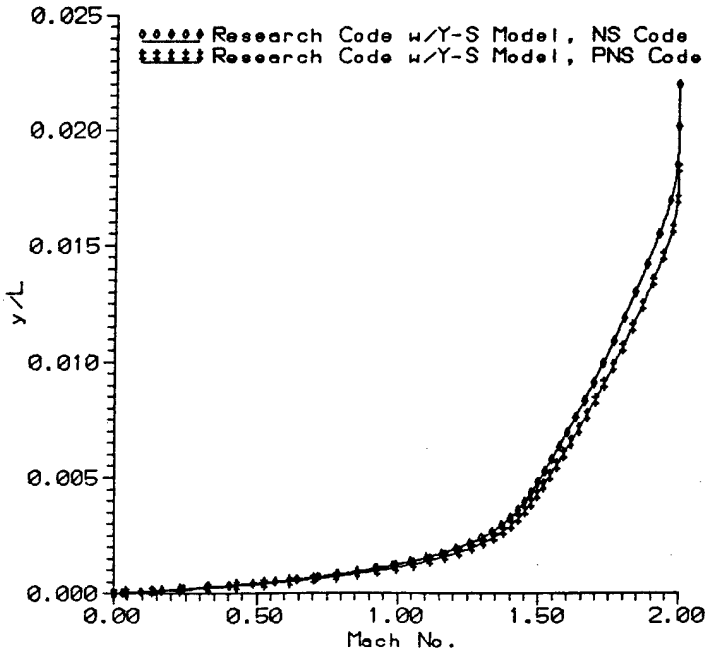

Fig. 73 CFD Comparison of Mach Number Profile for Mach 2.0 Flat Plate, Y-S Model Used

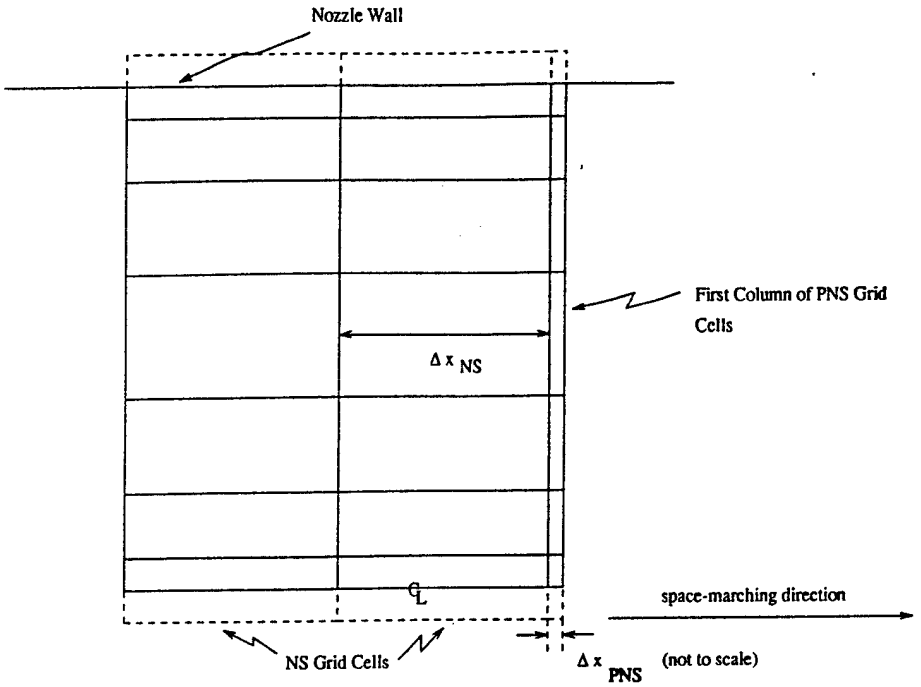

Fig. 74 Disparity in Grid Cell Size When Transitioning from NS Solution to PNS Inflow

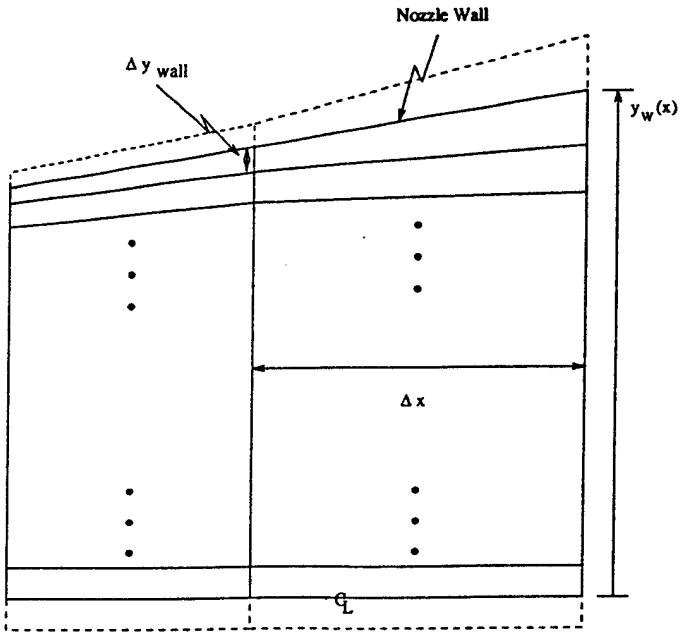

Fig. 75 Determination of Wall Spacing for WL Mach 12 Nozzle

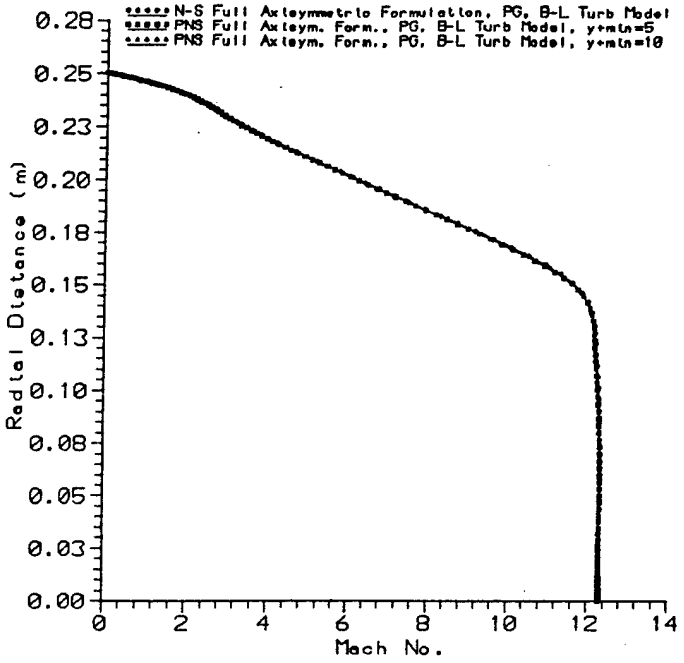

Fig. 76 CFD Mach No. Comparison Near Mach 12 Nozzle Exit (2.950 m)

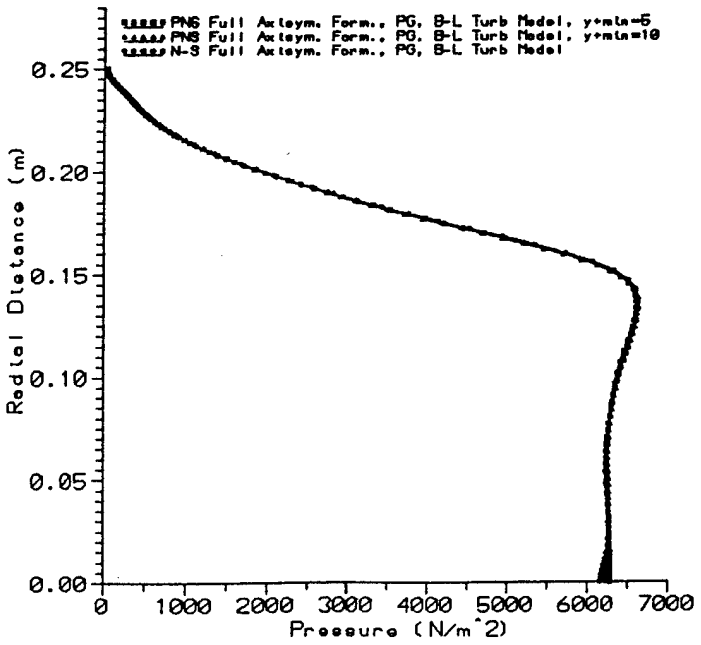

Fig. 77 CFD Pitot Pres. Comparison Near Mach 12 Nozzle Exit (2.950 m)

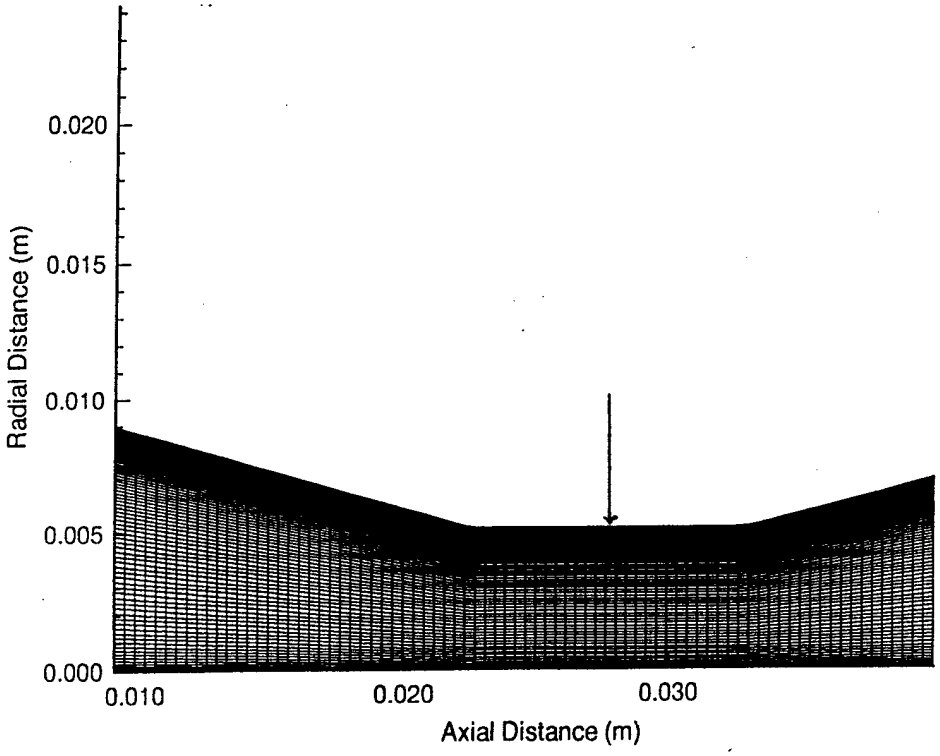

Fig. 78 Location of Original PNS Inflow Data in WL Mach 12 Nozzle

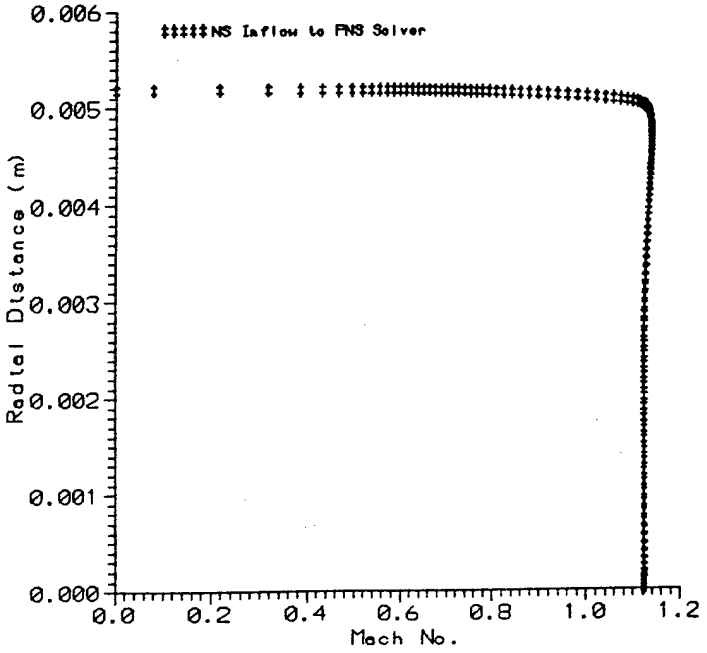

Fig. 79 Mach No. Profile at Initial PNS Inflow for Mach 12 Nozzle

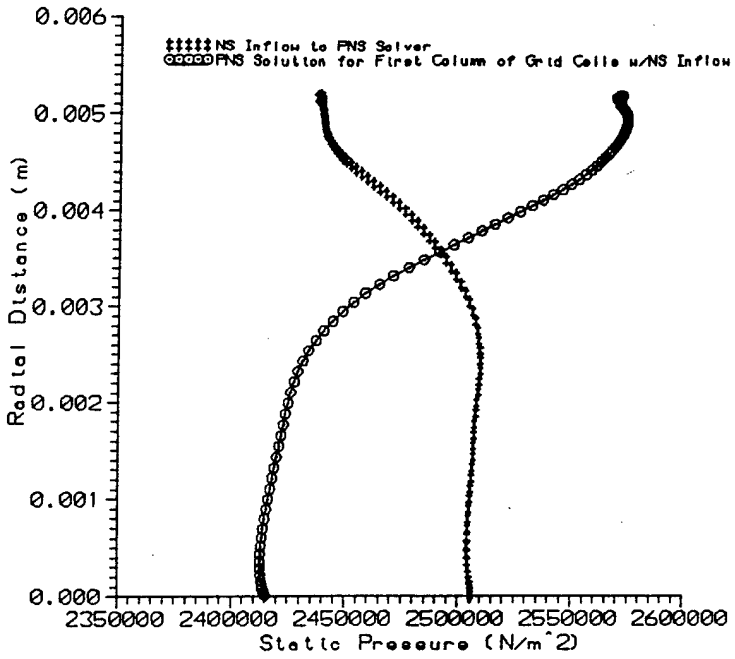

Fig. 80 Change in Pressure at PNS Inflow Due to Activation of Vigneron's Coefficient in Inviscid Core

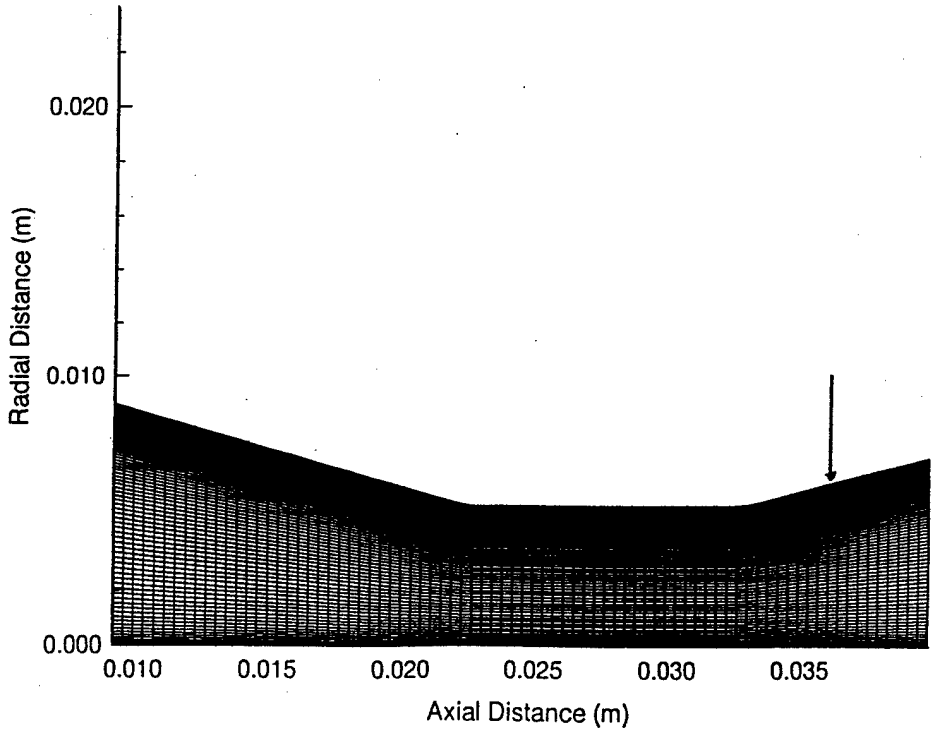

Fig. 81 Revised Location of PNS Inflow Data in WL Mach 12 Nozzle

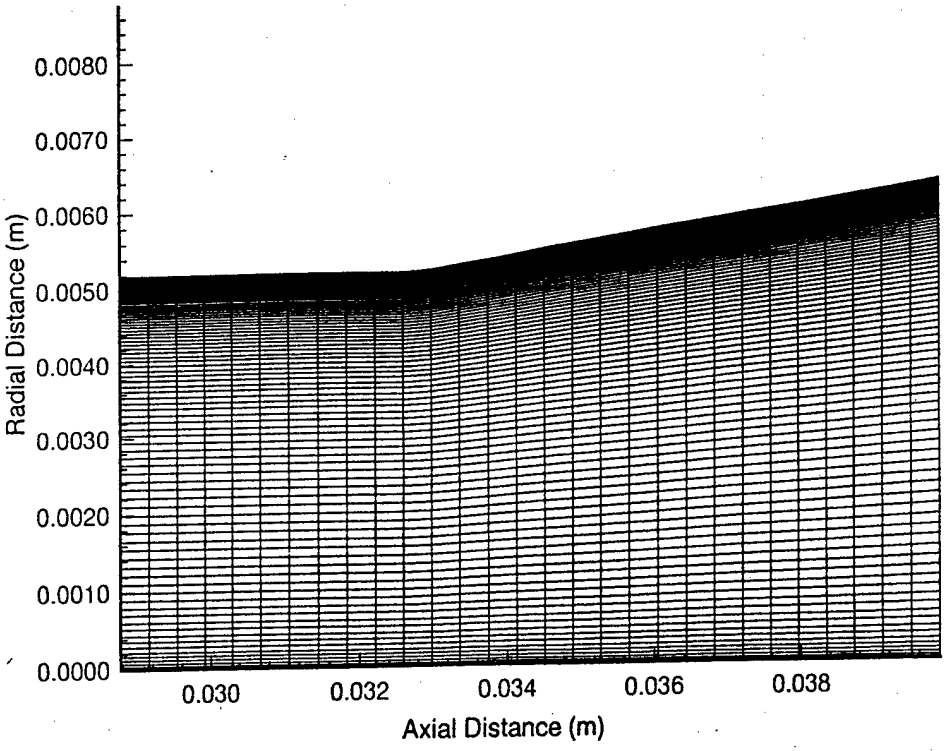

Fig. 82 Grid C, Mach 12 Nozzle Throat Region

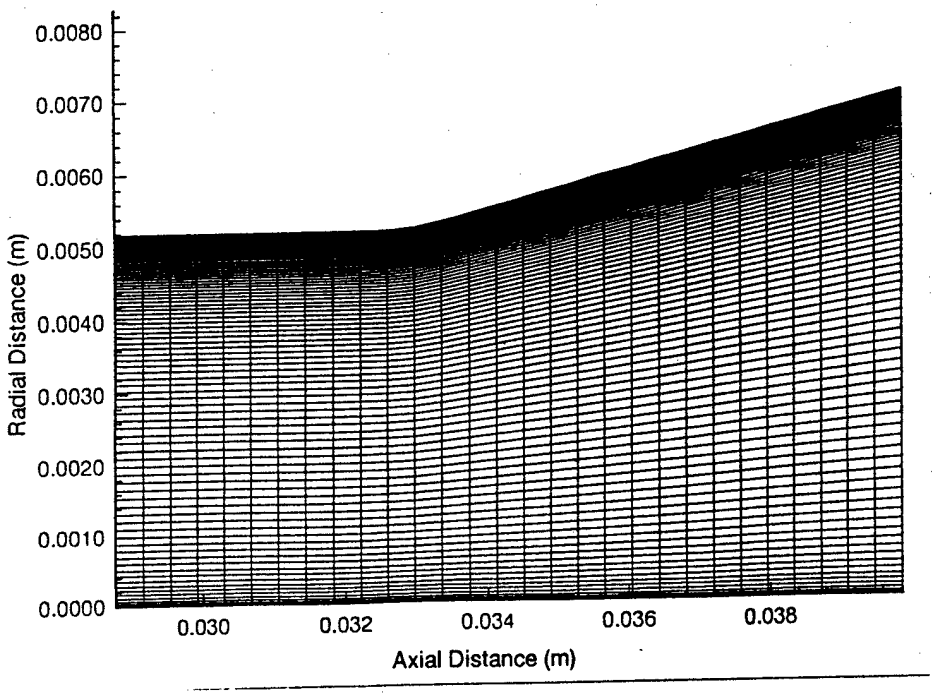

Fig. 83 Grid D, Mach 12 Nozzle Throat Region

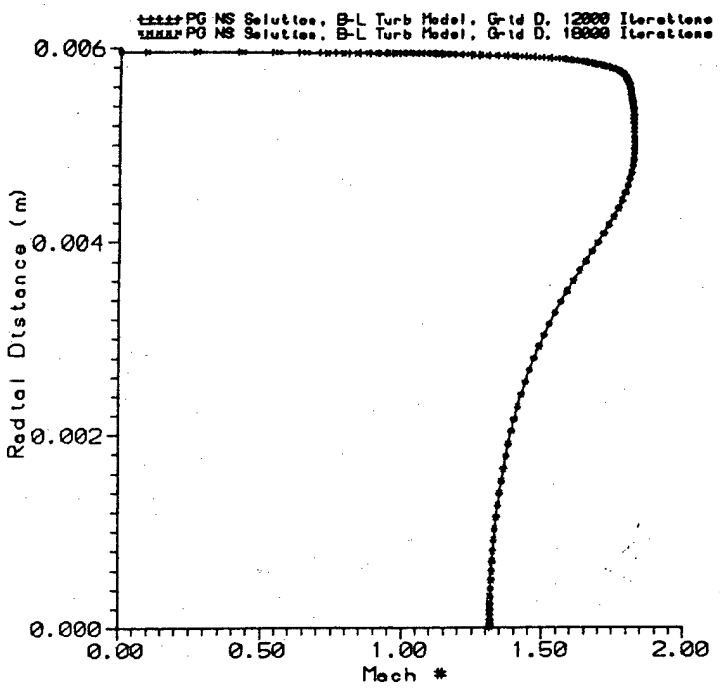

Fig. 84 Convergence of Mach No. Profile at New Location for PNS Inflow of Mach 12 Nozzle

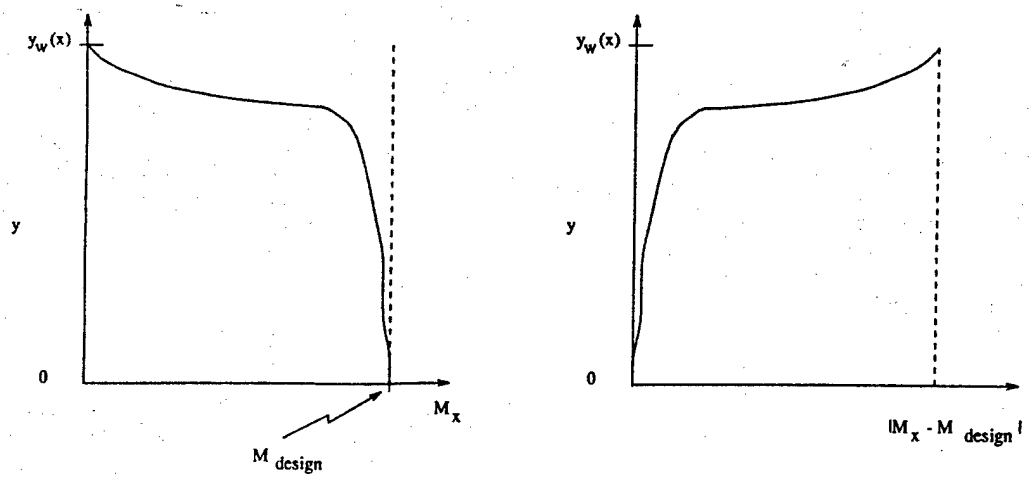

Fig. 85 Nozzle Exit Mach Error

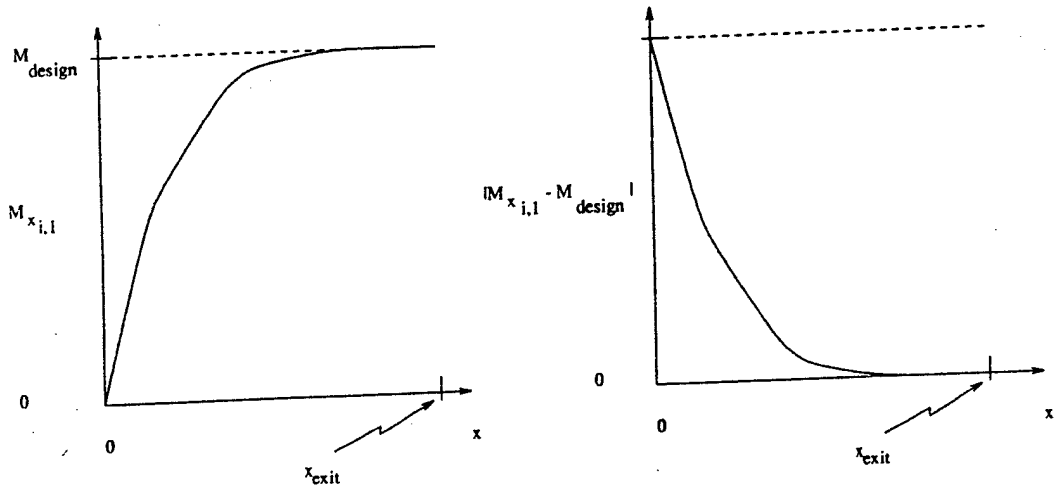

Fig. 86 Nozzle Centerline Mach Error

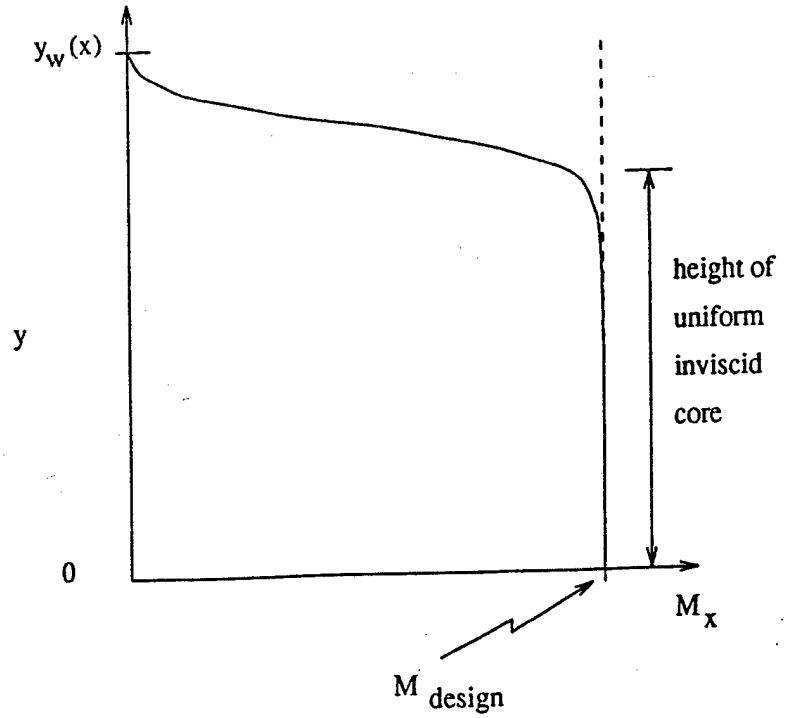

Fig. 87 Height of Inviscid Uniform Mach Core at Nozzle Exit

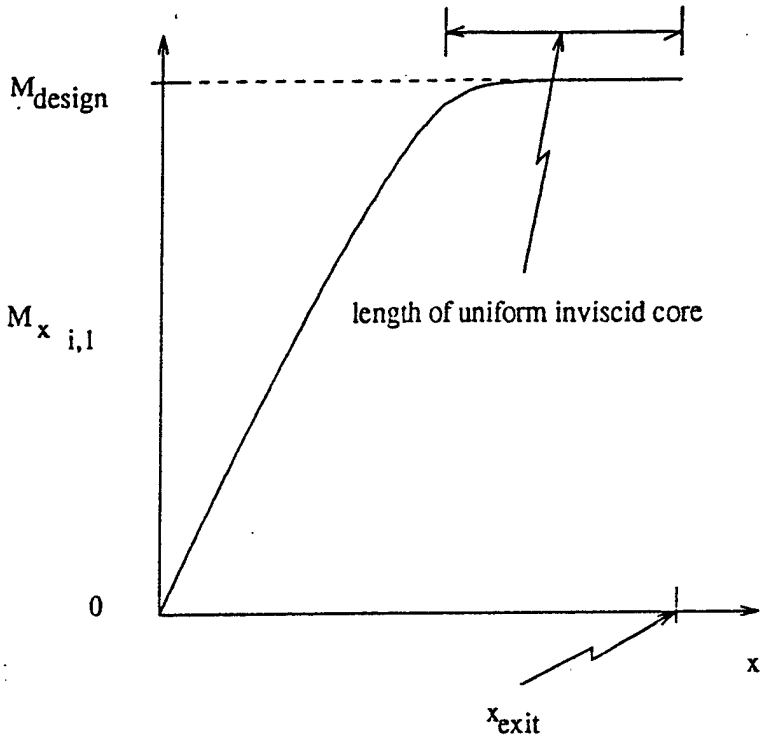

Fig. 88 Length of Inviscid Uniform Mach Core along Nozzle C/L

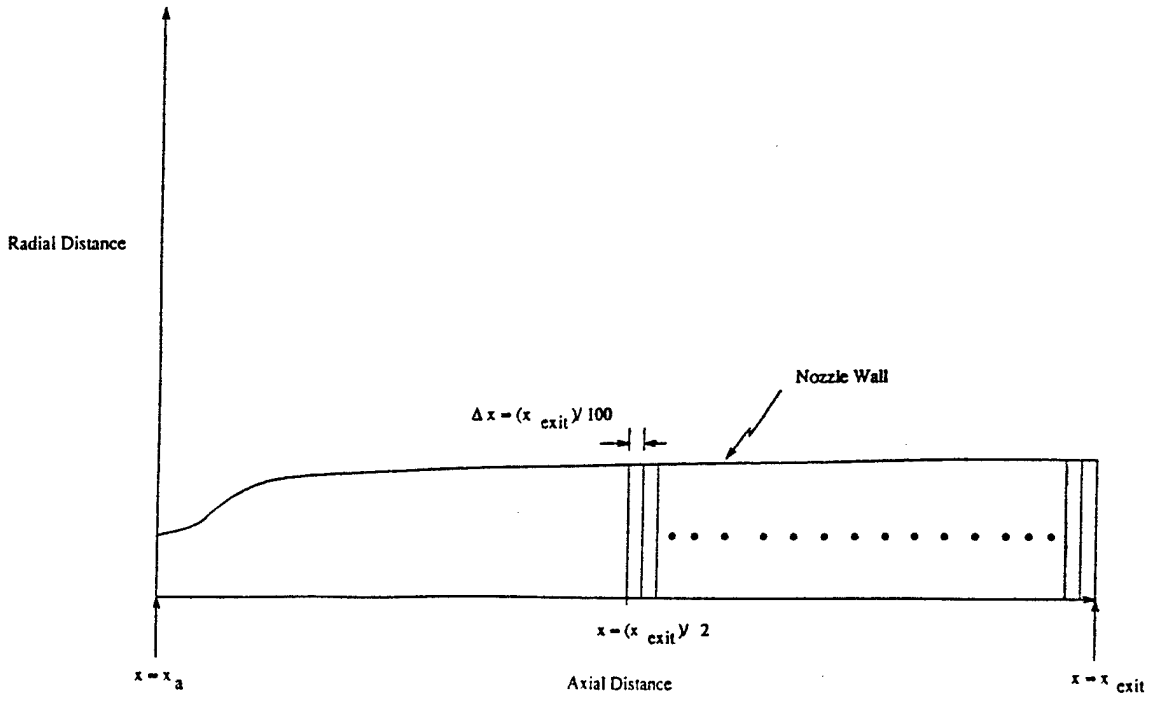

Fig. 89 Last Half of Nozzle Separated into 50 Equal Regions

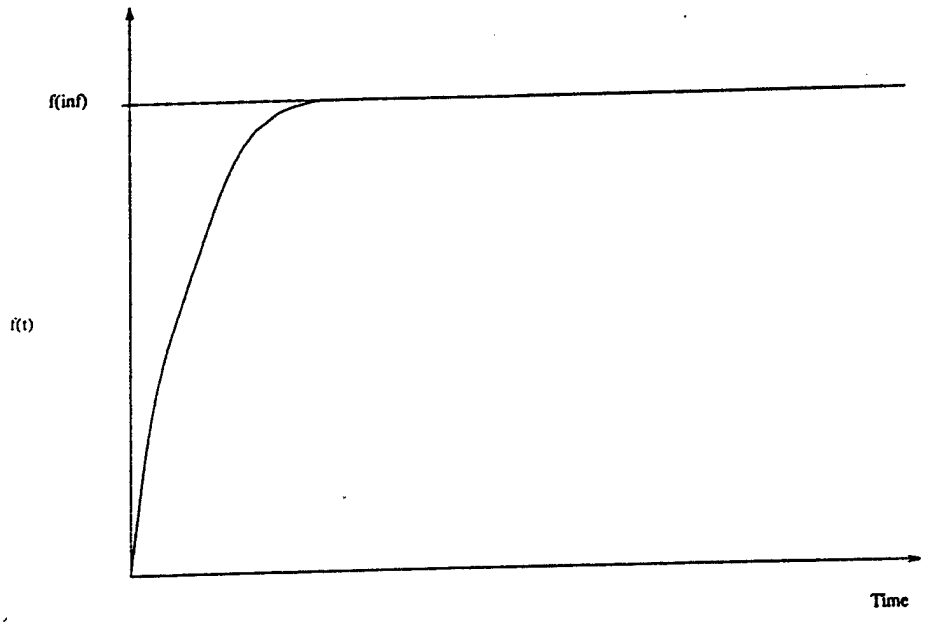

Fig. 90 Step Function Sketch

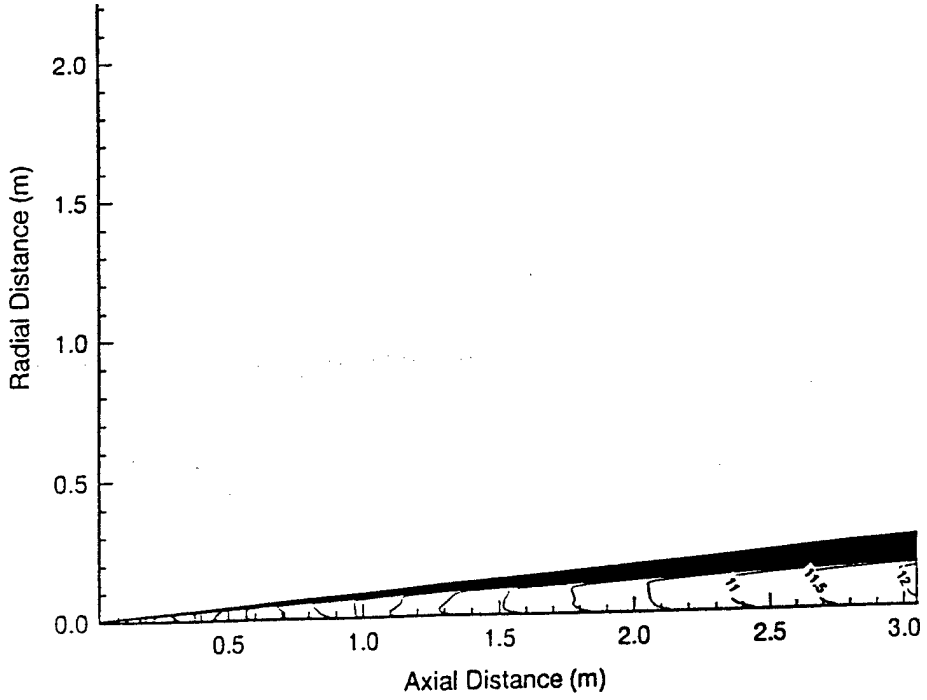

Fig. 91 Mach Contour Plot for Nozzle Design with Uniform Exit Mach Contour and Nonuniform Upstream Inviscid Core

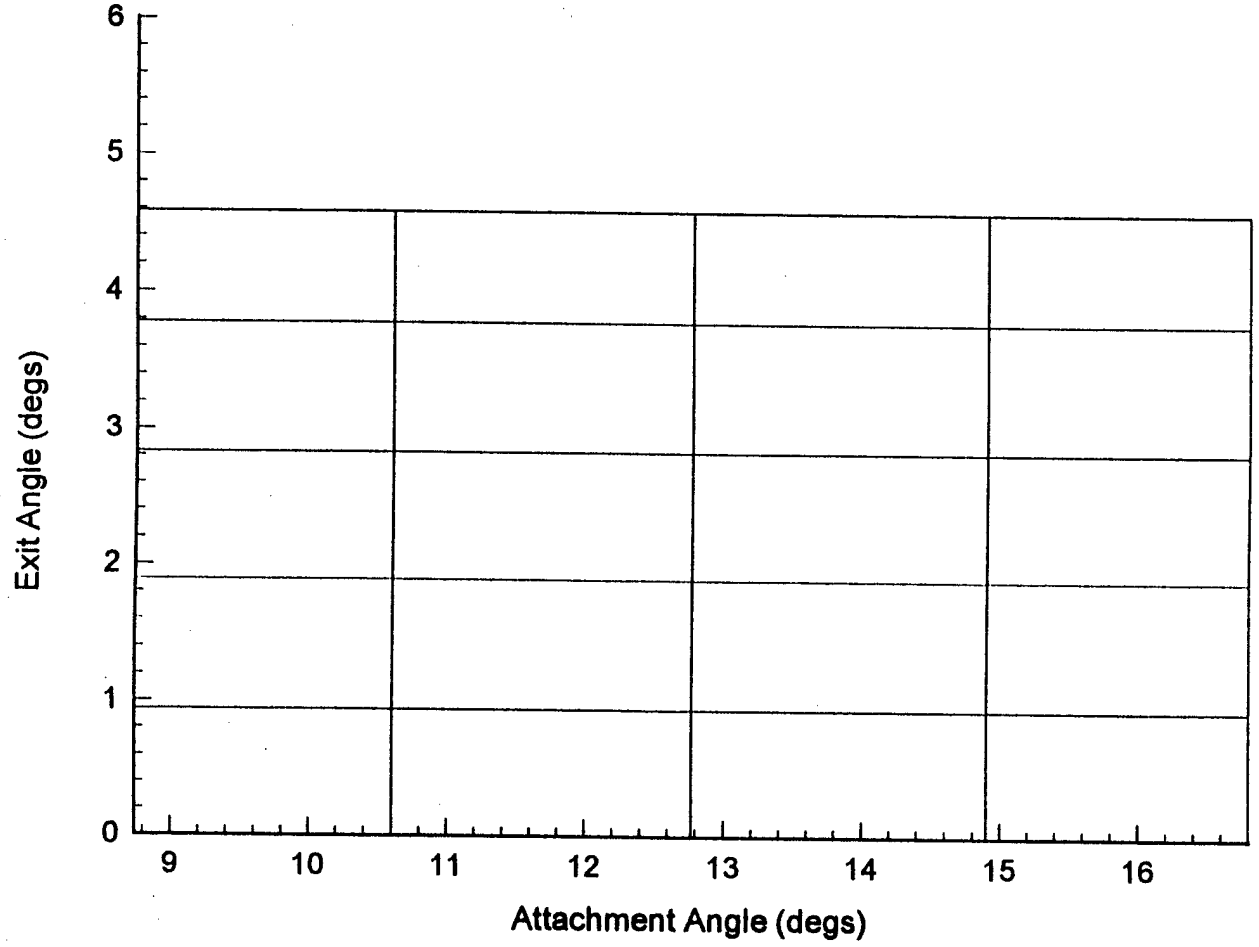

Fig. 92 Design Parameter Sampling Stencil for Response Surface Mapping

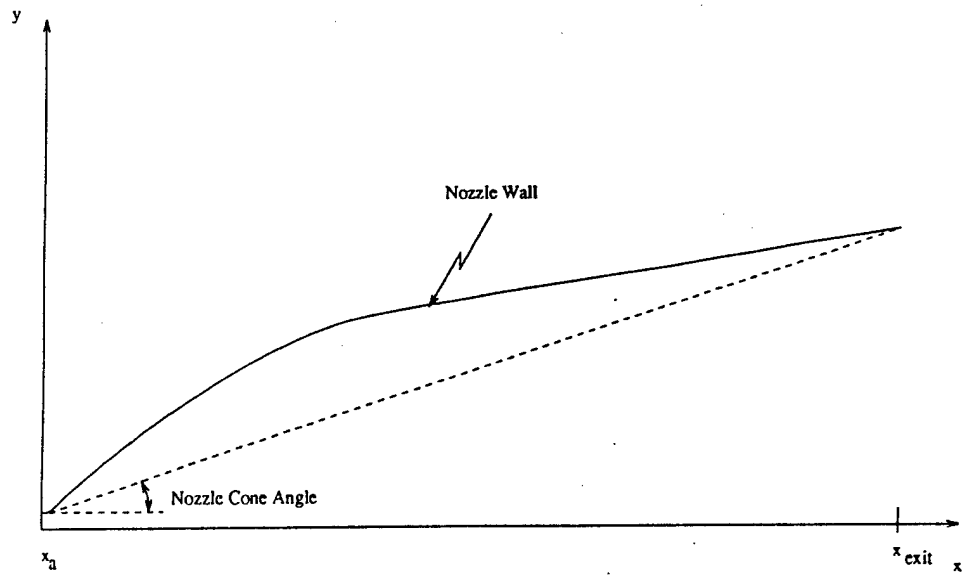

Fig. 93 Illustration of Nozzle Cone Angle

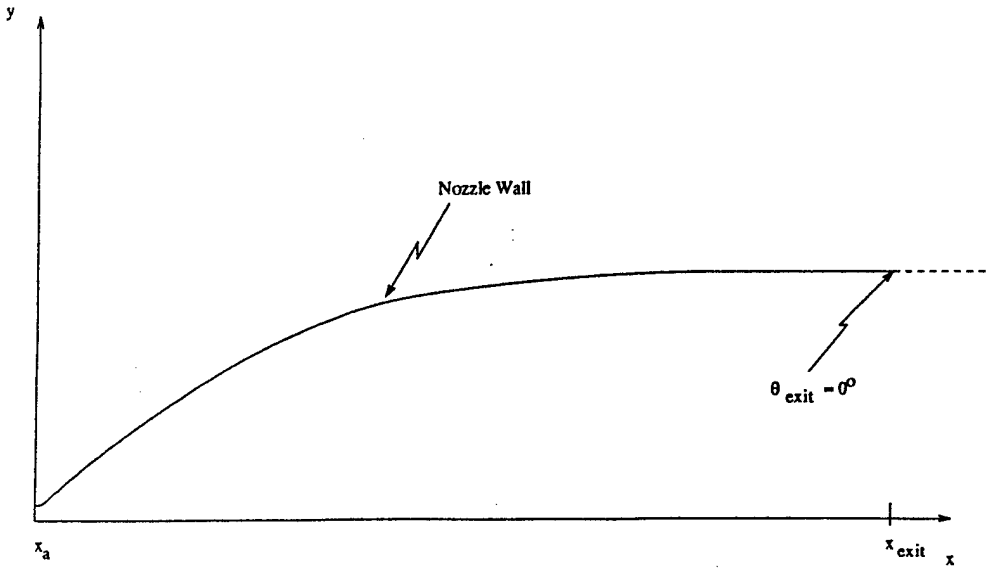

Fig. 94 Illustration of Nozzle Zero Exit Angle

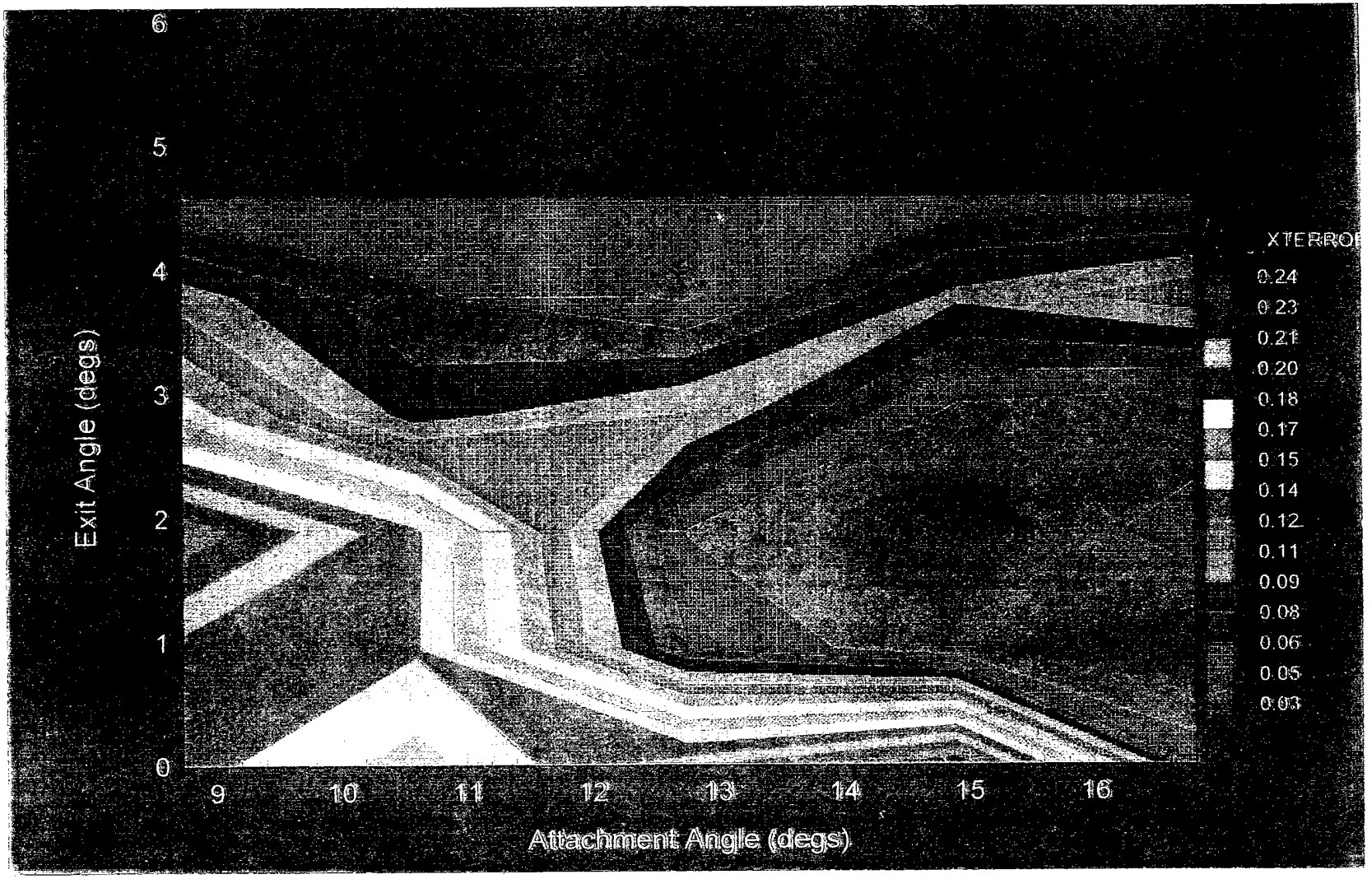

Fig. 95 Response Surface Map of Er Response Function, Mach 12 Nozzle

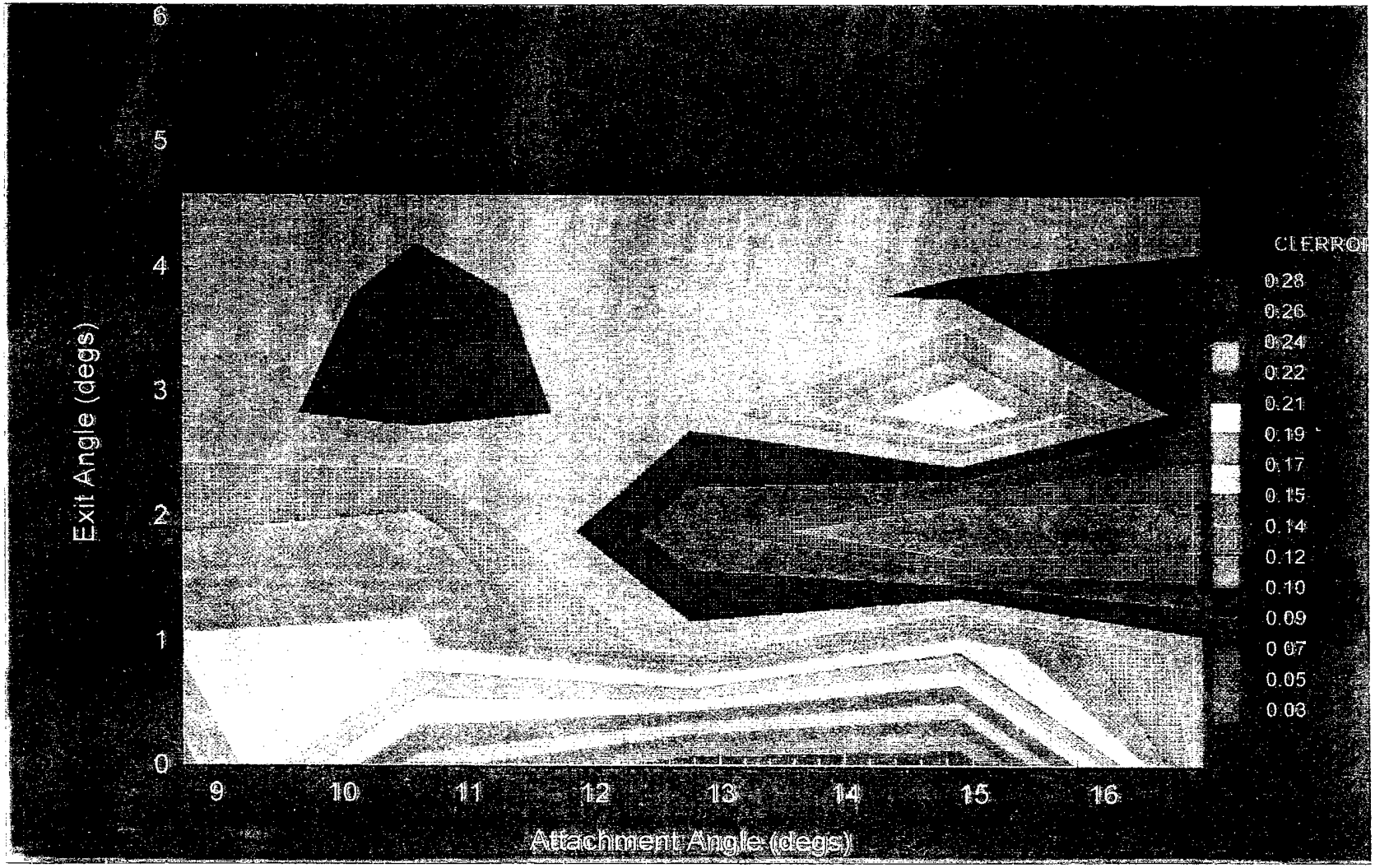

Fig. 96 Response Surface Map of Er1 Response Function, Mach 12 Nozzle

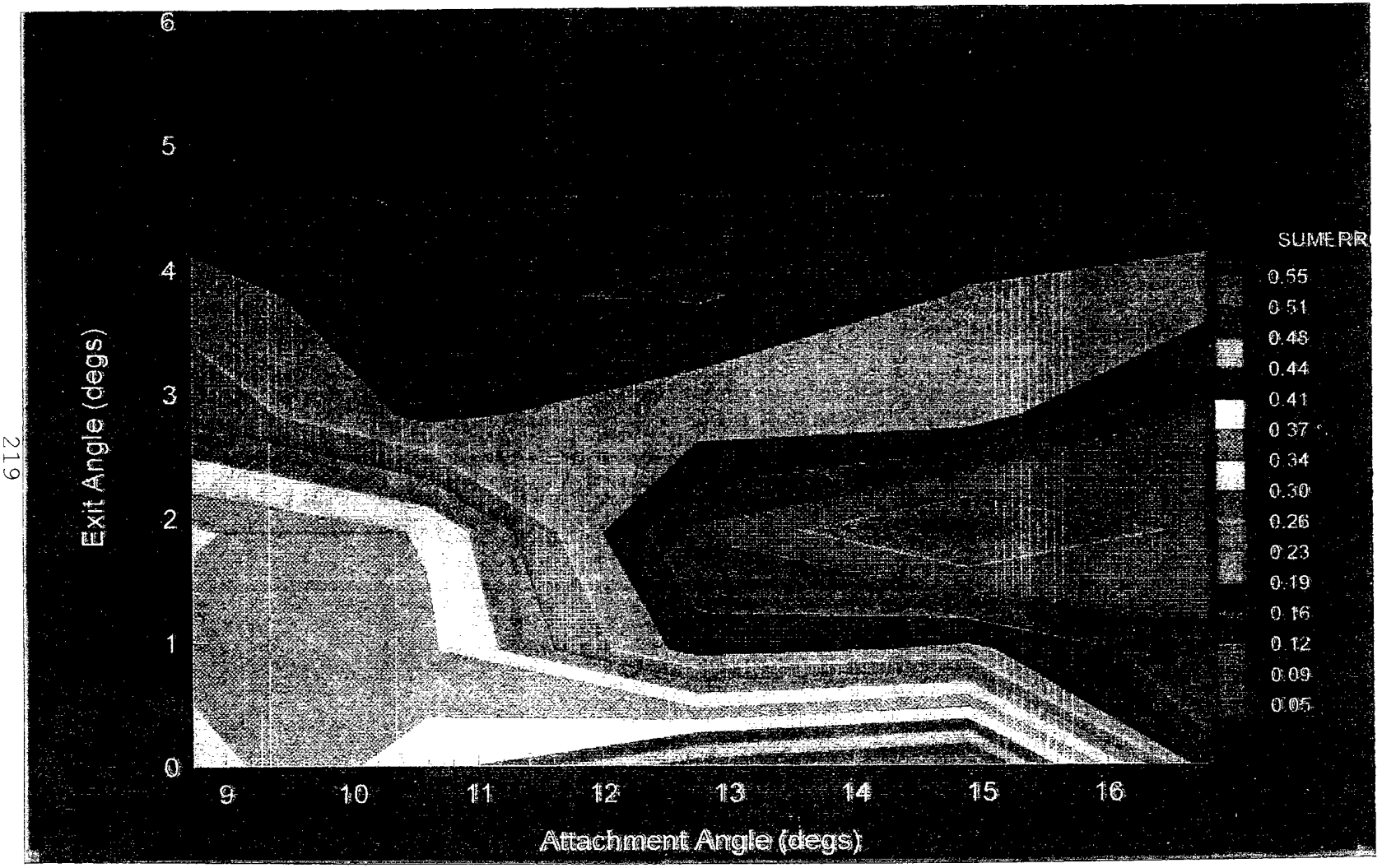

Fig. 97 Response Surface Map of Ert Response Function, Mach 12 Nozzle

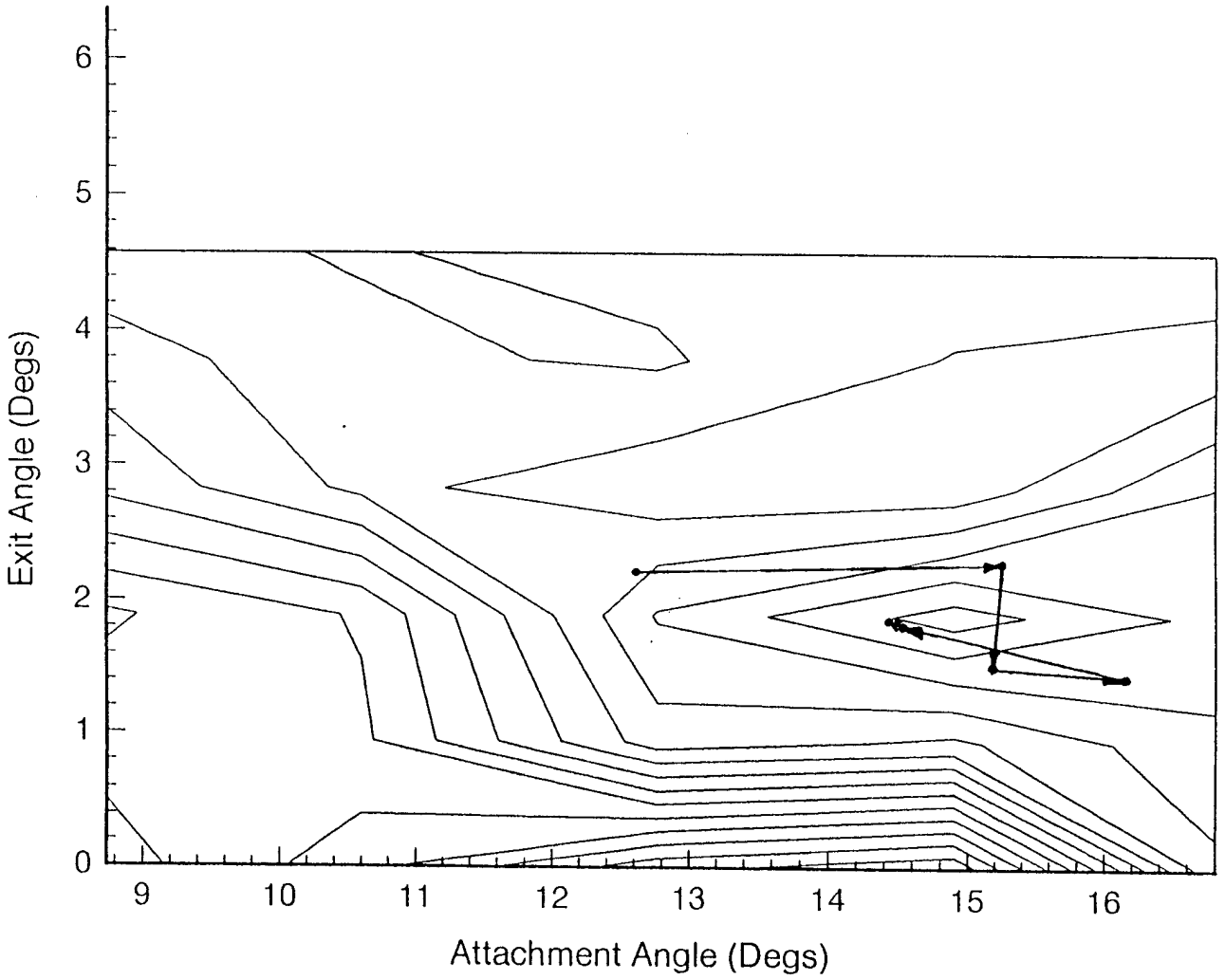

Fig. 98 Search Path Undertaken with Second-Order Search Method, Sect. 5.2.3.1

Fig. 99 Three Point Stencil Used in Korte LS Method, Sect. 5.2.4

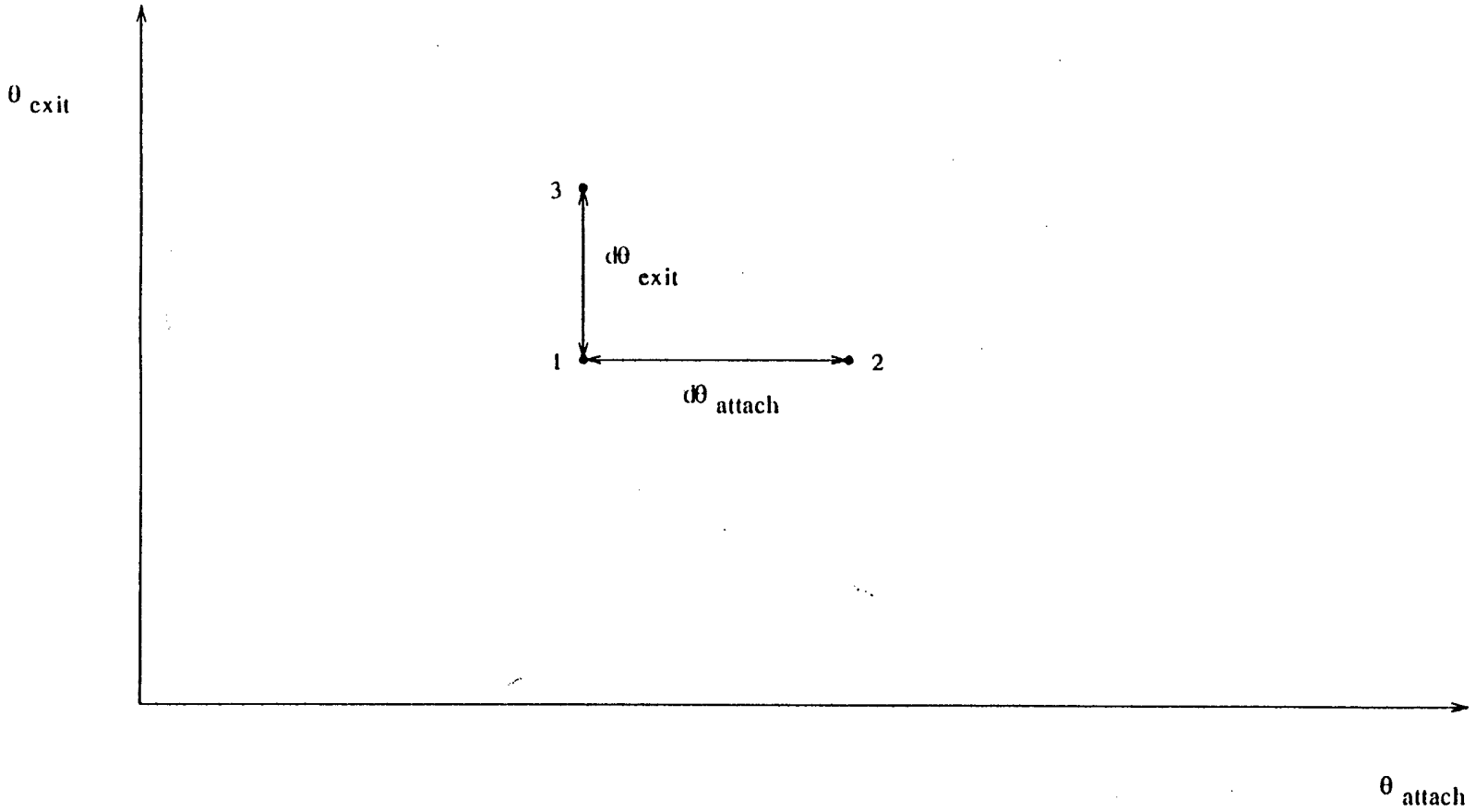

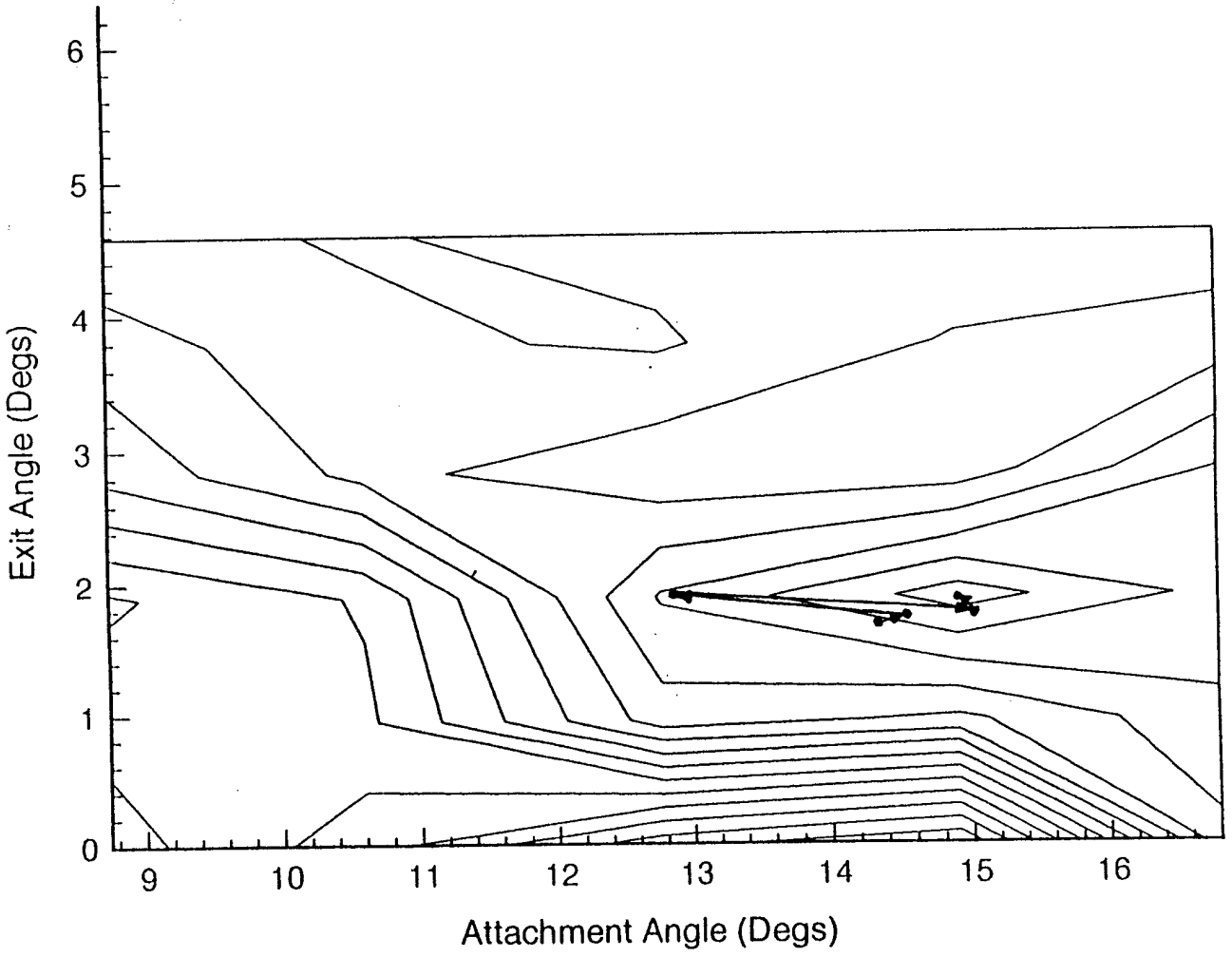

Fig. 100 Search Path Undertaken with Korte LS Method, Sect. 5.2.4.1

Fig. 101 Local Minima Detected when Using Korte LS Method

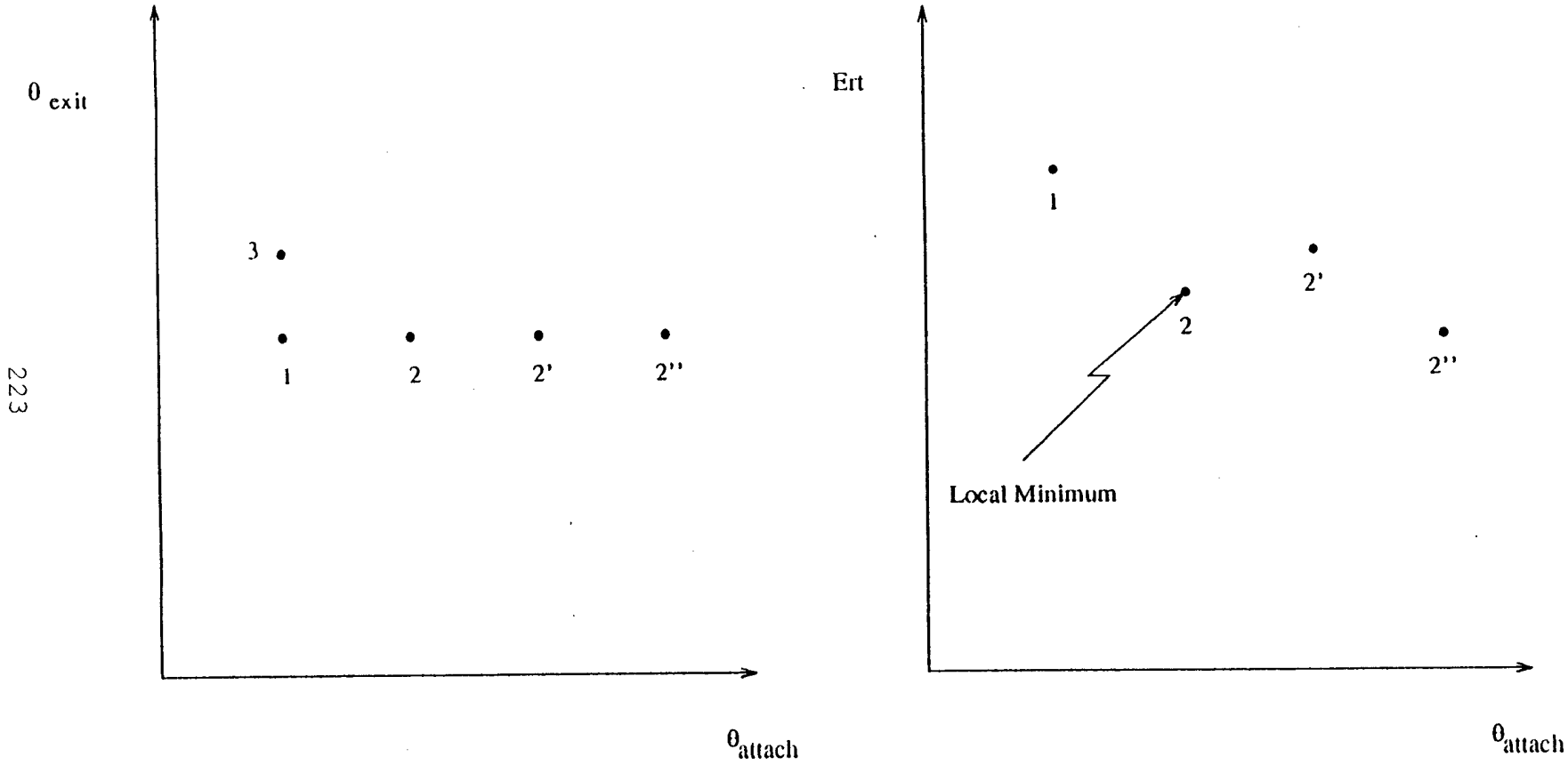

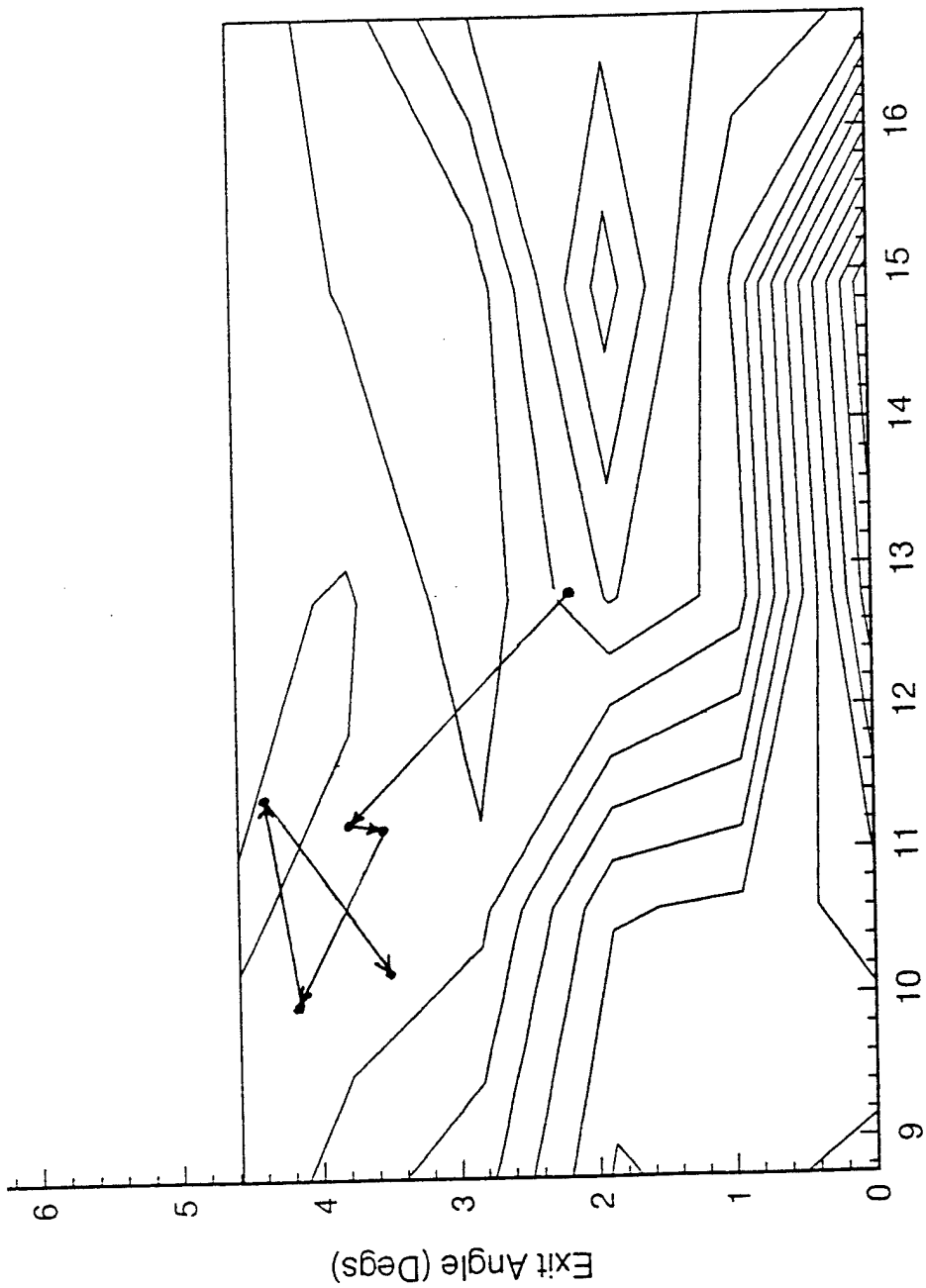

Fig. 102 Second Search Path Undertaken with Korte LS Method

Fig. 103 Inflection Point on Response Surface in Direction of Steepest Descent

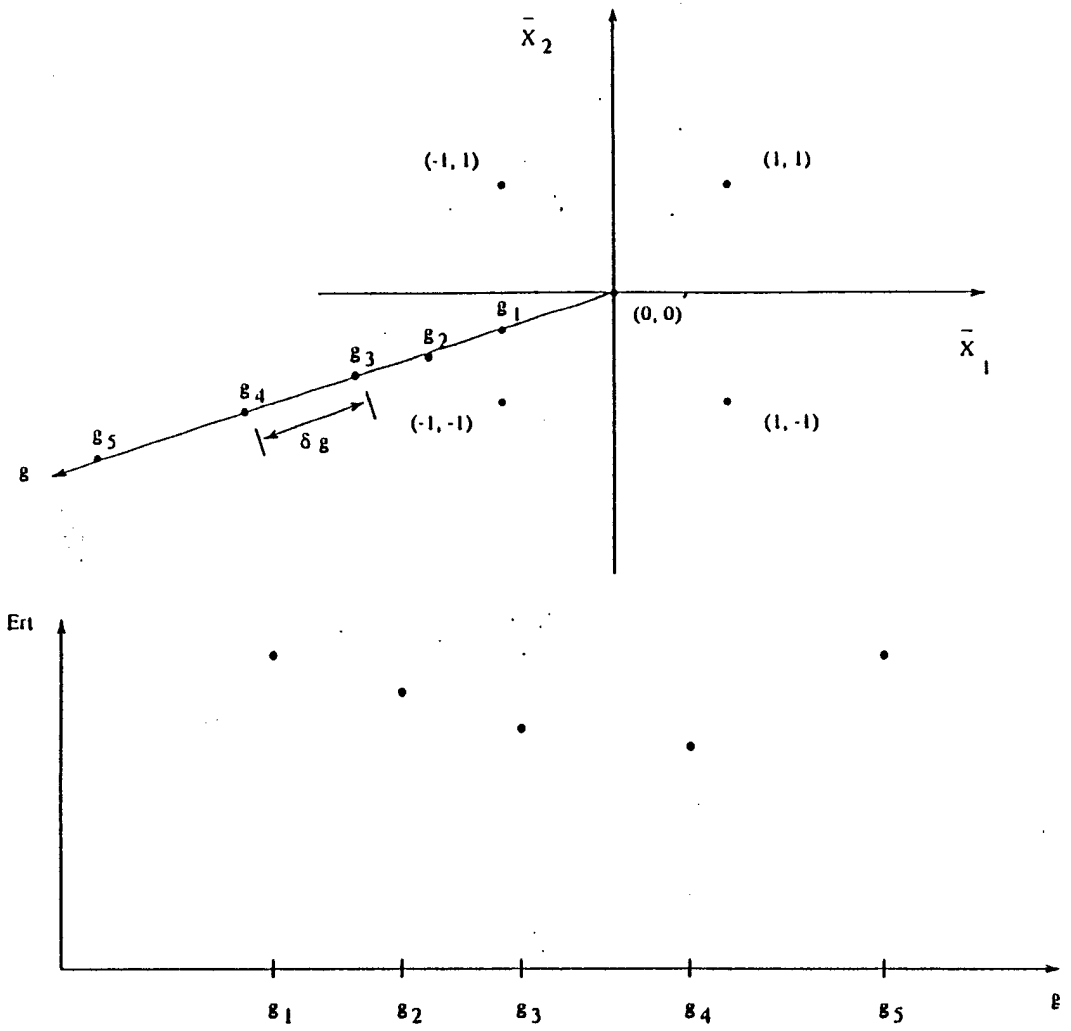

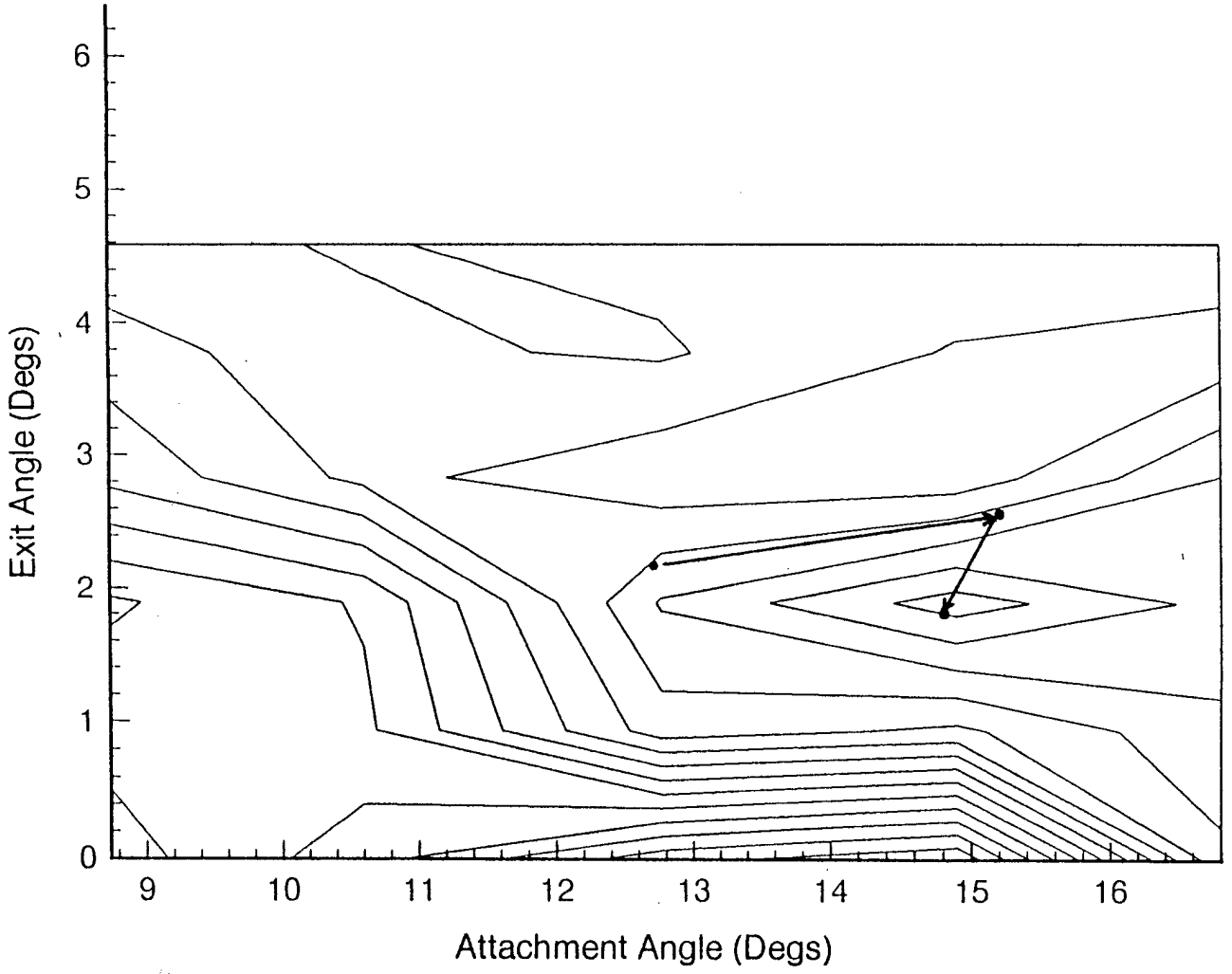

Fig. 104 Search Path Undertaken with Steepest Descent Method, Sect. 5.2.5.1

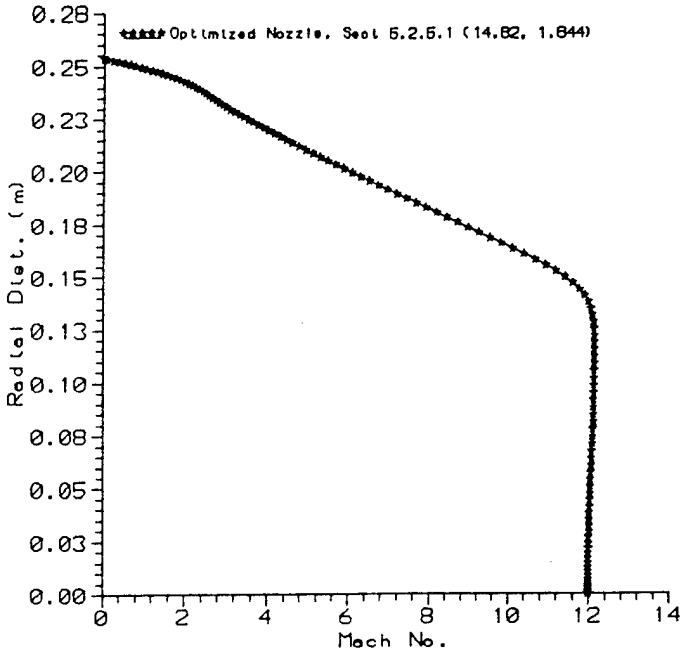

Fig. 105 Exit Mach Number Profile vs. Radial Distance for Optimized Nozzle Obtained Using Steepest Descent Method, Sect. 5.2.5.1

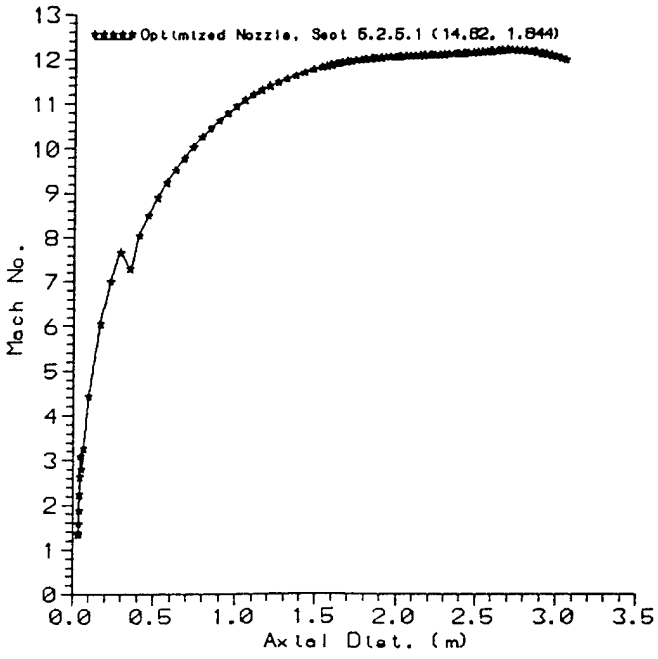

Fig. 106 C/L Mach Number Profile vs. Axial Distance for Optimized Nozzle Obtained Using Steepest Descent Method, Sect. 5.2.5.1

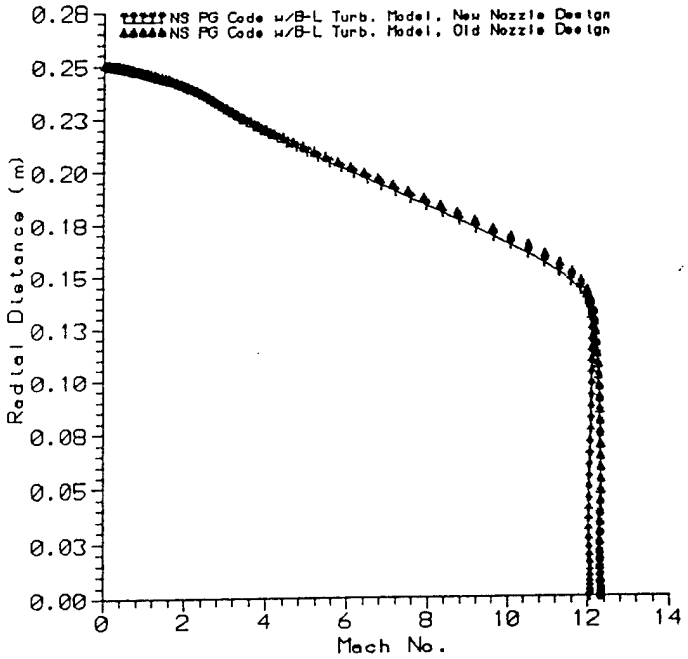

Fig. 107 Mach No. Comparison Near End of New and Old Nozzle Designs (2.950 m)

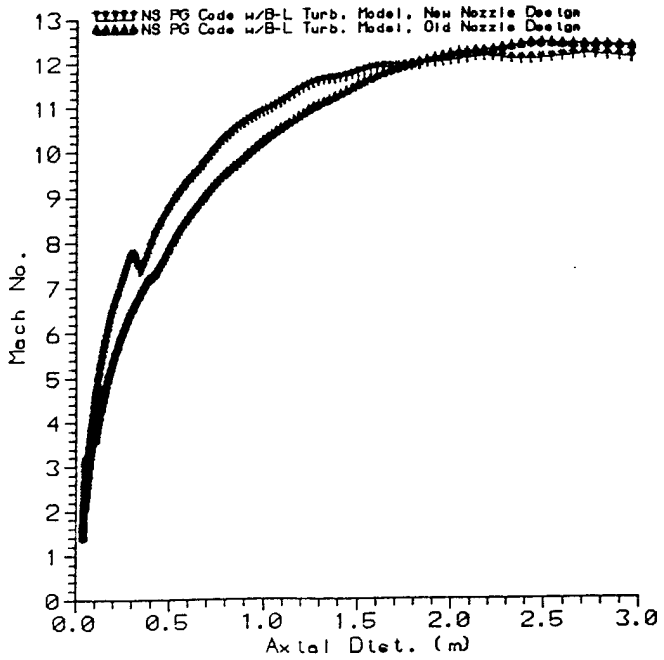

Fig. 108 Mach No. Comparison Along C/L of New and Old Nozzle Designs

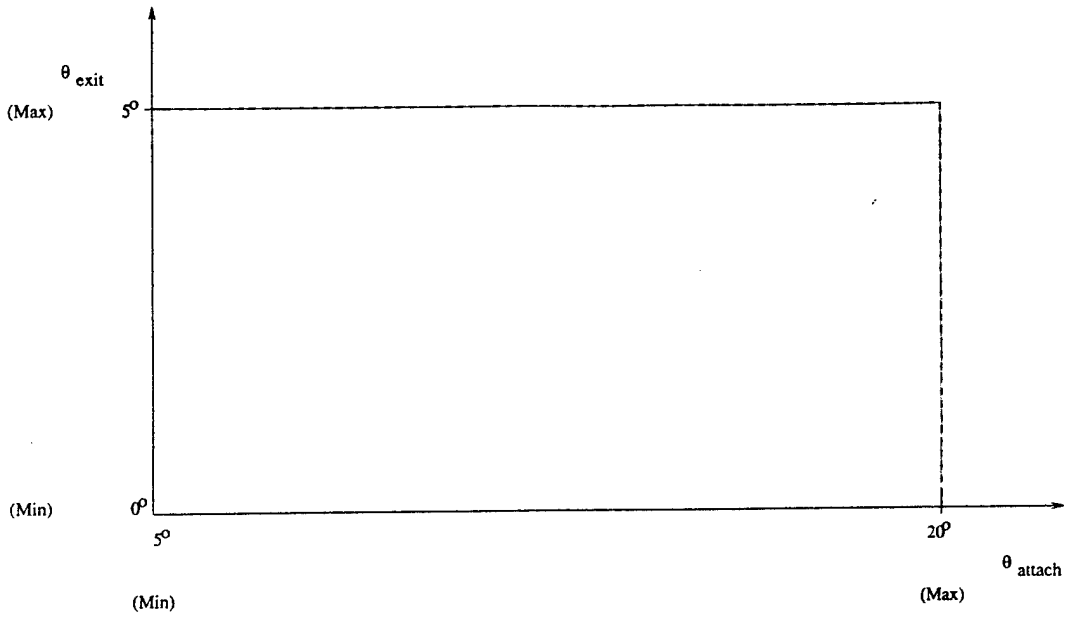

Fig. 109 Mach 12 Nozzle Sampling Coordinate Limits

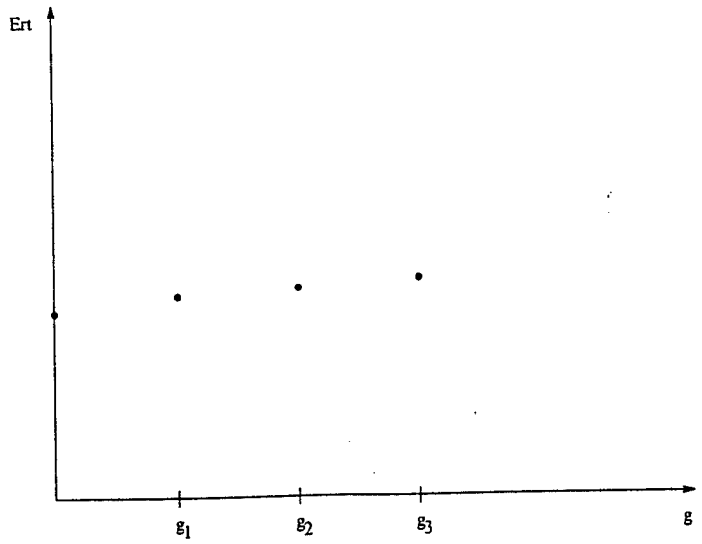

Fig. 110 Response Function Increasing In Calculated Direction of Steepest Descent

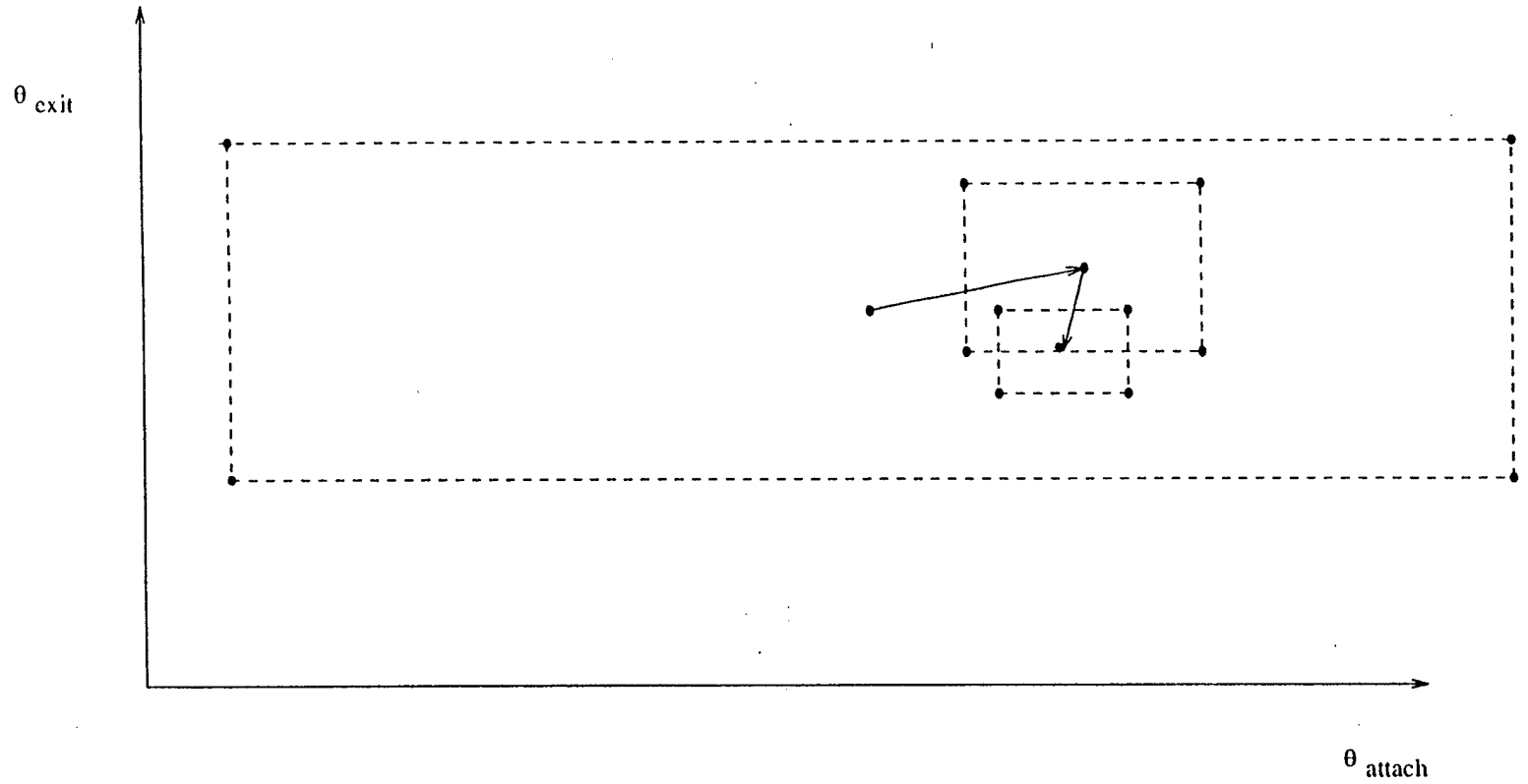

Fig. 111 Decrementing of Sampling Stencil Size in Sect. 5.3

Fig. 112 Decrementing of Sampling Stencil Size in Sect. 5.4

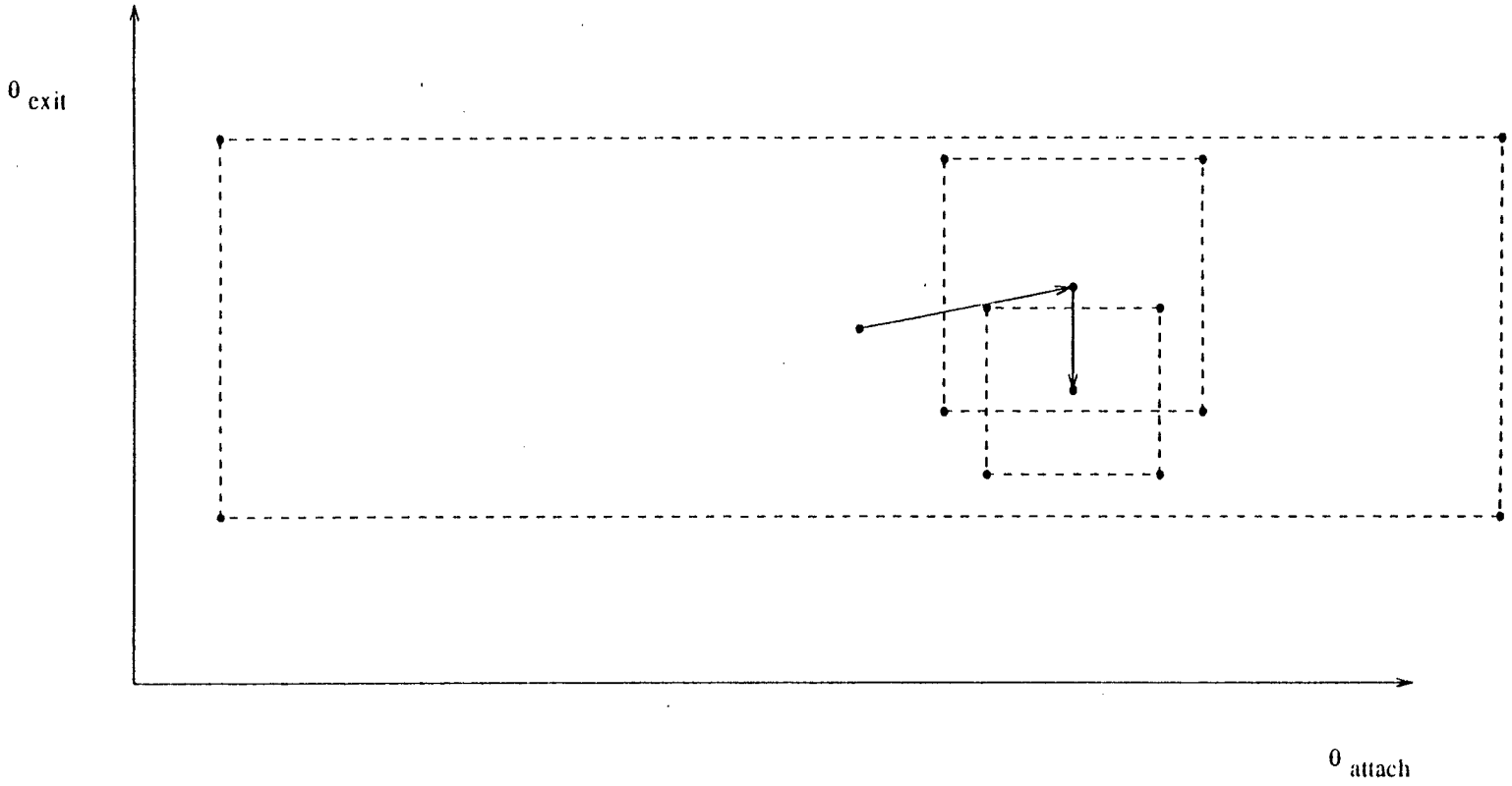

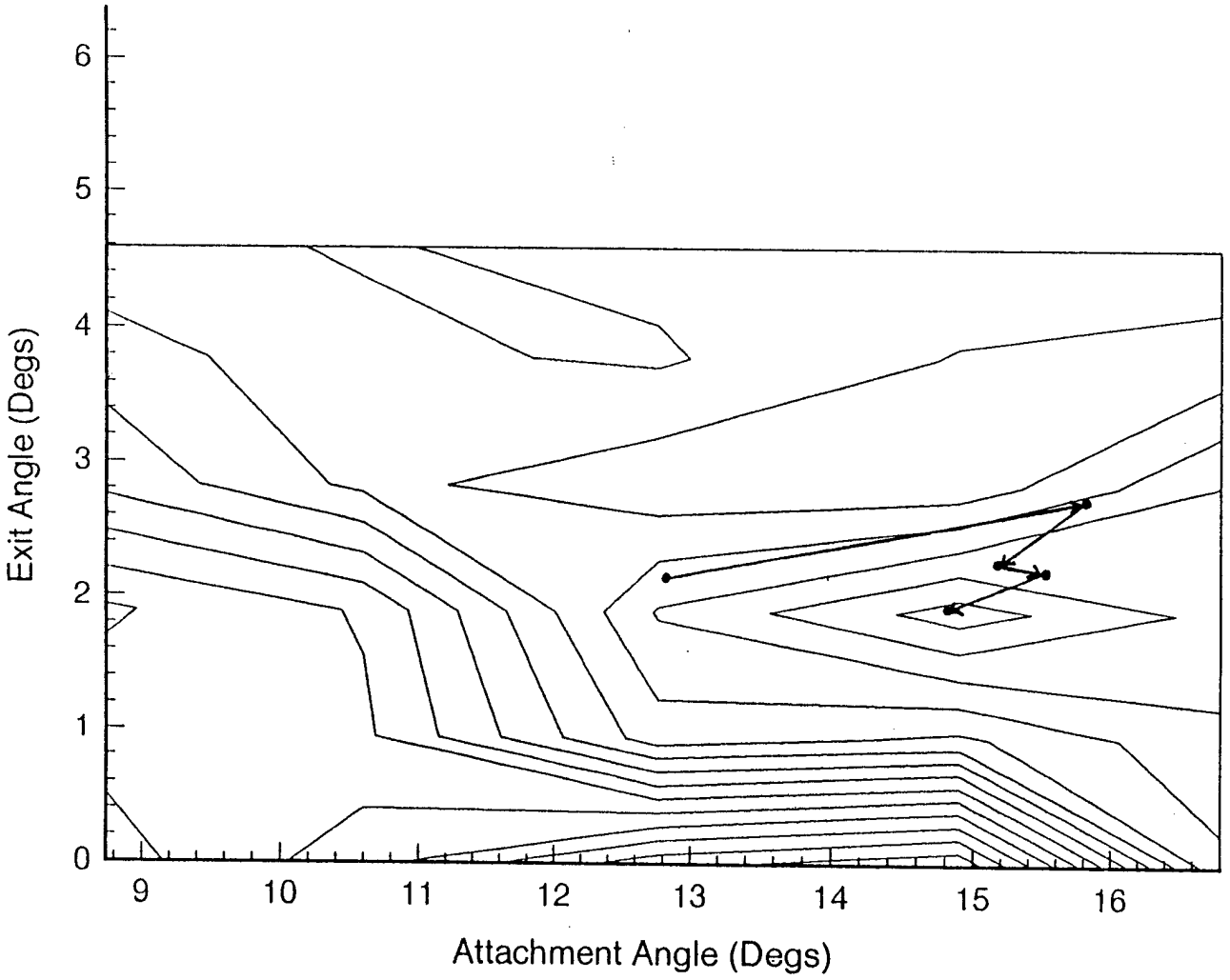

Fig. 113 Search Path Undertaken During Automatic Search, Sect. 6.1

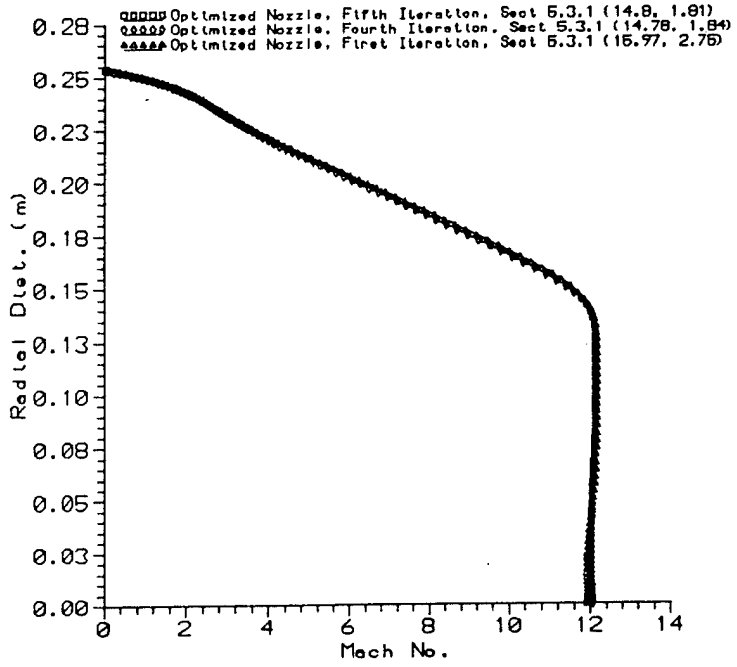

Fig. 114 Mach No. Profile at Exit of Automatically Optimized Nozzle (3.048 m)

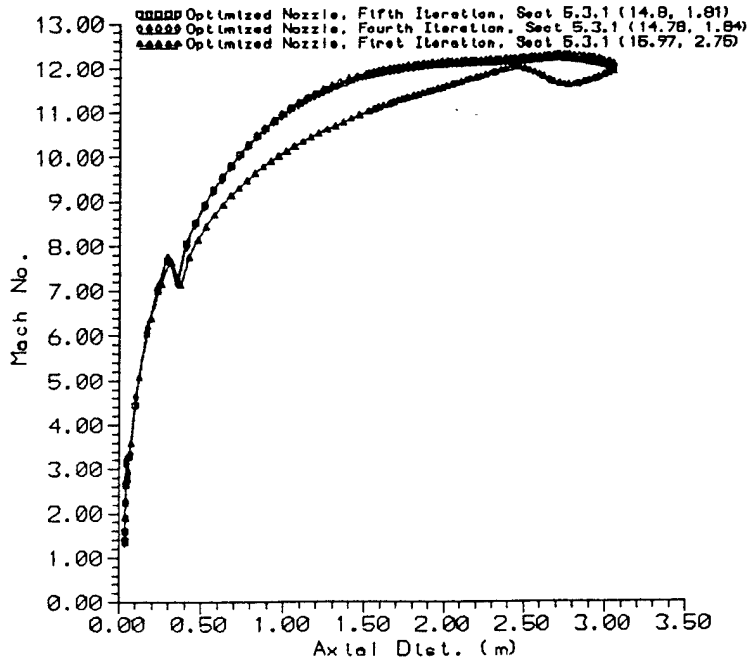

Fig. 115 Mach No. Along C/L of Automatically Optimized Nozzle, (3.048 m)

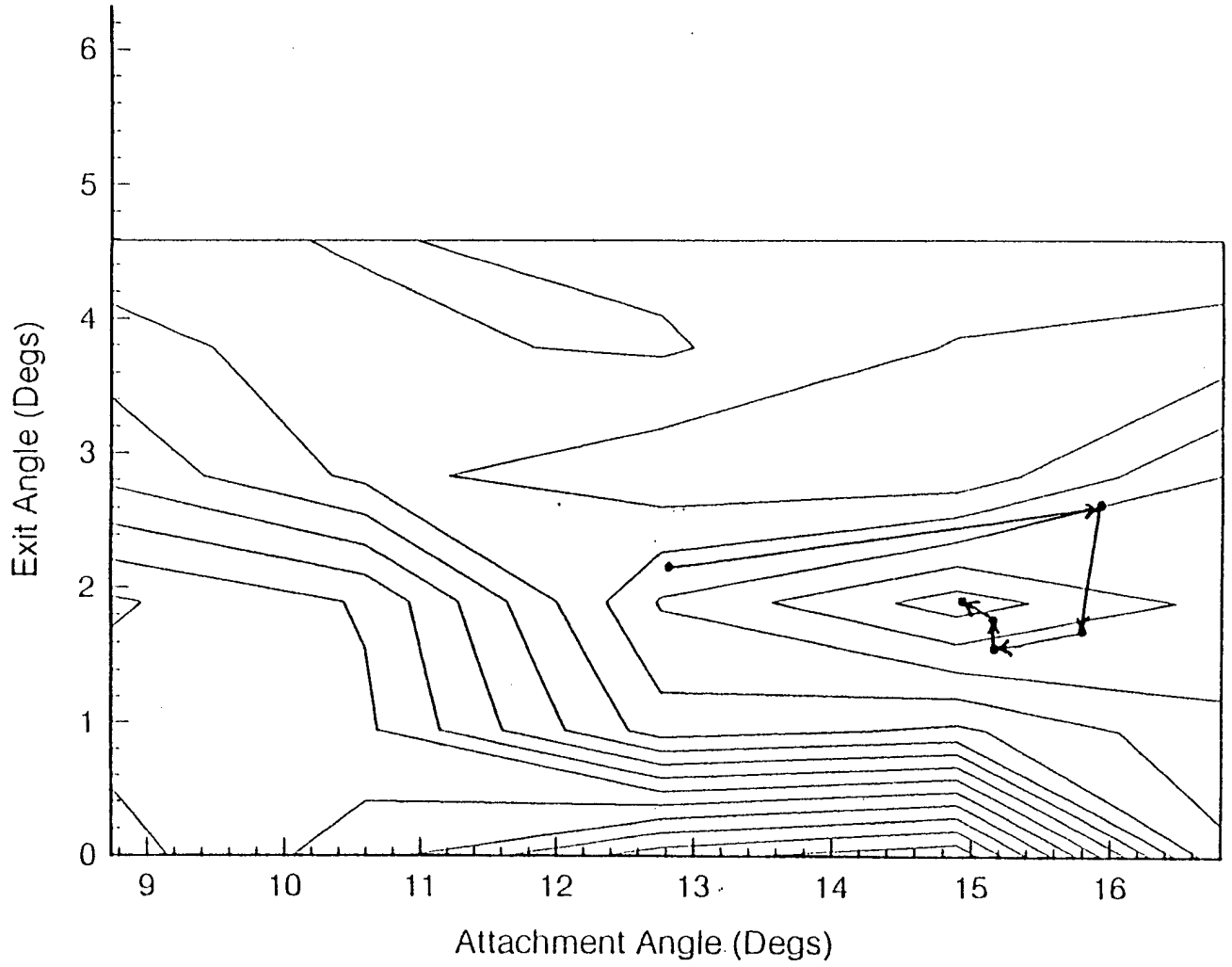

Fig. 116 Search Path Taken During Efficiency Check, Sect. 6.2

Fig 117 Search Path Taken During First Robustness Test, Sect. 6.3

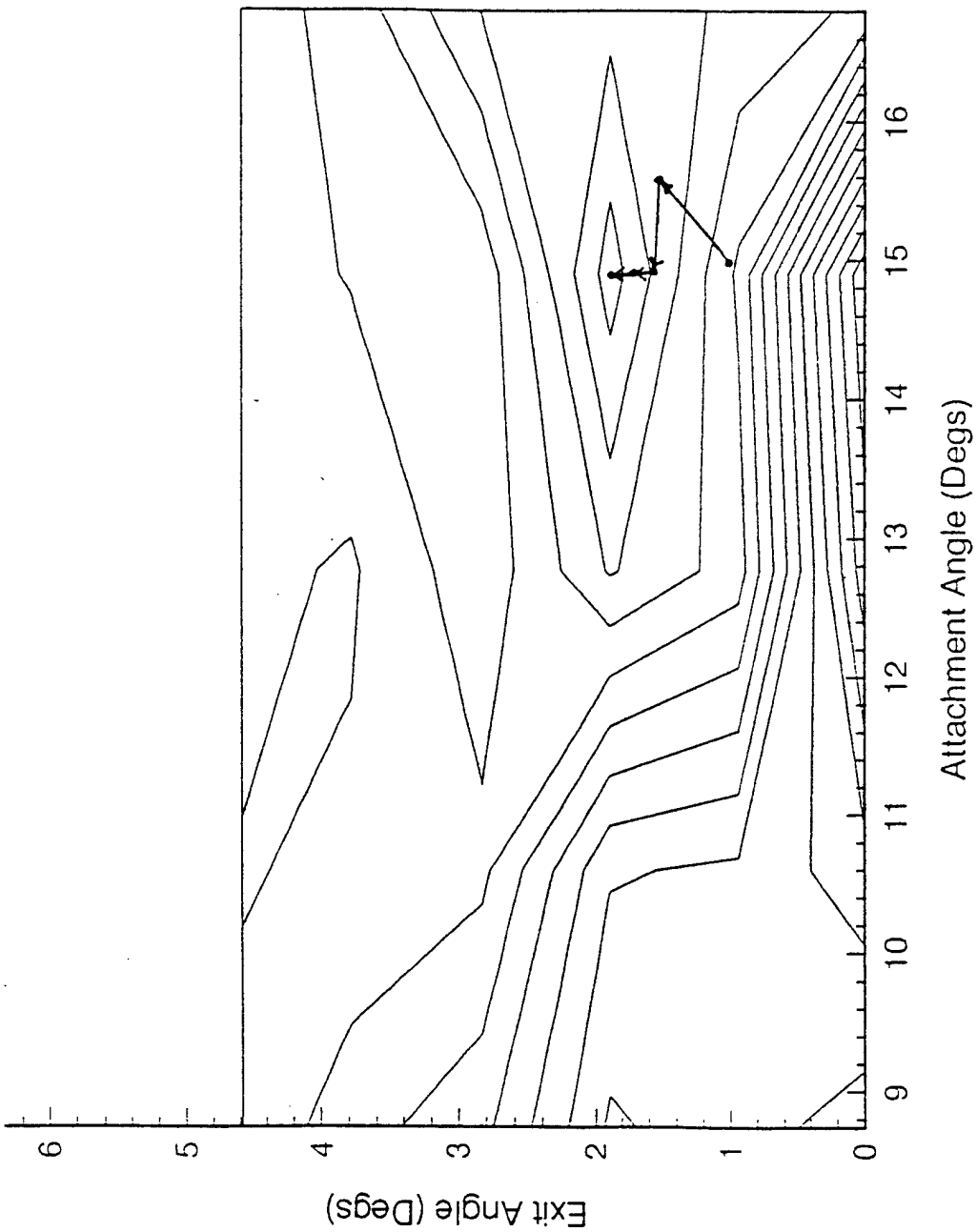

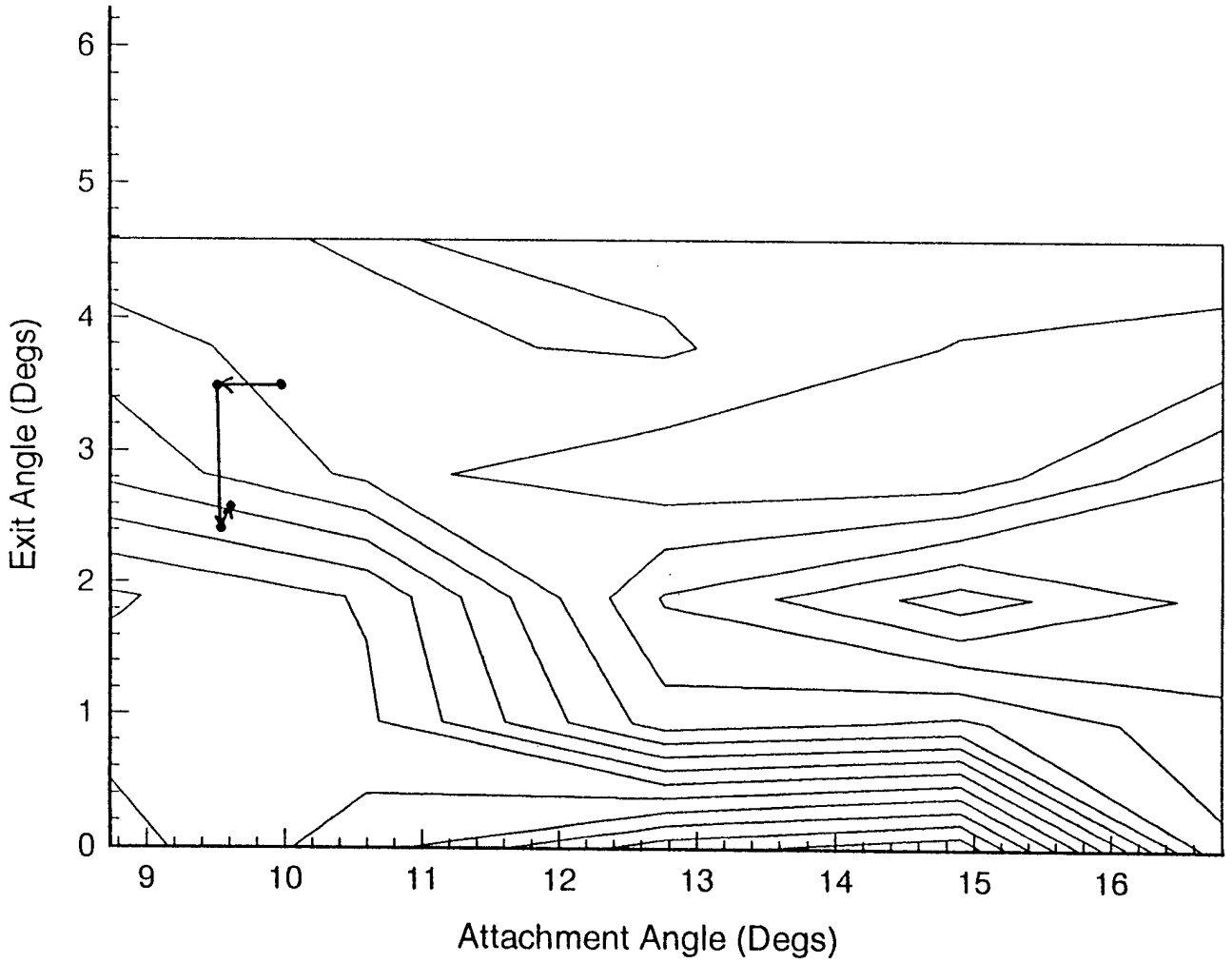

Fig. 118 Search Path Taken During Second Robustness Test, Sect. 6.4

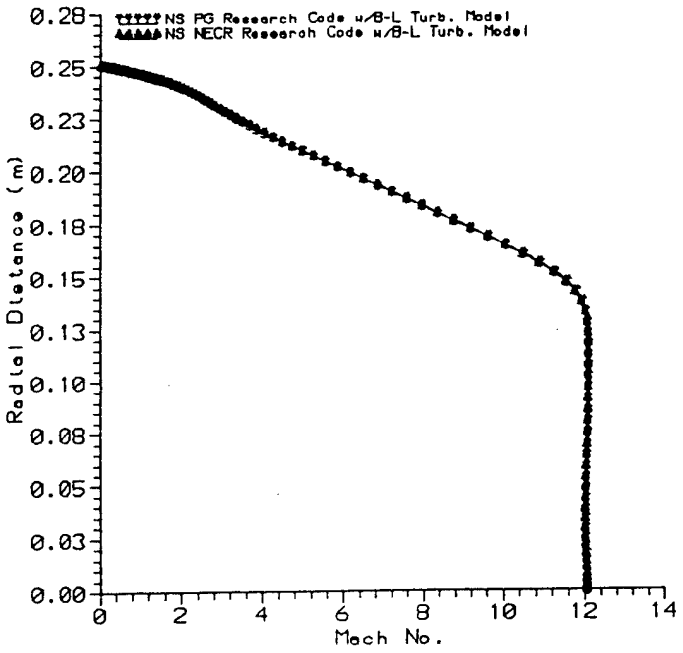

Fig. 119 Mach No. Comparison Near End of Newly-Designed Nozzle, Sect. 6.5 (2.950 m)

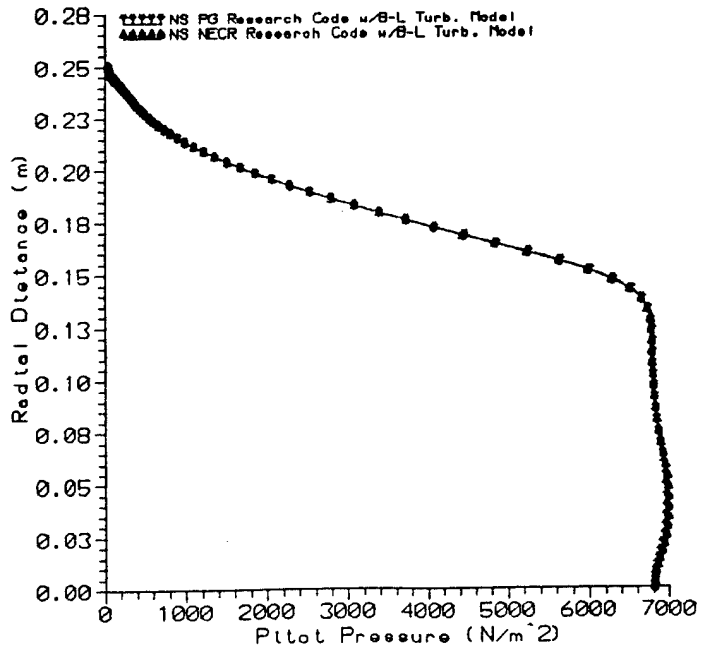

Fig. 120 Pitot Pressure Comparison Near End of Newly-Designed Nozzle, Sect. 6.5 (2.950 m)

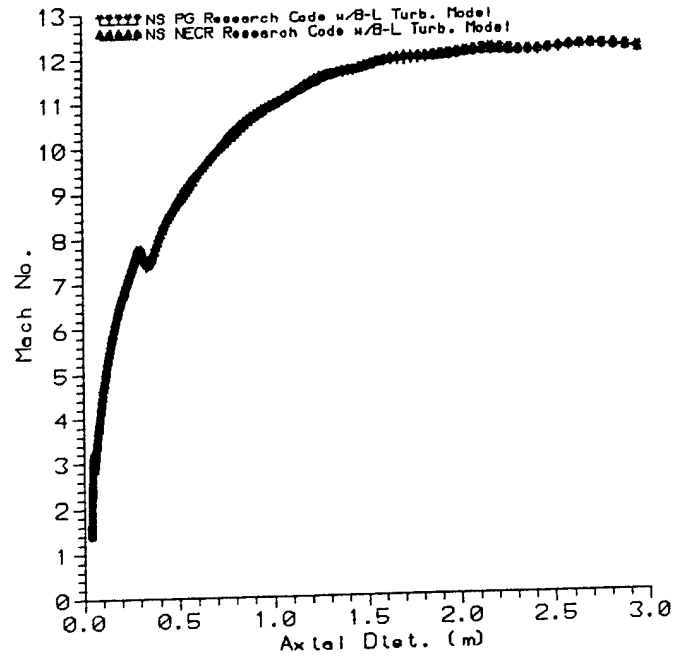

Fig. 121 Mach No. Comparison Along C/L of Newly-Designed Nozzle, Sect. 6.5

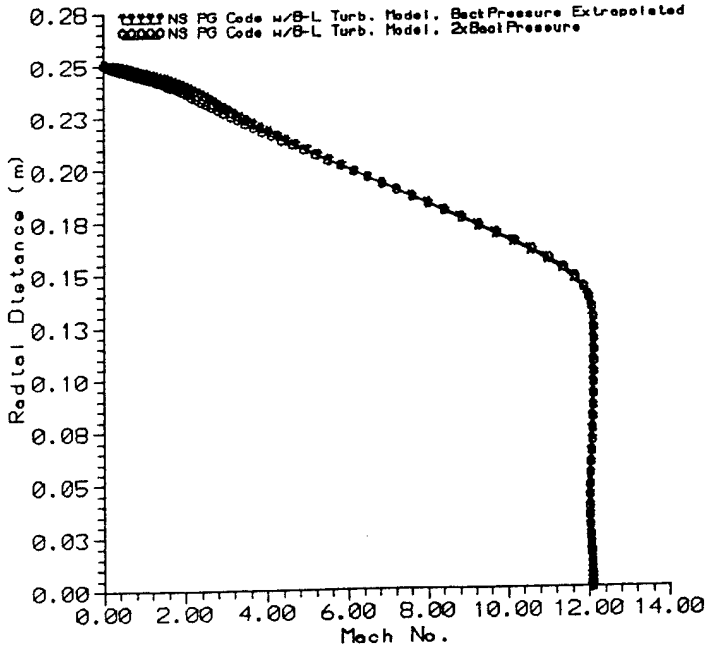

Fig. 122 Mach No. Comparison Near End of Newly-Designed Nozzle w/Increased Back Pressure, Sect. 6.6 (2.950 m)

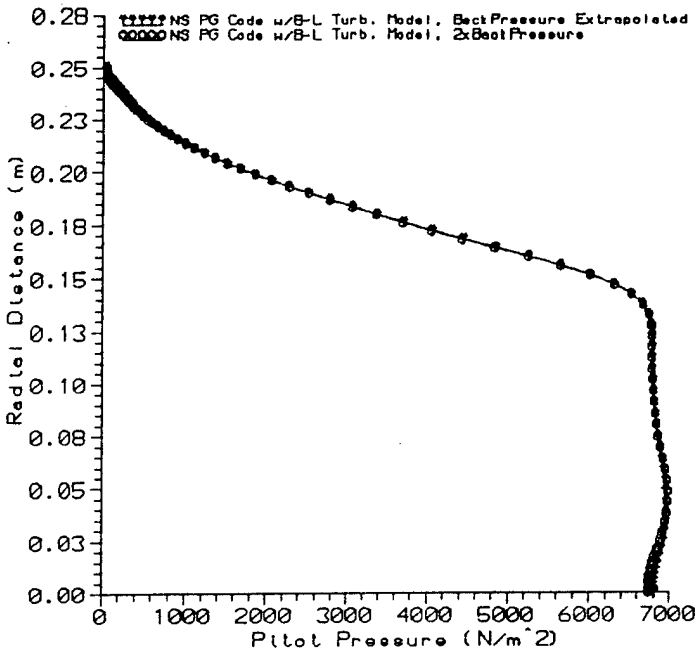

Fig. 123 Pitot Pressure Comparison Near End of Newly-Designed Nozzle, w/Increased Back Pressure, Sect. 6.6 (2.950 m)

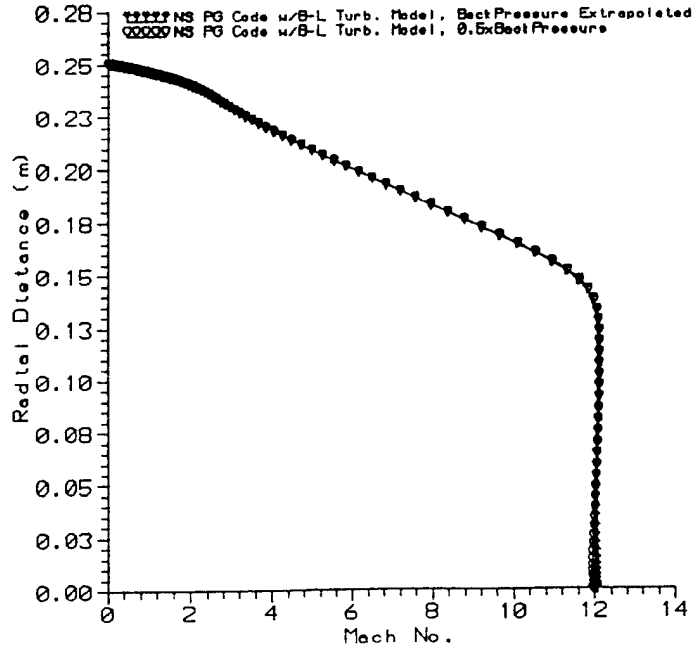

Fig. 124 Mach No. Comparison Near End of Newly-Designed Nozzle, w/Decreased Back Pressure, Sect. 6.6 (2.950 m)

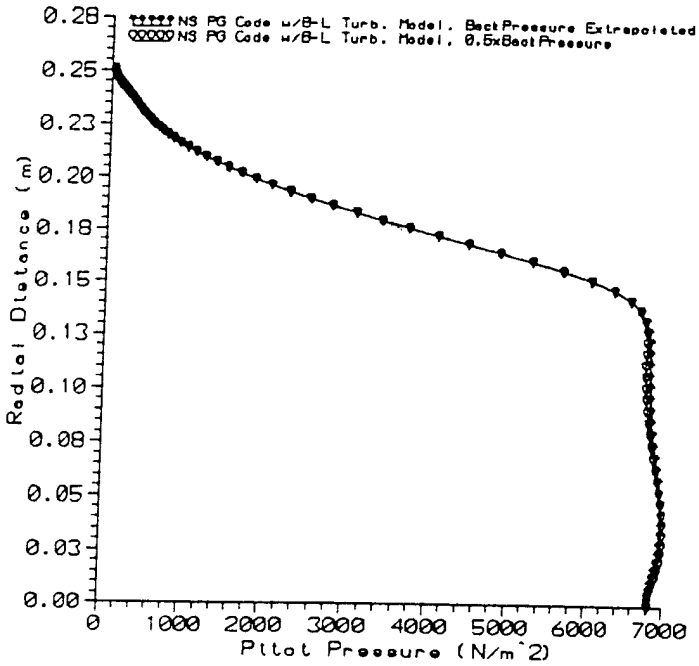

Fig. 125 Pitot Pressure Comparison Near End of Newly-Designed Nozzle, w/Decreased Back Pressure, Sect. 6.6 (2.950 m)

Vita

Captain Ralph C. Tolle was born on 23 April, 1955 in Lesigny, France. He graduated from Los Amigos High School in 1973 and enlisted in the Air Force, serving as a Voice Processing Specialist from 1974 to 1982. He attended the University of Southern California under the Airman Education and Commissioning Program, graduating Magna Cum Laude and receiving the degree of Bachelor of Aeronautical Engineering in December 1984. Upon graduation, he attended Officer's Training School at Lackland Air Force, where he was a distinguished graduate. After commissioning, his first assignment was to the 1st Manned Spaceflight Squadron at NASA Johnson Space Center, where he was a Senior Space Shuttle Simulations Instructor. In 1989 he entered the Graduate School of Engineering, Air Force Institute of Technology and was awarded the Master of Science degree in December of 1990. He immediately entered the doctoral program in January of 1991, and was transferred to the Experimental Operations Branch of Wright Laboratory in January of 1994.

Permanent Address: 18020 4th Ave NW
Seattle, WA 98177